GPU-BASED MONTE CARLO APPLICATIONS IN RADIATION MEDICINE

by

YOUFANG LAI

Presented to the Faculty of the Graduate School of

The University of Texas at Arlington in Partial Fulfillment

of the Requirements

for the Degree of

DOCTOR OF PHILOSOPHY

THE UNIVERSITY OF TEXAS AT ARLINGTON

December 2021

ACKNOWLEDGEMENTS

Time flies. This is the first thought when I am looking back the whole period at the very time point now. Pursuing a Ph.D. degree is not like an easy game, which you know eventually will be conquered or could be restarted when you fail. There came with all kinds of negative feelings during the process, ambiguity, hesitation, anxiety and loneliness, which could devour you, especially when quarantine in pandemic becomes a new common standard. But now I am able to stand at this point, summarizing the past three years. It is impossible without others' support and guidance. I do want to sincerely thank all the people who have supported and guided me.

I would like to thank my supervisors Dr. Chi and Dr. Jia for their invaluable advice during the course of my doctoral studies. They are constantly motivating and encouraging me, which supports me as a newcomer from condensed matter physics to medical physics. They also provided massive chances for me to collaborate with other researchers and to present myself. This is quite important in finding joys of research. I wish to thank Dr. Qiming Zhang, Dr. Mingwu Jin, Dr. Zui Pan and Dr. Amir Shahmoradi for their interest in my research and for taking time to serve in my dissertation committee. I want to thank my colleagues in UT Arlington and UTSW and collaborators from other facilities for providing excellent academic environment and inspiring discussions.

I would also like to extend my appreciation to Dr. Chenyang Shen and Dr. Liyuan Chen for their advice to my career and the joy we shared as friends. I would like to thank Dr. Jianbo Fu and Dr. Zhigang Song for encouraging me to pursue

graduate studies and inspiring me when I felt frustrated. I also want to express thanks to Guo Long, Yuting Peng and other friends, whose names are too long to list completely here, for helping me settle down, uniting me in a group and encouraging me.

Finally, I would like to express my deep gratitude to my girlfriend Yuhuan Wang and my family for their sacrifice, encouragement and patience throughout the graduate studies. Physical separation did not cause emotional distance, which might have been more severe due to the pandemic. In contrast, we stood closer. I am extremely fortunate to be so blessed.

November 18, 2021

ABSTRACT

GPU-BASED MONTE CARLO APPLICATIONS IN RADIATION MEDICINE

Youfang Lai, Ph.D.

The University of Texas at Arlington, 2021

Supervising Professor: Yujie Chi

Co-supervising Professor: Xun Jia

Radiation can be used to image tumor site or kill tumor cells noninvasively, playing an important role in tumor diagnosis and treatment. Because of the increasing burden that cancer brings to the society, there always exists the demand of improving imaging resolution and contrast and improving radiation conformity for therapy. This depends on not only the advances of techniques, but, probably more importantly, the accurate and efficient modelling of radiation transport, enabling research on proof-of-concept for new tech and more complicated physics and chemical process in a quantitative way. Monte Carlo (MC) simulation method has been extensively used in medical physics to model particle transport and calculate corresponding desired information such as dose deposition, because it can describe the physics and chemical process in a faithful way and handle different geometry configuration flexibly. Recent years have witnessed the success of MC method in guiding design of new detectors, scattering correction, dose calculation and simulation of DNA damage to better understand radiation induced damage etc.. Yet, MC simulation still suffers

from low computational efficiency, which restrict the problem size or complexity for research and shows difficulty in meeting clinical on-site requirements.

Graphical Processing Unit (GPU) provides a solution to this issue, because it can accelerate program by parallelism. However, the adaption of MC code into GPU compatible version is not trivial, considering the possible slowdown or even mistakes due to improper handle of race condition and thread divergence in parallel programming. It is of great importance to develop stable GPU-based codes and validate them. The developed codes should hide details like memory operation to users but allow flexible input, thus being beneficial to both research and clinical communities. This thesis targets on this purpose and has conducted a lot of code development and application tests. Specifically, We developed gPET for simulation of positron emission tomography (PET) and studied performances of designs of PET scanner. We also developed source models for MRI-LINAC based on gDPM, a code for MeV photon and electron transport. We pointed out again the defects in determining dose for biological experiments by gCTD, a code for keV photon transport. The simulated results deviated from hand-calculated results by look-up table or the assumption that dose is uniform.

In addition, We did a lot of studies in microscopic simulation, along with the development of gMicroMC. We gradually added support for electron transport, heavy ion transport, presence of DNA in chemical stage and presence of oxygen in chemical stage. We used it to study the parameter sensitivities, showing that the cross section and the damage model for DNA strand break are still the biggest issues. We studied the dose inhomogeneity in proton irradiation scenario. DNA damage was shown to vary in different cells and its relationship to cell survival fraction was updated as well. We also studied radio-protective effect of hypothermia, where diffusion and chemical reaction rates were thought be altered by temperature change. The curves of normal

tissue complexity probability (NTCP) and number of DNA doubles strand breaks (DSBs) coincided for different temperature. Our results showed that less initial DNA damage at low temperature was the reason for radio-protective effect of hypothermia.

Further, we studied the radical yield with different oxygen concentrations. We concluded that oxygen was not likely to be depleted purely by water radiolysis no matter how large the dose rate was for given dose 30 Gy. We also built a model for oxygen enhancement on DNA damages. This model was applied to high dose rate condition again to study the effect of pulse width, pulse interval, dose in the pulse on the DNA damage yields. It was shown that only when pulse was short enough that DNA damage yield had a decent reduction. Our results might provide an explanation for FLASH therapy sparing normal tissues.

TABLE OF CONTENTS

Appendix

LIST OF ILLUSTRATIONS

LIST OF TABLES

CHAPTER 1

INTRODUCTION

1.1 Cancer and radiotherapy

Cancer is a group of diseases characterized by the development of abnormal cells that divide uncontrollably with the potential to invade or spread to other parts of the body. It causes approximately ten million deaths over a year and leads to one in five deaths worldwide as of 2020 [1]. What is even worse is that the number of cancer cases is increasing continuously and quickly. Cancer has even been the leading cause of death in many parts of the world, resulting in a great burden to the society and demand of effective treatment method [2, 3].

There are a few ways to fight cancer [4]. Surgery could serve as a direct method to remove tumor part, reducing the threat and possibly allowing the body to heal by itself. Radiotherapy, which uses radiation to cause DNA damage and thus cell death, is also a good alternative if we can focus radiation in tumor site. Chemotherapy uses drugs to prohibit cell proliferation, preventing cancer cells from multiplication, invasion or metastasis and eventually killing cancer cells [5, 6]. Recently, immunotherapy attracts a lot of attention, which targets on stimulating immune cells rather than killing cancer cells directly [7]. Among all of these methods, radiotherapy stands out for its availability, effectiveness and reliability. It applied to almost all kinds of cancers [8] and achieved excellent tumor control for non-metastasized tumor. Nowadays, Approximately 50% of all cancer patients receiving radiation therapy at some point of their treatment process. It contributes towards 40% of curative treatment for can-

cer [8–10]. Substantial numbers of patients with common cancers achieve long-term tumour control largely by the use of radiation therapy.

Application of radiation in cancer management dose not have a very long history, but it has witnessed fast evolution over the last few decades [11–13]. Short after the discovery of X-rays by Wilhelm Roentgen at 1895, radiation was used to treat breast cancer, gastric carcinoma [12] and skin cancers [14], although poor knowledge was known on how it worked. Almost in the same time, Antoine Becquerel discovered natural radioactivity and Curie couples discovered radium and polonium, indicating a new era to use radioactive seed as internal radiation source (brachytherapy) for cancer treatment. Later due to the development of particle accelerators, particles could be accelerated to energies exceeding those occurring in natural radioactivity with a controllable way [15, 16]. Especially, the microwave accelerator for electron could generate stable MV electron beam easily, laying the foundation of a most important clinical modality – LINear ACcelerator (LINAC). The development of accelerator also gave birth to electron therapy, neutron therapy and heavy ion therapy including proton therapy [17]. The last one – heavy ion therapy is gaining more and more attention now because of their unique dose-depth curves and higher relative biological effect (RBE), which allows for better dose delivery in tumor while sparing normal tissues. Nowadays, radiation therapy has become an important component of cancer treatment. Particularly, the technology advances in image guidance and treatment delivery techniques enables radiation targeting on tumor more precisely while reducing the margins and high gradients outside the target, for example Stereotactic radiosurgery (SRS) and Stereotactic Body Radiation Therapy (SBRT) [18] and pencil beams for heavy ion therapy [19].

1.2 Radiobiology and imaging for radiotherapy

The role that radiotherapy plays in cancer treatment emphasizes the importance of improving understanding of radiotherapy. In fact, radiation oncology has always been at the interface of physics, engineering, biology and medicine. This is because radiation kill cells regardless whether the cell is abnormal or not. Hence, it is of great prominence to deliver more radiation damage into tumor cells while sparing normal tissues as much as possible to achieve better performance of treatment. To achieve this goal, we should first identify the quantity that indicates the level of radiation damage so that we could optimize a treatment plan. Second, we must have some label techniques that could help us differentiate tumor cells from normal tissues.

1.2.1 Quantification of radiation damage

Historically [20], exposure, number of electron freed in air by X-rays per unit mass, was first introduced to describe the radiation intensity. But it is neither applicable for other radiation types like proton beam nor related to radiation received by the medium [1], being not a good indicator. Later, concept of absorbed dose, energy absorbed by unit mass of medium, was proposed. This concept well represents radiation damage from physical viewpoint. Human body could be viewed as water and the average ionization energy per event could be obtained. Thus, absorbed dose gave average number of ionization events per unit mass equivalently, which could be related to number of chemical bond breaks, describing the radiation damage to initial system. It indeed achieved great success in describing many variables, for instance linear quadratic (LQ) model for cell survival [21, 22]. Dose values are widely used in determining safety thresholds and medical standards as well.

[1] Transformation might be conducted but there exists restrictions

On the other side, experiments have found that different radiation types, for example X-ray and proton, may result in different biological outcome even when dose is same. Oxygen level has also been shown to critically affect cellular response to radiation. The existence of oxygen could increase cell kill by 3-fold [23, 24]. These findings push us to investigate deeper and understand cellular behavior better.

Modern developments in cellular and molecular biology have shown that the primary target of radiation damage is DNA through many experiments [25–27]. For instance, integration of radiation source into cell nucleus greatly enhanced the cell death [26]. The complete picture for radiation damage should include chemical part as well. Besides damaging DNA molecules directly, source particles mainly interact with water molecules since water is the most abundant component in cell, making them ionized or excited through electromagnetic interactions. Heavy ions and neutrons could also induce nuclear reactions. The ionized or excited water molecules then need to decay into ground state, through which numerous radicals are generated. One of them, hydroxyl, needed to be specially pointed out because they could cause DNA damage by abstracting hydrogen atoms from DNA molecules, particularly on sugar-phosphate group, which could eventually cause DNA strand breaks (SBs). Other radicals like $H^{\cdot}$ and hydrated electron e_h that could also cause DNA damage, but it would be mainly on base pairs due the difference of chemical reaction rates. The base damage could be transformed into SBs in some studies [28, 29]. These SBs, including those induced by energy deposition directly, determine the DNA damage patterns, i.e. single strand breaks (SSBs) and double strand breaks (DSBs). Upon the SBs are formed, cells would evaluate the circumstances and determine whether to undergo apoptosis, repair process or ignore the damage. This is a complex signal cascades, which requires participation of a lot of proteins [4]. DSBs are thought to

be the principal lethal factor [30] for they are harder to repair. It will be very helpful if one can simulate DNA damages from a given beam geometry.

1.2.2 Medical imaging techniques

Besides the increasing deeper understanding of radiobiology, the development of imaging techniques is another important reason for ensuring quality of tumor treatment. With improvements of de-noising and reconstruction in both hardware and software aspects, the resolution of current medical images could easily reach 1 mm, increasing the diagnosis accuracy. Moreover, the technique advances also enable the real-time image guidance [31], which is better for correcting uncertainties due to dynamic movements.

There are many medical imaging techniques that can assist diagnosis or treatment of cancer in a non-invasive way. The concerning techniques in this thesis are X-ray radiography, X-ray computed tomography (CT), Positron emission tomography (PET) and single photon emission computed tomography (SPECT) because radiation is involved. Their mechanisms have been well explained in many references [32, 33]. Here, we just briefly summarize them for a completeness. The above methods can be divided into two categories based on the mechanisms. One is transmission tomography, including X-ray radiography and X-ray CT. The other one is emission tomography, including PET and SPECT.

For transmission tomography, the essential part is photons that go through a medium may undergo different interactions such as Compton scattering, photoelectric effect, which causes the reduction of number of photons travelling in the same direction as its original one. Mathematically, the beam intensity I' after a medium with thickness l should be $I' = I_0 * e^{-\mu l}$ where I_0 is the original intensity and μ is called linear attenuation coefficient. μ is a physical property and can be used to

distinguish materials. When the path consists of different materials, one can divide the path into many small segments and view it as uniform in each segment. Thus, $I' = I_0 * e^{-\sum_i \mu_i l_i}$. Each line from source to detector unit defines a line integral of μ. By rotating photon source and detector, equations of line integral of μ are obtained and mathematical methods could be applied to find their values. Finally, 3D figure of the imaged region could be obtained.

As for emission tomography, the imaging mechanism is trying to find the distribution of radionuclides. Typically, specially designed drugs with radionuclides can accumulate in tumor sites. Hence, the imaging of radionuclides is also an imaging of tumor site. Take PET for example [34], tumor consumes glucose faster than normal tissues. Then glucose analogue FDG, labeled with ^{18}F, will accumulate in tumor site. The emitted positron only travels several mm from its emitter and annihilate to two photons that go towards almost opposite direction. One photon pair gives possible location of source along the line that connects the pair. And many photon pairs depicts the region that source located, namely the profile of tumor site. The advantage of using labeled molecules also provides us a way to track drugs dynamically.

The mechanism described here is definitely too ideal. In practice, source size, scattering correction, beam hardening etc. should be considered for CT and positron range, non-linearity, scattering etc. should be considered for PET, for example. All of these factors need to be modelled carefully and correctly. The model needed here and that for calculating dose distribution or DNA damage are quite similar. The purposes of these models are trying to transport particles and obtain information like distributions of energy depositions and locations, particle speeds and production of secondary electrons along the path. In this way, either dose distribution in a phantom or photon energy deposition on a detector after a phantom could be obtained and analyzed. And this is why magnetic resonance imaging (MRI), ultrasonography and

other imaging methods are not listed here. Nevertheless, it requires the modelling method to be faithful in describing physics and flexible in describing geometry. And Monte Carlo method can help a lot in these two aspects.

1.3 Monte Carlo Method in radiation medical physics

1.3.1 Definition and methods

Monte Carlo (MC) was described by Metropolis and Ulam [35] as "a statistical approach to the study of differential equations, or more generally, of integro-differential equations that occur in various branches of the natural sciences." The core of outlined MC schema for a practical physics problem is to formulate physics problem mathematically and relate quantity of interest with statistical parameters of the problem such as mean value of a distribution [36]. For example, one of the important step in transporting particles is to find step length s, provided we know the mean free path $\bar{l}$ at current point. This physics problem could be formulated as drawing samples from a distribution, namely $P(s) = \frac{e^{-s/\bar{l}}}{\int e^{-s/\bar{l}}}$.

Basically, the aims of MC methods are try to solve two kinds of problems [37]:

1. generate samples from a given probability distribution $p(x)$;
2. estimate the integration of a function under a given probability distribution $p(x)$, namely

$$\overline{f} = \int dx p(x) f(x). \tag{1.1}$$

And the second one could actually be solved by solving the first one. Estimator $\hat{f} = \frac{1}{N} \sum_{x \sim p(x)} f(x)$, where $x \sim p(x)$ means drawing samples from $P(x)$ and N is the sample size, is an unbiased estimator for $\overline{f}$ and variance approach 0 when N goes to infinity. So, the essence of MC methods is to draw samples from a distribution related with a physics problem.

There are many MC methods to draw samples. Here, we only briefly introduce four methods that are employed in this work.

Direct inverse method Suppose we could integrate $p(x)$ to find the cumulative distribution function $P(x)$

$$P(x) = \int_{-\infty}^{x} f(t)dt. \tag{1.2}$$

To generate samples X from $f(x)$, we could sample ξ from $U(0,1)$, where $U(0,1)$ means uniform sampling between 0 and 1. Then,

$$X = P^{-1}(\xi) \sim f(x). \tag{1.3}$$

P^{-1} means the inverse function of P.

Rejection Sampling Suppose $q(x)$ is a distribution that could be easily draw samples, for instance uniform sampling. And $q(x) > p(x)$ for each point x. Then, we could draw sample X from $q(x)$ and ξ from $U(0,1)$. If $\xi > p(X)/q(X)$, we abandon the sample and redo this process. Otherwise, we accept it. The remaining sequence of X follows distribution $p(x)$.

Metropolis sampling Suppose the range of x, where $p(x)$ is defined, is known and denoted as R_x . In other words, $\int_{R_x} p(x)dx = 1$. The sequence of samples after n times sampling is $\{X^1, X^2, \cdots, X^n\}$. For the $n+1$th sampling, we draw ξ uniformly from R_x and have $a = \frac{p(\xi)}{p(X^n)}$. If $a > 1$, we accept ξ. Otherwise, we draw another sample $\psi \sim U(0,1)$, we accept ξ if $\psi < a$. Here, "accept" means $x^{n+1} = \xi$.

Importance sampling This is actually not a method to draw independent samples, but to calculate integrals. Suppose both $p(x)$ and $q(x)$ are normalized, we then have

$$\hat{f} = \frac{1}{N}\sum_{x\sim p(x)} f(x) = \frac{1}{N}\sum_{x\sim q(x)} \frac{p(x)}{q(x)} f(x) \tag{1.4}$$

1.3.2 Applications in medical physics

Advantages The interest in MC method in radiation medical physics has grown rapidly [38–40]. One reason is that the rising need of accurate numerical methods for a variety of transport problems. For example, treatment planning with constraints on 3D dose distributions. Dose calculation error is suggested to not exceed 2% [36]. From above text, we know MC method provide accurate description solution to a problem that could be formulated. Another advantage of applying MC method is the flexibility in describing geometry by voxelization, namely gridding the space. For example, the voxelized geometry could be consistent with the step-by-step transport schema of MC. Although it increases the difficulties in dealing with crossing voxel boundaries, voxelization is an effective method to describe geometry with any shape.

Classification MC simulation in medical physics could be generally divided into two categories based on the step length: macroscopic one with step length of mm or cm scale and microscopic one with step length of μm or nm scale. The simulation schemes for two scenarios are pretty different. The macroscopic simulation usually transport particles to get dose deposition in a large volume, for instance, dose deposition in side patient body with a therapeutic MV beam. For such simulations, scattering events are merged so that large step size could be used. The strategies of photon interaction with medium, continuous slowing down approximation for transporting charged particles etc. have been extensively discussed in many works [36, 39–45] and therefore are omitted here. The microscopic simulation usually transport charged particles to get the so-called track structure [46], namely detailed information for every scattering events, for example, scattering event types, status of excited water molecules. The step size is thus very small to allow explicit simulation of each events. From the track structure, one can calculate the quantities for microdosimetry [47–49] or further simulate DNA damages with proper DNA structure [50–52]. The usage

of microscopic simulation in calculating DNA damages will be further elaborated in chapters 4 and 5.

Disadvantages MC simulation is a computationally demanding task in radiation medical physics. For dose calculation purposes, although MC is an accurate method, it remains accurate in terms of statistical context. A large number of particle histories have to be simulated to achieve a desired level of statistical precision. Further, the increasing number of voxels with increasing problem size putting an even more heavy burden on computational efficiency. As for the computations of track structure, the continuous slowing down approximation for charged particles cannot be used, and the event-by-event simulation scheme substantially increases the number of computational steps. In addition, reactions among the large number of radicals and DNA structure with billions of base pairs (bps) further increase computational complexity dramatically for interacting many-body problem, not to mention that such process has to be gone through thousands times for temporal length spanning multi magnitudes. Over the years, improving the computational efficiency of MC simulations to facilitate large-scale research uses and clinical applications is always an active field [40, 53].

1.4 GPU applications

One straightforward way to improve the computational performance is to apply parallelism. If the task could be divided into several small tasks with same physics but different problem size, one may distribute those small tasks to different computational units. Therefore, a decent speedup could be expected. For examples, if a dose calculation requite 10^{10} photons to achieve required dose uncertainty levels, we might use 100 CPU cores and each of them runs 10^8 photons. At last, the summed dose

deposition from 100 CPU cores is equivalent to running 10^{10} photons in one core, but the computational time is expected to be only $\frac{1}{100}$ of that for one core.

GPU is a computing architecture originally designed to handle extensive computational tasks in computer graphics, such as rendering images in computer games. But later, this design was found to be suitable for many scientific problems, for example, matrix multiplication [53, 54]. GPU offers several advantages for applications in radiotherapy. First, GPUs offer a relatively low-cost solution than CPU clusters. One common GPU card costing only thousands of dollars could easily have thousands of computing units while it is not that easy to have thousands of CPU cores. Second, GPU is very easy to install and maintain as it can be integrated into personal desktop. Third, the GPU performances have been greatly improved and is continuously evolving [55]. And due to the technology advances, the latent due to data transfer in GPU computing is usually negligible because of the high bandwidth between the CPU and GPU memory and between GPU memories.

However, previously developed MC packages in CPU cannot be launched on GPU without modifications. Improper use of GPU may hurt the computational efficiency due to possible memory transfer latent and thread divergence. It is necessary to develop GPU-specific packages, including rewriting codes in a programming language compatible with GPU, redesigning the data structure and even algorithm for better performance of parallel computation. Additionally, recent years witnessed the great advance of GPU hardware, for instance, improvement of communication between multi GPUs. It requires developments and very studies for these technique advances. These issues have posed significant challenges for the developers and solving these problems has been an active research topic.

Table 1.1. Brief summary of GPU-based MC packages

Applications		Package name	Reference
Photon only	Light transport	CUDAMCML	[56]
		GPU-MCML	[57]
		CUDAMCFL	[58]
	Light Imaging	MCGPU	[59]
		gCTD	[60]
		gDRR	[61]
	Brachytherapy	gMMC	[62]
		bGPUMCD	[63]
		gBMC	[64]
		irtGPUMCD	[65]
Coupled photon-electron transport		GPUMCD	[44]
		gDPM	[42, 66]
		GMC	[67]
Proton and heavy ions		gPMC	[68, 69]
		goCMC	[70]
Microscopic simulation		MPEXS-DNA	[71]
		gMicroMC	[52, 72]

1.5 Purpose of this work

As summarized in Table 1.1, there are a lot of GPU-based MC packages targeting on general macroscopic dose simulation, especially with photons and electrons. Instead, there are few GPU-based MC packages on microscopic simulation. Particularly, there is no open-source package for microscopic simulation. Thus, this work will focus on two aspects:

1. For macroscopic simulation, we try to provide more GPU-based applications for specific scenario. It should be more practical and clinical.
2. For microscopic simulation, we develop new GPU-based package and apply it to DNA damage calculation, expecting more fundamental research on related phenomena with a prospect of first principle.

With the above two aims bear in mind, this thesis is structured as following. The thesis involved could be divided into two sections. One is for macroscopic simulation with GPU packages, which is related to chapters 2 to 3. We will discuss the development of gPET in chapter 2, which is dedicated to positron emission tomography (PET) simulation. We used it to do a systematic study on the scanner performance and scanner geometry designs. Later in chapter 3, we discuss a source model based on our previous gDPM package. This source model is specifically designed for LINAC. We will also discuss the issue of dose inaccuracies in many biological experiments based on our previous gCTD package.

The other section is microscopic simulation with GPU-based package developed by us, which is related to chapter 4 to chapter 8. In chapter 4, we discuss our initial development of microscopic simulation package gMicroMC, including the electron transport model, DNA model and DNA damage model. We will also talk about the parameter sensitivity. In chapter 5, we will describe our continuous development on gMicroMC for the support of proton transport and concurrent transport of DNA structure during chemical stage. In chapter 6, we then discuss two applications of gMicroMC in sophisticated scenarios. One is the nonuniform DNA damage distribution for proton case and the attempt to connect number of DSBs with SF. The other is the attempt to explain radioprotective effect for hypothermia. In chapter 7, we further update gMicroMC with oxygen included in chemical stage. We use it to study the variation of radical yield under FLASH condition and point out that oxygen is not likely to be depleted by radicals. But, this simulation is done for pure water radiolysis. In chapter 8, We build an OER model on DNA damage enhancement that is suitable for x-ray and proton cases. At the end of this chapter, we reinvestigate FLASH in terms of the change of number of DNA DSBs by incorporating oxygen diffusion and recovering effect.

At last, we will give a short summary about this thesis and future directions in Chapter 9.

CHAPTER 2

GPU APPLICATIONS FOR MACROSCOPIC SIMULATIONS

2.1 Developments for gPET

2.1.1 Background

Positron emission tomography (PET) has increasing importance in modern medicine for both diagnostic and therapeutic applications. Monte Carlo (MC) simulation methods are essential tools for refining current PET systems and developing future systems. In the past few decades, MC simulation has been used extensively for optimizing PET hardware/prototype designs, improving image reconstruction algorithms, and removing image artifacts, etc. [73–77]. In addition to the conventional PET applications, there is an increasing interest in MC simulations for advanced PET applications [78], for example, the MC-simulation-assisted PET system design for online and offline beam verifications in particle therapy [79–85].

To meet the tremendous simulation demands from both conventional and advanced PET applications, several MC packages for PET have been developed. These can be divided into two categories, based on the purpose for their development: the general purpose and the PET-dedicated. The general purpose MC packages, such as Geant4 [86], EGS4 [87] and MCNP [88], are known for their accuracy and versatility. However, there are two obstacles for the wide application of these packages in solving practical PET problems: the complex customization process and the unsatisfyingly long execution time for routine clinical usage, since they were all built on CPU platforms. PET-dedicated MC simulation packages, such as GATE [89], PETSIM [90], SIMSET [91] and PeneloPET [92], usually have user-friendly designs with

pre-customization of the general-purpose-based packages to PET/SPECT specifications. However, the underlying physics cores of these packages are still the same as those in the general-purpose-based ones. Hence, the non-efficiency problem continually exists.

To overcome the obstacle of long execution time, a cost-effective option is to take advantage of the parallel computing via advanced graphics processing units (GPUs). Over the past several years, GPU-based MC simulations for general imaging and therapeutic applications have enjoyed rapid advancements [**despres˙review˙2017**, 42, 93, 94] However, these packages were all general photon/electron transport focused, instead of PET-dedicated. For example, in the hybrid GPU/CPU Geant4 package [94] for PET applications, although the photon transport inside the phantom was realized via GPUs, the pre-processes, from radioactive source decay to positron annihilation, and the post-processes inside the PET detector, from energy deposition to coincidence-pair generation, were still performed on CPUs, which limited the overall speed of PET simulations.

To address this issue, we developed a GPU-based, accurate and efficient MC simulation tool, gPET, dedicated for PET simulation. gPET has three unique features. First, we used a combination of parametrized (for detectors) and voxelized (for patient phantoms) geometries to make gPET applicable for various geometry setups. Second, we used GPU computing to accelerate not only gamma transport, but also other computationally intensive processes, including positron decay, transport and annihilation, and complex PET signal processing inside the detector. Third, we made various input and output quantities available for users such that different aspects of the PET simulation can be examined flexibly.

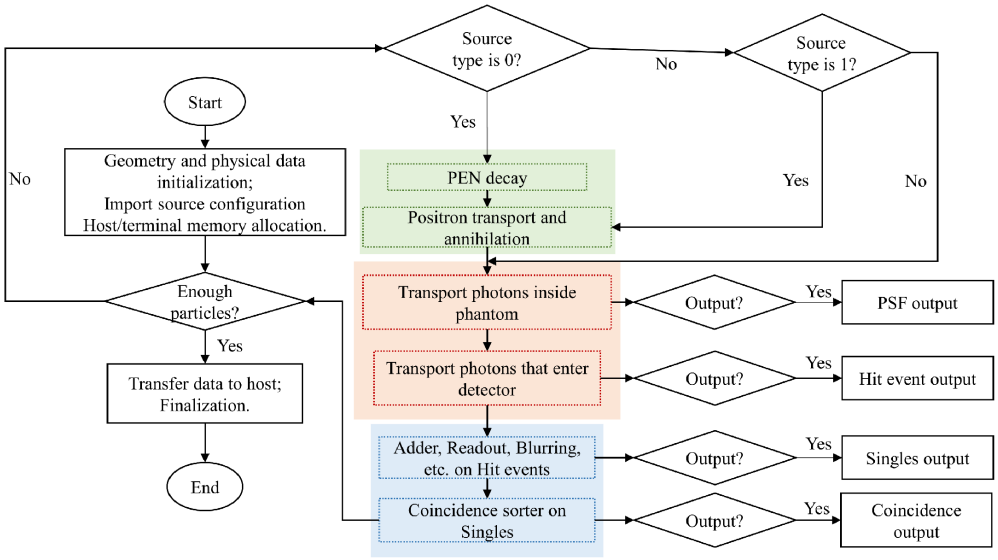

Figure 2.1. Flowchart of the gPET package. The parallelization on the GPU terminal (dash boxes) includes gamma pair generation (green), gamma transport inside the phantom (orange), and gamma signal detection and processing inside the detector (blue)..

2.1.2 Methods and materials

gPET is built on the NVidia CUDA platform. Its overall workflow is illustrated in Figure 2.1. The simulation starts with the geometrical and physical data initialization, data transfer from CPU to GPU, and random number seed generation. The physical simulation process, mainly carried out by the parallel threads at the GPU terminal, is performed for each given history and categorized into three functional modules: 1) gamma pair generation, including positron emission nuclei (PEN) decay, and positron transport and annihilation; 2) gamma transport inside the voxelized phantom, governed by the gDPM algorithm [66]; and 3) signal detection and processing inside the parametrized detector [95], which includes not only electromagnetic processes such as hit recording, but also detector responses such as spatial, tempo-

ral, and energetic resolutions. The detector consists of three levels: panel, module and crystal scintillator (Fig. 2.2). The user can control multiple inputs and outputs for the simulation. The adjustable inputs are mainly particle source-related, including PEN, positron, and gammas. The optional outputs include intermediate photon phase space files (PSFs), hit events (initial energy deposition events inside the detector by incident gammas), single events (detectable energy deposition events after considering the detector response), and coincidence pairs (paired detectable events). After the physics process, the code ends with a data transfer and memory release. The next three subsections will describe the three functional components in detail.

2.1.2.1 Gamma pair generation

Positron Decay from PEN In gPET, if a PEN source is of simulation interest, a user can provide its distribution in a predefined format with voxelized geometry. For each voxel, the following quantities are needed: PEN types, radiation activity (in Bq) of each type, the voxel sizes (in mm3), and the coordinates (in mm) of the voxel center in the global coordinate frame. It is worth mentioning that under this input format, a point PEN source can be simply defined by setting the voxel size to (0, 0, 0). PENs of common clinical or research interests, like Fluorine-18 (18F) in nuclear medicine [96], Carbon-11 (11C) and Oxygen-15 (15O), etc. in hadrontherapy [97] are supported in gPET. The branching ratio of the positron emission mode Γ_{e^+} and the half-life $t_{1/2}$ are pre-generated based on data from the ENSDF database [98].

The total number of decayed atoms can be calculated from the source distribution and simulated time interval. If the total number is too large, smaller time slice will be used. Each thread deals with an atom. If the sampled decay time, which follows the exponential distribution, is inside the time slice, this atom will be dead. And if another sampled number from a uniform distribution is less than the branch

ratio Γ_{e^+} , a positron will be generated. Its position is sampled uniformly from the voxel related to it and its energy is sampled from a polynomial-fitted energy spectrum, whose parameters are extracted from [89] or given by the user.

Positron Transport After the decay process, the created positron can transport for several millimeters depending on its kinetic energy before it annihilates with an electron. It is important to develop reliable positron-range estimation methods for two reasons. First, since the positron generated from the decay process typically has a broad energy spectrum, a simple point-spread function-based estimation is not accurate. Second, when an inaccurate positron range is used, PET reconstruction with resolution recovery algorithms will introduce artifacts into the reconstructed image due to inaccurate range correction [99, 100]. Historically, there have been methods for simulating positron range, including analytical-function-based methods [99, 101] and MC-simulation-based methods [86, 92, 102]. In gPET, we adopt the empirical Palmer and Brownell's algorithm [103], which is also used in simSET [101]. The readers are encouraged to refer the paper of Harrison et al. [101] if the details of method are of interest. In gPET, the phantom information needed for the positron transport and next-step gamma transport is pre-customized by the user. Patient phantom from CT scanning in voxelized geometry is supported. Based on its location and orientation in the global coordinate, it can be easily related to the PEN/positron locations to provide material type and density information.

Positron Annihilation After simulating the positron range, we simulate the positron annihilation process. Non-collinearity of the generated gamma pairs, which can result from the thermal kinetic energies of the positron-electron pairs during annihilation, is another factor that causes blurring in the PET reconstruction. In gPET, the non-linear property is sampled from a Gaussian distribution with mean $m = \pi$ and standard deviation $\sigma = 0.0037rad\ (= 0.5^0 FWHM)$ for the gamma pairs,

while the energies for both gammas remain at 511 keV for simplicity. This process is combined with the previous positron transport process and executed by the same GPU parallel thread. Since two photons are generated per thread constantly, a continuous memory space is pre-created with memory addresses $2t_{id}$ and $2t_{id}+1$ for the two photons generated in the thread with index t_{id}. The corresponding gamma indices are then $2n \bullet N_{pt} + 2t_{id}$ and $2n \bullet N_{pt} + 2t_{id} + 1$ if the gamma pairs are generated in the (n+1)th time slice. For each gamma generated, the following quantities are used to tag its state: the three components of current position, the three components of moving direction, energy, global time-of-flight (TOF) and its index. The global TOF is defined in the global time frame, with t=0 corresponding to the moment when the PENs are at their initial read-in activities. During the next-step gamma transport, all other tags of the gamma will also be updated accordingly.

2.1.2.2 Gamma transport inside the voxelized phantom

In the gamma transport module, gDPM algorithm is utilized to govern the physics transport. Photon scattering and absorption effects are considered. The physics cross-sections are well validated for photons above several keVs in tissue-equivalent materials [41, 42]. It's also worth noting that in gDPM, the Woodcock method (Woodcock et al., 1965) is applied to get rid of the frequent boundary checking issue when there is an inhomogeneous area along the photon traveling path.

Once the gammas escape from the phantom boundary and reach a predefined surface, gammas with the tags mentioned above are recorded as a transient PSF, which can be saved as an intermediate output by the user.

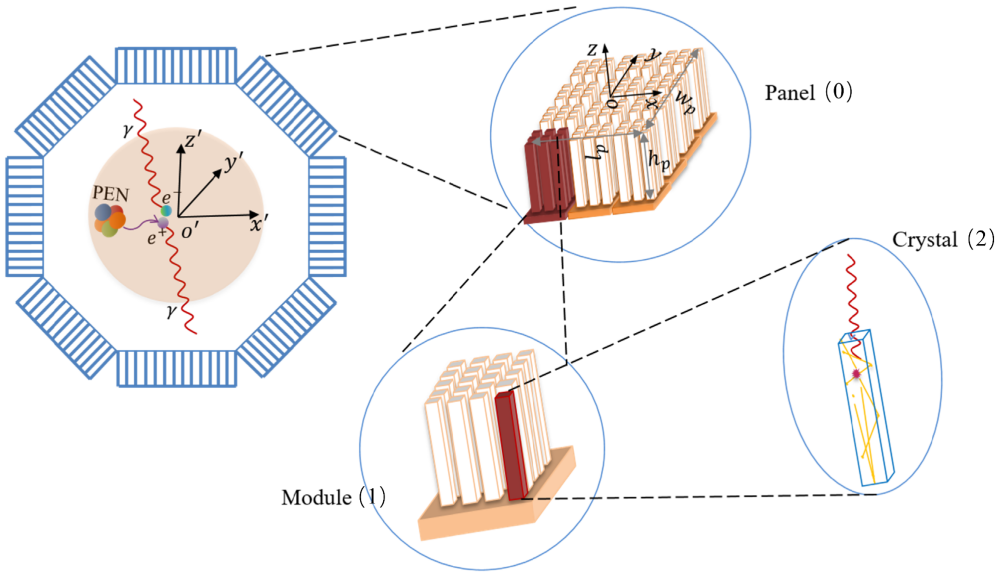

Figure 2.2. Illustration of the three-level configuration for an eight-panel PET detector: cuboidal panel, module, and crystal. The local coordinate of one panel is defined based on the front surface (the surface facing the phantom) of the cuboidal panel, as indicated by O_{XYZ}..

2.1.2.3 Gamma detection and processing inside the PET detector

In this gamma detection and processing module, we especially consider two components for the MC simulation. First, in advanced PET detection systems, fine structures such as discretized crystal scintillators are used to improve the spatial resolution. To reflect these structural details, we configure the PET detector in parameterized geometry [95]. Second, the electronic response of detector need to be considered to get a comparable results with experiment. In gPET, we utilize the gDPM algorithm [66] to govern the electromagnetic process. We then develop a functional module, named "digitizer", to model the detector response process to form the detectable signals. The details of these geometrical and physical developments are listed as follows.

Parametrized Detector Configuration We configure a detector with fine structures in three levels: panel, module and discretized crystal scintillator, labeled as 0, 1 and 2, respectively (Fig. 2.2). As shown in Figure 2.2, a single cuboidal panel with a detecting area of $l_p \times w_p$ and a thickness of h_p is divided into $N_m^l \times N_m^w \times N_m^h$ repetitive modules. Each module has a size of $l_m \times w_m \times h_p$ with an interval of $l_{mi} \times w_{mi} \times h_{mi}$between each two of them. Each module is then divided into $N_c^l \times N_c^w \times N_c^h$ repetitive crystal scintillators, with each crystal having size of $l_c \times w_c \times h_p$ and the repetition interval of $l_{ci} \times w_{ci} \times h_p$ between them. Here, though "crystal" is used to represent the smallest repetition unit, a PET detector can be configured with other materials in gPET.

With the three levels hierarchy and the repetition property of a detector, we can easily locate and index the gamma position during its transport inside the detector. To do this, we define a local coordinate frame for assistance (O_{XYZ} in Fig. 2.2). We then transform the locations and directions of the gammas from the global coordinate $O'_{X'Y'Z'}$ to the local coordinate O_{XYZ} based on the transform matrix between the two. During the gamma transport, we update its location in O_{XYZ} based on its current position, direction and the sampled free travel length. We then index the locations of the gammas in panel, module and crystal levels. For example, we calculate the module index along the X direction for a gamma located at $[x\ y\ z]$ in O_{XYZ} as:

$$I_m^x = floor\left[\frac{x - \left(-\frac{x_p}{2}\right)}{x_m + x_{mi}}\right], \tag{2.1}$$

with $\left(x - \left(-\frac{x_p}{2}\right)\right) - I_m^x * (x_m + x_{mi}) \leq x_m$, where $floor(x)$ denotes the largest integer that is smaller than or equal to x.

Altogether, we use 21 floating numbers to configure a single cuboidal panel with fine structures, 4 floating numbers to define the material type and density for the smallest repetition unit and its interval, and 12 floating numbers to define the co-

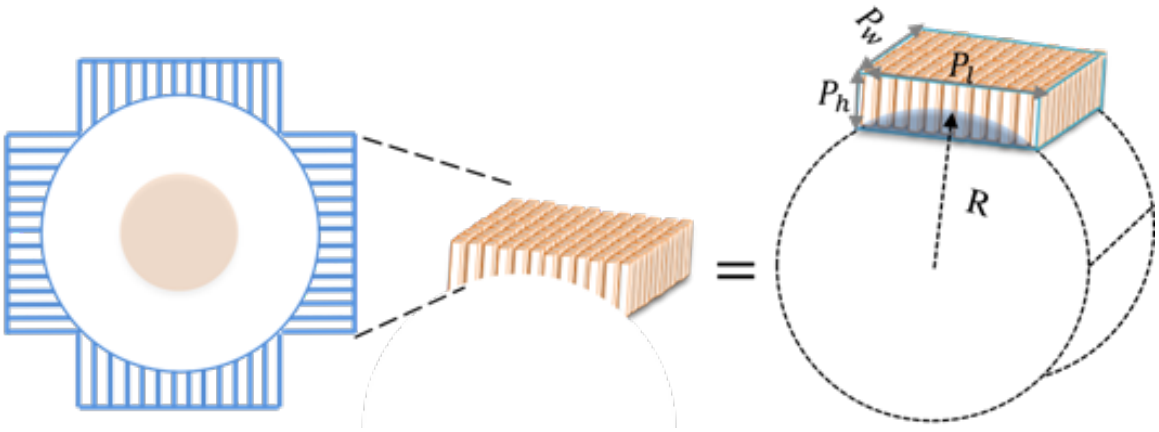

Figure 2.3. Illustration of an irregularly shaped panel (left), which can be parametrized in two steps: the fake cuboidal region (in green box) for fast repeatable configurations and the extra restriction from the cylindrical surface to eliminate the blue region from the real detector volume. .

ordinate transform matrix. Totally, we use 37 floating numbers to describe a cuboidal panel with sufficient support for the gamma transport inside it.

In addition to the cuboidal panel type, gPET also allows user-specified panels with irregular geometry, as illustrated in Figure 2.3. In this case, the effective detecting sizes of the panel, modules and crystals vary from one position to another, making it hard to adopt the repetition property in detector configuration. Consequently, more memory is required to accurately describe the panel geometry, and it can be more complex to navigate the gamma transport inside it than in the cuboidal case.

To solve this problem, we develop a novel method in gPET to efficiently manage the geometry of irregularly shaped detectors. The idea of this method is to model the given detector with a repeatable cuboidal mother volume, and then obtain the effective detection region with additional boundary constraints. Take the OPET system shown in Figure 2.3 as an example. As indicated by the blue box in Figure 2.3, we make a mother volume as a least expansion over the given detector, and

correspondingly extend the inner detecting unit, like the single crystal scintillator, to fill its volume. A local coordinate is then defined based on the mother volume the same way as for the regular cuboidal detector. In this way, we resume the repetition property of the detector. When a particle enters this volume, its location can be easily indexed in different detector levels. A cylindrical surface boundary is then added for constraint as shown in Figure 2.3 to simulate the curved inner surface of effective detector region. With the boundary constraint, though the geometric repetition property is resumed in the non-effective region, the material will be set to air for this region. In the current version of gPET, we define the boundary in the local coordinate with quadratic functions as:

$$f(x,y,z) = a_1x^2 + a_2y^2 + a_3z^2 + a_4xy + a_5yz + a_6xz + a_7x + a_8y + a_9z + a_{10}. \quad (2.2)$$

The sign of a_i for i=1, 2,..., 10 is defined in a way that for an arbitrary point (x, y, z) belonging to the effective detector region, $f(x,y,z) > 0$. With this definition, the parameters for the cylindrical surface boundary shown in Figure 2.3 are $a_1 = a_3 = 1$, $a_9 = -2\sqrt{R^2 - (\frac{P_l}{2})^2}$ and $a_{10} = -(\frac{P_l}{2})^2$, with the rest a_i's being zero. All $a_i (i = 1,\ 2, \ldots,\ 10)$ are prescribed from user input. With these 10 floating numbers to represent one quadratic boundary, we need $10N_b$ extra floating numbers for a panel having N_b boundaries. Plus the 37 geometric parameters for the repetition component configuration, we use $37 + 10N_b$ floating numbers to completely describe an irregularly shaped panel.

After configuring the single panel, we form the entire PET imaging system in two formats: repetitive or non-repetitive. For a repetitive detector, we add another three quantities in 5 floating numbers, the repetition axis (3 floating numbers), repetition angle, and repetition times, leading to a total of 42 or $42 + 10N_b$ floating numbers to represent an entire PET system. For the non-repetitive detector, each

panel has its own geometry, hence, 37 or $37 + 10N_b$ floating numbers per panel would be required, leading to a total floating number of $(37 + 10N_b) \times N_p$, with N_p the number of panels, to configure a detector. In both cases (repetitive and non-repetitive), the detector geometric information is manageable by the GPU shared memory, which is much faster than the global memory. In this way, we can fully accelerate the gamma transport process in gPET by maximally reducing the time consumption in the frequent boundary data accessing subprocess.

It is worth mentioning that the above method for PET detector configuration in both cuboidal and irregular shapes works for monolithic scintillators. This is because a monolithic scintillator is just a special configuration with one crystal per module and one module per panel.

Gamma Detection and Digitizer After accurately defining the geometry of a detector in gPET, we simulate the gamma detection process in two stages. Stage 1 is to record the "hit" events generated from the electromagnetic processes and stage 2 is to mimic the response of the electronic devices to form singles and coincidence pairs with a digitizer process.

Specifically, in stage 1, we feed the GPU parallel threads with gammas from the transient PSF in a one-gamma-per-thread format. In each thread, the gamma is transported with its energy deposition event recorded as a "hit". The process is repeated until its kinetic energy is lower than the cutoff energy or the gamma escapes the detector. For each hit event, quantities such as the global time for the event to happen, the index for the parent gamma, the index of the physics process for its generation, its energy, 3D location, and indexed location (crystal index, module index and panel index), are recorded. When a user chooses hits as an output, the hit events will be recorded in a GPU global memory with a predefined length of $n * N_{pt}$, where n is the estimated average hit yielding rate per parent gamma for the pre-defined

system. Otherwise, the hit generation process will only be processed in the local GPU memory for each thread.

As for the digitizer process in stage 2, gPET utilizes similar logical module as in GATE, which contains six components: adder, readout, spatial and energy blurs with lower-bound energy cutoff, dead time, energy window and coincidence sorter. Considering that the electronic readout parts can be incorporated with the scintillation detector in different layers, a user-specified level for the "readout" and "dead time" subprocesses (level indices 0, 1 and 2 for panel, module and crystal, respectively) can be prescribed from user input. A new parameter, "site ID" S_j for an event j, is then defined and used to tag the recorded events, as

$$S_j = \sum_{i=0}^{d-1} I_i * \prod_{k=i+1}^{d} N_k + I_d, \tag{2.3}$$

where d is the given "readout" or "dead time" level, I_i (for $i = 0,\ 1,\ \ldots,\ d$) is the ID for the event at level i, and N_k (for $k = i + 1,\ \ldots,\ d$) is the total count of the detector substructures in the kth level. With this linearized ID, when two events are found to have the same site ID, they will be treated as belonging to the same unit at the defined level.

The details of the digitizer process are then described as follows. 1) Adder The first digitizer module adds up the hit events belonging to the same parent gamma and with same site ID on the crystal level to form a single "pulse." Hence, for each thread dealing with one gamma, a local memory is used to store the pulses belonging to different site IDs. When a hit is recorded, its site ID will be compared to the existing pulse list in the local memory. If the same site ID is not found, the hit event will be added to the end of the pulse list. Otherwise, it will be added to the corresponding pulse, with the pulse energy updated as a direct sum of the list energy and the new hit, and the position updated as an energy-weighted average of the two positions.

2) Readout When the adding process is finished and the readout level from the user input list is different from the crystal level, the readout process is performed in the same thread. The site ID is calculated for each pulse. The pulses with the same site ID are added again by either an "energy average" or a "winner takes all" policy. The former treats the pulses the same way as in the adding process, while the latter only keeps the pulse with the greatest energy. After the readout process, the pulse list in the local memory of each thread is transferred to the global memory with a predefined length of $n * N_{pt}$, with n denoting the average pulse yielding rate per parent gamma for the defined system.

3) Spatial and energy blurring with lower-bound energy cutoff To simulate the resolution of the electronic devices, spatial and energy blurring can be performed to each pulse using a certain distribution, e.g. Gaussian, according to the user's preference. A cutoff energy of E_{min} is then applied to discard those pulses with energies lower than E_{min}. In other words, E_{min} serves as the minimum energy to trigger a response.

4) Dead time The detecting component can be saturated when it is triggered by an incident signal, thus requiring some time td to recover. During the recovery (dead response) period, new incident signals will not be detected. Two modes are used to simulate this effect: paralyzable and nonparalyzable. In the paralyzable mode, the start time ${t_i}^a$ of a dead response period $[{t_i}^a,\ {t_i}^a + t_d]$ triggered by the a^{th} pulse will be reset to a new starting point ${t_i}^b$ if the bth pulse is within $[{t_i}^a,\ {t_i}^a + t_d]$, and the ending time will then be reset to ${t_i}^b + t_d$ correspondingly. For the nonparalysable mode, the start time will not be reset. For both modes, the search for the pulses to be excluded is serial, because whether a particular pulse should be kept depends on the previous pulse. Nevertheless, two kinds of pulses are always kept: when their site numbers differ from the previous one, or when they are out of the dead period

td of the previous pulse. These always-kept pulses then serve as independent start points for the search. Hence, parallelization of the searching process is achieved by dividing the entire pulse list into sub-lists based on these independent starting points and feeding the sub-lists into parallel threads. For this purpose, the pulse list in the dead time part must be sorted in advance to make it ordered according to the site ID first, and then ordered chronologically for those with the same site ID.

5) Energy window An energy window defined according to the user's preference is then applied to the pulse list that survived the dead time to form the final pulse list labeled as "singles". At this stage, the singles can be output by the user.

6) Coincidence sorter Finally, the coincidence sorter is applied to singles to select paired coincidences based on their positions, TOF intervals. When the TOF interval between two singles is less than a predefined window t_c and the angle between their displacements relative to the origin is larger than a predefined value, the two singles will be paired into a coincidence. One singles can be paired with more than one other singles, which is called multi-coincidence. There are different ways to deal with the multi-coincidence, such as discarding them all or taking them all. The policy used in the simulation is the former one, namely if more than two singles within t_c satisfy the conditions, they will be discarded.

2.1.3 Case studies for gPET accuracy and efficiency

2.1.3.1 Performance test for the three functional modules in gPET – simulation case 1

To test the performance of the first two modules of gPET, we adopted the following simulation case: a 11C point source with an activity of 1e7 Bq is put at the center of an 8 cm3 cubic water phantom. A history of 1e7 positron decays from the

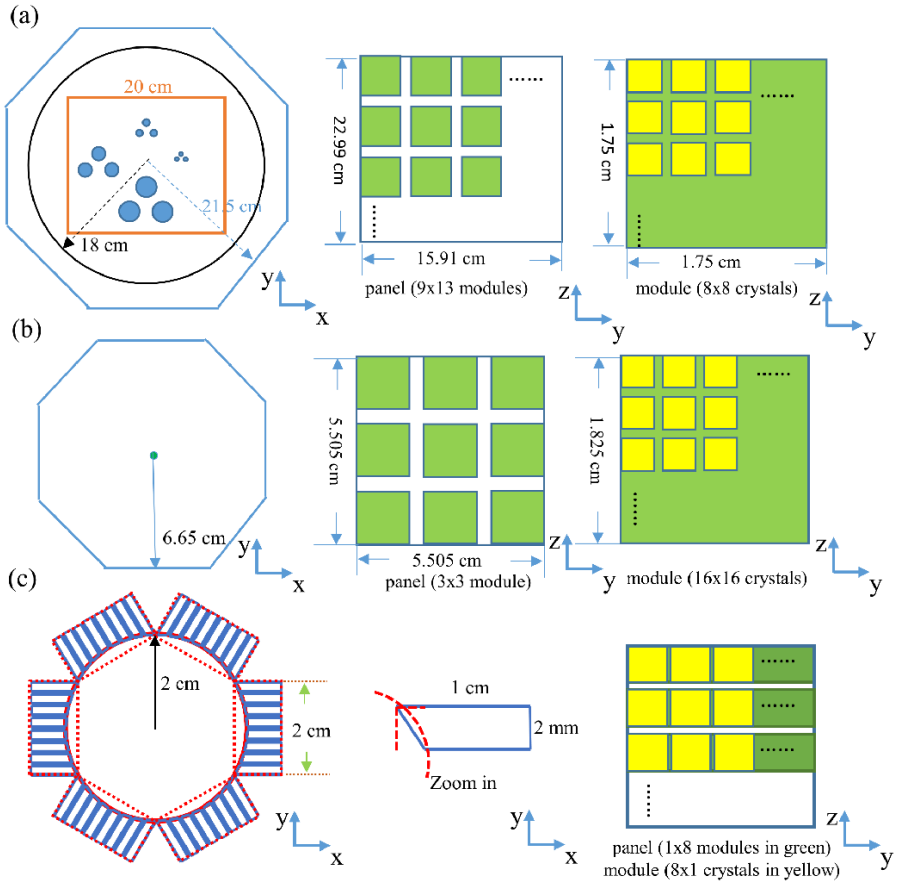

Figure 2.4. The simulation setups for (a) cases 1 and 2, where the black circle indicates the recording sphere for gamma PSF; and (b) case 3, the OPET detector, where red dashed lines represent the setting of gPET, and the blue lines represent the setting of GATE. In all setups, a three-level repeatable structure is used for the detector configuration in gPET: panel, module (green), and discretized crystal scintillator (yellow).

11C point source is simulated in both gPET and GATE/Geant4. The annihilation position of the positron is tracked inside the water phantom. After the annihilation process, the generated gamma pairs are further transported. A virtual spherical surface with a radius of 3 cm is assumed outside the phantom with its center coincident with that of the water phantom. When the gammas travel outside the phantom, they are recorded on the spherical surface to form the PSF. The positron range and spatial spectrum distributions of the gamma PSFs from gPET and GATE are compared.

With the PSF validated, the third module of gPET is tested by incorporating a detector part as shown in Figure 2.4(a). The detecting system is co-centered with the origin of the global coordinates with an origin to panel distance of 6.65 cm. Each panel is composed of 3×3 modules with each module containing 16×16 LSO crystal scintillators. The panel has a size of $2 \times 5.505 \times 5.505\ cm^3$ with a single module of $2 \times 1.825 \times 1.825 cm^3$ and a single LSO scintillator of $2 \times 0.1 \times 0.1 cm^3$. Both the intervals between the modules and the intervals between the LSO scintillators are 0.015 cm. In both gPET and GATE, the energy resolution obeys the inverse square law of $R = \sqrt{\frac{E_0}{E}} * R_0$, where the reference energy resolution is $R_0 = 0.19$ for $E_0 = 511 keV$. The cutoff energy is 50 keV. The dead response time is 2.2 μs followed by an energy window of [350, 700] keV. The coincidence window is 5 ns. Based on the coincidences generated from each package, 3D images are reconstructed by a simple retrace-back method. The spatial and energy distributions of the intermediate signals and the spatial distributions of the reconstructed images are compared between gPET and GATE.

It needs to mention that, to focus on the entire functional module test, we choose a similar physics model as that used in gPET for the gamma transport in GATE. Specifically, gPET uses the Klein-Nishima (KN) formula to sample Compton

scattering and ignores the shell structure for the photoelectric effect. Accordingly, we choose the EmStandard model in GATE, and label it as "GATE_Sta" for convenience.

2.1.3.2 Performance test for the accuracy of the physics model in detector—simulation case 2

The assumption that the electrons of a material are free particles reduces the complexity of the simulation by ignoring binding effect, relativistic effect, and Doppler effect. However, the validity of this assumption depends on the energy of the incident photons and the effective Z number of the material. The higher the incident energy and the lower the effective Z number, the better the assumption holds [104]. In the PET simulation, though the Z number of the phantom material is usually similar to that of water, the detector typically contains high Z materials for effective gamma detection. For example, the effective Z number of an LSO scintillation detector is as high as 66 [105]. Hence, it is necessary to quantify the performance of gPET in the detector simulation by comparing it with more accurate models in GATE.

For this reason, we employ the EmPenelope model in GATE, labeled as "GATE_Pen" for simplicity. This model considers both the shell structure and the movement of electrons. The results from GATE_Pen are taken as ground truth. The setup for this test is as follows: a mono-energetic isotropic point gamma source of 511 keV in air is set at the origin of a global coordinate frame. The configuration of the detector is the same as in Case 1 (Figure 2.4(a)), but the material for the phantom is air. Ten million gamma pairs are simulated. Hit events, singles, coincidences and the reconstructed images from gPET, GATE_Sta, and GATE_Pen are compared.

In addition, we simulate gammas with energies of 59 keV and 662 keV (corresponding to gamma peaks from calibration sources of 241Am and 137Cs, respectively), under the same experimental setup as for the 511 keV simulation, out of the

consideration of the detector energy calibration purpose. Based on the inverse square law, the energy windows of [0, 100] keV and [500, 800] keV are applied to generate singles for the two calibration energies, respectively.

2.1.3.3 Geometry configuration of irregularly shaped PET detector – simulation case 3

To demonstrate the accuracy and efficiency of the geometric configuration for the irregularly shaped PET detector in gPET, we simulate the gamma transport in a six-panel OPET detector as shown in Figure 2.4(b). The front surface of the OPET detector is close to a cylindrical surface with a radius of 2 cm. Each panel has 8 modules distributed along the z direction while each module has 8 crystals distributed along the tangential direction. The main difference between gPET and GATE in the geometry description of OPET lies on the front surface of the crystal, as illustrated in the middle zoom-in figure of Figure 2.4(b). In gPET, each crystal is modeled as a repeatable cuboidal volume, as indicated by the red box, while the effective detection volume is defined by the cylindrical surface. In GATE, eight different trapezoids are used to model the detector volume. In both simulations, the dimensions of the panel are $1 \times 1.99 \times 1.99$ cm^3 along radial, tangential, and z directions, respectively. The crystals are 0.2×0.2 cm^2 along the tangential and z axes. The gaps between the modules and the gaps between the crystals are both 0.057 cm. The dead time part is used in module level here rather than crystal level as in simulation cases 1 and 2 because of the constraint of setting in GATE. Fifteen million gamma pairs are randomly sampled to travel from the center of the OPET detector. Hit events, singles, coincidences and the reconstructed images from gPET and GATE_Sta are compared.

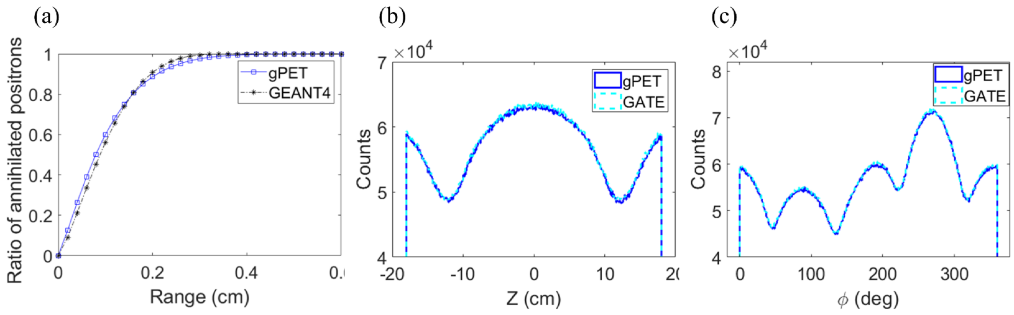

Figure 2.5. Simulation results for case 1. (a) The distribution of the accumulated annihilation ratio with respect to its range. (b) Gamma distribution along the z axis for the PSF. (c) Angular distribution for the gammas from the PSF..

2.1.4 Results

2.1.4.1 The performance of the three functional modules in gPET

Positron Range The accumulated percentage counts of the positrons versus the positron ranges from gPET and Geant4 in simulation case 1 are plotted in Figure 2.5(a). Here, Geant4 is used because it is the physics core of GATE and the extraction of the positron track lengths from it is easier. As is shown, the percentage distributions for positrons generated in gPET and Geant4 are comparable. The mean and maximum positron ranges are 0.99 mm and 4.2 mm for gPET, and 1.14 mm and 4.2 mm for GATE/Geant4, respectively.

Gamma Distributions from the PSFs The distributions of the gammas from the PSFs along the z and the azimuthal directions are shown in Figures 2.5(b) and 2.5(c). Here, we define the difference of two histograms h and g, with g the benchmark result from GATE, as $\frac{\sum_i |h_i - g_i|/g_i}{N}$, where h_i is the value of the i^{th} bin of histogram h and N is the total number of bins. Using 0.1 cm and 10 bin sizes, the differences between the PSFs from gPET and GATE/Geant4 are found of 0.6% and 0.5% along the z and the azimuthal directions, respectively.

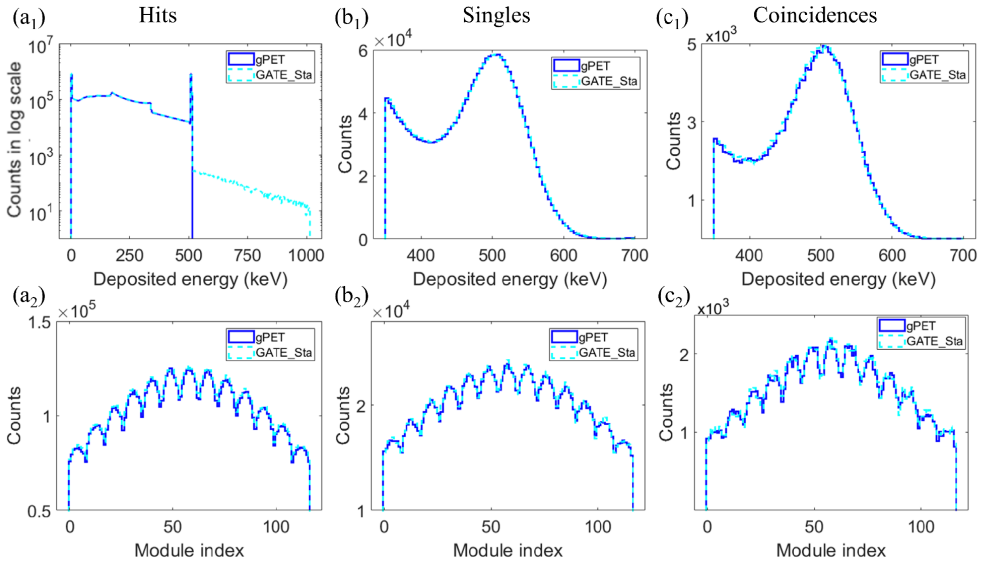

Figure 2.6. Comparison of the energy and module distributions of (a) hits, (b) singles, and (c) coincidences from gPET and GATE in simulation case 1. Note, log scale is used for Hits in (a1)..

Gamma Detection and Processing inside the PET Detector The energy and spatial distributions of the recorded hits, singles and coincidences from gPET and GATE_Sta are shown in Figures 2.6. Specifically, the first row illustrates their energy distributions with an energy bin of 4 keV. The corresponding differences between gPET and GATE_Sta are 1.97%, 1.61%, and 1.96%, respectively. The second row shows the spatial distribution in crystals. The corresponding differences between gPET and GATE_Sta are 1.88%, 1.51%, and 2.37%. The central slice (1 mm thick) of the reconstructed images from the simulation results of gPET and GATE_Sta are shown in Figure 2.7 (a) and (b). As can be seen, the distributions of the reconstructed point source are comparable. With a voxel size of 0.2 mm along the x axis, the peak intensity is located in the center for both images. Figure 2.7(c) further illustrates the profiles of the reconstructed images from gPET and GATE_Sta along the central

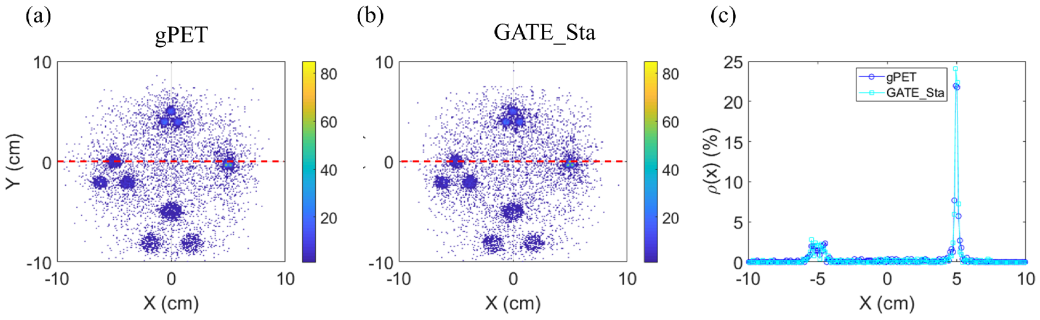

Figure 2.7. Comparison of the corresponding central slices of reconstructed images from (a) gPET and (b) GATE_Sta in simulation case 1. (c) The profiles along the red dashed line in (a) and (b). $\rho(x)$ denotes the normalized distribution..

lines (red dashed lines in Figs. 2.7(a) and (b)). The standard deviations of the line profiles are 1.39 mm for gPET and 1.38 mm for GATE_Sta, respectively.

2.1.4.2 Accuracy of the physics model

The energy distributions of the hit events generated in all inelastic processes by gPET, GATE_Sta, and GATE_Pen in simulation case 2 are shown in Figure 2.8(a). As is shown, in the entire energy range, the hit distributions from gPET and GATE_Sta match very well. As for GATE_Pen, fewer hit events are generated in the low keV range (zoom-in subfigure of Figure 2.8(a)), but more around the Compton edge of 340.6 keV, than for the other two models. We further compare the distributions for hits generated from the Compton channel and the photoelectric channel, as shown in Figures 2.8(b) and 2.8(c), respectively. As can be seen, GATE_Pen has an obvious broadening at the Compton edge and drop-off at the low energy range mainly from the Compton channel. This can be explained by the relativistic effect and the Doppler effect considered in the GATE_Pen model. Nonetheless, the two deviations only influence a small portion of the total yield, 0.6% for the Compton edge broadening and

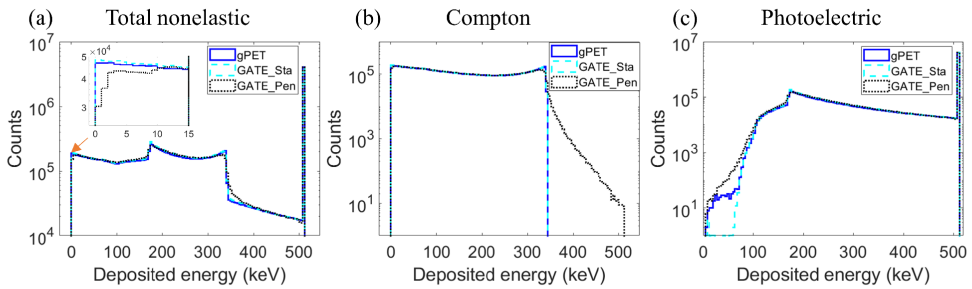

Figure 2.8. Energy distributions of (a) total inelastic interaction, (b) Compton interaction, and (c) photoelectric interaction..

0.3% for the low energy range, respectively. The energy and crystal distributions for hit events generated from all interactions, including those elastic processes, are shown in the first row of Figure 2.9. Taking the results from GATE_Pen as benchmarks, the mean differences in hit distributions over the energy (with bin size of 4 keV) and crystal indexes are 4.56% and 1.89% for gPET, and 3.2% and 0.53% for GATE_Sta, respectively. The corresponding single distributions after the digitization process are shown in the second row of Figure 2.9. The mean differences of singles with respect to energy and crystal index distributions are 1.58% and 0.92% for gPET, and 0.71% and 0.73% for GATE_Sta, respectively. The smaller differences from the singles than that from the hits are mainly due to the energy window of [350, 700] keV applied in the digitization process, which discards the discrepancies outside the energy window. The coincidences from the singles are illustrated in the last row of Figure 2.9. The mean differences of the coincidences with respect to the energy and crystal index distributions are 1.52% and 1.49% for gPET, and 0.92% and 1.27% for GATE_Sta.

Figures 2.10 further illustrates the central slices of the reconstructed images with a thickness of 1 mm from gPET, GATE_Sta, and GATE_Pen, respectively. With a

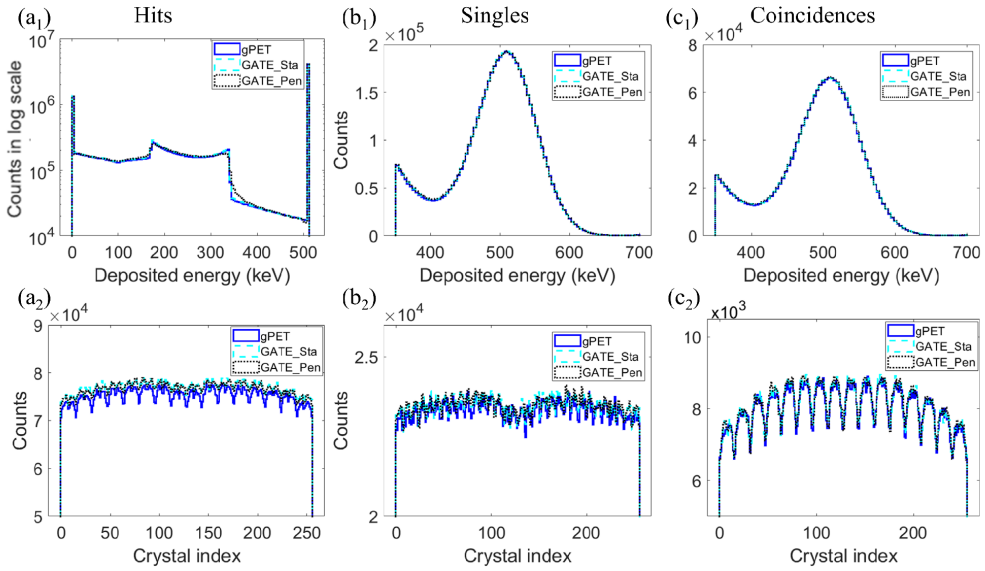

Figure 2.9. Comparison of the energy and crystal distributions of (a) hits, (b) singles, and (c) coincidences from gPET and GATE in simulation case 2..

voxel size of 0.2 mm along the x axis, the standard deviations of the line profiles (Figure 2.10(d)) along the red dashed line shown in Figure 2.10 (a-c) are 0.94, 0.93, and 0.93 mm for the gPET, GATE_Sta, and GATE_Pen models, respectively.

The comparisons for simulations with gamma energies of 59 and 662 keV are shown in Table 2.1, in which we take the results from the GATE_Pen as benchmark. From the table, for both energy and crystal distributions of the hits and singles in the 662 keV simulation case, the differences between gPET and GATE_Pen are the same level as those in the 511 keV one, indicating the stable performance of gPET in the high energy range. As for the 59 keV simulation case, the main difference is found for the energy distribution of the hit events, which is 15.12%, much higher than that in the other two simulation cases. A more detailed examination reveals that the difference mainly comes from the Compton edge. Noticing that gammas

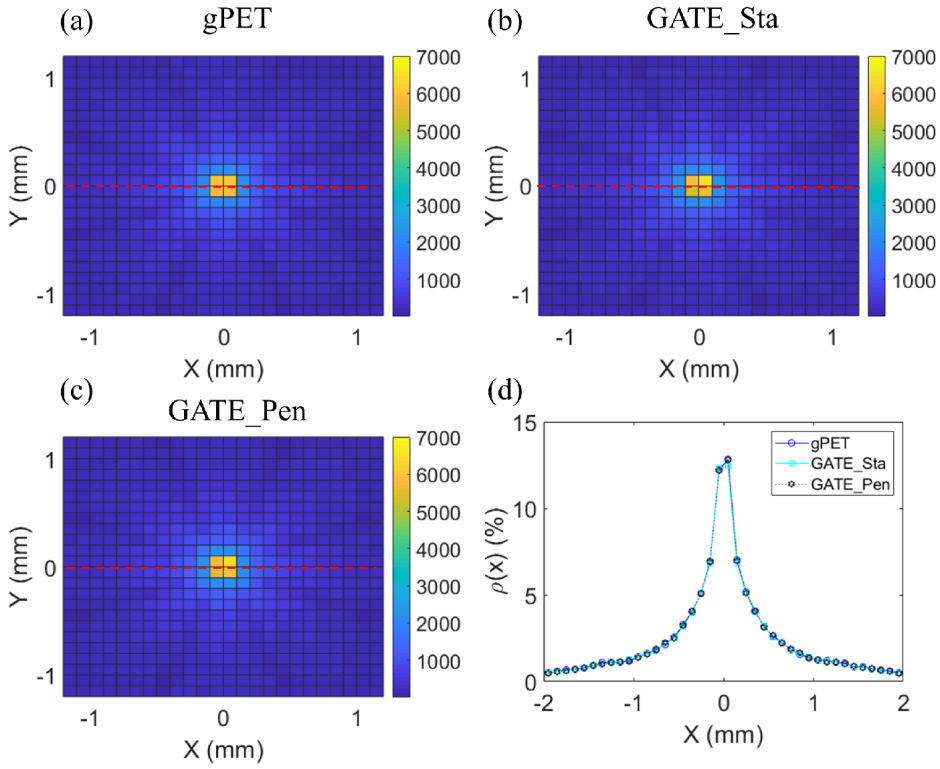

Figure 2.10. Comparison of the central slices of the images reconstructed from (a) gPET, (b) GATE_Sta and (c) GATE_Pen in simulation case 2. (d) The profiles along the red dashed line in (a), (b), and (c). $rho(x)$ denotes the normalized distribution..

with energy of 59 keV can only travel a few millimeters inside the crystal scintillator, after adding up the hit events from the same parent gamma at the crystal level, the differences for the distributions of the singles significantly drop to less than 1%. These simulation results indicate that the physics models used in gPET are sufficient for PET simulation.

Table 2.1. The differences of simulation results for gammas with energies of 59 and 662 keV between gPET and GATE_Pen in simulation case 2.

Gamma energy (keV)	Differences of energy distributions with total bins of 75 (%)		Differences of crystal IDs distributions (%)	
	Hits	Singles	Hits	Singles
59	15.12	0.95	0.77	0.79
662	5.69	1.56	2.46	1.30

2.1.4.3 OPET geometry test

In Figure 2.11, we show the hit events, singles and coincidence distributions from gPET and GATE_Sta in simulation case 3. Taking the results of GATE_Sta as benchmark, the differences in the energy spectrum of gPET over a 4 keV bin for hits, singles and coincidences are 4.39%, 1.49% and 3.18%, respectively. The corresponding differences in module index distributions are 3.50%, 1.11% and 2.48%, and that in crystal index distributions are 3.49%, 1.13%, and 2.54%, respectively.

The central slices of the reconstructed images in a 1 mm thickness are shown in Figure 2.12 (a) and (b). The two images are very similar to each other. The profiles (Fig. 2.12 (c)) of the reconstructed slices along the central lines (red dashed lines in Figs. 2.12 (a) and (b)) further shows the resemblance of two images, with the mean±standard deviations of 0±0.59 mm for GATE and 0±0.58 mm for gPET. The consistence between gPET and GATE in this simulation case indicates that the strategy of using repeatable geometry with parameterized surfaces to define an irregularly shaped detector in gPET is sufficient for accuracy.

2.1.4.4 Computational time

The simulation time of gPET and GATE8.0 for the above three cases is listed in Table 2.2. The simulation time does not differ much between the Penelope model

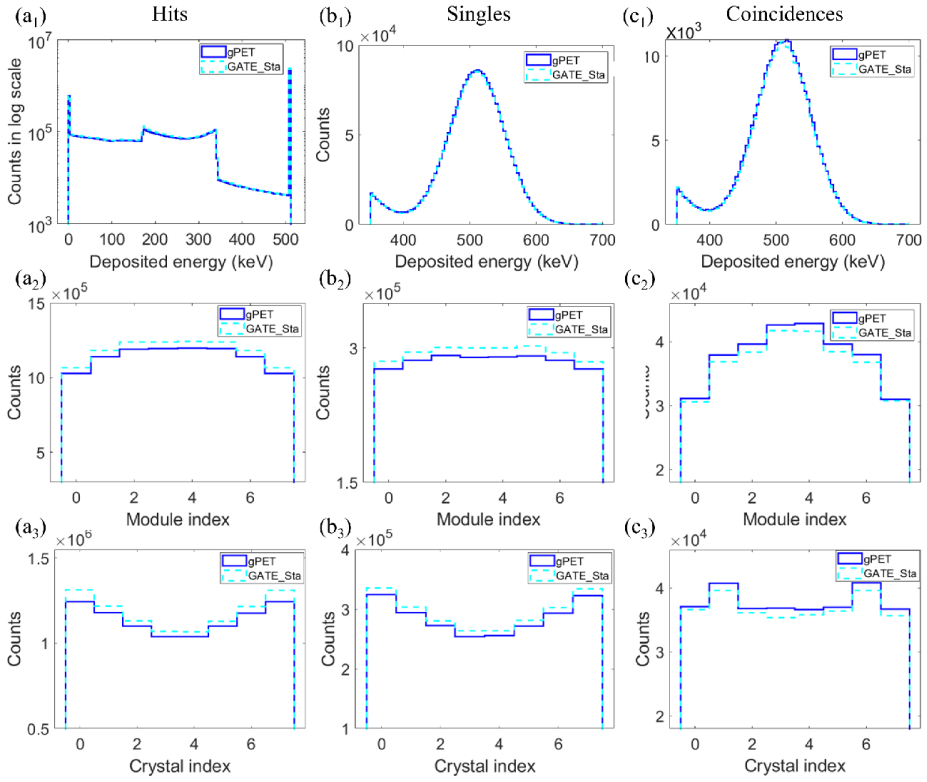

Figure 2.11. Energy, module, and crystal distributions of (a) hits, (b) singles, and (c) coincidences..

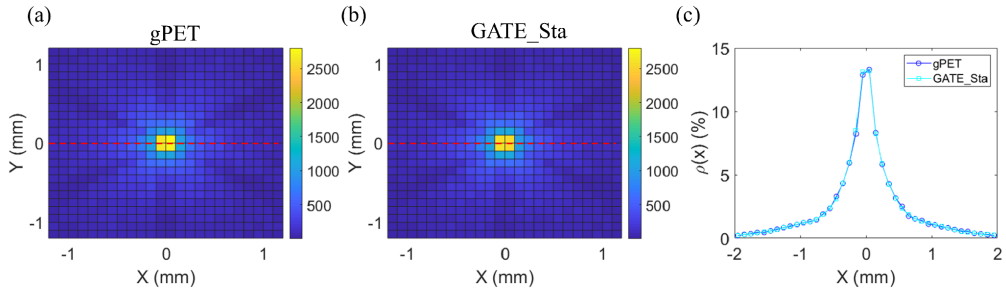

Figure 2.12. Energy, module, and crystal distributions of (a) hits, (b) singles, and (c) coincidences..

Table 2.2. The comparison of time expended for the three simulation cases between gPET and GATE.

Package	Platform	Computational time (s/1e7 gamma pairs)		
		Case 1	Case 2	Case 3
gPET	Titan Xp GPU (1.58GHz, one card)	19.8	16.7	11.5
GATE	Intel i7-6850K CPU (3.6GHz, single CPU)	2625	1803	2394

and the Standard model in GATE, so we summarized them as "GATE." As the table indicates, gPET is around 110 to 200 times faster than GATE.

2.1.5 Discussions

Although our current development of gPET achieves validated accuracy for main functions of PET simulation, some physics processes are approximated with loss of accuracy. For instance, we treat the annihilated gamma pairs as mono-energetic with 511 keV energy, which is inconsistent with the experimental measurement, where the gammas are found with energetic spread-outs [106]. This leads to a discrepancy in energy distribution of the gamma pairs between gPET and GATE. This discrepancy is, then, transferred to the gamma detection inside the PET detector, as indicated by the energy tails >511keV for the hit distributions in Figure 2.6(a1). Yet, these events only account for 0.5% of the total yield, and they are further suppressed in the single distribution after the energy blurring and energy window cutoff, as shown in Figure 2.6(b1). This indicates that the current positron annihilation model used in gPET has an acceptable accuracy for PET simulations. Nevertheless, we plan to incorporate more accurate physics modeling for this process to make gPET more robust in the future development.

Table 2.3. Physics model comparison between gPET and GATE_Sta.

Cases	Packages	Compton (%)	Rayleigh (%)	Photoelectric (%)
Case 2	gPET	50.65	5.51	43.85 (19.85[a])
	GATE_Sta	49.95	5.66	44.39 (19.36[a])
Case 3	gPET	54.03	5.34	40.63 (24.21[a])
	GATE_Sta	53.01	5.54	41.45 (23.41[a])

[a] The ratio of photoelectric event whose deposited energy is 511 keV.

In both simulation cases 2 and 3, the numbers of hit events from gPET are always smaller than that from GATE. We summarize the hit generations from different interactions in gPET and GATE for both cases and show the results in Table 2.3. As is shown, the main differences exist in the Compton and photoelectric processes. More Compton scattering but less photoelectric absorption are found in gPET than in GATE. Quantitatively, it accounts for 1 2% difference in hits energy distributions, as inferred from Table 2.3. In the current development stage of gPET, this discrepancy is acceptable. More precise cross sections and elaborate models will be considered in future development of gPET.

Another potential extension of gPET is to incorporate the scintillation photon transport process [86, 107, 108] into the PET detector simulation. When the incident gamma deposits energy inside the scintillator, the characteristic photons can be generated, transport, and get reflection and refraction among the different components of the detector, potentially affecting the statistical distribution of the detecting signals. However, due to the complexity of this optical process and its heavy dependence on the material surfaces, MC simulation for the optical process is very time consuming and challenging [107]. Inspired by the recent development of GPU-based optical photon simulation for particle physics [109], we plan to develop a GPU-based functional

module for PET-dedicated optical photon simulation in the future development of gPET.

2.2 PET simulation for small animal

2.2.1 Background

Small-animal positron emission tomography (PET) is a well-established nuclear medical imaging technique. With the aid of positron-emitting radionuclides, small-animal PET can image a wide range of molecular processes in vivo and hence is broadly used in the pre-clinical studies of pharmaceutical biodistributions and temporal disease progression [110–112]. It also serves as a critical platform for the development, validation, and characterization of the paradigms and protocols for clinical PET studies [113, 114]. Several hundred small-animal PET scanners are now installed worldwide, and most academic medical research centers and pharmaceutical companies have access to and routinely use this technology [115, 116] .

Key performance features of small-animal PET systems are spatial resolution, sensitivity, and count rate capability [34, 116]. Spatial resolution strongly affects the quantitative accuracy of PET imaging due to the partial volume effect, the single largest quantitative error in almost all small-animal PET studies. Sensitivity significantly impacts the quantitative precision due to the statistical uncertainties that are governed by Poisson counting statistics. Improving spatial resolution reduces the partial volume effect, thus improving accuracy. Increasing the scanner sensitivity increases the number of detected events thus increasing the precision of PET measurements. Increasing sensitivity also enables faster dynamic imaging, and improves the quality of temporal data that can feed into tracer kinetic models, such as the image-derived input functions (IDIF) from major arterial vessels [117, 118].

Since its early development in the 1990s [119], both academia and industry have put substantial effort to improve the spatial resolution and sensitivity of small animal PET [116, 120–124]. However, none of the currently available small-animal PET

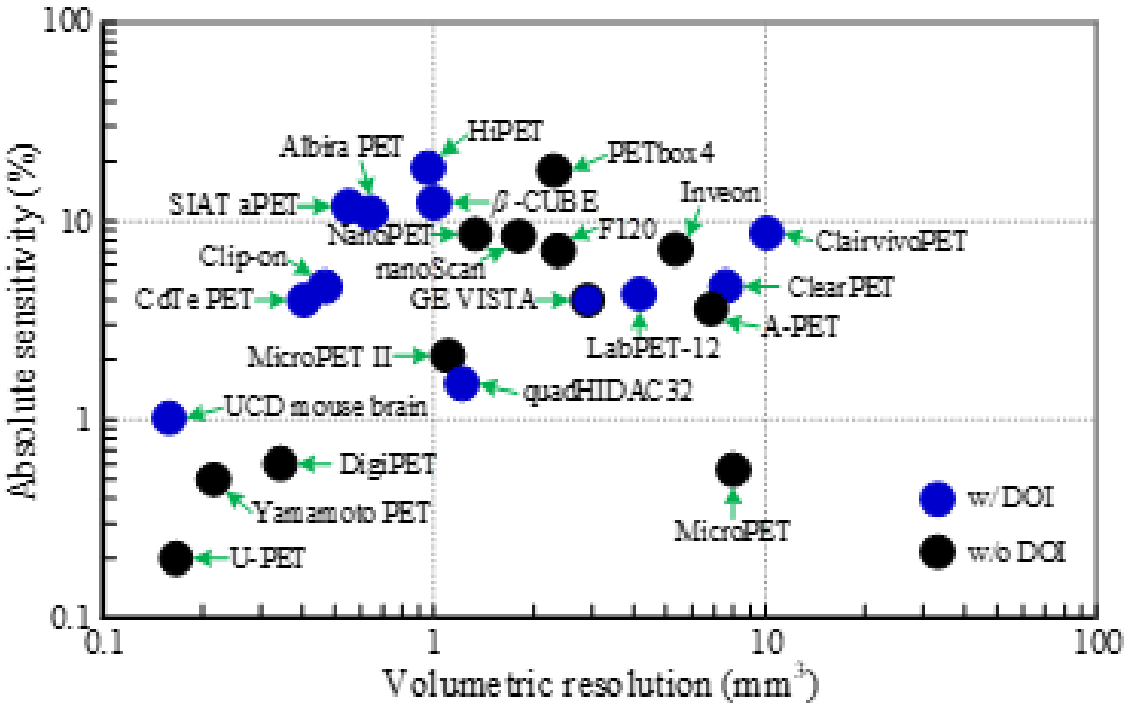

Figure 2.13. The performance of small animal PET scanners. Only scanners with published results were selected. The resolution and sensitivity values obtained at the center of the scanners were used..

scanners provide a combined performance of the theoretically achievable high spatial resolution (<0.5 mm) and high sensitivity (figure 2.13). Because the resolutions in the axial, tangential, and axial directions were different, volumetric resolution, which is the product of the resolution in each of the three directions, was used. Detailed performance of the scanners including reconstruction method are shown in Table 2.4. There have been three small animal PETs developed with 0.5 mm resolution at the center of the field of view (FOV), however, they all suffer from low sensitivity. Specifically, the commercially available U-PET achieves 0.5 mm resolution at the center of the FOV using a collimator, which adversely reduces its sensitivity to a very low level of 0.1% [116]. The PET system developed by Dr. Yamamato and colleagues using lutetium yttrium oxyorthosilicate (LYSO) arrays with a pitch size of

0.42 mm and thickness of 5 mm has a resolution of 0.6 mm and sensitivity of 0.5% at the center of the FOV [123] . The dedicated mouse brain PET developed by the University of California at Davis using lutetium oxyorthosilicate (LSO) arrays with a pitch size of 0.5 mm and thickness of 13 mm obtains a resolution of 0.5 mm, but its sensitivity is only 1% at the center of the FOV [122]. The low sensitivities of these systems limit their applications to static studies or situations where the animals are subject to very high injected doses. Additionally, the small geometry of the latter two systems, diameter ¡ 61 mm and axial length ¡10 mm, further limits their primary applications to static mouse brain studies.

Table 2.4. The performance of small animal PET scanners shown in Figure 2.13

Scanner name	Volumetric resolution (mm^3)	Sensitivity (%)	Energy window (keV)	Timing window (ns)	DOI information	Reconstruction method	Reference
MicroPET	6	0.56	250-650	12	No	FBP	[119, 125]
MicroPET II	1.1	2.1	250-750	6	No	OSEM	[126]
A-PET	8.7	3.6	250-665	7	No	FRP	[127]
quadHIDAC32	1.2	1.5	350-650	Unknow	Yes	FBP	[120]
GE VISTA	2.9	4	250-700	5/6.5/10*	Yes	FBP	[128]
CdTe PET	0.4	4	Unknow	20	Yes	MLEM	[129]
F120	2.4	7.1	250-750	10	No	FBP	[130]
Inveon	5.4	7.2	350-650	3.43	No	FBP	[131]
nanoPET	1.2	7.7	250-750	5	No	FBP	[132]
ClearPET	7.6	4.7	250-750	Unknow	Yes	FBP	[133]
PETBox4	3.4	18	150-650	20	No	MLEM	[134]
nanoScan	1.8	8.4	250-750	5	No	FBP	[135]
LabPET-12	4.6	4.3	250-650	22	Yes	FBP	[136]
DigiPET	0.34	0.3	400-650	20	No	MLEM	[137]
ClairvivoPET	10	8.7	250-750	10	Yes	FBP	[138]
U-PET	0.17	0.3	400-600	Unknow	No	OSEM	[116, 139]
UCD mouse brain	0.13	0.68	-250	60	Yes	MLEM	[122]
Yamamoto PET	0.22	0.5	Unknow	16	No	FBP	[123]
Clip-on	0.47	4.7	250-750	12	Yes	OSEM	[140]
β-CUBE	1	12.4	255-765	5	Yes	FBP	[141]
HiPET	0.9	10.4	350-650	20/15/8*)	Yes	OSEM	[124]
Albira PET	0.64	11	Unknow	Unknow	Yes	MLEM	[142]
SIAT aPET	0.55	11.9	350-750	6	Yes	OSEM	[143]

*Dual-layer crystal arrays with different crsytals were used.

In this study, with a goal to design a small animal PET system with a resolution of 0.5 mm and a high sensitivity ¿10% for total-body mouse/rat studies, we simulated four scanners with similar solid angles but different diameters (110 mm vs. 160 mm), axial lengths (167 mm vs. 254 mm) and crystal thicknesses (10 mm vs. 20 mm) (table 2.5 and figure 2.14) using gPET, a graphics processing unit (GPU) based Monte Carlo (MC) package dedicated for PET simulation (Lai et al 2019). The performance in terms of spatial resolution and sensitivity of the four PET scanners was compared to find the optimal scanner for different applications.

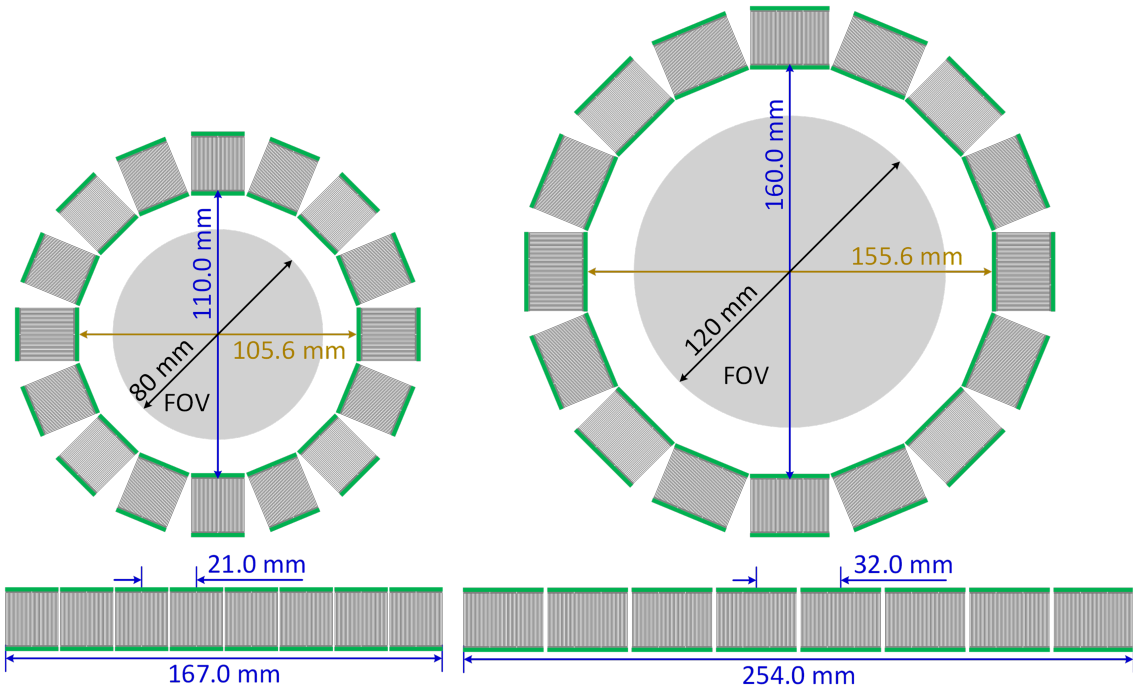

Figure 2.14. The schematics of (left) the H^2RS110-C20 PET and (right) the H^2RS160-C20 PET. The H^2RS110-C10 PET and the H^2RS160-C10 PET have the same diameter and axial length as those of the H^2RS110-C20 PET and the H^2RS160-C20 PET, respectively. C10 denotes a crystal thickness of 10 mm, and C20 of 20 mm..

Table 2.5. Characteristics of the four small-animal PET scanners

Parameters	H^2RS110-C10	H^2RS110-C20	H^2RS160-C10	H^2RS160-C20
Crystal material	LYSO			
Ring diameter (mm)	110		160	
Axial length (mm)	167		254	
Solid angle (4π)*	0.84		0.85	
Crystal cross section (mm^2)	0.44x0.44			
Crystal length (mm)	10	20	10	20
Crystal pitch (mm)	0.5			
Crystal array size	40 x 40		60 x 60	
Detectors per ring	16			
Number of detector ring	8			
Transaxial FOV (mm)	80		120	
Axial FOV (mm)	167		254	

*The solid angle is the one subtended from the center of the FOV. The solid angles of the gaps between detector modules were not subtracted.

2.2.2 Methods

2.2.2.1 *Characteristics of the four small-animal PET scanners*

The characteristics of the four scanners are shown in Table I. The four scanners were named H^2RS110-C10 PET, H^2RS110-C20 PET, H^2RS160-C10 PET, and H^2RS160-C20 PET. The schematics of the H^2RS110-C20 PET and H^2RS160-C20 PET are shown in figure 2.2. The four scanners are all composed of 128 dual-ended readout depth-of-interaction (DOI) encoding detector modules arranged in 8 detector rings. LYSO, the most widely used scintillator in state-of-the-art PET scanners, was selected because of its high light output, fast decay time, and high stopping power [144, 145]. Compared to other DOI encoding detectors, such as detectors based on multi-layer crystals, crystal arrays with specially designed reflectors and

monolithic crystals [146–149], the dual-ended readout detectors in combination with finely-segmented and thick crystals can simultaneously provide better DOI resolution, better spatial resolution and higher detector efficiency [150, 151].

The H^{2}RS110-C10 PET and the H^{2}RS110-C20 PET were composed of 128 40 $\times$ 40 LYSO arrays with a pitch size of 0.5 mm, and both have a diameter of 110 mm and axial length of 167 mm. They are expected to provide high-resolution and high-sensitivity imaging across the whole body of the laboratory mice, which have a nose-to-anus-length of 8-10 cm[152]. The H^{2}RS160-C10 PET and the H^{2}RS160-C20 PET were composed of 128 60 $\times$ 60 LYSO arrays with a pitch size of 0.5 mm, and both have a diameter of 160 mm and axial length of 254 mm. They are supposed to provide high-resolution and high-sensitivity imaging across the whole body of the laboratory rats, which have a nose-to-anus-length of 10-20 cm [153] . The H^{2}RS110-C10 PET and the H^{2}RS160-C10 use LYSO arrays with a thickness of 10 mm, whilst the H^{2}RS110-C20 PET and the H^{2}RS160-C20 PET use LYSO arrays with a thickness of 20 mm.

2.2.2.2 *Selection of the pitch size of the LYSO arrays*

The pitch size of the LYSO array affects the resolution and the sensitivity of the PET scanners. The fundamental resolution at the center of the FOV of PET scanner can be roughly estimated using [34, 154]

$$spatial\ resolution = \sqrt{(\frac{crystal\ size}{2})^2 + (positron\ range)^2 + (0.0022 * diameter)^2} \tag{2.4}$$

Based on this formula, we estimated the resolution of the proposal PET scanners with diameters of 110 mm and 160 mm as a function of the crystal size, as shown in figure 2.15. Here, we assumed a 0.102 mm FWHM positron annihilation point distribution

from the 18F label source [155]. Better resolution can be obtained using smaller crystals [156]. Reflectors are used to separate the LYSO elements, and optical glues are used to glue the reflector to the LYSO element in LYSO arrays. Both the reflectors and optical glue cannot detect gamma photons, hence they reduce the sensitivity of the PET scanner via reducing the fractional active area of the LYSO array. The lower the fractional active area, the lower the detection efficiency of the detector. The fractional active area of the crystal arrays can be estimated using

$$fractional\ active\ area\ (\%) = (\frac{crystal\ size}{array\ pitch\ size})^2 \times 100\% \tag{2.5}$$

Dual-ended readout detectors based on polished LYSO, Toray E60 with a thickness of 50 µm and 10 µm optical glue between crystal elements, can provide good crystal resolvability, energy resolution, and DOI resolution [151, 157]. The fractional active area of these LYSO arrays is also shown in figure 2.15 (red line), which decreases when the crystal size reduces. Based on our previous experimental results [151], LYSO arrays with a crystal size of 0.44 mm and pitch size of 0.5 mm were chosen in this work, which gives a good trade-off between the fractional active area of the LYSO array and the estimated resolution of the PET scanners (figure 2.15).

2.2.2.3 *Simulations*

Simulations of the four PET scanners were performed using gPET [158]. NEMA NU 4-2008, a standard for performance measurement of small animal PET systems, was followed to simulate the scanners and to report the resolution and sensitivity whenever possible. A 22Na point source with an activity of 1500 Bq and a varying diameter of 0, 0.1, and 0.3 mm was used in all simulations. The source was embedded in an acrylic cube of 10.0 mm on each side. In the simulation, the energy resolution was set to be 16%, and the timing window was set to be 4 ns, based on experimental

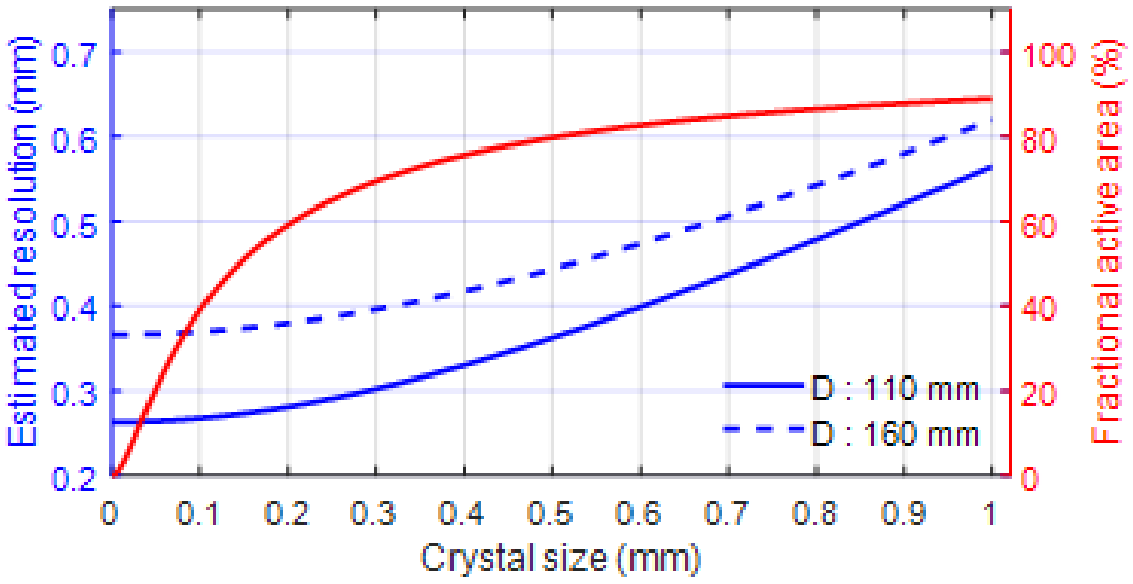

Figure 2.15. The estimated spatial resolution at the center of FOV for two scanners with ring diameters of 110 mm and 160 mm. The red line shows the fractional active area of the LYSO array with 50 µm Toray E60 reflector and 10 µm optical glue..

results [151]. Because we do not have the measured experimental energy resolutions for different crystal geometries, the 16% energy resolution was used to set the energy distribution of the gamma photons for all the four scanners in the simulation. Based on our previous experimental results, the energy resolutions of the four detector geometries will not have significant differences [151, 159] .

Table 2.6. Positions for sensitivity studies

Parameters	H^2RS110-C10	H^2RS110-C20	H^2RS160-C10	H^2RS160-C20
Radial offset from center (mm)	0, 5, 10, 15, 25, and 40		0, 5, 10, 15, 25, 50 and 60	
Axial offset from center (mm)	From 0 to 80 with steps of 10		From 0 to 120 with steps of 10	

Sensitivity The sensitivities of the four PET scanners were simulated at different radial offsets and axial offsets, as shown in Table 2.6. At each position, more than 106 coincidence events were collected. For each scanner, sensitivities obtained from the same data set but using three energy windows of 150-750 keV, 250-750 keV, and 350-650 keV were compared.

Table 2.7. Positions and DOI resolutions for resolution simulation

Parameters	H^2RS110-C10	H^2RS110-C20	H^2RS160-C10	H^2RS160-C20
Radial offset from center (mm)	0, 5, 10, 15, 25, and 40		0, 5, 10, 15, 25, 50 and 60	
Axial offset from center (mm)	0 and $\frac{1}{4}$ offset			
DOI resolution (mm)	0, 0.5, 1, 2 and 3			
Source diameter (mm)	0, 0.1 and 0.3			

Spatial resolution The resolutions of the four PET scanners were simulated at different radial offsets and axial offsets, as shown in Table III. In the real experiment, a 22Na point source with a diameter of no more than 0.3 mm in all directions is recommended to measure the spatial resolution following the NEMA NU 4-2008 standard. To investigate the effect of source size on the resolution, sources with three different diameters of 0, 0.1, and 0.3 mm were used in the simulation. In all simulations, an energy window of 250-750 keV was used to select events, and at each position, more than 106 coincidence events were collected. In our simulation, the center of mass

location (x_c, y_c, and z_c) of the interaction of the annihilation photons in the LYSO array was recorded using

$$x_c = \frac{\sum_{i=1}^{N} x_i E_i}{\sum_{i=1}^{N} E_i} \tag{2.6}$$

$$y_c = \frac{\sum_{i=1}^{N} y_i E_i}{\sum_{i=1}^{N} E_i} \tag{2.7}$$

$$z_c = \frac{\sum_{i=1}^{N} z_i E_i}{\sum_{i=1}^{N} E_i} \tag{2.8}$$

where the x_i, y_i, and z_i ($i = 1 \ldots N$) are the positions along axial, tangential, and radial directions for each interaction, respectively. E_i ($i = 1 \ldots N$) are the deposited energies blurred by energy resolution at each interaction, and N is the number of the interactions before one gamma photon deposited all its energy or escape from the crystal array. To model the effect of finite DOI resolution, the recorded position along the radial direction was added by a random displacement following a Gaussian distribution with the full width at half maximum (FWHM) being the DOI resolution [160].

Although the filtered back projection (FBP) method is recommended by the NEMA NU 4-2008 protocol, the maximum likelihood expectation maximization MLEM algorithm is more popular for the reconstruction of data from most modern PET scanners (Hallen et al 2020). And MLEM is also more robust against noise and systematic inconsistencies than FBP (Nuyts et al 2001). Hence, the MLEM method with 12 iterations was used to reconstruct the images of the point source in our studies, and a voxel size of $0.04 \times 0.04 \times 0.04 mm^3$ was used to make the voxel size at most one fifth of the finest resolution, following the NEMA NU 4-2008 standard. To avoid the artificially enhanced resolution measured using MLEM to fairly compare the four scanners with different geometries, a uniform background was used during our

simulation. The contrast of point source to background in the reconstructed images was 10:1 [161, 162].

The spatial resolution of the reconstructed image along the radial, tangential, and axial direction was taken to be the FWHM of the point spread function (PSF) of the reconstructed point source along that direction. To calculate the PSF along one direction, the 3D reconstructed point source image was summed over the other two directions, following the NEMA NU 4-2008 standard. For example, to calculate the FWHM resolution along the axial direction, the reconstructed image was summed along the radial and tangential directions.

2.2.3 Results

2.2.3.1 Energy spectrum

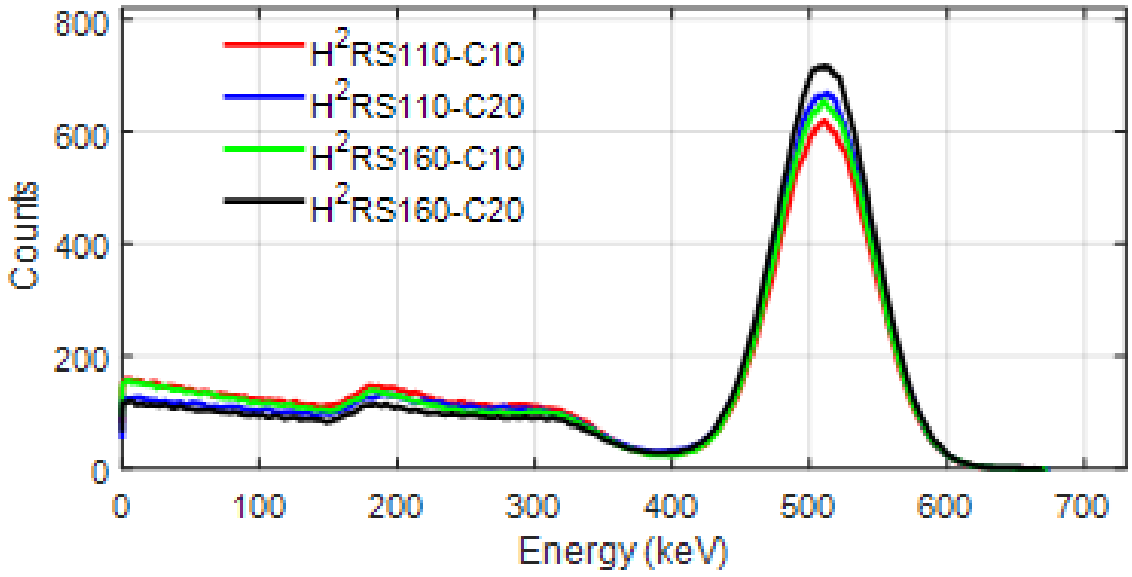

Figure 2.16. Energy spectra for the four scanners obtained by locating the ^{22}Na source at the center of FOV. For each energy spectrum, one million coincidence events were used..

Figure 2.16 shows the energy spectrum of the four scanners with the 22Na source located at the center of the FOV of the scanners. Each spectrum was generated using 106 coincidence events. The energy spectrum of the H^{2}RS160-C20 PET had the fewest low-energy events, whilst the H^{2}RS110-C10 PET had the most. The percentages of events in a 250 – 750 keV energy window are 67.0%, 71.6%, 68.8%, and 74.7% for H^{2}RS110-C10, H^{2}RS110-C20, H^{2}RS160-C10, and H^{2}RS160-C20, respectively. This can be understood by the fact that the larger the detector size, the higher the probability that a photon can deposit all energy inside the detector through multiple interactions.

2.2.3.2 Sensitivity

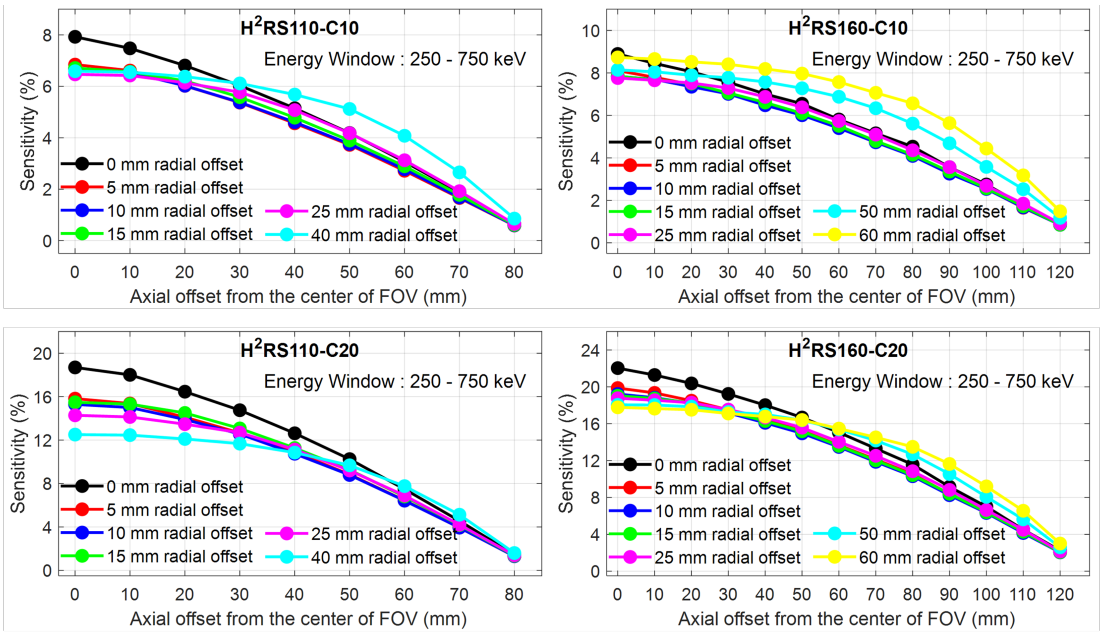

Figure 2.17. Sensitivity versus radial offset and axial offset for (left top) H^{2}RS110-C10, (left bottom) H^{2}RS110-C20, (right top) H^{2}RS160-C10 and (right bottom) H^{2}RS160-C20. A 250-750 keV energy window was used to select events..

Figure 2.17 shows the NEMA NU 4-2008 sensitivity of the four scanners obtained at different radial offsets and axial offsets using a 250-750keV energy window to select events. At the center of the FOV, the sensitivities of the H^{2}RS110-C10 PET and the H^{2}RS110-C20 PET are 7.9% and 18.7%, respectively, and the sensitivities of the H^{2}RS160-C10 PET and the H^{2}RS160-C20 PET are 8.9% and 22.0%, respectively. The sensitivities of the H^{2}RS110-C20 PET and the H^{2}RS160-C20 PET were more than 2 times higher than those of the H^{2}RS110-C10 PET and the H^{2}RS160-C10 PET, respectively. For a given crystal thickness, the scanner with a diameter of 160 mm had a slightly higher sensitivity than that with a diameter of 110 mm, which is due to the fact that the solid angles of the gap/dead space between crystals and detectors were smaller for the scanner with a larger diameter. The slightly lower ratio of low-energy events also contributed to higher sensitivity (figure 2.16).

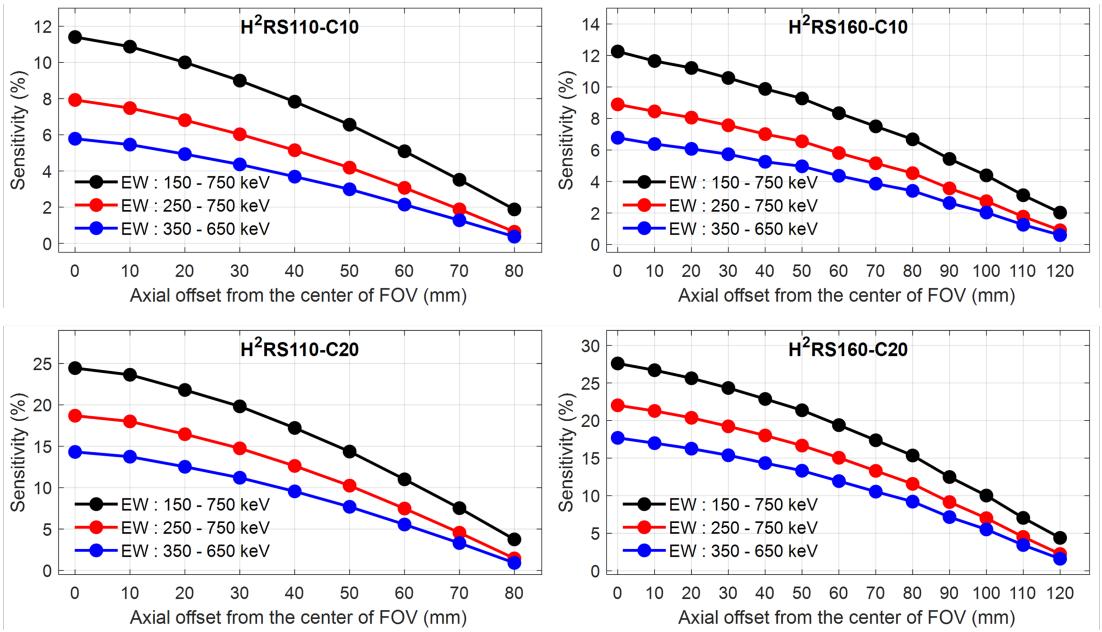

Figure 2.18. Sensitivity along center axial obtained using three different energy windows. H^{2}RS110-C10 (left top), H^{2}RS110-C20 (left bottom), H^{2}RS160-C10 (right top) and H^{2}RS160-C20 (right bottom)..

Figure 2.18 shows the sensitivities of the four scanners along the central axis under three different energy windows. A higher sensitivity was obtained when a wider energy window was used, which is consistent with common expectations.

2.2.3.3 Spatial resolution

Figure 2.19 shows the spatial resolution of the four scanners obtained at different radial offsets for varying DOI resolutions and at the axial center of the FOV using an ideal point source (diameter of 0 mm). The resolutions obtained at one-fourth of the axial FOV from the center of the axial FOV were similar to those obtained at the axial center of the FOV and omitted here for conciseness. From the resolution shown in figure 2.7, we made the following observations:

First, as expected, the radial resolution strongly depends on the source position and DOI resolution. However, the tangential and axial resolutions did not change significantly with source positions and DOI resolutions. A better radial resolution can be obtained if the scanner has a better DOI resolution. These are consistent with previous studies and suggest the importance of designing detectors with a good DOI resolution [156, 160, 163].

Secondly, the spatial resolution of the scanners with the same diameter are similar if the scanners have the same DOI resolution.

Finally, for a given DOI resolution, the tangential and axial resolutions of the scanners with a diameter of 110 mm are better than those with a diameter of 160 mm for all radial offsets studied because non-collinearity is smaller for the detector ring with a smaller diameter (110 mm) than that with a larger one (160 mm). In contrast, the behavior of the radial resolution is quite different. The radial resolution is better for the scanners with a diameter of 110 mm than those with a diameter of 160 mm at the positions close to the center of the FOV, while the relation is reversed at the

positions near the edge of the FOV. The reasons are detailed as follows. Aside from the non-collinearity effect, the radial resolution is affected by DOI as well. Under a given DOI resolution, the closer the source moves to the detector, the larger the DOI effect in the radial direction. Hence, moving from the center to the edge of the FOV, although the 160 mm systems start with a worse spatial resolution than the 110 mm systems, their resolution evolves with a smaller slop. Depending on the relative contribution of the DOI effect and the non-collinearity effect [34], the resolution trends of the two types of systems cross at a certain radial offset point. After this point, the radial resolution is worse for the 110 mm systems than for the 160 mm systems. Note that for perfect DOI resolution (0 mm), such a crossing phenomenon was not observed (top left of figure 2.19).

Although substantial efforts have been devoted to improving the DOI resolution [157, 163, 164], the current experimentally achievable DOI resolution are 1 and 2 mm for dual-ended readout PET detectors with 10 mm and 20 mm LYSO arrays, respectively [151, 159]. Taking this into account, we compared the resolutions of the H^2RS110-C10 PET and the H^2RS160-C10 PET with 1 mm DOI resolution, and the H^2RS110-C20 PET and the H^2RS160-C20 PET with 2 mm DOI resolution. The results are shown in figure 2.8. As expected, for a given scanner diameter, scanners with 1 mm DOI resolution (H^2RS110-C10 PET and H^2RS160-C10 PET) have a better spatial resolution than those with 2 mm DOI resolution (H^2RS110-C20 PET and H^2RS160-C20 PET), especially for the radial resolution at positions away from the center of the FOV. This indicates that if high spatial resolution was the primary selection criteria, the H^2RS110-C10 PET and the H^2RS160-C10 PET would be a better choice.

Figure 2.21 shows the resolutions obtained using the 22Na point source with three different diameters of 0, 0.1, and 0.3 mm for the scanners with DOI resolutions

listed in 2.7. The source size effects on the resolution obtained at other DOI resolutions exhibit similar trends as the ones shown in figure 2.9 and are omitted here for conciseness. As can be seen from figure 2.21, the point source with a diameter of 0.1 mm has a negligible effect on the spatial resolutions, while the point source with a diameter of 0.3 mm had a significant effect on the spatial resolution. These results indicate that to measure the intrinsic resolution of the proposed PET scanners in a real experiment, the point source should have a size as small as possible and the widely used ^{22}Na point sources with diameters of 0.2 0.3 mm can lead to an underestimated resolution, i.e. an estimated resolution that is worse than the true resolution.

2.2.4 Discussion

The simulation results show that all four scanners can provide high spatial resolution and high sensitivity performance across their FOV and there is no clear-cut winner out of the four candidate designs. The best design choice depends on the specific applications and their requirements on resolution and sensitivity. Here, we recommend several choices among four designs for the following scenarios based on our current simulation study: 1) for studies that only use mouse models, the H^{2}RS110-C10 PET and the H^{2}RS110-C20 PET may be preferred, as these two scanners provide better spatial resolution (figures 2.18 and 2.19) at a lower cost, and 2) for rat studies, H^{2}RS160-C10 PET and the H^{2}RS160-C20 PET may be more appropriate as they provide a larger FOV to cover the entire rat body. The volume of LYSO needed for the H^{2}RS160-C20 PET and the H^{2}RS160-C20 would be 2.25x of those for the H^{2}RS110-C10 PET and the H^{2}RS160-C10 PET, respectively.

The spatial resolutions of the scanners at the center of the FOV are all better than 0.5 mm. The radial resolution strongly depends on the radial offset and the DOI resolution as summarized in figure 2.22. When the DOI resolution was better, the

radial resolution was greatly improved. This indicates the importance of developing detectors with a high DOI resolution. The tangential and the axial resolutions were also affected by the DOI resolution, but with a much smaller magnitude (figure 2.19), which is consistent with previous studies [160]. Since the DOI resolution of 10 mm thick LYSO can be twice as good as that of 20 mm thick LYSO, the H^2RS110-C10 PET and the H^2RS160-C10 PET provide better resolution than the H^2RS110-C20 PET and the H^2RS160-C20 PET, respectively (figure 2.19).

The sensitivities at the center of FOV of the H^2RS110-C20 PET and the H^2RS160-C20 PET are 20%, which are more than 2-fold higher than those of the H^2RS110-C10 PET and the H^2RS160-C10 PET (10%) (figures 2.16 and 2.17). The sensitivities of the four proposed scanners are much better than currently available PET scanners with 0.5 mm resolution (the UCD mouse brain PET, U-PET, and Yamamoto PET shown in figure 2.13). The high sensitivity and larger FOV of the four scanners will also enable fast total-body dynamic imaging of mice and rats.

A ^{22}Na point source with a diameter smaller than 0.3 mm was recommended to measure the spatial resolution in NEMA NU 4-2008 protocol, and point sources with diameters of 0.25 mm have been widely used [**krishnamoorthy2018performance**, 122, 123, 131] . However, our simulation results show that to precisely measure the spatial resolution of scanners with an intrinsic resolution of 0.5 mm, a point source with a diameter smaller than 0.1 mm is preferred. Otherwise, the resolution will be overestimated (figure 2.21). To obtain the intrinsic resolution using sources with diameters larger than 0.1 mm, the intrinsic resolution can be estimated by subtracting the intrinsic resolution of the source, instead of the diameter or radius in quadrature from the measured resolution. We will study the intrinsic resolution of the source as a function of its diameter with the Monte Carlo in the future.

The inter-crystal and inter-detector scatter were not corrected in our studies, although the inter-crystal scatter correction can improve the spatial resolution and the inter-detector scatter correction can improve the sensitivity, respectively [165]. The inter-crystal scatter and inter-detector scatter were not corrected in our studies for two reasons. First, to design a high-resolution PET scanner, position-sensitive SiPMs (PS-SiPMs) are one attractive option [150, 151]. However, PS-SiPMs use center-of-gravity methods to calculate the gamma interaction position in the scintillator array, thus the inter-crystal scatter information is lost. Second, the inter-detector scatter was ignored to mimic the case that the readout electronics for each detector module work independently and in parallel, which can minimize the dead time of the readout electronics and increase the event processing rate of the electronics, hence, the peak noise equivalent count rate (NECR) will be maximized.

The NEMA image quality phantom and the micro Derenzo phantom were not investigated in our studies, because the four scanners had different diameters and our main focus is on comparing their sensitivity and spatial resolution. If the NEMA image quality phantom with its relatively small diameter of 33 mm is used, the H^2RS110-C10 and the H^2RS110-C20 will give misleading results, as the H^2RS160-C10 and the H^2RS160-C20 provided a better resolution for positions far from the center (figures 2.19 and 2.20). The same is true for the Derenzo phantom. The resolution and sensitivity results from point sources at different locations already showed that there is no winner for all tasks, and that the best choice depends on the specific applications. In the future, before adopting any design, a simulation using custom phantoms that reflect a specific small-animal imaging task is necessary to assess whether the image quality can achieve the specific requirement of the small animal PET imaging applications.

The NECR was not investigated in our studies, which is due to that the NECR depends both on the performance of the detector modules and the deadtime of the readout electronics, and readout electronics for the proposed scanners is not available at this moment. We will conduct the NECR simulation when we further develop our readout electronics in the future. However, based on our previous experimental results, we expected that each of the proposed detector modules can handle higher than 100,000 events per second without performance degradation [151].

In our simulation, we chose to use LYSO crystals, which have similar properties as LSO crystals, such as high light output, fast decay time, and high stopping power [144, 145]. Gadolinium aluminum gallium garnet (GAGG) has a higher light output than LYSO, and a dual-ended readout detector based on GAGG can provide a better DOI resolution. However, the stopping power of GAGG is lower than that of the LYSO, hence, the inter-crystal and inter-detector scatter ratios are much higher in PET scanner with GAGG than that with LYSO [165] , making GAGG a less optimal choice for high-resolution PET than LYSO or LSO.

To build the proposed scanners, the most complex and difficult part is the LYSO arrays of $0.44 \times 0.44 \times 20 mm^3$ polished crystal pixels. During the past 10 years, working with our industrial collaborators, we have optimized the LYSO array fabrication methods, and it is now routine to produce reliable scintillator arrays with crystal elements in the $0.4 \times 0.4 mm^2$ cross-section range [122, 151, 166, 167]. The reliability of the proposed scanners will also depend on the carefully designed electronics and gantries, which will not be a problem based on currently available technologies [122, 168, 169].

2.3 Conclusions

We developed gPET, a GPU-based, PET-dedicated MC simulation tool. gPET has three functional modules carried out by the GPU parallel threads. It employs voxelized and parametrized geometries in phantom-related and detector-related modules, respectively. Multiple inputs and outputs are available for users. We simulate three test cases to demonstrate the accuracy and efficiency of gPET with benchmarks from GATE. An average differences around 3% for the final coincidence pair distributions are found between gPET and GATE, while the simulation speed of gPET is 100 200 times faster than GATE. In conclusion, gPET is an accurate and efficient MC simulation tool for PET. The open source code of gPET version 1 is available for the research community via email request.

Furthermore, with the efficient package gPET, we are able to conduct a large scale PET simulations (approximately 1000 simulations in this work) and thus examine the performance of four PET scanners with different configuration. Their resolution and sensitivity were investigated to test the goal of building a 0.5 mm resolution high-sensitivity small animal PET system. The simulation study shows that the H^2RS110-C20 PET and H^2RS160-C20 PET have more than 2x the sensitivity of the H^2RS110-10 PET and H^2RS160-10 PET (20% vs 10%), while the latter two scanners provide a higher and more uniform spatial resolution across the FOV when taking the realistic DOI resolution into account. The H^2RS160-C10 PET and H^2RS160-C20 PET provide a larger FOV, which can be used for both total-body mouse and rat imaging. The H^2RS110-C10 PET and H^2RS110-C20 PET provide a smaller FOV, which is only suitable for total-body mouse imaging but provide a better resolution across the entire mouse body at a lower cost. Our simulation also suggest a source with diameter smaller around 0.1 mm to find the intrinsic resolution of PET system with high resolution.

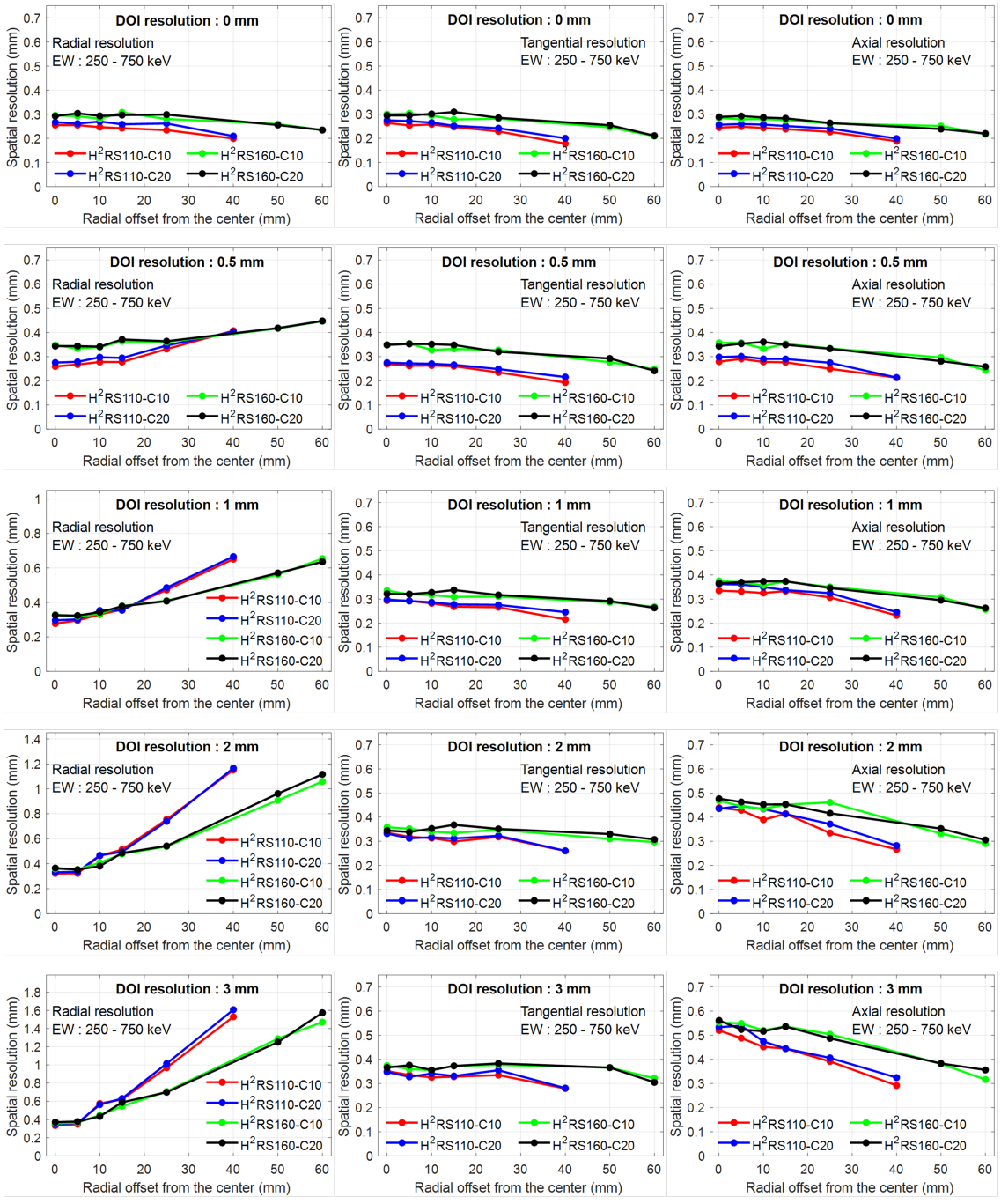

Figure 2.19. Radial (left column), tangential (middle column) and axial (right column) resolution versus radial offset and DOI resolution. A 250-750 keV energy window was used to select events..

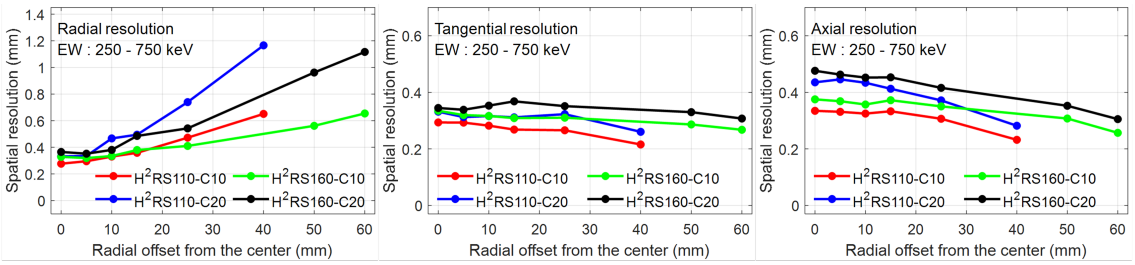

Figure 2.20. Radial (left column), tangential (middle column) and axial (right column) resolution versus radial offset with realistic DOI resolutions. A 250-750 keV energy window was used to select events. The DOI resolution for H^2RS110-C10 PET and H^2RS160-C10 PET was 1 mm, and it was 2 mm for H^2RS110-C20 PET and H^2RS160-C20 PET..

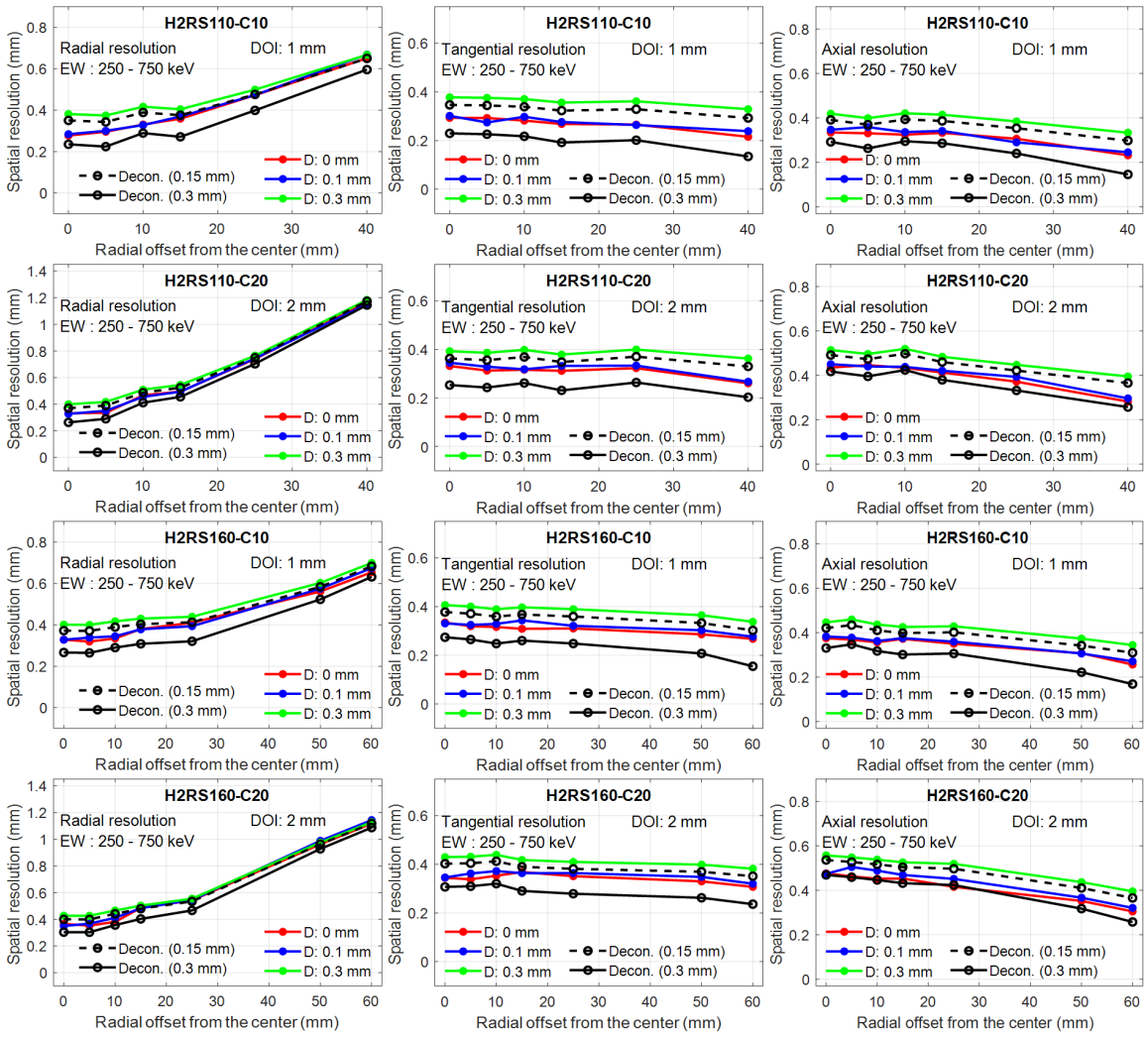

Figure 2.21. Effect of the radiation point source size on the resolution. H^{2}RS110-C10 PET and H^{2}RS160-C10 PET have a DOI resolution of 1 mm, and H^{2}RS110-C20 PET and H^{2}RS160-C20 PET have a DOI resolution of 2 mm..

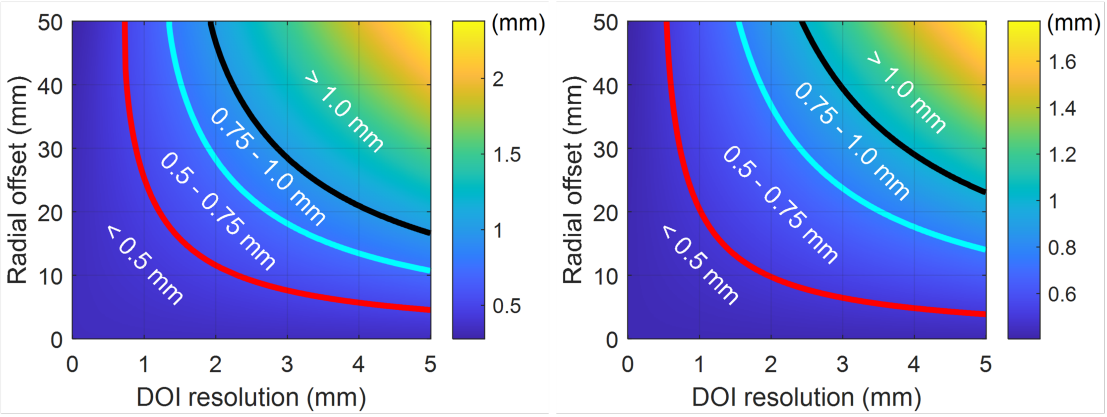

Figure 2.22. Resolution map as function of radial shift and DOI. left:H^2RS110-C10 PET; right:H^2RS160-C10 PET .

CHAPTER 3

DOSE SIMULATIONS FOR THERAPEUTIC BEAMS

In this chapter, We divert to a different field – dose calculation. As used in countless papers, dose is an indicator of radiation damage. Typically, the more it is, the more damage radiation brings to the target. And also, many thresholds of radiation safety or treatment plan quality are given in dose values in a certain volume. Hence, it is important to calculate dose accurately. And the calculation should be fast as well to meet clinical demand for on-site planning and optimization.

MC method is accurate in terms of macro dose calculation as the physics between particles and medium is understood quite well. But it is also computational demanding. One way to reduce the burden is to simplify the geometry, considering less component. Such simplification requires a proper modelling of source particles at a certain surface. We here reported a source model for a MRI-LINAC machine.

3.1 Simulation for MV beams

A source model is a description of virtual sources that could replace the source in a real machine. There are two meanings for using the term "replace". First, particles from the virtual source could produce same dose distribution in the phantom as that from the real source. Second, the specific components of the interested machine should not have to be considered when we transport the particles from virtual source. Otherwise, we could just sampling particles from the real source and transport them from the beginning to the end. In this manner, dose calculations could be accelerated and might meet the clinical requirements of speed.

The virtual source could be in any shape and defined in anywhere as long as photons from it could reproduce the dose distributions. However, due to the simplicity of source sampling and requirement of physics symmetry, virtual source is usually defined on a plane [170–172]. Specifically to our work on MRI-LINAC, we use a curved plane to define the virtual source.

3.1.1 Source model for MRI-LINAC

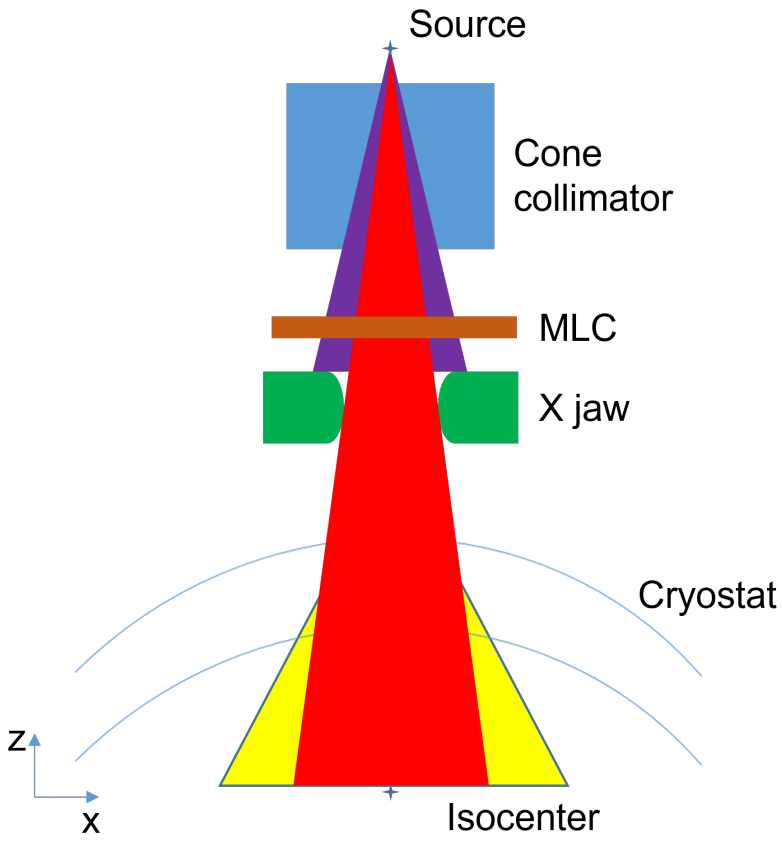

Figure 3.1. Illustration of photon paths from LINAC machine to isocenter. For better readability, please check online colorful version..

Before we present the source model, we have to clarify some concepts. Figure 3.1 listed the major components considered to construct our model. The opening of MLC is along y direction and not shown. The cone collimator, MLC and X jaw are made up of lead. They together determined the irradiated shape and size on isocenter. The largest rectangular shape is denoted as F. Photons from the source have three destinies: blocked by the collimators and jaw as shown in purple; directly go through all components as shown in red; scattered by cryostat as shown in yellow. Note, there were scattered photons in the the red region. We named these three photons as blocked, primary and scattered photons, respectively. Here, we ignored the scattered photons from the edge of collimators and jaw. On the one side, cryostat contains about 50 cm thick liquid helium [173], which means around 23% of all photons go through scattering for 2 MeV photons, estimating from $e^{-\frac{\mu}{\rho}\rho\times 50\ cm}$ with material data from NIST [1]. On the other side, only very small portion of the edge part of collimators and jaw could have effective scattering photons because the very large attenuation of lead. Furthermore, we ignored the contribution from electrons because of the block from thick cryostat and small contributions even without cryostat [170].

We could define two kinds of 2D map. First, we could find the distribution of primary photons and scattered photons on F', denoted as $P(x, y)$ and $S(x, y)$, respectively, when largest field F was achieved. Here, F' denotes a field larger than F to include scattered photons and $P(x, y)$ and $S(x, y)$ were directly related the number of photons. In addition, the opening of different leaves of MLC and X jaw generate a 2D map of opening time, say on a plane between X jaw and cryostat. The sequence of opening leaves and jaw could be read from a treatment plan while the design of a sequence is out of the scope of this thesis. Such time map could be transformed to fluence map or MU map, which corresponds to number of photons

[1] https://www.nist.gov/pml/x-ray-mass-attenuation-coefficients

passing through. And we could always project the map onto the plane that crosses isocenter. Because of this, all the maps mentioned in the following are defined on a plane crossing isocenter, if necessary, by means of projection. We denoted this fluence map on F as $f(x, y)$.

3.1.1.1 GEANT4 simulation of $P(x, y)$ and $S(x, y)$ for largest field F

We simulated the source in MRI-LINAC as 7.2 MeV electrons bombarding at a target tungsten with thickness 0.28 cm. Cone collimator is a cuboid of lead with a cone hollow in the middle part. The half cone angle is 20 degrees. MLC and X jaw were modeled as a cuboid with curved surface to define F. F is with dimension 58 $cm \times 22cm$. Cryostat was modeled as cylinder shell with inner radius 51.5 cm and outer radius 88.7 cm, whose center was isocenter, 143.5 cm away from the source. This shell was filled with liquid helium. We then recorded the photon positions and momentum on F', whose dimension was 60 $cm \times 60$ cm. We distinguished scattered photons by monitoring if there was momentum change along the transport. From these information, we traced back these photons to a cylinder with radius 70.1 cm (mid plane) and then projected to F to obtain $P(x, y)$ and $S(x, y)$. The reason for choosing radius 70.1 cm was that we assumed it was the average interaction depth. Note, $P(x, y)$ would be same as what was recorded on F' yet there would be difference between $S(x, y)$ on F' and that on F through projection.

3.1.1.2 Analysis of $P(x, y)$ and $S(x, y)$

Figure 3.2 shows our GEANT4 simulation results of primary photons and scattered photons. It could be seen that the distribution of scattered photons is sort of a smeared version of primary photons. Form a physics viewpoint, every photon passing through the cryostat may undergo scattering and hence deviated from its original

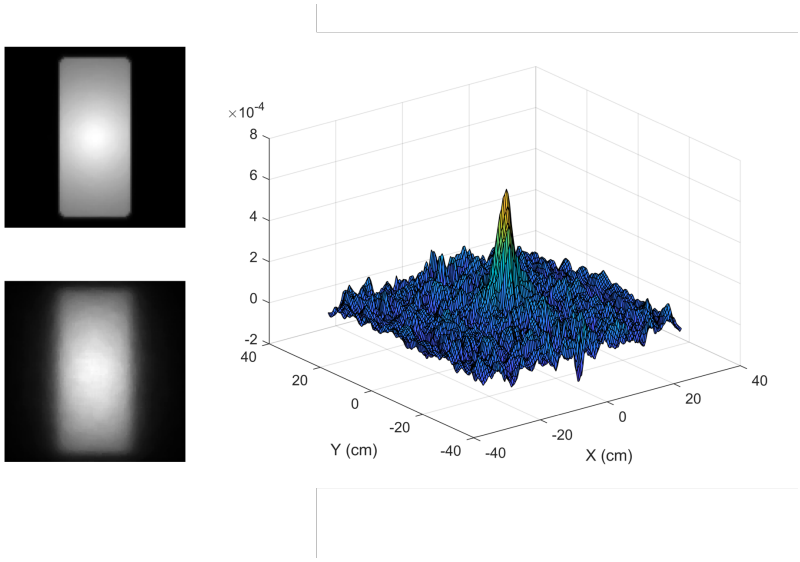

Figure 3.2. Deconvolution between two maps $P(x, y)$ and $S(x, y)$. left top: $P(x, y)$; left bottom: $S(x, y)$; right: deconvolution kernel..

path, namely direction from source to this point. Since we chose a cylinder shell with radius 70.1 *cm* as sampling plane, the deviation actually caused a blur on this curved plane if we traced all photons to this plane. Since the region on the curved plane covered by F is rather flat, we could assume the blur effect is quite the same for each point. In fact, the largest angle to isocenter on the curve plane is about 20 degrees. Therefore, we wrote

$$S = P * K \tag{3.1}$$

for which we used *deconvwnr* function in MATLAB [2] to find the convolution kernel K

$$K = deconvwnr(S, P, 100000000) \tag{3.2}$$

The large value used in the function is to adjust noise ratio.

[2] version R2020a

The result was shown in Figure 3.2. We found that the kernel could be well represented by a 2D Gaussian distribution

$$K = R_{SP} \times \frac{1}{\sqrt{2\pi\sigma_x}} \frac{1}{\sqrt{2\pi\sigma_y}} e^{-\frac{x^2}{2\sigma_x^2}} e^{-\frac{y^2}{2\sigma_y^2}} \tag{3.3}$$

where $\sigma_x = 3.7\ cm$, $\sigma_y = 1.85\ cm$ and $R_{SP} = 0.0873$. R_{SP} basically represented the ratio between number of scattered photons and that of primary photons. Note, We did not set the thickness of helium shell to about 50 cm because we could not have an exact and unique value of thickness for its irregular shape. Hence, R_{SP} may not reflect the real ratio between number of scattered photons and that of primary photons. But this will not change the core of the problem where scattered photons could be represented by a smearing effect on primary photons. When we commission the beam to a measurement result, we could adjust R_{SP}, σ_x and σ_y accordingly. For a purpose of generalization, the code supported input of two maps as well.

3.1.1.3 Description of scattering photons

The above section only describes the location of photons' start positions. Yet, it did not mention the speed direction. For primary photons, its speed direction is a direction from source to sampled position. But for scattered photons, their directions must deviated from the direction of corresponding primary photons. Considering scattered photons mostly come from Compton scattering for photons with MeV energy, we may safely estimate there was only one Compton scattering effect for scattered photons because the mean free length between two Compton events should be larger

than $\lambda = 1/\mu \sim 180\ cm$ for 2 MeV photons in liquid helium [3]. From Klein-Nishina formula [174], which was

$$d\sigma/d\Omega = pe(\gamma,\theta)^2 * (pe(\gamma,\theta) + 1/pe(\gamma,\theta) - \sin\theta^2)$$
$$pe(\gamma,\theta) = \frac{1}{1+\gamma*(1-\cos\theta)}, \tag{3.4}$$

we could plot cross section as function of deviation angle θ. Here, $\gamma = E_\gamma/m_e c^2$ means the ratio between photon energy and electron rest energy. The results were shown in Figure 3.3 and could be well presented by a Gaussian distribution with standard deviation σ_θ. Like what was done for position sampling, the code supported input of σ_θ map as well.

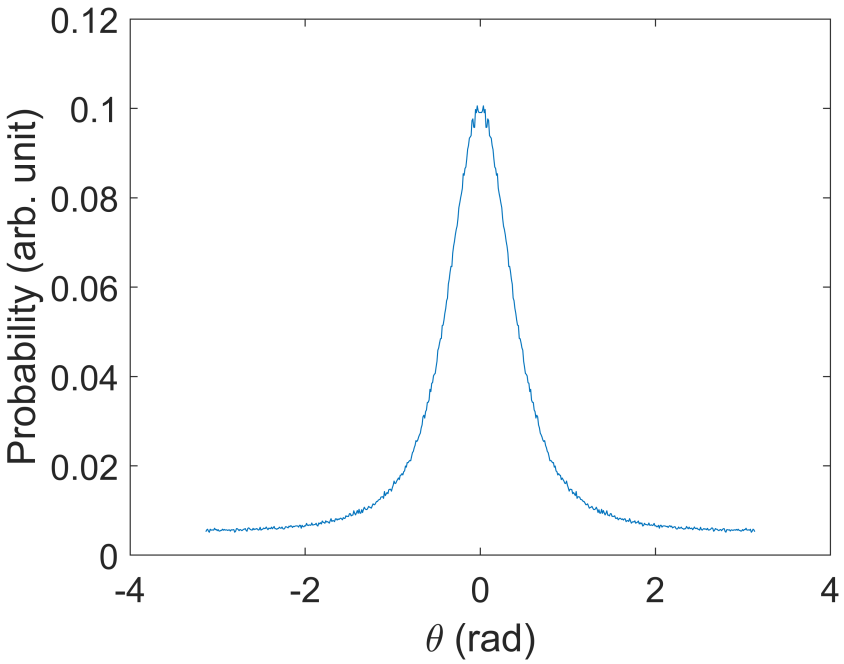

Figure 3.3. Sampling angle distribution of one million Compton scattering events for photons with 2 MeV..

[3] https://physics.nist.gov/PhysRefData/XrayMassCoef/ElemTab/z02.html

3.1.1.4 Sampling of energy

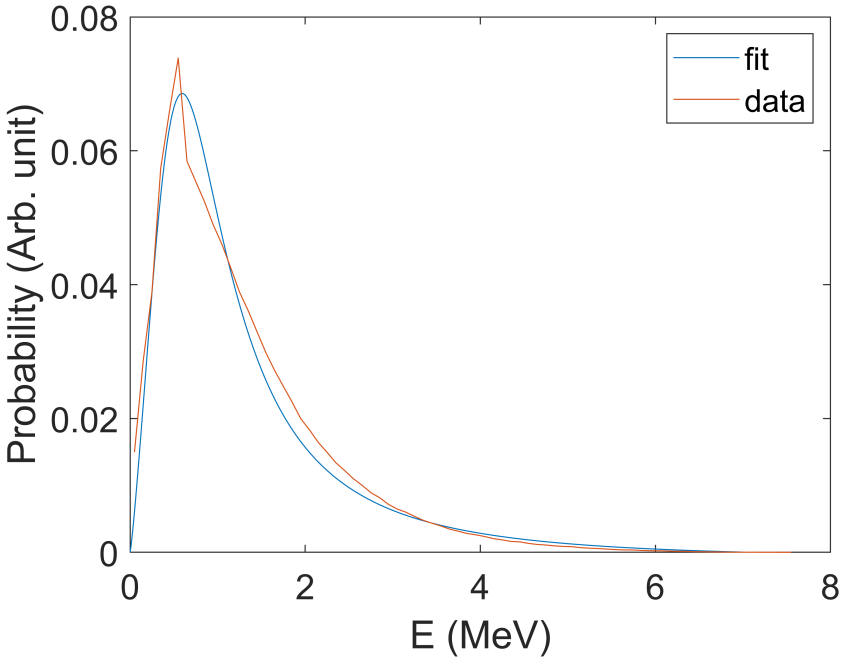

Figure 3.4. Comparison between energy fitting and energy histogram for scattering photons..

Then we need an energy model for sampling source photon energies. By observing energy histograms of primary and scattered photons, we found out that the energy spectrum could be expressed by

$$P(E) = a * \frac{E^n}{1 + b * E^m} * (E_{max} - E) \tag{3.5}$$

for both photon types. $E_{max} = 7.2MeV$ is the maximum photon energy for this work. An illustration figure was shown in Figure 3.4 for scattered photons.

3.1.1.5 Source size effect

3.1.1.6 Source size effect

Because sometimes $f(x, y)$ can be very concentrated, namely large value in mm scale, the source size has non-negligible effect on the dose profiles, especially when we consider the long distance between MLC and isocenter. A source of diameter 7 mm would affect around 2 cm on the edge part of the field ($7\ mm * (143.5 - 37)/37$). We used a Gaussian distribution with standard deviation σ_S to represent the source size effect.

3.1.1.7 Sampling of beamlets location

In this section, we will talk about how to do the sampling so that the MC simulation gives absolute dose values. This actually consisted of two part: how to sample photons and how to assign weights. From the importance sampling theory, we have

$$\sum_{X \sim p(X)} g(X) = \sum_{X \sim q(X)} \frac{p(X)}{q(X)} g(X) \tag{3.6}$$

Here, $X \sim p(X)$ means X is sampled from a distribution $p(X)$ and same for $X \sim q(X)$. $p(X)$ and $q(X)$ are normalized probability density. N is the number of sampling points. Hence, if we grid the field F and hence grid the maps of $P(x, y)$, $S(x, y)$ and $f(x, y)$, the product $f(x, y) \times (P(x, y) + S(x, y))$ represents the number of photons passing through pixel (x, y). We could always just use one variable X to represent the pixel index (x, y), for instance linear index. Thus, we have

$$\begin{aligned} D(\vec{r})_{MC}/N &= \frac{1}{N} \sum_{X \sim f(X) * (P(X) + S(X))} 1 \times D(\vec{r}|X)_{MC} \\ &= \frac{N_f}{N} \times \sum_{X \sim \frac{f(X)}{N_f}} (P(X) + S(X)) \times D(\vec{r}|X)_{MC} \end{aligned} \tag{3.7}$$

with

$$N_f = \sum_{X \sim U(F)} f(X). \tag{3.8}$$

$U(F)$ means uniform sampling in field F. $D(\vec{r})_{MC}$ means the dose simulated by MC at location $\vec{r}$ and $D(\vec{r}|X)_{MC}$ means the dose produced by MC at location $\vec{r}$ with photon starting from X. The reason to perform such transformation is to sample photon position with $f(X)$ with weight $P(X) + S(X)$ to accelerate the dose calculation. The reason for not choosing $f(X)$ as weight is because $f(X)$ can be very focused sometimes that makes the uncertainty of dose difficult to reduce. Usually we need to run much more photons to achieve same uncertainty as the method we used here.

After making the assignment of weight clear, the next step is to sample specific photons and transport them to get $D(\vec{r}|X)_{MC}$. The algorithm is stated as following.

1. Read photon history N and 2D map of $P(x, y)$.
2. If Equation (3.1) was used, $S(x, y) = R_{SP} * P(x, y)$ and read σ_x and σ_y. Otherwise, read $S(x, y)$ from file.
3. Prepare θ map. It is either a single value σ_θ or a map read from a file.
4. Read $f(x, y)$ and calculate N_f from Equation (3.8).
5. Sample X from $f(X)$ by metropolis sampling or directly assign photon location based on the number of photons on each pixel $N(X) = N \times \frac{f(X)}{N_f}$.
6. Based on sampled X_r, determine photon types by sampling $\xi \sim U(0, 1)$ and compare it with $p = P(X_r)/(P(X_r) + S(X_r))$. If $\xi < p$, the sampled location should belong to a primary photon and continue with Step 7. Otherwise it is a scattered photon and go to Step 8.
7. Put its position to a plane on MLC.Sample source location from $N(0, \sigma_S)$. Its speed direction was from source to X_r. Energy was sampled from Equation (3.5) with $n = 1.6$, $m = 3$ and $b = 3$.

8. Find the crossing point between cylinder shell with radius 70.1 cm and line from source to X_r. Sample two random variables u_1 and u_2 from $N(0,1)$. The x and y location should be blurred by adding $\sigma_x * u_1$ and $\sigma_y * u_2$, respectively. Energy was sampled from Equation (3.5) with $n = 1.1$, $m = 2.8$ and $b = 2.5$. Sample θ from $N(0, \sigma_\theta)$ and rotate the primary photon speed direction by θ.
9. Assign weight $(P(X_r) + S(X_r))$ to either type of photons and transport. Record dose.
10. Repeat until we finish simulation of N photons.
11. Final dose $D = C * N_f/N * D_M C$, where C is a calibration factor, which could be determined by a comparison to dose in water phantom.

3.1.2 Implementation of electron transport in magnetic field

The algorithm of transporting electron has been stated clearly in reference [41, 66]. The electrons transport straightly until a hard collision event happens when there is no magnetic field. Energy is continuously lost along the track and for those hard collision events. Things became a little bit different When electrons were put inside a magnetic field – the electron path should be bent. Although the existence of magnetic field does not affect the amount of energy for each energy deposition event physically, it altered their positions, which brought the issues checking between voxel boundaries and a curved path and energy split between different voxels if a curve line penetrate multi voxels. If the check is too complex, the computational efficiency will be greatly reduced. For example, trying to get the exact positions for the curved path and six faces of one voxel. However, as we are trying to match dose deposition in voxels, we only need to make sure that the straight line will not deviate from the curved one more than a threshold value d_t. We empirically used $d_t = 1.25\ mm$, half of a voxel side length, in our simulation. Hence, we restricted step length less than

d_t for each straight line. And we made the deviation angle of speed larger than it should be so that it could compensated the error in next step as shown in Figure 3.5. The turning points of speed for two frameworks do not coincide with each other. However, as long as we keep the relative distance between two turning points not far away from each other, the energy depositions still fall into the same voxel for both frameworks.

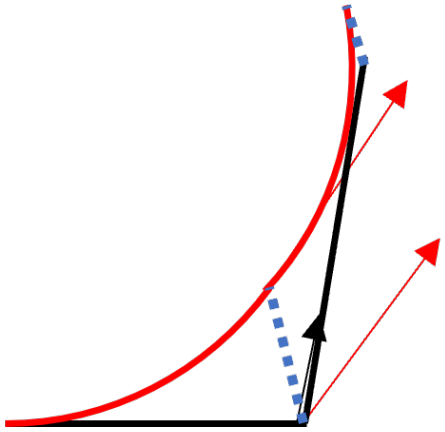

Figure 3.5. Electron transport inside magnetic field. Red lines and arrows represent expected paths and speed directions. Black lines and arrows represent real path and speed directions in our code. Dashed lines represent errors..

Mathematically and physically, for a step s in an uniform magnetic field with strength $\vec{B}$, the deviation angle ψ of speed $\vec{v}$ projected on a plane perpendicular to magnetic field is

$$s_\perp = \frac{p_\perp}{eB}\psi \tag{3.9}$$

$\perp$ is the vector component perpendicular to magnetic field and $s_\perp$ can be calculated as

$$s_\perp = s * |\vec{e_B} \times \vec{e_v}| \tag{3.10}$$

and p is the momentum and can be expressed as

$$p_{\perp} = \gamma m v_{\perp} = \gamma m v * |\vec{e_B} \times \vec{e_v}| \tag{3.11}$$

where $\gamma = 1 + E_k/m_e c^2$ and E_k the electron kinetic energy. Here, $\vec{e_v}$ means the unit vector for $\vec{v}$ and similar for $\vec{e_B}$.

With all the above equations, we could solve ψ and then finally obtain the deviated speed $\vec{v'}$ as

$$\psi = \frac{eBs}{\gamma m v} \tag{3.12}$$

$$\vec{v'} = \vec{v} * \cos\psi + (\vec{e_v} \bullet \vec{e_B}) * (1 - \cos\psi) * \vec{e_B} + \vec{e_B} \times \vec{e_v} \sin\psi. \tag{3.13}$$

From the idea we mentioned above, Equation (3.12) should be updated as

$$\psi = \alpha \frac{eBs}{\gamma m v} \tag{3.14}$$

with

$$\alpha = 1 + \frac{s_{\perp}}{d_t} * (r_m - 1) \tag{3.15}$$

We used $r_m = 1.15$.

3.1.3 Results

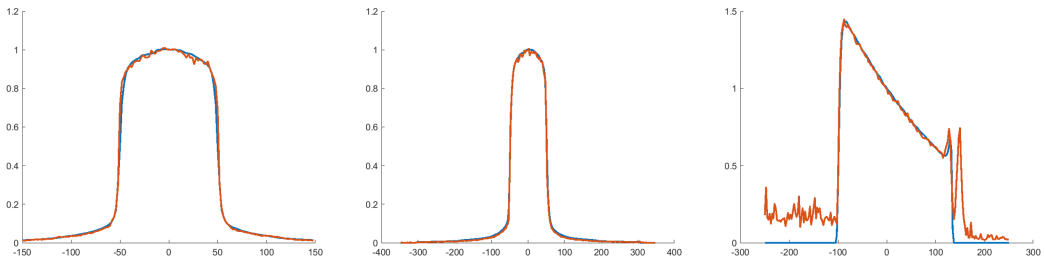

Figure 3.6. Dose deposition in water phantom with 10×10 cm^2 field. Left: cross plane. Middle: in plane. Right: along depth direction.

We first apply this model to dose calculation in water phantom with $10\times10\ cm^2$ field. We adjust the parameters in source model to match the profiles. The results were shown in Figure 3.6. We could see quite good agreement was achieved. Large error existed on both ends along depth direction because dose in air and couch was not recorded by TPS. And we determined the calibration factor C by comparing the average dose of dose region higher than 80% of maximum dose for MC results and TPS results. $C = 0.00042$ in this work.

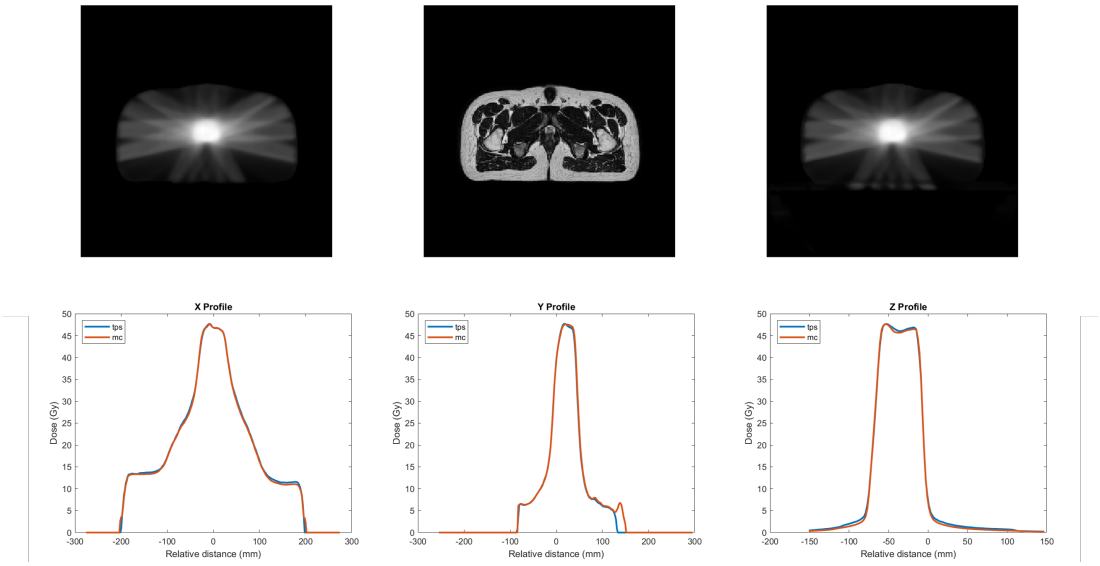

Figure 3.7. Comparisons between simulated results and that from TPS for a prostate case. Top row from left to right: TPS, CT and simulated results. Bottom row from left to right: LR, IS and AP directions..

We then present two dose simulation with the parameters determined by water phantom on two different body part. One is prostate and the other one is lung. We could see the model we constructed achieved good agreement for both cases. It was a little bit worse for lung cases, possibly due the deviation brought by material

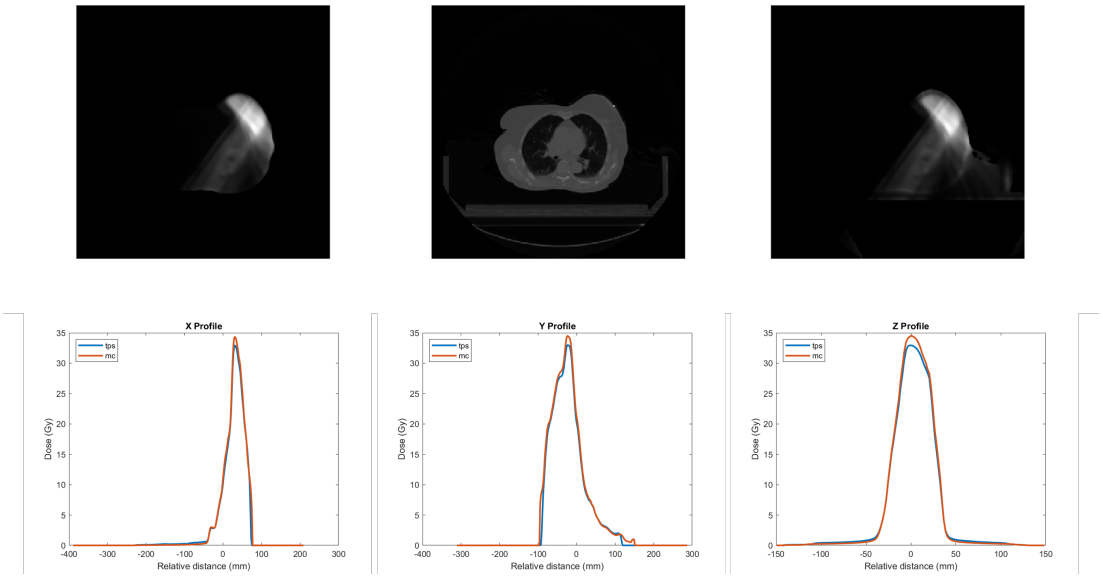

Figure 3.8. Comparisons between simulated results and that from TPS for a lung case.Top row from left to right: TPS, CT and simulated results. Bottom row from left to right: LR, IS and AP directions..

segmentation. Although we used water for all voxels, but their density values were segmented from MRI or CT images.

3.2 Simulation for kVp beams

We now talked about some developments with kVp beams. kVp beams are usually used for imaging purpose (tens of keV) or therapeutic purpose (two hundred eV). Physically, it shows some differences compared to MV beams.

1. No pair production interactions because of too small photon energy, which means no need to consider positron transport and annihilation.
2. Electrons could be viewed as depositing energy locally because secondary electron cannot travel far. In fact, The CSDA range [4] for 200 keV electron in water is only around 0.45 mm while there is few secondary electrons with such high energy for kVp photon beams and voxel size is usually about 2 mm.
3. Rayleigh scattering needs to be considered for certain photon energy.

So for the works in this section, we just used gCTD [60], which was initially developed for CT/CBCT calculations. In this code, electron transport was ignored while Rayleigh Scattering was included. We also used GATE (The Geant4 Application for Tomographic Emission, version 8.1) [86, 89] was also used for some cases for valiadating the results from gCTD. The things we did were revising the code for different source spectrum inputs and large phantom with millions of voxels and comparing the results with experimental results.

3.2.1 Motivation

The accuracy of delivered radiation dose and the reproducibility of employed radiotherapy methods are key factors for preclinical radiobiology applications and research studies. The prerequisite for accurate evaluation of dose and dose uncertainty is traceability to the reference radiation standard. In the U.S., the standard is determined and maintained by the National Institute of Standards and Technology (NIST)

[4] https://physics.nist.gov/cgi-bin/Star/e_table.pl

or by the Accredited Dosimetry Calibration Laboratories (ADCLs). NIST or ADCLs calibrated dosimetry equipment ensures that there is a documented unbroken link to the reference standard which provides known dose uncertainty under calibration conditions. A variety of different dosimetry protocols are available for irradiator calibrations depending on the type (gamma rays, x-rays, charged particles) and energy (kV, MV) of the radiation source. Superficial and orthovoltage x-ray energies are predominantly utilized in contemporary commercial small animal irradiation platforms. The American Association of Physicists in Medicine (AAPM) published a guidance document, developed by Radiation Therapy Committee Task Group 61 (TG-61), with recommendations for 40–300 kV x-ray beam reference dosimetry. NIST traceability and a properly calibrated irradiator, however, only provide a good starting point. The ultimate goal is to determine dose and the corresponding dose uncertainty for any given irradiation setup which is likely to be different from calibration conditions.

Key factors for dose calculations include reference output at the calibration point, distance from the source, dose falloff as a function of depth and attenuation of the medium, radiation field size (FS), the presence of beam modifiers such as filters and lab equipment used to aid the experiments, etc. In addition, somewhat less obvious dose variables include objects and materials beyond the irradiated target, dose rate variations, walls and components of self-shielded irradiator systems, the number of interfaces between different media, etc. These factors in conjunction with a given experimental geometry may not ensure charged particle equilibrium, a fundamental requirement necessary for accurate measurements.

In practice, the aforementioned considerations are neither trivial nor easy and present traps for remarkable dosimetric fails. An expert panel consensus document [175], emphasizing the importance of dosimetry standardization in radiobiology studies and reporting dosimetry details in research articles, was published as a result of

the workshop hosted in 2011 by the National Cancer Institute (NCI), the National Institute of Allergy and Infectious Diseases (NIAID), and the National Institute of Standards and Technology (NIST). Publications without crucial dosimetry information clutter valid scientific findings with results difficult or impossible to reproduce and compare with similar studies. A study analyzing radiobiology publications in last 20 years found that highly cited journals and articles are systematically more likely to be lacking dosimetry details related to irradiation protocols and that such practice may have contributed to the data interpretation and reproducibility crisis.

3.2.2 Case and simulation descriptions

3.2.2.1 Case 1: total body irradiation

We started this work from a quality assurance after a service call and repair of the irradiator for small animals. The in-air irradiator calibration was confirmed but an additional phantom measurement did not agree with a basic hand calculation. This puzzle was unraveled only after the series of additional measurements and MC simulations presented in this work. This work exemplifies such a necessity for one of the most commonly used experimental methods, total body irradiation (TBI), still commonly utilized in contemporary studies of radiobiology and immunology.

The x-ray tube was treated as an isotropic point source emitting photons in a cone with a half angle θ. The photon energies were sampled from a x-ray spectrum, which was calculated using SpekCalc [176] with the electron incident angle of 30^o and an extra 1.35 mm thick Al filtration, yielding the same HVL as the experimental value of 0.45 mm Cu. The x-ray beam was collimated with a 1.90 cm thick Pb square opening to produce a 26.4 $\times$ 26.4 cm^2 field at 65 cm from the source.

The simulated geometry was shown in Figure 3.9. We set SSD=65 cm first to study the the effects of different kVp. Then we replace the 3 cm water layer with other phantom and set different SSD to match the experiments. The values were summarized in Table 3.1. 250 kVp source was used for the consistence with experimental results. For banchmarking with experiments, the reference simulation was performed for the in-air calibration setup, MC-1 simulation in Table 3.1. The center of an 1.0 mm3 water voxel was placed at 65.0 cm from the x-ray source. Dose calculation was performed yielding dose to water at the center of the voxel. The number was further corrected for the attenuation by the 0.5 mm water above the center of the voxel and then a correction factor could be obtained, namely

$$D_{exp} = N \times D_{MC}. \tag{3.16}$$

Then for all other simulations, we could use N to transform simulation results and compared with experiments. In all cases, the simulations yielded 3D dose distributions throughout the phantoms. Point doses at the position corresponding to the measurement points were extracted.

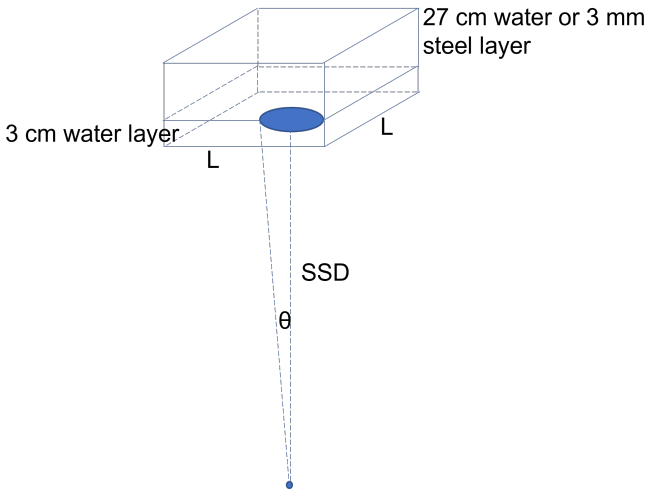

Figure 3.9. Setup of the TBI simulation. Cone beam is used to cover the phantom.

Table 3.1. Summary of geometries and materials in MC simulations

MC run	Setup description	Phantom dimensions (cm^3)	Phantom material	Voxel size (cm^3)	SSD (cm)	Depth (cm)
MC-1	In-air calibration	0.1×0.1×0.1	Water	0.1x0.1x0.1	64.95	NA
MC-2	Solid water phantom	30.0x30.0x3.0	Water	0.5x0.5x0.1	62.0	1.5
MC-3	Small water box	5.0x5.0x3.0	Water	0.5x0.5x0.1	62.0	1.5
MC-4	Mouse phantom	3.8x10.0x2.1	Water	0.1x0.1x0.1	62.9	1.05
MC-5	Rat phantom	8.0x21.0x3.5	Water	0.1x0.1x0.1	61.5	1.75
MC-6	Mouse phantom in a pie cage	3.8x10.0x2.1[a]	Water	0.1x0.1x0.1	62.0	1.05

[a] mouse phantom only in off-center position

3.2.2.2 Case 2: high throughput cell experiments

Multi wells plate is often used in biological experiments to have high throughput cell experiments. The radiation dose is considered uniform on the plate and average could be done on several wells to have better statistics uncertainty for the results. Here, we chose a Thermo-Fast 384 PCR plate, which consists of 16 rows and 24 columns of wells. Each well looks like a cone and could be filled with liquid. Specific tech details could be found in Pub No. MAN0014446. The illustration of the phantom modelled in our MC simulation is shown in Figure 3.10. The plate was put under a cone beam with isotropic fluence. Each well is filled with about 80 mL water, which made the liquid height 6.5 mm. The tough part for this simulation is the large number of voxels. Fine resolution (0.1 mm) have to be used to take care of the details of wells.

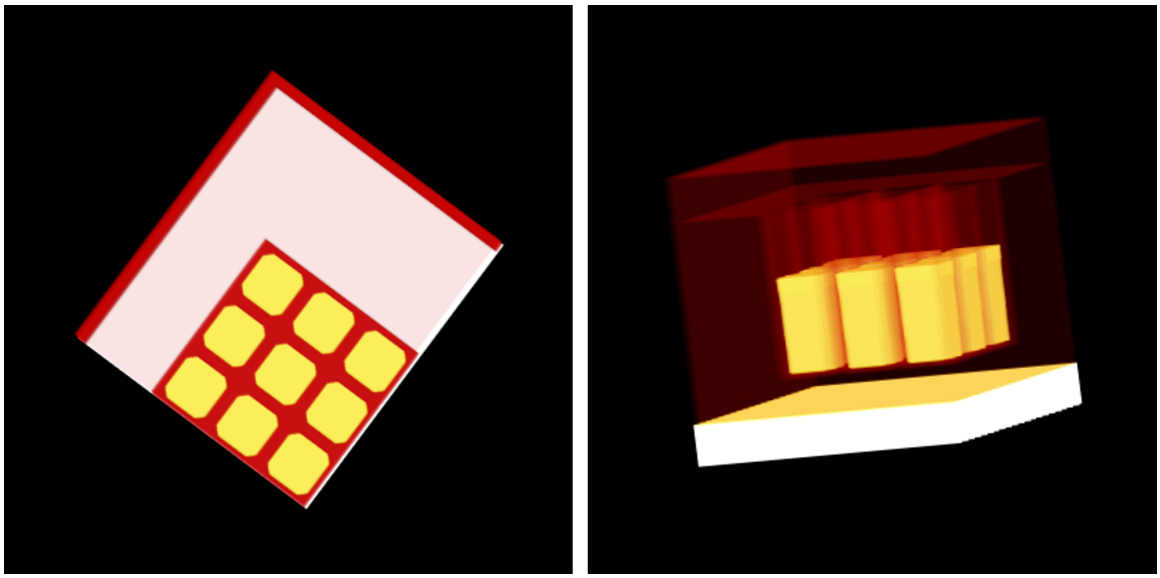

Figure 3.10. Illustration of phantom with 384 wells. Only part of the phantom is plotted.

3.2.3 Results and discussions

3.2.3.1 Case 1: total body irradiation

From Figure 3.11, we could first know that the substrate has large influence on the dose yields. More water along the beam direction increased the dose values primarily because the back-scatter effect, where photons and secondary electrons have a chance to travel backwards the beam direction. However, for thin steel or water, this effect could be ignored. When we changed the energy spectrum from 80 kVp to 250 kVp, the resulted difference by using different substrates is altered as well, 3 mm water and 3 mm steel showed prominent difference under 250 kVp photons. This illustrate the difficulty of calculating dose just by lookup tables for a real case. Many factors should be taken into consideration.

The dose rate values at the points of interest corresponding to the measurement points in various phantom configurations are summarized in Table 3.2. Overall, the

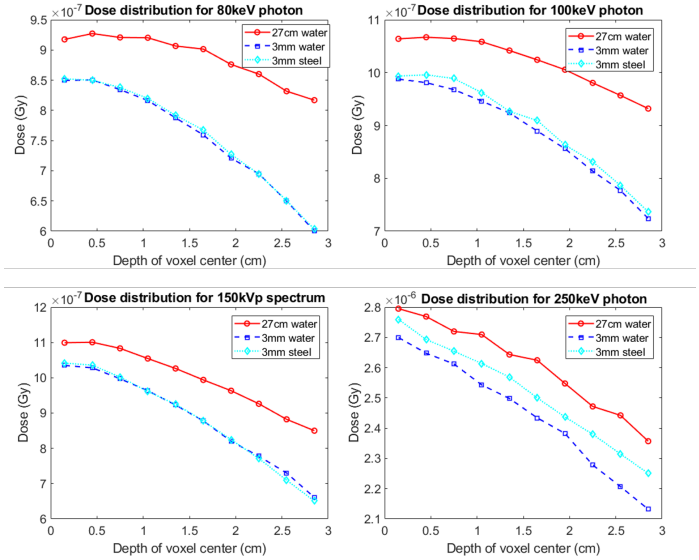

Figure 3.11. Dose versus depth along center axis for photon source with different kVp.

MC calculated dose rates were in good agreement with the measured dose rates. The relative dose rate difference $e = |D_{exp} - D_{MC}|/D_{MC}$ was 2.6% and 0.9% for the solid water and small water box, respectively. The difference was found to be somewhat larger for the mouse phantom, the rat phantom, and the mouse phantom in the pie cage scenarios, 3.3%, 3.9%, and 0.8%, respectively. This was attributed to the uncertainties in geometry, such as phantom setup and chamber placement, as well as to the unknown phantom material composition which was simulated as water for the mouse and rat phantoms. The PDD in small water box phantom computed by MC simulation is plotted in Figure 3.12. The computed PDD generally agreed well with PDD measured using a film, and the average difference between the two curves was 0.74%. The relative difference between MC and measured PDD at 1.5 cm depth was 0.9% for the small water box.

The hand calculation of point dose is very simple and not setup specific.

$$D' = D_0 \times (\frac{SSD_0}{SSD})^2 \times PDD(z)/100. \tag{3.17}$$

Table 3.2. Measure and simulated dose for different configurations

Setup description	SSD (cm)	Measurement depth (cm)	D_{exp} (Gy/min)	D_{MC} (Gy/min)	e (%)
In-air calibration	65.0	NA	1.537	1.537	0.0
Solid water phantom	62.0	1.5	1.314	1.349	2.6
Small water box	62.0	1.5	1.155	1.166	0.9
Mouse phantom	62.9	1.05	1.070	1.106	3.3
Rat phantom	61.5	1.75	0.976	1.014	3.9
Mouse phantom in a pie cage	62.0	1.05	1.105	1.114	0.8

The first term represents the inverse proportional with SSD square which accounts for the energy conservation through a sphere shell and the second term represents dose drop inside a phantom. We would use in-air calibration as D_0 in Equation (3.17) and finding corresponding dose D' at certain depth z by look up tables of PDD line. In real case, $z = 1.5\ cm$ is usually adopted. The general discrepancies induced by this method versus experiments ranged from 16% to 37% [177]. Note that the irradiator was initially calibrated following the in-air TG-61 procedure and that the 3 mm steel plate was removed to facilitate the calibration. For all subsequent setups, the steel plate was put back to support phantom measurements. Apparently, the steel plate did not provide sufficient backscatter relative to the in-air reference condition, yielding the observed dose rate overestimation for hand calculations. The 16% overestimation for the solid water phantom increased to 27% for the small water box, which can be ascribed to the reduction of the lateral photon scattering. For rodentomorphic phantoms, the overestimation was further amplified from 31% for the mouse to 37% for the rat phantom. In general, the overestimation was larger for smaller phantoms due to reduced phantom dimensions. This was not the case when comparing the rat with the mouse phantom. While the rat phantom was able to provide more scattered

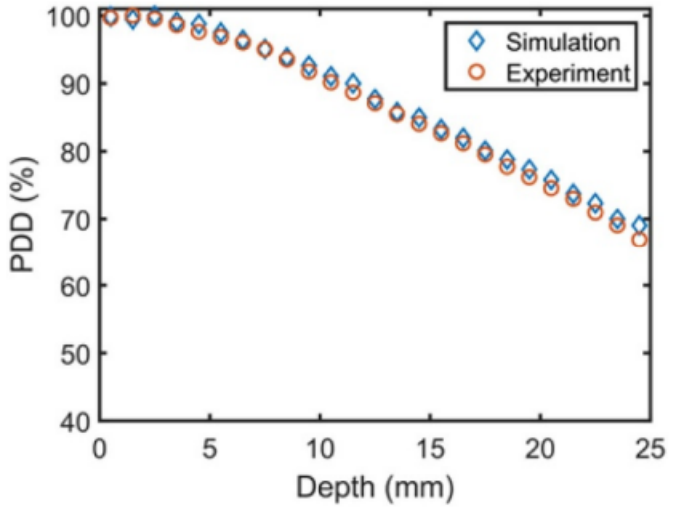

Figure 3.12. Dose versus depth along center axis for photon source with different kVp.

photons relative to the mouse phantom, the measurement points were at 1.75 cm and 1.05 cm, respectively. This was different than the assumed 1.5 cm depth for hand dose calculation and it represented the largest contribution to the dose rate discrepancies.

3.2.3.2 Case 2: high throughput cell experiments

We presented the simulation results in Figure 3.13. Although the center part has quite uniform dose (2% difference), the edge part showed 9% lower dose than the center part. If we further considered that there are more photons in the beam center than edge part or a larger plate was used, the dose difference between center and edge parts should be even larger. To compensate the dose variation for different wells, bolus with well-designed shape could be used to reduce the photon fluence in the center and therefore achieve dose uniformity. However, this requires extra efforts and care. Even for the same well, the dose at different depth shows large difference.

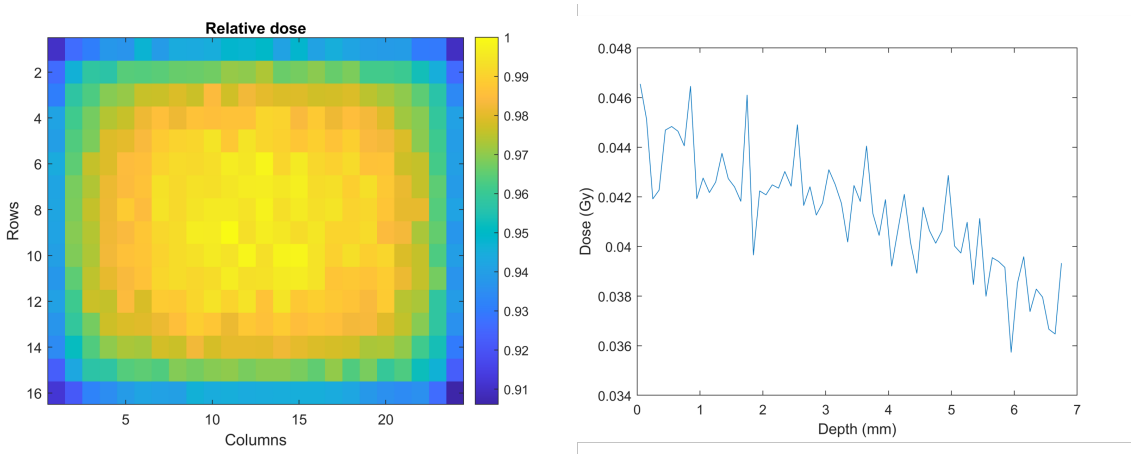

Figure 3.13. Left: cross section of dose distribution at the center plane of wells. Right: dose distribution versus depth along a well center axis.

Dose difference could be 20% different for bottom and top part. It means if the water depth is not controlled very precisely at the same value or the cells were not located at the same depth, say bottom, the dose experienced by the cells are not the same. Hence, the survival data or other analysis that depends on dose might be invalid.

3.2.4 Conclusion

We did dose calculation for two different cases but both were related to specific real experiments. We found although dose was a simple concept, its correct calculation was not that trivial if MC simulation is not involved. Dose was affected by many factors such as the support material for the phantom, the size of phantom etc.. Unfortunately, in practice, the dose were assumed to be uniform (384 wells) or calculated by some lookup tables (TBI). This leads to dose errors in biological experiments. There are two bad results. One is that the quantitative conclusion from biological experiments may be wrong and the other is that the comparison of experimental results among different facilities is meaningless. It certainly causes confusion and waste of resources. From the results we showed in this section, we suggest all biological

experiments should have physician as consultant or the dose calculation should be done by MC simulation. The application of GPU makes sure that the simulation time is not a problem for most clinical cases, where geometry could be simplified or the number of voxels is just several million.

CHAPTER 4

GPU APPLICATIONS FOR MICROSCOPIC SIMULATIONS

4.1 Introduction

When ionizing radiation interacts with water, energy transfer by a series of energy deposition events in the physical stage results in ionization or excitation of the water molecules. These physical events lead to direct damages to the DNA. The highly unstable molecular ions and excited water molecules then generate a large number of free radicals in the physicochemical stage. In the subsequent chemical stage, diffusion and mutual chemical reactions of the radicals generate further damages to the DNA. These initial DNA damages caused by ionizing radiation triggers subsequent biological processes [178].

Computing the DNA damages caused by radiation is of central importance for understanding radio-biology and for quantitatively testing hypotheses regarding radio-biological effects. Monte Carlo (MC) simulation is one of the most widely used approaches for the computations of the water radiolysis process and DNA damages. Based on fundamental physics and chemistry principles, MC method can precisely calculate the time-dependent behavior of energy deposition by a particle, the reaction-diffusion process of radicals, and their damages to DNA using probabilistic methods. Over the years, several packages have been developed, such as TRAX [179], PARTRAC [180, 181], GEANT4-DNA [182–185] and RITRACKS [186, 187]. These packages have demonstrated tremendous value in supporting research in related areas. For example, simulations of the energy deposition in biomolecules and cells from radiation track structures have been performed by a number of groups [50, 188, 189].

Estimations on the spectrum of DNA damages using MC simulations has played an indispensable role in understanding radiation-induced biological effects in organisms [190, 191].

4.2 Development of gMicroMC

4.2.1 General description

gMicroMC currently supports simulations of water radiolysis introduced by electrons. Since the simulation models have been widely studied by many other groups and can be found elsewhere, we will only briefly present the models for completeness. Interested readers can refer to relevant literature for more details. Physical stage (¡10-15 s). In the physics stage, an electron undergoes different types of physical interactions, until its energy falls below a cutoff level. In gMicroMC, we used a step-by-step simulation scheme to transport the initial electron and all subsequently generated secondary electrons. We considered four types of interactions between water molecule and electrons: ionization, excitation, elastic collision, and dissociative electron attachment. We employed the relativistic extension of the binary-encounter-Bethe (rBEB) model [192, 193] to compute ionization cross sections of electrons with the water molecular orbitals for energy range from 10 eV to 100 MeV. Specifically, we generated the cross section data for five different shells of a water molecule (four outer shells and one inner shell (K-shell)) based on the model. The electron binding energies came from the work of Dingfelder et al [194]. Due to the lack of available data on the absolute values of the excitation cross sections of H_2O, the semi-analytic model introduced by Olivero et al [195] was employed to model excitation interaction. The electron excitation levels came from the work of Dingfelder et al [194] and we considered energies for excitation levels of A1B1, B1A1, Rydberg A+B, Rydberg

C+D and diffusion. For the modeling of elastic collisions, the cross sections were given by a parameterized expression with adjustable parameters determined by fitting to experimental data at various incident energies for energies below 200 eV. We adopted the semi-empirical differential cross sections of Brenner and Zaider [196]. Above 200 eV, we used the Rutherford formula. Elastic scattering is known to be described well by the Rutherford formula, which includes a correction for atomic screening effects theoretically described by Moliere [197]. Finally, based on the study on dissociative attachment reactions of H and O by Melton [198], $H^{\cdot}, O^{-}$ and OH^{-} ions were produced at electron impact energies of about 6.5 eV. H^{-} was by far the most abundant product and it was also observed at around 8.5 eV. The cross section data of dissociative attachment in our work were extracted from Melton's curve.

Let us denote the generated cross section data as σ_i, where i is the index for different interactions and subtypes (e.g. excitation from a certain shell). The transport simulation sampled the distance to the next interaction as $s = -\frac{1}{\rho \sum_i \sigma_i} ln\zeta$, where ρ is the density of water and ζ is a random number uniformly distributed in [0,1]. After advancing the electron by s, we sampled the interaction type and subtype based on the relative weight of $\sigma_i / \sum_i \sigma_i$. For an ionization event, the energy of the secondary electron was determined by means of the composition sampling method, which was developed originally in CPA100 code [199, 200]. The scattering angle θ_p of primary electron for both an ionization and an excitation event was computed as $sin^2\theta_p = \frac{W/T}{(1-W/T)T/(2m_0c^2)+1}$, where W and T are energy loss of the primary electron and its energy before the event, respectively. m_0 and c are the rest mass of an electron and the speed of light. As for the secondary electron generated from the ionization process, the ejection angle θ_s followed $sin^2\theta_s = (1 - W/T)/(1 + W/(2m_0c^2)) for W > 200eV$. θ_s was uniformly distributed in $[\pi/4, \pi/2]$ with a 90% probability and in $[0, \pi]$ for the rest 10% probability, when 50eV¡W¡200 eV. For W¡50 eV, θ_s was uniformly dis-

Table 4.1. Branching ratios for ionized and excited water molecules used in gMicroMC.

Excited status	Shell	Pathway	Decay channel	Branching ratios (%)
Ionized water molecules	${}^1b_1$, ${}^3a_1$, ${}^1b_2$, ${}^2a_1$, K	Dissociation	$H_3O^+ + HO^\cdot$	100
Excited water molecules	A^1B^1	Dissociation	$HO^\cdot + H^\cdot$	65
		Relaxation	$H_2O + \Delta E$	35
	B^1A^1	Auto-ionization	$H_3O^+ + HO^\cdot + e^-_{aq}$	55
		Dissociation	$H_2 + 2HO^\cdot$	15
		Relaxation	$H_2O + \Delta E$	30
	Rydberg A+B,Rydberg C+D and diffusion	Auto-ionization	$H_3O^+ + HO^\cdot + e^-_{aq}$	50
		Relaxation	$H_2O + \Delta E$	50

tributed in $[0, \pi]$. For an elastic collision event, the primary electron did not have energy loss and the scattering angle was sampled using the inverse transform method [60]. As for the dissociative attachment reactions, the primary electron disappeared, and products were produced. This process was repeated, until the electron was absorbed, or its energy was below the cut off energy $E_c = 5eV$, which deposited energy locally.

Physicochemical stage (10^-15–10^-12 s). During this stage, the types and locations of initial radiolytic chemical species entering the subsequent chemical stage were determined. We adopted the same simulation models used in PARTRAC, including the pathways of ionized and excited water molecules and the thermalization of hot dissociation fragments and subexcitation electrons [180]. Specifically, ionized water molecules were assumed to undergo dissociation as the sole pathway. Excited water molecules had three possible pathways, relaxation, dissociation and auto-ionization, depending on the excitation type. The decay channels and the corresponding branch-

ing ratios used in our package are shown in Table 4.1 . After determining a pathway according to the branching ratio, the hot dissociation fragments had to be thermalized by getting rid of kinetic energy released in the dissociation process. Here, we sampled the thermalization displacements r isotropically from a radial density function $f(r) = \sqrt{\frac{2}{\pi}}\frac{1}{\sigma^3}r^2 exp\left(-\frac{1}{2}\frac{r^2}{\sigma^2}\right)$, where σ is the standard deviation of one dimensional normal distribution [180]. Sub-excitation electrons transferred their excess energy to the surrounding medium until thermal energies through a number of inelastic processes. The thermalization displacement r was sampled according to a distribution $f(r) = 4re^{-2r}$, where the unit of r is nm. At the end of the thermalization process, a low energy subexcitation electron formed a cluster in aqueous solution by attaching surrounding water molecules.

Chemical stage ($10^{-}12{-}10^{-}6\ s$). The chemical stage of water radiolysis consists of two types of chemical kinetics: diffusion of the radiolytic molecules e^{-}_{aq}, $HO^{\cdot}$, $H^{\cdot}$, H_3O^{+}, H_2, OH^{-}, and H_2O_2 and their mutual chemical reactions. Brownian motion was used to model the diffusion of the radiolytic molecules with each being considered as an individual Brownian object with random independent motions. All the chemical reactions considered in our package were assumed to be diffusion-controlled, as in PARTRAC and GEANT4-DNA. A reaction would occur, when the distance of the reactants was no greater than the reaction radius. The diffusion constants and reaction constants were taken from published data. Detailed descriptions of modeling can be found in Tian et al [201].

4.2.2 DNA model

We built a DNA geometry model to describe the DNA structure inside a lymphocyte cell nucleus. The model was constructed in a multi-scale fashion with its structure described at six scales. From the finest to the coarsest scale, they were

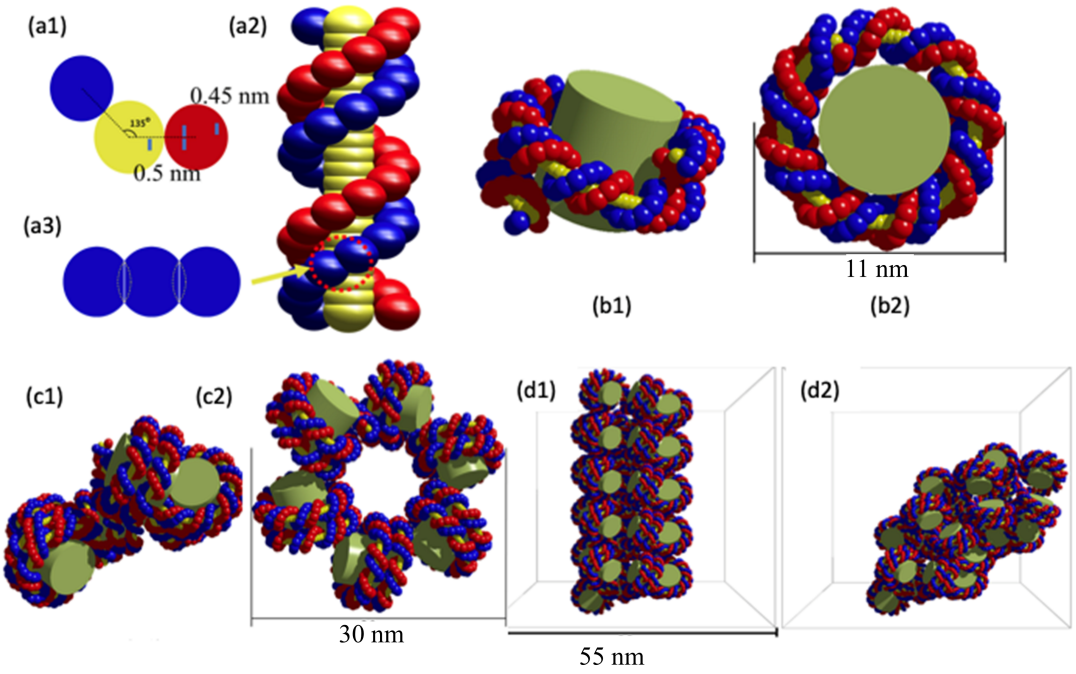

Figure 4.1. (a1) The nucleotide pair including a base pair (yellow) and two sugar-phosphate groups (blue and red), (a2) a B-DNA segment, and (a3) the overlap between two neighboring groups. (b1) (b2) Nucleosome structure. (c1) (c2) Chromatin fiber loop. (d1) A straight chromatin fiber unit and (d2) a bent chromatin fiber unit. For colorful figures, please see online version..

nucleotide pair, DNA double helix, nucleosome, chromatin fiber loop, chromatin fiber unit, and finally the cell nucleus.

Nucleotide pair According to Bernal et. al. [202], the nucleotide pair is separated into three parts as shown in Figure 4.1 (a1): the base pair (yellow) and a left and a right sugar-phosphate group (blue and red). In our model, the base pair was represented by a cylinder with 1 nm in diameter and 0.34 nm in height. Each of the two sugar-phosphate group was described as a sphere with a radius of 0.45 nm. The two groups were separated by 135°, as presented in Figure 4.1 (a1).

DNA double helix The B-DNA double helix was formed with each nucleotide pair turned by 36° relative to the previous nucleotide pair and shifted by 0.34 nm

along the central axis of the helix, as shown in Figure 4.1 (a2). The sugar-phosphate spheres at two adjacent levels overlapped. The overlapping volume was cut into two equal parts, each assigned to the nearest sphere (Figure 4.1 (a3)). With these settings, the volume of the modified sphere equaled to the volume of all atoms in a sugar-phosphate group.

Nucleosome The nucleosome was made of a histone octamer and the DNA double helix. The histone octamer was modeled as a cylinder with a 3.13 nm radius and the DNA double helix winded 1.75 times with a 2.7 nm pitch around the histone octamer to form a nucleosome of 11 nm in diameter and 6 nm in height. Each nucleosome contained 147 base pairs (bps) as shown in Figure 4.1 (b1) and (b2) in two different views.

Chromatin fiber loop A chromatin fiber loop contained six nucleosomes. The six nucleosomes were placed around a circle separated by 60^o and each nucleosome was rotated about the radial direction of the circle by 20^o. This formed a chromatin fiber loop with a diameter of 30 nm and height of 11 nm, as shown in Figure 4.1 (c1) and (c2).

Chromatin Fiber Unit With the chromatin fiber loop, we constructed two chromatin fiber units that served as the building blocks of a cell nucleus. Both were defined in a cubic volume with a side length of 55 nm. The first type was a straight chromatin fiber unit extending from one face of the cube to the opposite face, and the second type was a bent fiber unit connecting one face of the cube to one of the adjacent faces. The straight unit contained 30 nucleosomes (six layers of chromatin fiber loop), while the bent unit contained 24 nucleosomes. The configurations are shown in Figure 4.1 (d1) and (d2), respectively. Depending on the starting and ending faces of the chromatin fiber, there are in total six types of straight units and 24 types of bent units. We generated a detailed geometry representation for one of each

type, and used simple coordinate transformation, e.g. rotations, to generate all types of the chromatin fiber units. For example, the straight unit connecting the left and right sides of the cube is equivalent to the one connecting the front and back sides with a rotation by 90° about the vertical axis.

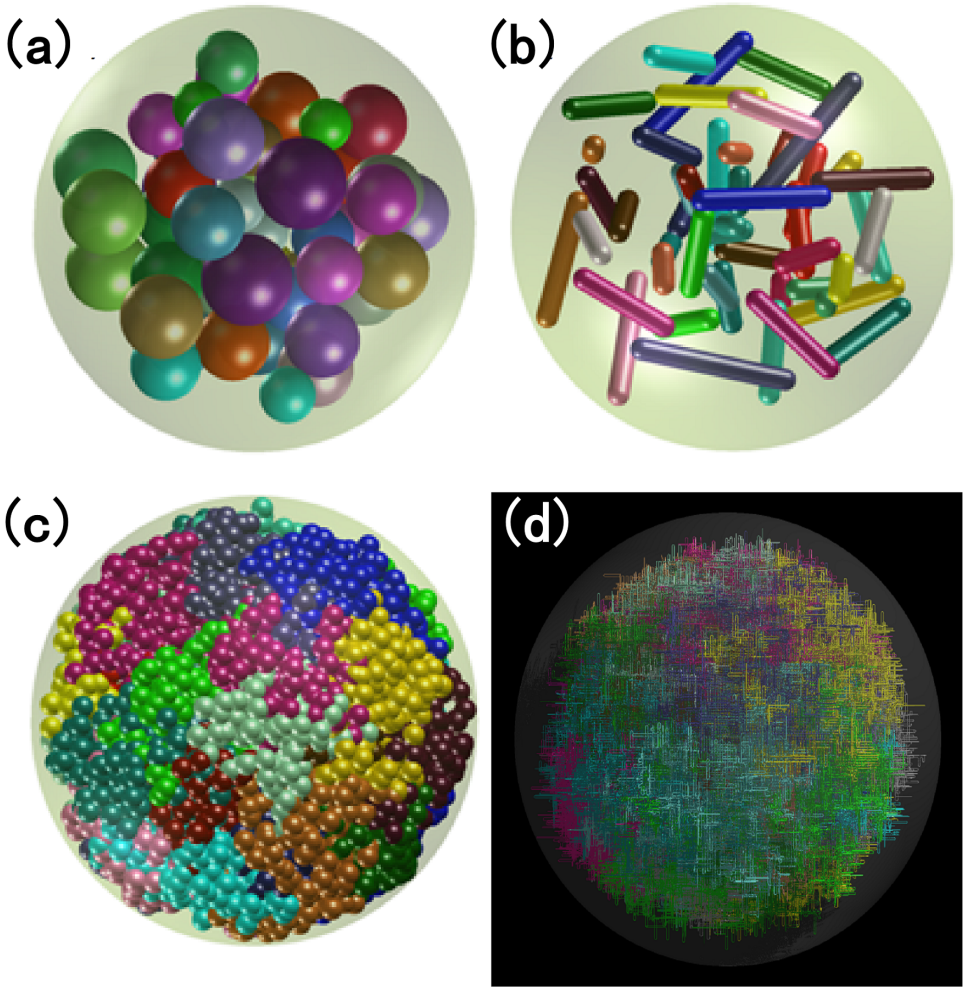

Figure 4.2. A DNA model of a human lymphocyte cell nucleus generated based on an SCD Model.

Cell nucleus We generated the DNA structure of a medium size lymphocyte cell nucleus in a sphere with a diameter of 11 µm. As such, we first employed the spherical chromatin domain (SCD) model [181, 203, 204] to simulate the arrangement of chromosome in the cell nucleus. This model assumed that every chromosome is composed of a chain of spherical chromatin domains (CDs). The diameter of each CD is 500 nm containing 1 Mbp DNA. To determine the locations of CDs, we followed the following three steps. First, we represented each chromosome by a sphere whose radius was proportional to the number of DNA it contained. The locations of the chromosome spheres were determined based on their radii with larger spheres placed closer to the nucleus center, as shown in Figure 4.2 (a). Second, each chromosome was filled with CDs, and the total number of DNA in all CDs of a chromosome was equal to the DNA content of the chromosome. The CDs were placed side-by-side with a 14 nm separation to form a linear arrangement of a 'start cylinder', as shown in Figure 4.2 (b). After that, a Markov process was used to model a relaxation process and generate the final configuration of CDs. During this process, there were three potential energies considered: entropic spring energy, volume potential, and weak potential barrier around each chromosome chain. In this way, the final configuration of the CDs was generated in equilibrium as reported in detail by Kreth et. al [203]. This configuration is shown in Figure 4.2 (c).

The next step was to generate a DNA structure using the CD positions and chromatin fiber units. We partitioned the spherical space of the lymphocyte nucleus with cubical voxels of 55 nm in size. After that, we placed chromatin fiber units in these voxels to connect the centers of the CDs computed previously using a self-avoiding random walk model. There were two constraints in this process. First, the total number of DNA linking two CDs should be 1 Mbp. Second, chromatin fiber units in two neighboring voxels should be connected smoothly. The cell nucleus

model constructed in this way contained 6.2 Gbp DNA (Figure 4.2 (d)) and the DNA density was around 6.8×10^{-12} g per cell.

4.2.3 DNA damage calculation

The particle and radical transport simulations resulted in locations and types of physics events, as well as locations of radicals at the end of the chemical stage. We overlapped these physical events and radical locations with the DNA geometrical model to compute DNA damages of different complexities [205]. The computation included two major steps. The first step was to calculate strand breaks (SBs) caused by physical events (direct damages) or radicals (indirect damages). For the direct strand breaks, we first identified if each physical event fell in a sugar-phosphate group. This was considered true, if the event location was within a distance of $R + R_p$ from the center of the sugar-phosphate group, where R is the radius of the group and R_p is reaction distance taken as the thickness of the first hydration layer, which is 0.1 nm [181]. If the event fell into multiple groups, the one with its center closest to the event location was chosen. After processing all energy deposition events, we aggregated all the energy deposit to each sugar-phosphate group. The strand was considered broken, if the deposited energy was over $E_{thres} = 17.5eV$.

As for the indirect strand breaks, we assumed that only the $HO^{\cdot}$ radical could lead to a break. Hence, for each $HO^{\cdot}$ radical location, we searched the DNA structure to find whether it was within a distance of $R + R_c$ from the center of the sugar-phosphate group, where $R_c = 0.08$ nm is the chemical reaction radius decided by the chemical reaction rate between the radical and the DNA according to Smoluchowski's diffusion equation $R_c = \frac{k \bullet N_A}{4\pi D}$ [206]. k is the chemical reaction rate between radicals and DNA, N_A the Avogadro constant and D the diffusion rate. Similar to the computations of physical damages, the sugar-phosphate group with its center closest to

the radical was selected, if the radical was found to be reacting with multiple groups. After that, the strand break was formed with a possibility P_c of default value 0.4, the same parameters chosen by GEANT4-DNA [205]. After processing all radicals, those sugar-phosphate groups damaged by at least one radical were considered as damaged.

The second step of DNA damage calculation was to compute damages of different levels of complexities. Specifically, after combining the list of damaged sites caused by physical events and radicals, we first removed duplicated sites and then analyzed the locations of these damage sites along the DNA double helix to identify damage of complexities of seven types [50]. We followed the definition in references [50, 207]. Two parameters d_S and d_{DSB} were used to define complexities of single strand break (SSB) and double strand breaks (DSB). d_S was the minimum nucleotide index difference for two SBs to be considered independently and d_{DSB} was the maximum nucleotide index difference for two SBs on the opposite sides of the DNA chain to be considered a DSB. The default values of d_S and d_{DSB} were set to 216 and 10, respectively. With the help of d_S and d_{DSB}, we can label SSB and DSB of different complexities. For example, the simplest break is SSB, defined as the one that has no nearby breaks closer than d_S. SSB+ refers to any number of SBs within d_S on the same DNA strand, while 2SSB refers to two SBs on both sides of the DNA chain that are closer than d_S but further than d_{DSB}. As for DSBs, one DSB is defined as two SBs on both sides that are closer than DSB, while DSB+, a type slightly more complex than DSB, refers to any number of SBs on both sides, whose largest distance is smaller than d_{DSB}. It should be noted that damages of two complexities can have at most one SB overlap in this classification.

4.2.4 Comparison with other works

4.2.4.1 *Physical stage*

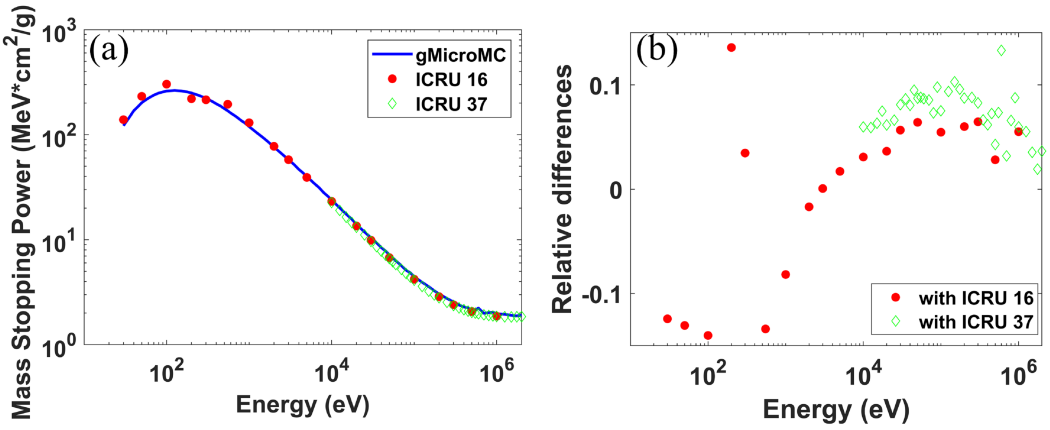

Figure 4.3. Mass stopping power for electrons in liquid water as a function of electron energy (a) and relative difference between gMicroMC results and ICRU data..

Figure 4.3 compares the electron mass stopping power given by ICRU 16, ICRU 37 reports and that computed by gMicroMC. Our result agreed with the ICRU 16 data, with the maximum percentage difference of 16% at 100 eV. The ICRU 37 stopping power data begins at electron kinetic energy of 10 keV. The maximum percentage difference between our result and ICRU 37 data were 15% at 0.6 MeV, which is likely due to random fluctuation in our MC simulation results.

Track lengths and penetration as a function of the incident electron energy from 12 eV to 250 keV were obtained by using GEANT4-DNA with the default model, GEANT4-DNA with the CPA100 model and were compared with our results in Figure 4.4. Relatively good agreements were observed at higher energies region (¿ 1 keV) and the differences were within 10%. Larger discrepancies were seen in the low energy range.

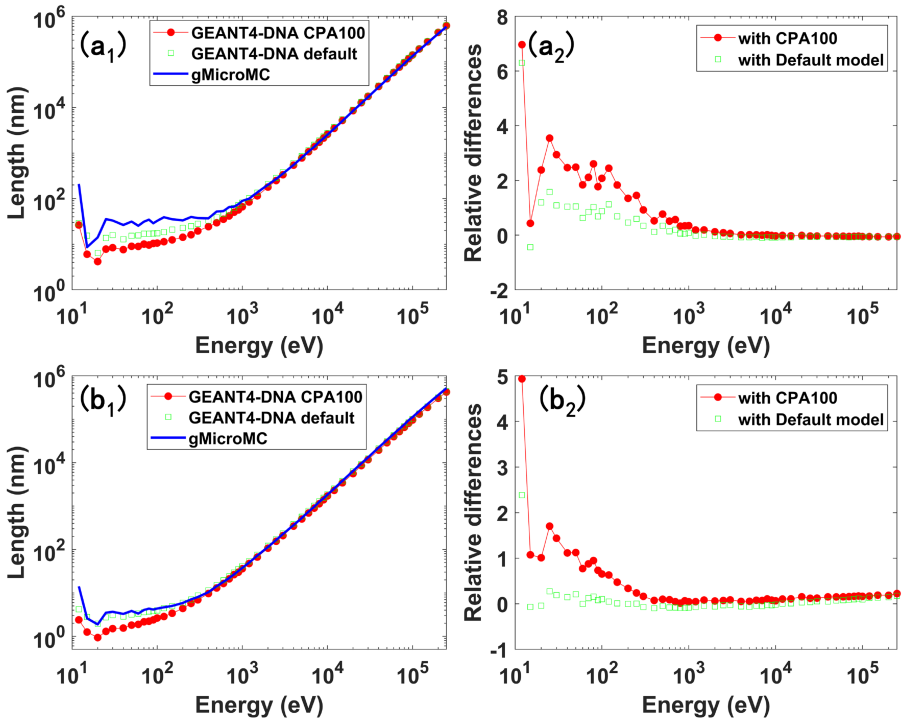

Figure 4.4. Track length (a) and penetration (b) as a function of incident electron energy. The right column shows the relative differences between gMicroMC results and GEANT4-DNA results..

The numbers of events computed by GEANT4-DNA were compared with those computed by gMicroMC in Figure 4.5. For ionization interaction, the percentage differences were within 10% between GEANT4-DNA CPA100 and our result, and within 20% between GEANT4-DNA default model and our result. For elastic interaction, the discrepancy between our result and that of GEANT4-DNA default model was within 20% (Figure 4.5 (c)). As for excitation interaction, the results between GEANT4-DNA default model and GEANT4-DNA CPA100 model already presented with large differences. Our results agreed with GEANT4-DNA CPA100 model better than with the default model, although a relatively large discrepancy appeared at the energy range higher than 1 keV

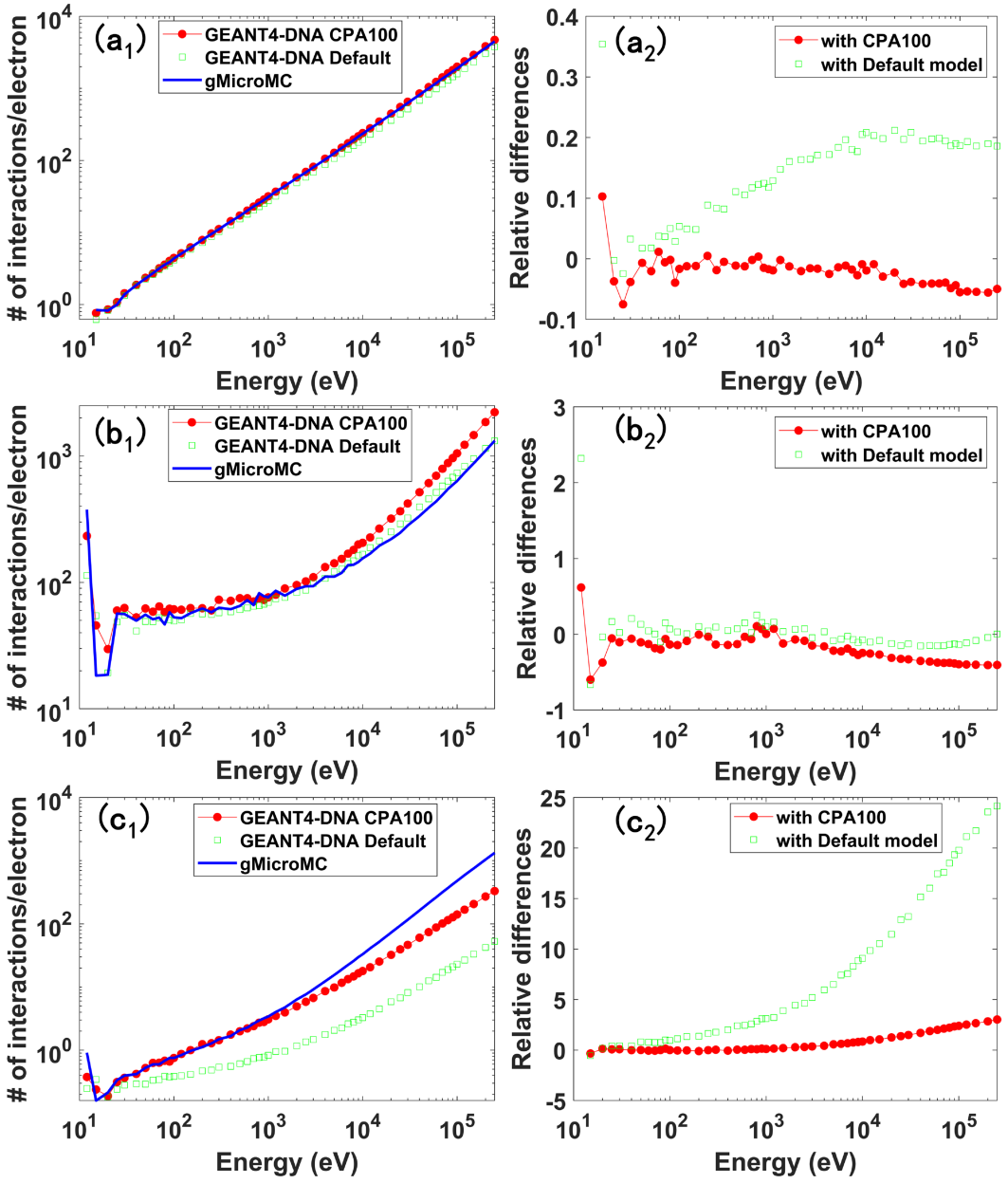

Figure 4.5. Number of interactions for ionization (a), elastic (b) and excitation (c) events per incident electron as a function of electron incident energy. The right column shows the relative differences between gMicroMC results and GEANT4-DNA results..

4.2.4.2 *Physicochemical and chemical stages*

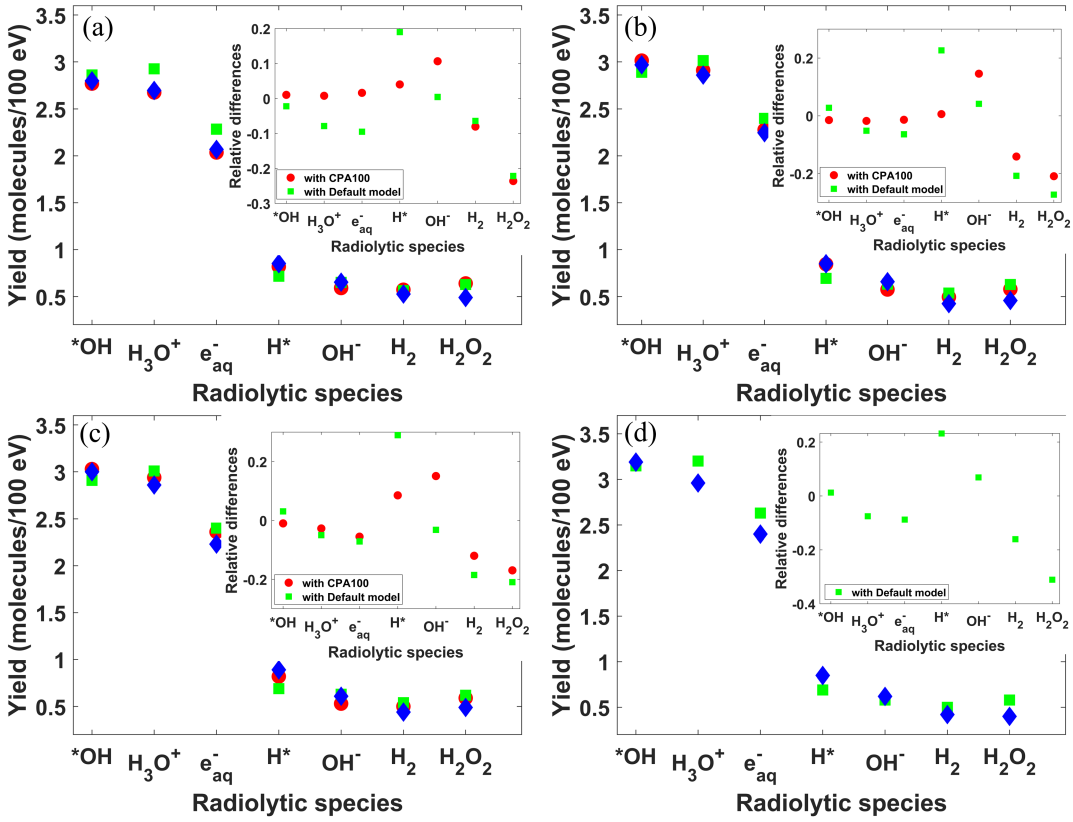

Figure 4.6. Yield values of different radiolytic species for (a) 100 keV, (b) 175 keV, (c) 250 keV and (d) 750 keV incident electrons computed by GEANT4-DNA CPA100 model (red filled circle), GEANT4-DNA default model (green filled square) and gMicroMC (blue filled diamond). The inset figures show relative differences between gMicroMC results and GEANT4 results..

We computed the yields of different free radicals at the end of the chemical stage (1 μs) triggered by an initial electron with energies of 100 keV, 175 keV, 250 keV and 750 keV. The results are presented in Figure 4.6 and compared with the results from GEANT4-DNA using different models. Since the maximum electron energy of GEANT4-DNA CPA100 model is 256 keV, this model was not included in the study

with an electron initial energy of 750 keV. In all the cases, relative differences were within 10% for those species with relatively large yield values, such as $HO^{\cdot}$, H_3O^+ and e^-_{aq}. Generally speaking, the yield values computed by gMicroMC agreed better with results computed by GEANT4-DNA CPA100 model than with GEANT4-DNA default model.

4.2.4.3 DNA damage yields

For the computations of DNA damages to the lymphocyte nucleus model caused by the 662 keV photons from $^{1}37Cs$ decay, the SSB yield was 196 ± 8 SSB/Gy/Gbp and the DSB yield was 7.3 ± 0.7 DSB/Gy/Gbp, which were in agreement with the result of 188 SSB/Gy/Gbp and 8.4 DSB/Gy/Gbp computed by Hsiao et al [208]. We also computed DNA damages caused by 1.0 keV electrons. Simulations gave the SSB yield of 177 ± 6 SSB/Gy/Gbp and DSB yield of 11 ± 1 DSB/Gy/Gbp. These numbers were consistent with the results in Bernhardt et al [209], where 150 SSB/Gy/Gbp and 10.5 DSB/Gy/Gbp were reported for 1 keV photons. At this energy level, photons generate electrons almost through the photoelectric process, and hence the generated electrons have energy 1 keV. In another study, DSB yield of 13.4 DSB/Gy/Gbp was found for 947 eV electrons [208].

4.2.4.4 Computational efficiency

As the main motivation of developing gMicroMC is to accelerate computations, we compared the computation time of gMicroMC running on one Nvidia TITAN Xp GPU (1.58 GHz) with GEANT4-DNA running on single core of Intel i7-6850K CPU (3.6 GHz). We report in Table 2 the computation time for the transport simulation of the physical stage for cases with an initial electron of energy of 750 keV and 500 keV. It was found that gMicroMC on GPU sped up computations by factors of 5.5x

Table 4.2. Efficiency test for cases with 750 keV and 500 keV electrons.

		GEANT4-DNA (s)	gMicroMC (s)	Speedup
Physical stage	750 keV	81.5	14.8	5.5
	500 keV	40.2	10.8	3.7
Chemical Stage	750 keV	71642	132.8	539.5
	500 keV	60747	113.4	537.6

and 3.7x over GEANT4-DNA on a single thread CPU. In the chemical stage, mutual and competitive reactions between molecules led to much longer computational time. In our previous study 19, the chemical stage in water radiolysis was substantially accelerated by GPU. In this study, we timed the simulation starting from the initial electron to the end of the chemical stage at 1 μs. gMicroMC using one GPU card was found to be 540x faster than GEANT4-DNA executed on a single thread CPU (Table 4.2).

As for the computations of DNA damages, due to parallel processing on the calculations of SBs, it took about 2 sec to complete the damage calculations.

4.2.5 Discussion

Aiming at overcoming the challenge of high computational burden associated with MC simulations for radiation interaction with water in physical, physicochemical, and chemical stages, as well as for the computations of DNA damages, we have developed a GPU-based fast microscopic MC simulation package, gMicroMC. Instead of developing and implementing new physics or chemistry models, as having been performed extensively by many groups, our study focused on developing novel GPU implementations to accelerate computations. We also built a human lymphocyte nucleus DNA model and implemented a DNA damage calculation method to compute SSBs and DSBs of different complexities. We compared our simulation results

with those generated by GEANT4-DNA. In the physics stage, mass stopping power, track length, penetration, and number of interactions were in good agreement with GEANT4-DNA results. For the results in chemical stage, yield values of major radical species differed from those computed by GEANT4-DNA by less than 10%. With the powerful parallelization capability of a GPU card, we achieved speed-up factors of 3.7 5.5 times for physics stage computations of 500 750 keV electrons, and 540 times for the entire simulation process, compared to the computations by GEANT4-DNA executed on CPU using a single thread.

We noticed that there are some discrepancies among results for the physical stage generated from gMicroMC and GEANT4-DNA models (Figures 4.4 and 4.5), which can be ascribed to the difference in cross section models used in the three packages (Table 4.3). For instance, for ionization interaction, rBEB model extended the uphold 256 keV of BEB model [210] in the origin CPA100 code [211]. Hence, the numbers of ionization events were consistent between gMicroMC and Geant4-DNA CPA100, while they were quite different from that obtained using Geant4-DNA default model (Figure 4.5 (a)). As for the electron excitation, the cross section data were similar between gMicroMC and Geant4-DNA CPA100 model up to 10^3 eV [195, 199], since the data in Olivero et al [195] only ranges up to this energy. This leads to a quite good agreement between gMicroMC and CPA100 model in the low energy range as shown in Figure 4.5 (c). In the low energy range, elastic scattering dominates. In this range, our model for the elastic scattering interaction agreed with Geant4-DNA default model better than the CPA100 model [199]. This explained the agreement between gMicroMC and Geant4-DNA default model in electron track length, penetration (Figure 4.4), and number of events (Figure 4.5 (b)) in the low energy range.

Table 4.3. Physical models of cross section data in gMicroMC, GEANT4-DNA default model, and GEANT4-DNA CPA100 model.

Channel	gMicroMC	GEANT4-DNA default model [182]	GEANT4-DNA CPA100 model [199]
Ionization	rBEB model [192, 193]	Emfietzoglou dielectric model [212]	BEB model [210] from CPA100 code [211]
Excitation	Semi-analytic model introduced by Olivero et al [195]	Emfietzoglou dielectric model [212]	Dielectric model from CPA100 code [211]
Elastic	scattering Brenner and Zaider for energies below 200 eV [196] Screened Rutherford formula [197, 213] for energies above 200 eV	Partial wave model [185]	Independent Atom Method model [214] from CPA100 code
Vibrational	N/A	Sanche's data [215]	N/A
Dissociative attachment	Melton's data [198]	Melton's data [198]	N/A

In contrast to some studies only considering DNA damages induced by ionization events [205, 216], in gMicroMC, all physics events were considered for two reasons. First, there is a lack of studies on the exact mechanism of physical damage formations in aqueous environment. Energy deposition events, regardless of ionization, may still cause DNA damages, such as by pressure wave [217]. Second, there are much more ionization events than other excitation events, as seen in Figure 4.5. Considering all physical events would not affect the DNA damage results significantly.

Compared to the achieved acceleration factors for the entire simulation process, the factors for the simulations of the physical stage (3.7 5.5) were much lower. The

reason for this fact was that the simulation in the physical stage was mostly a serial computation and hard to be parallelized. At the beginning of the physical stage, only one electron existed, and we had to compute its transport step by step sequentially. After that, a number of secondary electrons were generated, and their transport simulation could be parallelized using different GPU threads. Hence, most of time the GPU was not used to its full capacity, yielding a much limited acceleration factor. The used GPU capacity increases with initial electron energy, as a higher energy electron generates more secondary electrons (all electrons generated by the primary electron), favorable for parallel processing. The efficiency also increases with the number of primary electrons.

In contrast, the acceleration of the entire simulation process was found to be much more substantial, because of the GPU-friendly algorithm used to effectively handle the chemical stage simulations [201] and the much small portion of the physics stage simulation time relative to the entire simulation process. Compared to the acceleration factors reported in our previous study [201], we achieved even higher accelerations in the current study, which can be ascribed to different GPUs and CPUs used in the current and the previous studies.

We would like to point out that microscopic simulations are typically performed for research purposes. A parallel computational platform such as a CPU cluster is often employed. The acceleration factors reported in Table 4.2 were with respect to a single CPU. We reported these numbers and clarified the corresponding hardware settings for readers to objectively interpret the results. We also emphasize that the advantage of GPU is clearly substantial, as it would require a cluster with hundreds of CPUs to achieve the performance of a single GPU. A CPU cluster of this size is not available to most of researchers. Meanwhile, computations using a multi-GPU or GPU cluster platform are increasingly performed nowadays in research and clinic.

With future extension of our tool to support these platforms, it is expected that the advantages of GPU over CPU will be clearer.

There are a few directions that we plan to pursue in the near future. First, gMicroMC currently only supports computations with an electron as the initial particle. It will be our future developments to add supports for the physical stage computations of other particle types, such as protons and heavy ions. This will enable studies on radiobiological effects in different contexts, e.g. carbon ion therapy, space radiation etc. Second, DNA damage computation is currently performed by simply overlapping the track structure with the DNA geometry as a post processing step. In reality, the presence of DNA affects radiation transport, e.g. scavenger effect, which in turn has impacts on DNA damage calculations. We plan to modify gMicroMC to perform transport simulations while considering the existence of the DNA structure for DNA damage calculations. It is expected that the simulations will be computationally more challenging, and hence GPU-based computations will be beneficial. Third, the search for DNA damages was done in a hierarchical multiscale way to reduce the expenses in computational memory and time. In principle, this can handle any kind of DNA geometry, if it is described in a similar multiscale way. However, for models with a greater number of scales, e.g. including atomic descriptions of the DNA, we expect that modifications on specific searching functions would be needed. It will be our future work to better support different types of DNA geometries and provide more examples, so that users can easily choose their own geometries.

gMicroMC is an open-source package available to the research community. Interested user could contact the corresponding authors to inquire our package.

4.3 Sensitivity of MC parameters

4.3.1 Introduction

In the first part of this study, we reported our recent developments on a new open-source Monte Carlo (MC) simulation package, gMicroMC, for microscopic transport simulations of electrons and free radicals in the physical, physico-chemical, and chemical stages of water radiolysis, as well as for DNA damage calculations. With rapid parallelization capability of a GPU and novel GPU-friendly parallel simulation schemes, substantially increased computational efficiency has been achieved. For the cases tested, speedup factors of 540x over simulations performed on a conventional CPU platform were observed using a NVidia TITAN Xp GPU card.

Computational efficiency is a critical factor affecting practical applications of MC simulation tools. There are situations in which efficiency is particularly important, such as in the studies requiring accurate descriptions of the complex physical, chemical processes, and the simulation geometry, or in the studies repeatedly conducting simulations to extensively investigate certain issues. One example problem is to evaluate the sensitivity and uncertainty of DNA damage calculations with respect to MC simulation parameters, which requires performing simulations under different parameter values. Hence, in the second paper of this series, we will conduct such a study on this scientifically important but computationally challenging problem to demonstrate the practical value of gMicroMC.

Investigating the uncertainty of DNA damage calculation is an important scientific problem. Computations of DNA damages inevitably involves many user-defined physical or biological parameters and the parameter values are associated with uncertainties for several reasons. First, it is usually hard to measure these parameters accurately in experiments and one must decide parameter values based on certain as-

sumptions. Hence, different values for the same parameter are often seen in different MC simulations. For instance, the probability of generating a single strand break (SSB) for the reaction between radicals and a sugar-phosphate group has been chosen as 0.4 [207], 0.65 [50], 0.7 [218] in different studies. Second, some parameters are measured experimentally with great uncertainties. For example, the cross section of low energy electrons with water could have 30% uncertainty [219, 220]. Third, some parts of the MC simulation process are simplified descriptions of physical reality and empirical parameters are introduced in the simplified model. Parameter values may critically affect the simulation results. Take the computation of a direct DNA damage as an example, one usually checks if energy deposition events are within a geometrical range of the sugar-phosphate group and uses an energy threshold model to decide the damage, whereas the underlying physics charge transport and electrical conduction are ignored [221]. With all these factors considered, it is of central importance to comprehensively quantify the impacts of the variations in different parameters on the simulation results, e.g. DNA SSB and double strand break (DSB). Doing so would be helpful to gain insight about robustness and reliability of the computation results. It would also serve as a guideline for us to pay attention to those parameters that may affect the results significantly in future studies.

As such, we performed a comprehensive evaluation regarding the sensitivity and uncertainty of DNA SSB and DSB calculations with respect to 12 parameters by using the rapidly accelerated GPU-based MC simulation tool gMicroMC. These parameters included 1) physics cross section, 2) cutoff energy for electron transport, 3)-5) three branching ratios of hydroxyl radicals in the de-excitation of excited water molecules, 6) temporal length of the chemical stage, 7)-8) reaction radii for direct and indirect damages, 9) threshold energy defining the threshold damage model to generate a physics damage, 10)-11) minimum and maximum energy values defining

the linear-probability damage model to generate a physics damage, and 12) probability to generate a damage by a radical. Extensively exploring the parameter space to understand their impacts would inevitably lead to a large number of MC simulations. Although the computation time for a single MC simulation using conventional CPU-based MC packages may be acceptable, as the number of simulations increases, the total time will quickly become a barrier for an comprehensive study. This fact indeed highlights the needs for a highly efficient MC tool. Take the current study as an example, gMicroMC is about 6 30 times faster than GEANT4-DNA running on single CPU in the targeted energy range of the current study, which makes the total computation time acceptable. The advantages of gMicroMC would be even higher for studies with a higher incident electron energy.

4.3.2 Methods and materials

We used the DNA model of the lymphocyte cell nucleus containing 6.2 Gbp, which was presented in section 4.2.2. We considered a water sphere with the cell nucleus at its center. The sphere's radius was $r = r_{\text{nucleus}} + R_{e^-}$, where r_{nucleus} is the radius of cell nucleus and $R_{e^-} = E_k/S(E_k)$ is the maximal distance that the initial electron can travel, with E_k and $S(E_k)$ being the initial kinetic energy and the stopping power in water at E_k, respectively. We sampled electrons once at a time with their initial position uniformly distributed in the virtual sphere and the initial direction isotropically sampled. We simulated the electron transport in the physical stage and the water radiolysis process in the subsequent physicochemical and chemical stages. During the transport in the physics stage, cartesian coordinates and deposit energy were recorded for each event. The incident and secondary electrons were tracked, until their energies were less than the cutoff energy E_c, where the electrons were assumed to deposit energy locally and became thermalized. In the

physicochemical stage, water molecules excited during the physics stage underwent de-excitation processes and produced radicals of different species [180]. At the chemical stage, diffusions of radiolytic molecules e^-_{aq}, $HO^{\cdot}$, $H^{\cdot}$, H_3O^+, H_2, OH^-, and H_2O_2, as well as mutual reactions among them were simulated by a step-by-step method for a total time interval T_c. Details of the simulation scheme for the chemical stage can be found in to our previous publications [201]. During the simulation, we did not consider the existence of the DNA model. At the end of the chemical stage, we recorded positions of the radicals. We repeatedly sampled electrons and performed simulations, until the dose accumulated inside the cell nucleus reached 2 Gy, a typical dose level of clinical interest. At the end, a series of energy deposition events (positions and energy deposit values) generated during the physical process and the positions of radicals were stored, based on which DNA damages were computed.

For the damages in the physical stage, we first compared every recorded position of the energy deposition events with the DNA geometry model. If the event fell in a sugar-phosphate group with a reaction radius R_p, we considered the event deposit the energy to the group. After processing all the physical events, we generated a list of DNA sugar-phosphate groups and the accumulated energy deposit E_{tot} to each of them. We considered two models to compute strand breaks (SBs). The first was a simple threshold damage model. A SB was generated if $E_{tot} > E_{thre}$, with E_{thre} being the threshold value. The second was a linear-probability damage model. Two model parameters E_{min} and E_{max} were used. The damage probability was zero if $E_{tot} < E_{min}$, unity if $E_{tot} > E_{max}$, and linearly interpolated between 0 and 1 for E_{tot} in the range $[E_{min}, E_{max}]$.

For the damages in the chemical stage, we compared recorded positions of hydroxyl radicals with the DNA geometry model. Only hydroxyl was considered, because the reaction rate between hydroxyl and DNA is much larger than other

radicals [205]. If the radical was found in a sugar-phosphate group with a reaction radius R_c, we considered the radical interacted with DNA, which generated a SB with a probability P_c. Once the distribution of SBs was generated, we followed the definition in references1,2 to search for SSBs and DSBs based on two parameters. Specifically, $d_s = 216$ was the minimum nucleotide index difference for two SBs to be considered independently and $d_{DSB} = 10$ was the maximum nucleotide index difference for two SBs on opposite sides of the DNA chain to be considered as a DSB. More complex damages were also computed. SSB+ referred to any number of SBs within d_s on the same DNA strand, while 2SSB referred to two SBs on the opposite sides of the DNA chain that were closer than d_s but further than d_{DSB}. As for DSBs, it was defined as two SBs on opposite sides that were closer than d_{DSB} while DSB+ referred to any number of SBs on opposite sides with the largest distance smaller than d_{DSB}. We finally computed SSB yield as $(N_{SSB} + N_{SSB+} + N_{2SSB})/(2Gy * 6.2Gbp)$ and DSBs yield as $(N_{DSB} + N_{DSB+})/(2Gy * 6.2Gbp)$, where N_{SSB}, N_{SSB+}, N_{2SSB}, N_{DSB}, N_{DSB+} were number of damages of different types.

4.3.3 *Simulation parameters of interest*

The aforementioned simulation process involved a number of parameters. In table 4.4, we list major parameters and their default values. In the following paragraphs, we will first present how we defined sensitivity and uncertainty in this study, the reasons to investigate impacts of those parameters of interest, as well as how we varied their values in our study.

To quantify sensitivities and uncertainties of SSB and DSB yields with respect to these parameters, we performed calculations in different runs but with these parameters varied from their default values. We changed one parameter at a time, while keeping all others fixed at the default values. For each parameter setup, we performed

five simulations to estimate the mean and standard deviation of the SSB and DSB yields.

Table 4.4. Summary of parameters studied and the default values for this work

Process	Notation	Descriptions	Default values
Physical	S_{CS}	Scaling factor to change the cross section of electron in water	1
	E_c	Cutoff energy of electrons in water	5 eV
Physico-chemical	Γ_1	Probability for dissociation pathway from A^1B^1 excitation status	0.65
	Γ_2	Probability for auto-ionization pathway from B^1A^1 excitation status	0.55
	Γ_3	Probability for auto-ionization pathway from Ryd A+B, Ryd C+D and diffuse bands excitation status	0.5
Chemical	T_c	Temporal length of the chemical stage	1.0 ns
DNA damage analysis	R_p	Reaction radius to search for a direct damage	0.1 nm
	R_c	Reaction radius to search for a direct damage	0.08 nm
	E_{thres}	Reaction radius to search for a direct damage	17.5 eV
	E_{min}	Minimum energy defining the linear-probability damage model for direct damage	5 eV
	E_{max}	Maximum energy defining the linear-probability damage model for direct damage	37.5 eV
	P_c	Probability of a radical to generate an indirect damage	0.4

We defined sensitivity S as the ratio between the percent change of the SSB or DSB yields and the percent change of the parameter values, i.e. $S = \frac{\Delta Y/Y_{def}}{\Delta X/X_{def}}$, with X_{def} being the default value for parameter X (listed in Table 4.4) and Y_{def}

being the corresponding yields of SSBs and DSBs at X_{def}. $\Delta X = X - X_{def}$ and $\Delta Y = Y - Ydef$, where X is the parameter value and Y is the corresponding yields under X. To compute S, we linearly fit data points and obtained the slope C_L as $\Delta Y/\Delta X$ to compute the sensitivity $S = C_L X_{def}/Y_{def}$. The linear fitting also reported uncertainty in C_L, which was used to compute uncertainty of the sensitivity. For some cases that SSB and DSB yields varied in a nonlinear fashion with respect to the parameter of interest, the fit only used three data points around the default parameter value, which will be specified clearly later. For each case, we will graph all the data points and fitted straight lines as a guidance.

As for the uncertainties of SSB and DSB yields, we first estimated the uncertainty of a parameter $\langle \Delta X/X_{def} \rangle$ based on literature search. We then multiplied the parameter uncertainty $\Delta X/X_{def}$ with the calculated sensitivity S to obtain the estimated uncertainty of the SSB and DSB yields $\Delta Y/Y_{def} = S \times \Delta X/X_{def}$ caused by the parameter uncertainty.

We performed studies in two cases with different initial energies of the electrons $E_k = 1\ keV$ and $4.5keV$. Considering the number of parameters studied in Table 4.4, the number of values per parameters, and five runs per parameter setup, we performed DNA damage calculations for a total number of 205 times for each energy. Again, the high performance of gMicroMC was helpful to conduct large-scale studies like this.

4.3.4 *S_{cs} and E_c in the physical stage*

Physical stage plays a fundamental role for DNA damages. Not only does the direct energy deposition in this stage trigger direct SBs, the number and spatial distribution of events also affects subsequently generated radiolytic chemical radicals, which cause indirect SBs. We considered two parameters relevant to the physical

stage: the cross section of electron interacting with water and the cutoff energy to stop the transport of an electron.

There are two sources that cause uncertainties in the cross section. First, cross section in the low energy range obtained via experiments can have uncertainties up to 30% [215, 220]. Second, the uncertainty could come from the assumption that the entire cell nucleus, including the DNA chromatin, is treated as water for particle transport calculation. Yet, materials other than water, e.g. DNA and proteins exist, which may affect physical interactions between electrons and the environment [209]. It is difficult to comprehensively study the impacts of the cross-section data in different interaction channels at different energy levels and different spatial location. Hence, we took a simplified approach. We used a scaling factor S_{cs} to generate new cross section data by uniformly scaling the cross-section data used in gMicroMC. This was expected to represent the overall effect of all factors leading to uncertainties in the cross section data. We chose $S_{cs} \in [0.7,\ 1.3]$ to cover the range of 30% uncertainty with an interval of 0.1 of $S_{cs} = 1$, indicating the original cross section data stated in part I.

As for the cutoff energy E_c, its value is expected to be around the first excitation energy of water, which is 7.445 eV [222]. For example, cutoff energy value for GEANT4-DNA default physics model is 7.4 eV [207]. However, there are two concerns. First, different studies reported different first excitation energy of water, for instance, 6.42 eV in Tachikawa et al [223]. Second, previous work showed that electrons with energy lower than 5 eV can still produces DNA damages due to the dissociative electron attachment [224]. While it is expected that the lower the cutoff energy is, the more accurate the simulation is, transport simulation of low energy electrons is very time consuming due to the rapid increase of elastic cross section 5. Hence, it is important to know the role of cutoff energy to have a better tradeoff

between accuracy and efficiency. In our study, four E_c levels of 4.5 eV, 5 eV, 7.5 eV and 10 eV were investigated. 4.5 eV was the minimum cutoff energy supported by gMicroMC.

4.3.5 Γ_1,Γ_2 *and* Γ_3 *in the physico-chemical stage*

There are five ionization shells (1b1,3a1,1b2,2a1, oxygen K-shell) and five excited states of the water molecules (two electronic excitations A1B1 and B1A1, two Rydberg series Ryd A+B and Ryd C+D and diffuse bands) [180]. A water molecule in each excited state can undergo three pathways to de-excite, namely dissociative, relaxation and auto-ionization, with different branching ratios. These branching ratios have impact both the number of radicals and their initial distribution in space. They were usually determined by matching simulation results with experiments. Different branch ratios were used in previous studies, which has been well summarized in Ballarini et al [225]. In this study, we studied three parameters Γ_1, Γ_2, Γ_3 related to the generation of hydroxyl radical, representing the branching ratio for the excited water molecules to de-excite through channel listed in Table 1. Values of 0.5, 0.65 and 0.8 for Γ_1, 0.4, 0.55 and 0.7 for Γ_2 and 0.35, 0.5 and 0.65 for Γ_3 were used. It is worth mentioning that in each simulation, only one of the three parameters were changed. The remaining branching ratios for pathways from the same excitation state were changed accordingly to maintain the sum of branching ratios to unity.

4.3.5.1 T_c *in the chemical stage*

After the radiolytic chemical species are produced at the end of the physico-chemical stage, they will react mutually through a diffuse-controlled process. Because we will compute DNA damage by overlapping the positions of hydroxyl with the DNA geometry after the chemical stage, the length of the chemical stage needs to be inves-

tigated, as this parameter affects the geometry configuration of radicals. According to the assumption that the radicals will travel in a random walk way, the root-mean-square (rms)-displacement of radicals in the three dimensional space can be estimated as $\sqrt{\langle r^2 \rangle} = \sqrt{6DT_c}$ where D is the diffusion rate and T_c is the diffusion time. Experimentally, the rms-displacement of the radicals in liquid water was reported as <8.6 nm [226]. With $D_{OH.} = 2.8 \times 10^{-9}\ m^2/s$, a displacement of 8.6 nm is equivalent to a diffusion time of 4.4 ns. In this study, we used 1 ns as the default value, which was also the choice in other works [227, 228]. $T_c = 2.5\ ns$ [229], 10 ns [51] were also used previously. Thus, we reported the dependences of SSB and DSB yields on T_c for five values, namely 1 ns, 2.5 ns, 5 ns, 7.5 ns and 10 ns.

4.3.5.2 *R_p, R_c, E_{thre}, E_{min}, E_{max} and P_c in DNA damage analysis*

When computing DNA damages, SBs are computed using an effective model, instead of performing simulations based on fundamental principles. A few parameters are estimated from statistical models and hence cause uncertainties in the DNA damage calculations. For example, recent study indicated that the energy deposited in the hydration shell can also cause DNA damage [28]. Hence, the reaction radius for a physical damage R_p was introduced when computing the direct SB. $R_p = 0.1\ nm$ was set as the default value in gMicroMC, similar to the value of 0.12 nm in reference [181]. The corresponding effective spherical volume of 0.582 nm^3 for searching a physics damage was similar to the value 0.573 nm^3 in a previous study [230]. To reflect uncertainty in the thicknesses of the hydration shell, we performed simulations with $R_p = 0.05$, 0.1 and 0.15 nm.

In addition to the reaction radius R_p, dependence of SB on the deposit energy is another factor to consider. Since the fundamental correlation between energy deposition events and SB is not clear, two models have been widely used in previous

studies. The first one was a simple threshold damage model that used a threshold $E_{thres} = 17.5eV$ to determine whether an SB can occur following a deposited energy level [231, 232]. The second one was a linear-probability damage model. The probability of generating a SB linearly increased from 0 to 1, when the accumulated energy increased from $E_{min} = 5eV$ to $E_{max} = 37.5eV$ [51, 233]. These energy parameters were determined by matching simulation results with experiment results. To study the effect of these energy parameters, we first studied the threshold damage model with E_{thres} = 12.5, 15, 17.5, 20 and 22.5 eV, respectively. We then explore the linear-probability damage model at different slopes by separately setting E_{min}=3, 4, 5, 6 and 7 eV with $E_{max} = 37.5eV$, and E_{max}=34.5, 36, 37.5, 39 and 40.5 eV with $E_{min} = 5eV$, respectively.

In the indirect damage calculation, to consider the dynamic process for a radical to react with a DNA strand, an effective chemical reaction radius R_c calculated as $R_c = \frac{k}{4\pi N_A D}$ is utilized, where k is the chemical reaction rate between the radical and the DNA strand, N_A is the Avogadro constant and D is the diffusion rate. The formula is deduced from Smoluchowski's diffusion equation [206], and represents the initial reaction radius between a diffusive and a static reactant. The reaction radius equals to 0.08 nm using published chemical reaction rate and diffusion rate [218]. To quantify the uncertainty in this formula, we changed R_c by 20% and hence 0.064 nm and 0.096 nm for R_c were also studied.

The last parameter we considered was P_c, the probability to generate an SB for a chemical reaction between a hydroxyl radical and a sugar-phosphate group. It is reported that P_c may vary for different sites of the DNA and even the hydroxyl-mediated base may also cause damage in sugar moiety [229]. However, a uniform P_c was typically used in current MC simulation packages. P_c = 0.4, 1, 0.65 [50] and 0.7 [218] have been used in different studies. The variation in P_c directly change the

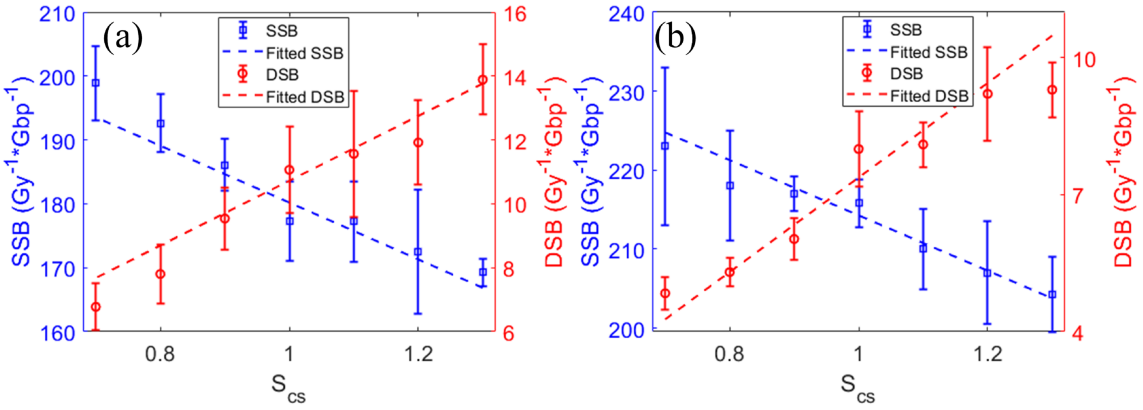

Figure 4.7. Dependences of SSB and DSB yields on the scaling factor S_{CS} of cross section data of electrons in water for electrons with initial energy of (a) 1 keV and (b) 4.5 keV.

distributions of the final SBs. In this study, $P_c \in [0.3,\ 0.7]$ with an interval of 0.1 was investigated.

4.3.6 Results

4.3.6.1 *Parameters in the physical stage*

Dependences of SSB and DSB yields on the scaling factor of cross section data S_{cs} are shown in Figure 4.7. As the scaling factor S_{cs} increased from 0.7 to 1.3, the DSB yield increased from 6.8 ± 0.7 $DSB/Gy/Gbp$ to 14 ± 1 $DSB/Gy/Gbp$, while the SSB yield decreased from 199 ± 6 $SSB/Gy/Gbp$ to 169 ± 2 $SSB/Gy/Gbp$ for the case of 1 keV incident electrons. As for the case of 4.5 keV electrons, the DSB yield increased from 4.8 ± 0.4 $DSB/Gy/Gbp$ to 9.3 ± 0.6 $DSB/Gy/Gbp$, and the SSB yield decreased from 223 ± 10 $SSB/Gy/Gbp$ to 204 ± 9 $SSB/Gy/Gbp$. With a larger cross section, the mean free path length decreases, reducing the distance between energy deposition events and making it easier to form DSBs. Hence, the DSB yield ratio increased with S_{cs}. On the other hand, scaling the cross-section data

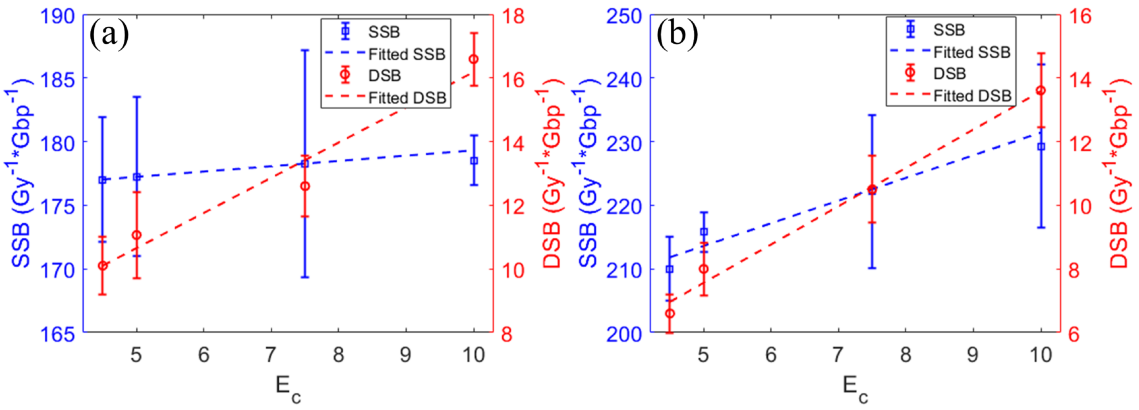

Figure 4.8. Dependences of SSB and DSB yields on the cutoff energy E_c of electrons in water for electrons with initial energy of (a) 1 keV and (b) 4.5 keV.

did not change the total number of physical interactions. With more SBs classified into DSBs, the SSB yield hence decreased. The variation of SSB and DSB yields were found to be approximately linear in the studied parameter range. After fitting the data, the sensitivities of SSB and DSB yields with respect to S_{cs} were -0.28 ± 0.03 and 1.02 ± 0.08 for the case with 1 keV electrons, and -0.14 ± 0.01 and 1.1 ± 0.1 for the case with 4.5 keV electrons, respectively.

As for the cutoff energy E_c, the results are summarized in Figure 4.8. As E_c increased, the SSB yield varied a little, but the DSB yield changed relatively more rapidly. Variation of E_c affects the last a few steps of an electron track, because it determines when the remaining energy of the electron should be deposited. With a higher cutoff energy value, the last few energy deposition events are grouped into a single event. This energy accumulation effect makes it easier to produce an SB. Meanwhile, the distances between the last few events are usually in the nanometer range. Increased SB will hence be more likely to form DSB than SSB. The sensitivities of SSB and DSB yields with respect to E_c were 0.008 ± 0.001 and 0.50 ± 0.07 for the case with 1 keV electrons and 0.07 ± 0.01 and 0.75 ± 0.06 for 4.5 keV electrons.

4.3.6.2 *Parameters in the physicochemical stage*

The results for the branching ratios of different channels are summarized in Figure 4.9. SSB and DSB yields were found to be insensitive to these three parameters. The sensitivities of SSB and DSB yields were -0.004 ± 0.002 and -0.08 ± 0.1 for Γ_1, -0.02 ± 0.04 and 0.02 ± 0.1 for Γ_2, -0.05 ± 0.03 and -0.02 ± 0.1 for Γ_3 in the case with 1 keV electrons. As for the case with 4.5 keV electrons, the values were 0.01 ± 0.04 and 0.1 ± 0.2 for Γ_1, -0.0218 ± 0.0005 and 0.2 ± 0.1 for Γ_2, -0.04 ± 0.04 and 0.1 ± 0.1 for Γ_3. The rather insensitive dependence of SSB and DSB yields can be ascribed to the low contribution of the three channels to the production of hydroxyl radicals. These three channels are related to de-excitation of excited water molecules. For both cases, the three channels considered here gave less than 10% of hydroxyl production.

4.3.6.3 *Parameters in the chemical stage*

As indicated in Figure 4.10, both SSBs and DSBs decreased as T_c increased. The reason was that the hydroxyl radicals are depleted, as the chemical stage length is prolonged because of radicals reactions with each other [180]. The sensitivity of SSB and DSB yields on T¬c were -0.012 ± 0.002 and -0.04 ± 0.01 for 1 keV electrons and -0.020 ± 0.002 and -0.033 ± 0.009 for 4.5 keV electrons, respectively.

4.3.6.4 *Parameters in DNA damage analysis*

The dependences of SSB and DSB yields on R_p and R_c are shown in Figure 4.11. All cases showed increased yields with respect to these reaction radii, as a large radius allows for more SBs to generate. The sensitivity of SSBs and DSBs were 0.119 ± 0.007 and 0.547 ± 0.006 for R_p, 0.054 ± 0.009 and 0.11 ± 0.02 for R_c with 1

keV electrons. As for the 4.5 keV electrons, the sensitivities of SSBs and DSBs were 0.12 ± 0.01 and 0.55 ± 0.02 for R_p, 0.07 ± 0.02 and 0.03 ± 0.04 for R_c.

Figure 4.12 shows the dependence of SSB and DSB yields on energy threshold E_{thres} in the threshold damage model. When increasing the energy threshold value, both SSB and DSB yields were reduced because of reduction in generated SBs in the physical stage. But DSBs decreased 5 times, while SSBs only decreased less than 2 times with E_{thres} increases from 12.5 eV to 22.5 eV. This can be understood as following. The threshold acts on the total energy deposited to a sugar-phosphate group. As shown in Figure 4.13, most energy deposit events have energy below 10 eV. Damages are likely generated, only when multiple events are within a sugar-phosphate group, so that the accumulated energy is higher than the threshold. However, only at the very end of the electron track can multiple events be more likely to be in the same group. Hence, reducing physical damages by raising the threshold energy mainly affect DSBs, since the distances between physical events are close in the end of the track. The dependence of SSB and DSB yields appeared to be nonlinear with respect to E_{thres}. Hence, we computed sensitivity using only data points close to the default value. The sensitivities were -0.7 ± 0.2 and -3.1 ± 1.0 with 1 keV electrons, -0.9 ± 0.2 and -3.3 ± 1.0 with 4.5 keV electrons, respectively. Considering the nonlinearity of the dependence of SSB and DSB yields on E_{thres}, the reported values underestimated the importance of E_{thres} at energy lower than 17.5 eV and overestimate it for energy higher than 17.5 eV.

Figure 4.14 shows the function of SSB and DSB yields on parameters E_{min} and E_{max} in the linear-probability damage model. Generally speaking, increasing either parameter would decrease the chance of SB formation, yielding the decreasing trend seen in these figures. The sensitivities of SSB and DSB yields were -0.15 ± 0.01 and -0.20 ± 0.01 for E_{min}, and -0.35 ± 0.05 and -1.1 ± 0.1 for E_{max} for 1 keV electrons.

As for 4.5 keV electrons, the sensitivities of SSB and DSB yields were -0.165 ± 0.002 and -0.37 ± 0.06 for E_{min}, and -0.37 ± 0.05 and -1.7 ± 0.4 for E_{max}.

SSB and DSB yields increased with P_c, the probability for a chemical reaction between the hydroxyl radical and the sugar-phosphate group to generate a SB (Figure 4.15). With a larger P_c, more SBs are induced and therefore more SSBs and DSBs are produced. The sensitivity of SSB and DSB yields on P_c are 0.57 ± 0.01 and 0.40 ± 0.03 for 1 keV, and 0.585 ± 0.007 and 0.40 ± 0.03 for 4.5 keV electrons, respectively.

4.3.6.5 *Convert sensitivities of DNA SSB and DSB yields to their uncertainties*

Table 4.5. Summary of sensitivities of SSBs and DSBs on different parameters

Parameters	1.0 keV electrons		4.5 keV electrons	
	SSB	DSB	SSB	DSB
S_{cs}	-0.28 ± 0.03	1.02 ± 0.08	-0.14 ± 0.01	1.1 ± 0.1
E_c	0.008 ± 0.001	0.50 ± 0.07	0.07 ± 0.01	0.75 ± 0.06
Γ_1	-0.004 ± 0.002	-0.08 ± 0.1	0.01 ± 0.04	0.1 ± 0.2
Γ_2	-0.02 ± 0.04	0.02 ± 0.1	-0.0218 ± 0.0005	0.2 ± 0.1
Γ_3	-0.05 ± 0.03	-0.02 ± 0.1	-0.04 ± 0.04	0.1 ± 0.1
T_c	-0.012 ± 0.002	-0.04 ± 0.01	-0.020 ± 0.002	-0.033 ± 0.009
R_p	0.119 ± 0.007	0.547 ± 0.006	0.12 ± 0.01	0.55 ± 0.02
R_c	0.054 ± 0.009	0.11 ± 0.02	0.07 ± 0.02	0.03 ± 0.04
E_{thres} *	-0.7 ± 0.2	-3.1 ± 1.0	-0.9 ± 0.2	-3.3 ± 1.0
E_{min}	-0.15 ± 0.01	-0.20 ± 0.01	-0.165 ± 0.002	-0.37 ± 0.06
E_{max}	-0.35 ± 0.05	-1.1 ± 0.1	-0.37 ± 0.05	-1.7 ± 0.4
P_c	0.57 ± 0.01	0.40 ± 0.03	0.585 ± 0.007	0.40 ± 0.03

* SSB and DSB yields depend on E_{thres} in a nonlinear way. The sensitivity value here was derived using three data points around default value.

We summarize all the sensitivity values with respect to different parameters of interest in Table 4.5. Sensitivity means how sensitive the result (SSB and DSB yields) is with respect to the variation of a parameter. Practically, it may be of more interest

to understand the uncertainty of SSB and DSB yields. As such, we first estimated uncertainty levels of the parameters (Table 4.6) based on a literature search, which covered both experimental and simulation studies.

Table 4.6. Summary of uncertainties of SSB and DSB yields due to the uncertainties of different parameters. Numbers in bold face are larger than 10% threshold and considered as large uncertainties.

Parameters	Estimated uncertainty level	1.0 keV electrons		4.5 keV electrons	
		SSB	DSB	SSB	DSB
S_{cs}	30%	8.3%	30.6%	4.2%	33.0%
E_c	39%	0.3%	19.5%	2.9%	29.4%
Γ_1	100%	0.4%	8.3%	1.3%	9.8%
Γ_2	100%	2.3%	2.3%	2.2%	18.0%
Γ_3	100%	5.1%	2.6%	4.4%	11.3%
T_c	85%	1.0%	3.0%	1.3%	2.8%
R_p	50%	6.0%	27.3%	5.8%	27.7%
R_c	35%	1.9%	3.7%	2.4%	1.1%
E_{thres}	48%	32.3%	147.4%	43.0%	158.9%
E_{min}	48%	7.3%	9.5%	7.9%	17.8%
E_{max}	48%	17.0%	54.9%	17.5%	83.8%
P_c	55%	31.2%	21.9%	32.2%	21.8%

The uncertainty of cross section data mainly exists in the low energy range (<100 eV) [185, 234], but the low energy electrons are of critical importance in determining the DNA damages. The overall uncertainty of cross section was estimated as 30%, same as reported in Munoz et al [220]. As for E_c, different values were used in previous studies, ranging from 7.4 eV for the default model of GEANT4-DNA to 11 eV for option 6 [207]. The uncertainty for E_c was hence estimated as 39% (3.6/9.2, range/mean value). As for the three parameters Γ_1, Γ_2, Γ_3, it is difficult to estimate their uncertainties due to lack of experiment information. We estimated the uncertainties to be 100% according to the Table 2 in Ballarini et al [225]. For the

chemical stage time T_c, the common values used in literatures were 1 ns and 2.5 ns. When it was larger than 2.5 ns, the scavenger effect was usually considered. Hence, we considered the uncertainty to be as 85% (1.5/1.75). Next, R_p is used to account for the damage transferred from the first hydration shell (quasi-direct effect) [235]. Yet, the reported thickness for the first hydration shell varies depending on studies. For example, 12 molecules/nucleotide [185], 12-15 molecules/nucleotide [181] and 20 molecules/nucleotide [28] were used previously. The uncertainty was thus estimated to be 50% (8/16). In terms of R_c, it is determined by the chemical reaction constant and the diffusion rate of hydroxyls. The reported variation for diffusion rate among published works can be 28% [225] and the variation for chemical reaction rate can be 20% [218, 236]. Hence, the uncertainty for R_c was estimated as 35% using error propagation. As for E_{thres}, others used 10.79 eV [229] instead of the commonly used value of 17.5 eV. The uncertainty is estimated as 48% (6.7/14.1). Same uncertainty level was hence applied to E_{min} and E_{max}. Finally, uncertainty of P_c was estimated as 55% (0.3/0.55) to account its change from 0.4 to 0.7 reported in previous studies [207, 218]. All these parameter uncertainties are summarized in the second column of Table 4.6.

Based on the estimated uncertainties of each parameter, uncertainties of SSB and DSB yields were calculated as the product of the parameter uncertainties and the corresponding sensitivities. The results are listed in columns 3-6 of Table 4.6. Negative signs are dropped here. Nowadays, the uncertainty of measuring DSB is about 10% [237–239]. If we choose 10% as the criterion for an uncertainty level to be consider as large, we highlighted those numbers in Table 4.6. It was found that E_{thres} for the threshold damage model, E_{max} for linear-probability damage model, and probability P_c can cause large uncertainties in both SSB and DSB yields. The scaling factor of the cross section S_{cs}, cutoff energy E_c, physics searching radius R_p

and E_{min} in the linear-probability damage model can cause more uncertainties in DSB yields than SSB yields. Although the uncertainties due to Γ_2 and Γ_3 were also found to be large for DSB yields in the 4.5 keV electron case, this was likely a consequence of the large error bars in the simulation results (Figure 4.9).

4.3.6.6 *Computation time*

Since one of the motivations of this study was to demonstrate the practical value of gMicroMC in the large-scale simulation problem of interest, we report computation time required to perform the study. The GPU code was executed on one Nvidia Titan Xp GPU (1.58GHz) card. It took gMicroMC 1.4 seconds to simulate one electron with energy 1 keV from the start of the physics stage to the end of the chemical stage. Meanwhile, we also ran a few cases using GEANT4-DNA on one single core of Intel i7-6850K CPU (3.6GHz) to estimate the computation time of GEANT4-DNA, if that were used to perform the same study. The computation time for GEANT4-DNA was found to be 9 seconds. For the total number of 205 simulation runs with each run accumulating 2 Gy dose (about 8000 electrons) inside the cell nucleus, the computational time was 28 days for gMicroMC to finish all the computations but would be 6 months for GEANT4-DNA. The speed up factor was relatively low due to the low usage of GPU resources in the low energy context. The advantages of gMicroMC increased with electron energy. The time to transport one 4.5 keV electron was 1.9 seconds for gMicroMC and 61 seconds for GEANT4-DNA. Hence, the time needed for gMicroMC to complete all the simulations in this case was 38 days but would be over three years for GEANT4-DNA. In reality, such a large-scale computation is usually conducted using CPU clusters for GEANT4-DNA, which could substantially reduce the overall computation time. However, with multi-GPU

platform, we could also further reduce computation time as well, which will allow us to perform more detailed studies.

4.3.7 Discussion

Calculations of SSB and DSB yields depend on microscopic radiation transport simulation and DNA damage computation. Hence, the resulting sensitivities vary with the specific methods in these two tasks. The current study focused on sensitivities computed using detailed MC simulation in the physical, physicochemical, and chemical stages for radiation transport and using a realistic DNA geometry model. It would be an important study to investigate sensitives in other methods, such DBSCAN method 35 that does not consider transport in the chemical stage and estimate damages using a probabilistic approach without involving a DNA geometry model. These investigations are beyond the scope of the current study and will be our future work. We expect the developed GPU tool will be beneficial for studies as such.

While conducting this study, we noticed that the research group at the Massachusetts General Hospital (MGH) performed a similar research to investigate the impacts of different simulation parameters on DNA damages in the context of proton irradiation [240]. They studied the effects of variation of physics model (G4EmDNAphysics opt2, opt4 and opt6), chemical stage model (TsEmchemistry model and G4Emchemistry model [241]), energy model (threshold and linear-probability damage models), chemical stage length (1 ns, 2.5 ns, 10 ns) and hydroxyl damage probability (0.4, 0.65) on SBs and DSBs under different linear energy transfer (LET) conditions. Our result generally agreed with theirs. For example, the ratio of SB yield with $P_c = 0.65$ to that with $P_c = 0.4$ was found to be 1.43 for protons with LET of 10 $keV/\mu m$, while our work gave 1.38 for 1 keV electrons that are approximately at the same LET level. For the DSB uncertainties, the MGH group reported 20% due to physics model, 30%

due to chemical stage time and 30% due to P_c, whereas the numbers were found to be 20 35%, 10% and 25% in our work, respectively.

4.4 Conclusions

We described the initial development of gMicroMC here, including its algorithm and implementation on GPU. Because of the advantages of fast MC simulation achieved by our gMicroMC package, we performed an extensive study using gMicroMC to evaluate the sensitivities of calculated DNA SSB and DSB yields with respect to 12 parameters in the computations. Based on calculated sensitivities, we further estimated the uncertainties of calculated SSB and DSB yields due to uncertainties in those parameters. It was found that, using a threshold of 10% uncertainty as a criterion, uncertainties of SSBs and DSBs were found to be largely affected by E_{thres} in the threshold damage model, E_{max} in the linear-probability damage model, and probability P_c for a radical to generate a damage. The scaling factor of the cross section S_{cs}, namely the accurate cross section data, cutoff energy E_c, physics searching radius R_p and E_{min} in the linear-probability damage model caused large uncertainties in DSB yield but not in SSB yield. Our study could serve as a starting point for future investigations to reduce uncertainties of those simulation parameters and hence to reduce uncertainties of the simulation results.

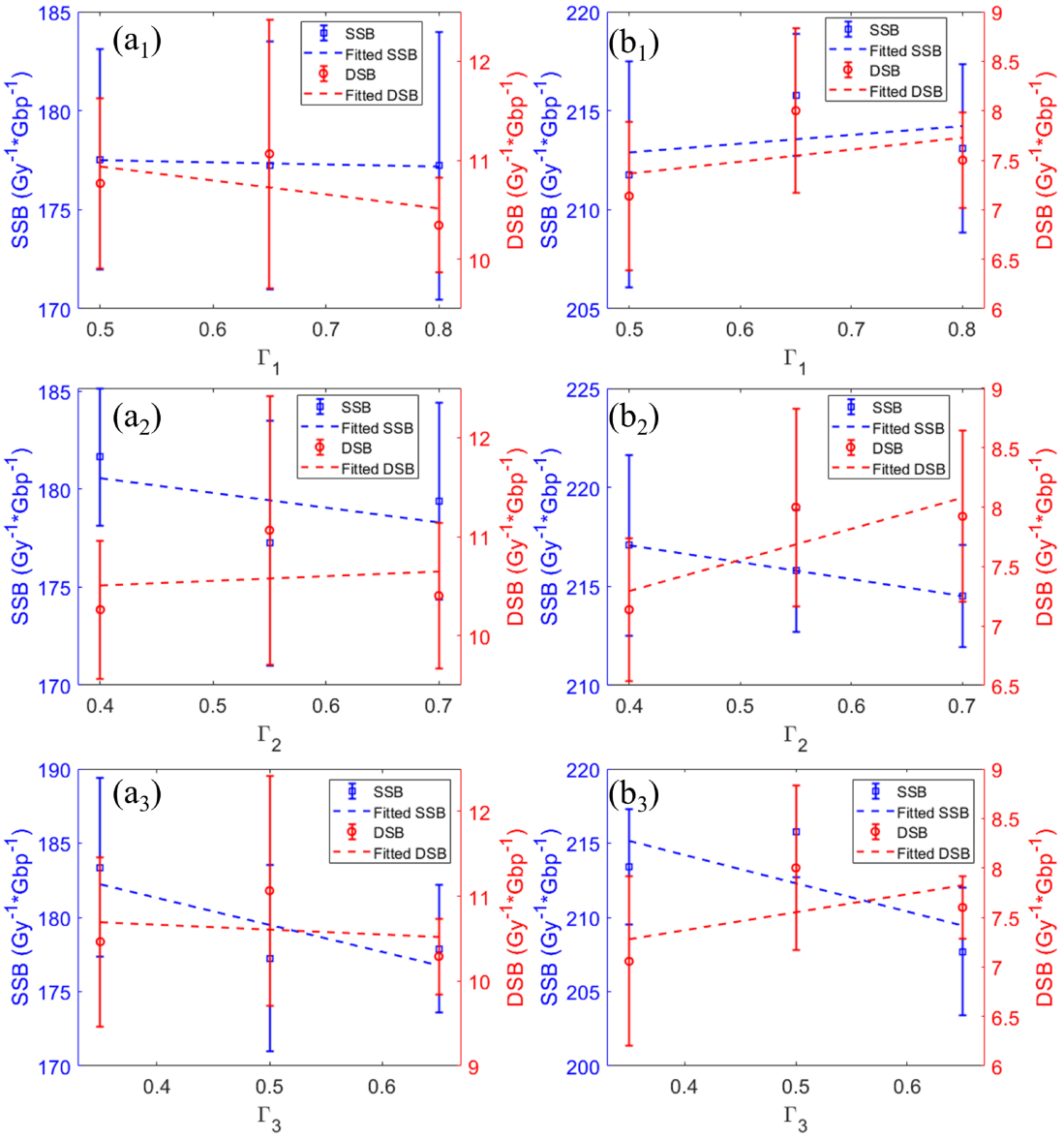

Figure 4.9. Dependences of SSB and DSB yields regarding different branch ratios for electrons with initial energy of (a) 1 keV and (b) 4.5 keV.

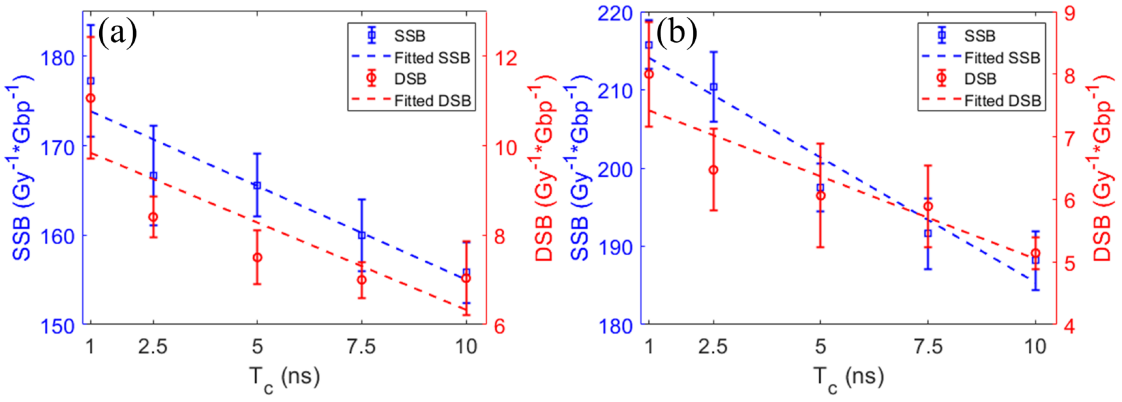

Figure 4.10. SSB and DSB yields for the case with (a) 1 keV electrons and (b) 4.5 keV electrons as a function of chemical stage length T_c. .

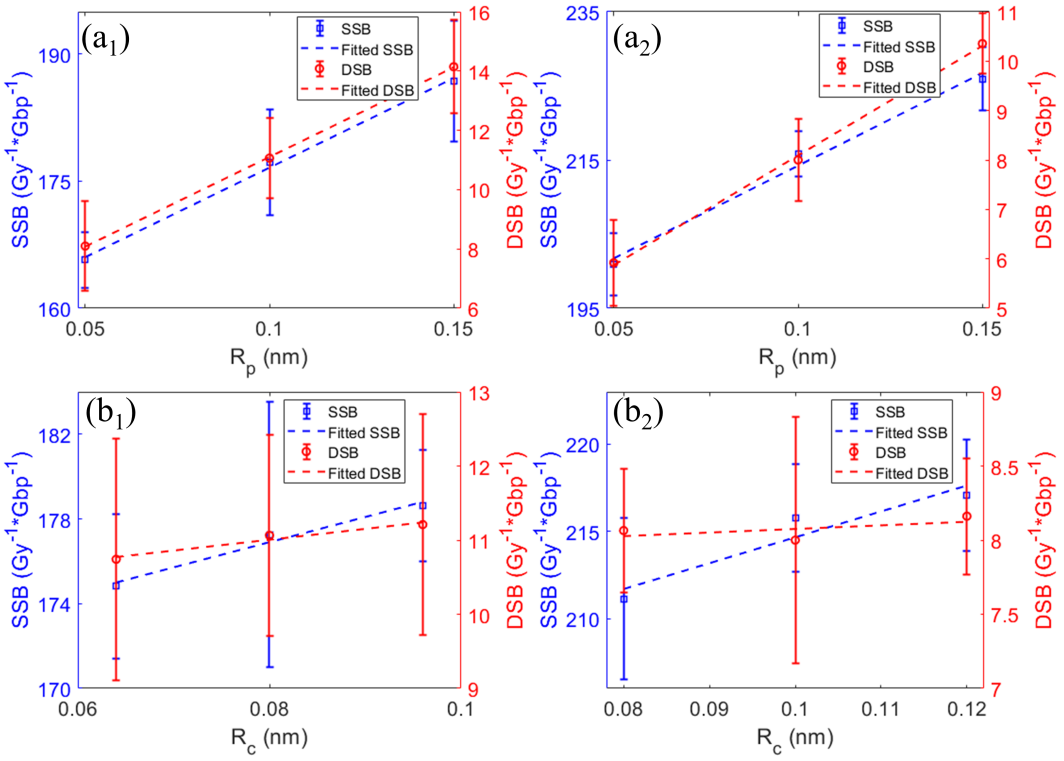

Figure 4.11. SSB and DSB yield regarding physics reaction radius (a) R_p and chemical reaction radius (b) R_c for cases with electron energy of 1.0 keV (left column) and 4.5 keV (right column)..

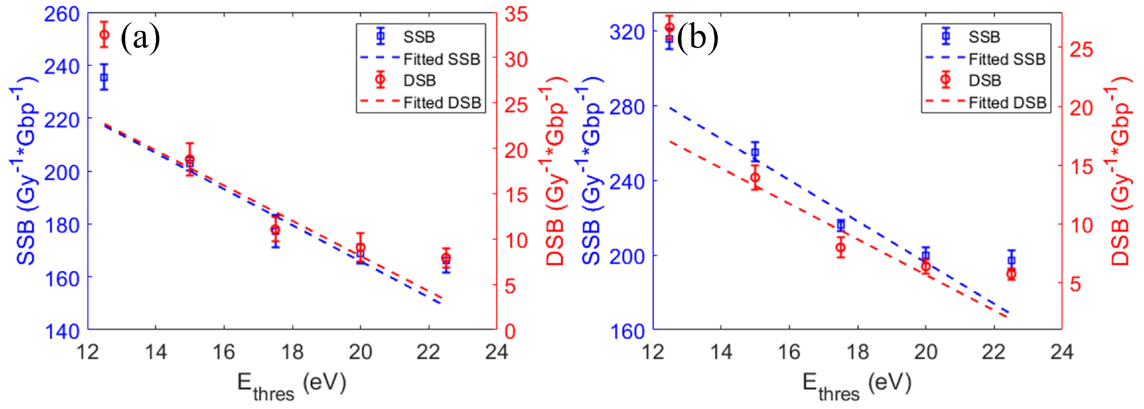

Figure 4.12. SSB and DSB for the case with (a) 1 keV electrons and (b) 4.5 keV electrons as a function of energy threshold E_{thres}..

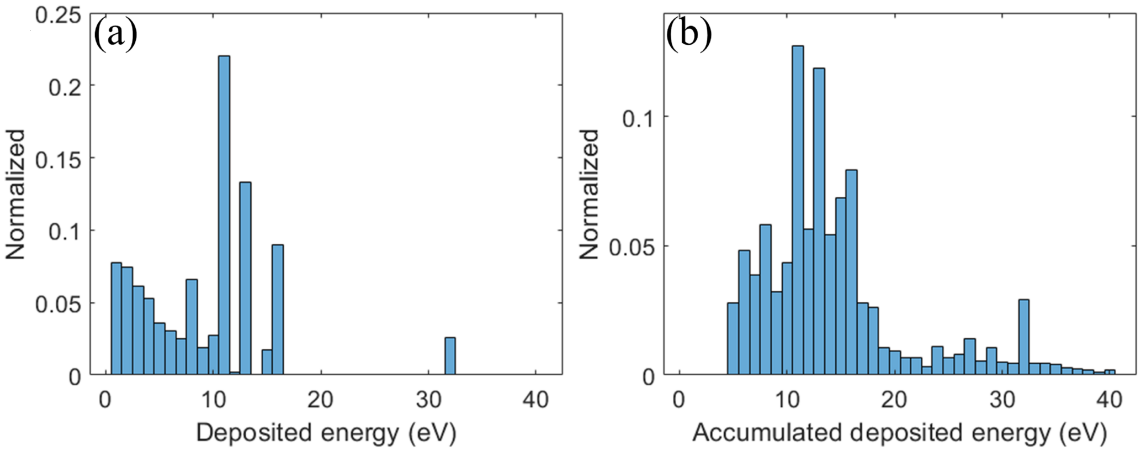

Figure 4.13. Distribution of deposit energy of events and accumulated deposit energy to DNA sugar-phosphate group for 1 keV electron. The distribution is averaged on 1000 simulations of 1 keV electrons..

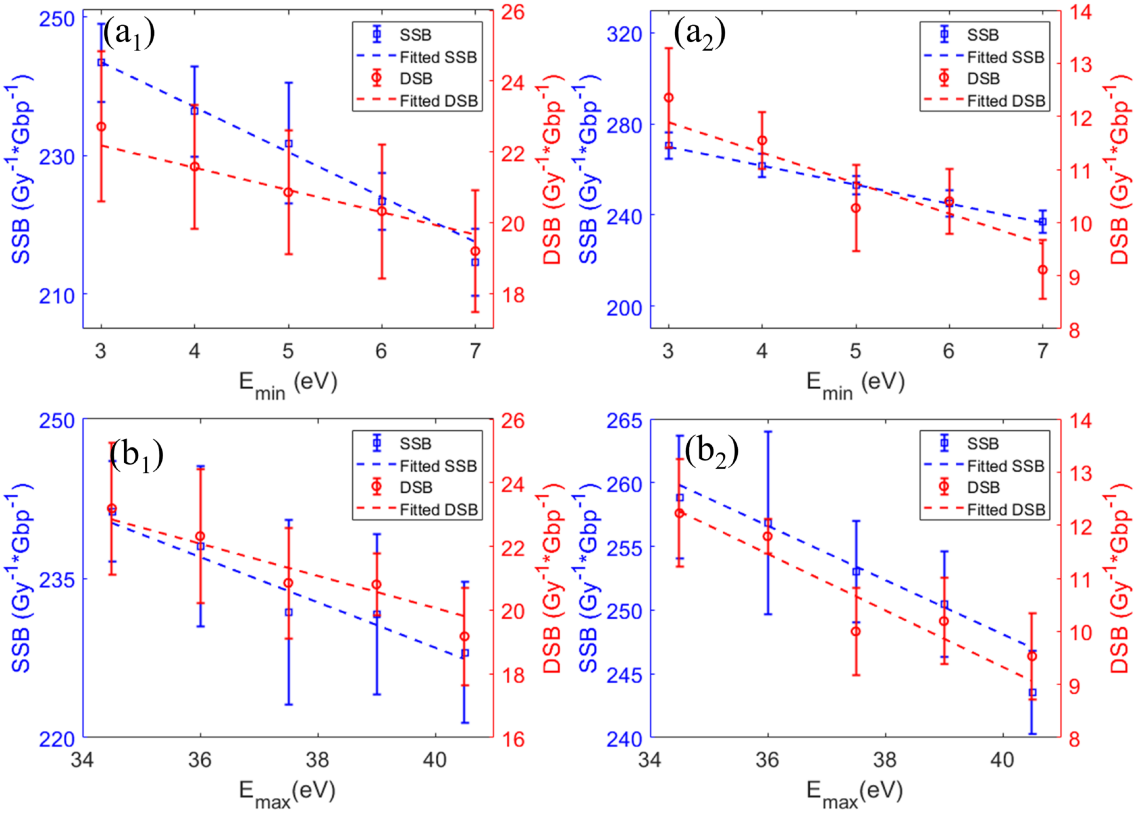

Figure 4.14. SSB and DSB yields as a function of (a) E_{min} and (b) E_{max}. The left column and right column are for 1 keV electrons and 4.5 keV electrons, respectively.

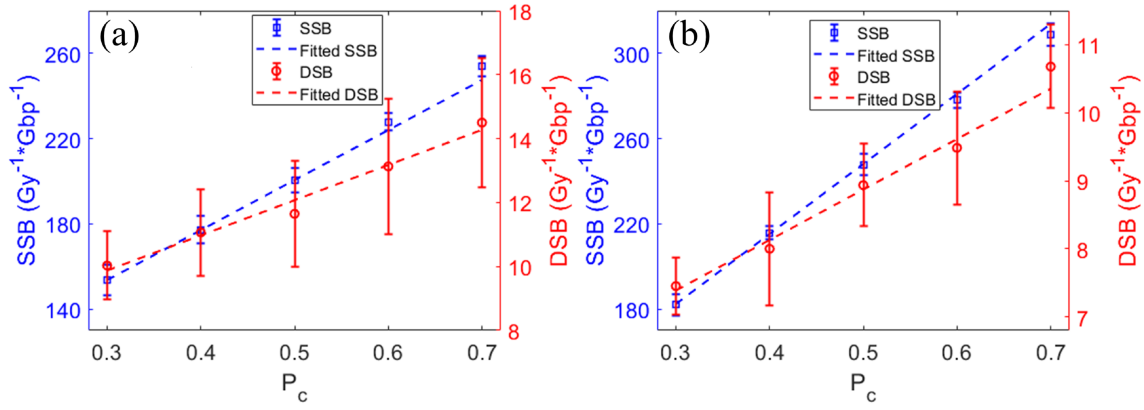

Figure 4.15. SSB and DSB yields for (a) 1 keV electrons and (b) 4.5 keV electrons as a function of P_c..

CHAPTER 5

FURTHER DEVELOPMENT OF GMICROMC

5.1 Introduction

Understanding biological responses to ionizing radiation is of crucial importance for cancer treatment using radiotherapy. Mechanistic Monte Carlo (MC) simulation of radiation effect on DNA in water medium is a promising tool for relevant studies after decades of development [242]. The central idea of such an approach is to obtain the initial DNA damage spectrum via mechanistic modeling of the radio-biological interactions at the atomic or molecular levels. This includes the development of track-structure codes [50, 52, 181, 185, 199, 243–251] and the subsequent computation of DNA damages by incorporating DNA models [181, 203, 245, 252, 253]. The track-structure simulation can be divided into the simulations for physical stage and chemical stage. The physical stage simulation deals with the ionization, excitation and elastic scattering processes between the ionizing radiation particles and the water media and records the 3D coordinates of energy deposition events. The chemical stage simulation computes how the chemical radicals, produced after the physical stage simulation, diffuse and react mutually with a recording of the residual radicals' positions. The positions for these energy deposition events and radicals are then utilized to compute the initial DNA damage sites, followed by an analysis to characterize DNA strand-break patterns.

Although a lot of developments have been performed to generate state-of-the-art mechanistic MC simulation tools, there are still needs to further improve the simulation methods to accommodate different scenarios [185]. For instance, to make

the code versatile for studies on oxygen enhancement ratio (OER) [254], the Fenton reaction effect [255], it is desired to include more types of molecules other than free radicals generated by initial radiation into the chemical stage simulation. However, due to the computation complexity of 'many-body' problem and the long temporal duration of the chemical stage, a step-by-step simulation of these relevant processes on conventional CPU computational platforms can be extremely time consuming [256]. Under the constraint of computational resources, studies typically suffer from restricted simulation region or shortened temporal duration [205, 207, 257], limiting their broad applications.

To overcome these obstacles, Graphical Processing Unit (GPU)-based parallel computing can be a cost-effective option [53, 54]. We have developed an open-source, GPU-based microscopic MC simulation toolkit, gMicroMC [52], with the first version available at GitHub https://github.com/utaresearch/gMicroMC. We initially focused on boosting the chemical stage simulation for radicals produced from water radiolysis, achieving a speedup of several hundred folds compared to CPU-based packages [201]. Later on, we supported the physical track simulation for energetic electrons and implemented an DNA model of a lymphocyte cell nucleus at the base-pair resolution for the computation of electron induced DNA damages [52]. Recently, we have also included oxygen molecules in the chemical stage simulation in a step-by-step manner, which enabled the study of the radiolytic depletion effect of dissolved oxygen molecules [258]. With these efforts, we were able to quantitatively study multiple critical problems that are computationally demanding. For example, we performed comprehensive simulations with gMicroMC to answer how uncertainties from simulation parameters affect the accuracy of final DNA damage computations [259]. We also studied the radiolytic depletion of oxygen under ultra-high dose rate radiation

(FLASH) to investigate the fundamental mechanism behind FLASH radiotherapy with the developed oxygen module in gMicroMC [258].

In this Chapter, we will report our recent progress on two new and important features that we recently introduced to gMicroMC, namely 1) enabling the physical stage simulations of protons and heavy ions, and 2) considering the presence of the DNA structure and its chemical reactions with radicals in the chemical stage simulation. It is expected that the first feature will contribute greatly to the mechanistic study for particle irradiation, such as particle radiotherapy [260, 261]. The presence of DNA structure in chemical stage simulation will allow us to realistically describe the indirect DNA damage process. With the GPU acceleration, we are able to afford computationally challenging simulations that include detailed physics modeling and chemical reactions that span over a large temporal duration, enabling more realistic simulations of the relevant processes.

5.2 Materials and Methods

5.2.1 Cross sections for transport simulation of protons and heavy ions

When a proton or heavy ion moves through a medium, it interacts with the atomic electrons inside the medium [262]. Considering that there have been various models developed and implemented to describe this process, in this work, we focused on a novel implementation of existing models on GPU parallel computing platforms. Specifically, we only considered the interactions between particles and water molecules because it is representative for modelling cell environment. We employed the Rudd's model[263] to compute the ionization of a water molecule by a proton at the energy range from 10 eV to 1 TeV. We implemented the Plante's model[264] and Dingfelder's model[265] to simulate the excitation of a water molecule for protons with energy

above and below 500 keV, respectively. We also applied the Booth's empirical formula [266] to include the charge effect on the cross section computation. Lastly, we used the charge scaling rule [267] to obtain the cross sections for heavy ions based on those for a proton. To make the manuscript easy to follow, we briefly introduced these models in the following subsections.

5.2.1.1 Ionization for proton

An energetic proton could eject a secondary electron from different atomic sub-shells when it ionizes a water molecule. In the Rudd's model [263, 268], the partial singly differential cross section (SDCS) can be described as

$$\frac{d\sigma_i^{ion}}{dw} = \frac{S_i}{B_i} \frac{\left(F_1\left(\nu\right) + wF_2\left(\nu\right)\right)}{\left(1+w\right)^3} \frac{1}{1+\exp\left[\frac{\alpha(w-w_i)}{\nu}\right]} \tag{5.1}$$

Here, i refers to the sub-shells of the water molecule, namely $^1b_1$, $^3a_1$, $^1b_2$, $^2a_1$, and $^1a_1$. B_i is the binding energy for electrons on shell i. $w = E_e/B_i$ and E_e the energy of the secondary electron. $S_i = 4\pi a_0^2 * N_i * \left(E_R/B_i\right)^2$, where $a_0 = 5.3 \times 10^{-11}\ m$ is the Bohr radius, $E_R = 13.6\, eV$ is the Rydberg energy, and N_i is the number of electrons on shell i. $\nu = \sqrt{T/B_i}$ denotes the scaled velocity of the projectile, with $T = \frac{m}{M} * E_k$. m and M are the masses of electron and proton, while E_k is the kinetic energy of proton. $w_i = 4\nu^2 - 2\nu - E_R/4B_i$ is the scaled cutoff energy and α is a numerical parameter related to the relative size of the target molecule. The specific values for B_i, N_i and α were listed in Table 5.1. $F_1(\nu)$ and $F_2(\nu)$ are fitting functions, defined as:

$$F_1\left(\nu\right) = L_1 + H_1 \tag{5.2}$$

$$F_2\left(\nu\right) = \frac{L_2 H_2}{L_2 + H_2} \tag{5.3}$$

where

$$L_1 = \frac{C_1 \nu^{D_1}}{1 + E_1 \nu^{D_1+4}}, \tag{5.4}$$

$$H_1 = \frac{A_1 \ln(1+\nu^2)}{\nu^2 + B_1/\nu^2}, \tag{5.5}$$

$$L_2 = C_2 \nu^{D_2}, \tag{5.6}$$

$$H_2 = \frac{A_2}{\nu^2} + \frac{B_2}{\nu^4}. \tag{5.7}$$

The values for the nine basic parameters $A_1, ..., E_1$ and $A_2, ..., D_2$ used in Equations (5.4)-(5.7) could be seen in Table 5.1. These values differed for inner-shell orbital and external orbital, and an orbital was regarded as an inner one when its binding energy exceeded twice the binding energy of the least-tightly bound orbital [263].

From Equation (5.1), we can calculate the total cross section for the sub-shell i as

$$\sigma_i^{ion} = \int_0^{w_m} \frac{d\sigma_i^{ion}}{dw} dw, \tag{5.8}$$

where $w_m = \frac{E_m}{B_i}$ and E_m is the scaled maximum transferable energy from the proton to the ejected electron. The relativistic expression of E_m is given by Plante *et. al.* [264] as

$$E_m = \frac{2mc^2(\gamma^2 - 1)}{1 + 2\gamma\left(\frac{m}{M}\right) + \left(\frac{m}{M}\right)^2}, \tag{5.9}$$

with

$$\gamma = 1 + \frac{E_k}{Mc^2}, \tag{5.10}$$

and c the speed of light. The relativistic format for the scaled velocity ν is then written as

Table 5.1. Parameters used in this work for Equations (5.1)-(5.7). Data were extracted from [265, 268]

Parameter	Inner orbitals		External orbitals		
	$^1a_1$	$^2a_1$	$^1b_2$	$^3a_1$	$^1b_1$
A_1	1.25	1.25	1.02	1.02	1.02
B_1	0.5	0.5	82	82	82
C_1	1	1	0.45	0.45	0.45
D_1	1	1	-0.80	-0.80	-0.80
E_1	3	3	0.38	0.38	0.38
A_2	1.1	1.1	1.07	1.07	1.07
B_2	1.3	1.3	14.6	14.6	14.6
C_2	1	1	0.6	0.6	0.6
D_2	0	0	0.04	0.04	0.04
α	0.66	0.66	0.64	0.64	0.64
N_i	2	2	2	2	2
B_i	539.7	32.2	18.55	14.73	12.61

$$\nu^2 = \frac{mc^2}{2B_i}[1 - \frac{1}{\gamma^2}]. \tag{5.11}$$

With the ionization model and parameters determined under both relativistic and non-relativistic formalism, we could integrate Equation (5.8) numerically to obtain the ionization cross section table for different sub-shells of a water molecule in a broad proton energy range. In our implementation, we computed the table for proton energies ranging from 10 eV to 1 TeV with a 0.01 increment along the logarithmic scale. It is worthy mentioning that the computation of the cross section table only needed to be computed once in an offline manner and was stored in a data file that can be loaded to GPU memory for query of cross sections of any incident energy. More detail of this usage was given in subsection 5.2.3.1.

5.2.1.2 Excitation for proton

Due to the lack of experimental data, different models could have differential configurations of the excitation pathways. In our implementation, we adopted the three-pathway model [269, 270] containing $\widetilde{A}^1B_1$, $\widetilde{B}^1A_1$ and plasma mode for protons with energy ¿ 500 keV, and the model with excitation channels of $\widetilde{A}^1B_1$, $\widetilde{B}^1A_1$, Ryd A+B, Ryd C+D and diffusion band [**dingfelder2000inelastic**] for proton energy ¡ 500 keV. Specifically, in the three-pathway model, the differential cross section for the excitation channel j is expressed as

$$\frac{d\sigma_j^{exc}}{dW} = \rho\left(W\right) W f_j\left(W\right) \ln\left(\frac{W}{Q_{min}}\right), \tag{5.12}$$

where

$$\rho\left(W\right) = \frac{8\pi Z^2 a_0^2}{mu^2}\frac{Ry^2}{W^2}, \tag{5.13}$$

$$Q_{min} = 2T\left(\frac{M}{m}\right)^2\left(1 - \frac{1}{2}\frac{m}{M}\frac{W}{T} - \sqrt{1 - \frac{m}{M}\frac{W}{T}}\right). \tag{5.14}$$

Here, j denotes different excitation channels, namely $\widetilde{A}^1B_1$, $\widetilde{B}^1A_1$ and plasma mode. u, Z and W are the velocity, charge and energy loss of the incident proton. Other parameters are the same as that used in section 5.2.1.1. When $\frac{m}{M}\frac{W}{T} = \frac{W}{E_k} \ll 1$, Equation (5.12) can be simplified as

$$\frac{d\sigma_j^{exc}}{dW} = \rho\left(W\right) W f_j\left(W\right) \ln\left(\frac{4T}{W}\right). \tag{5.15}$$

At the relativistic situation, mu^2 in Equation (5.13) can be expressed as

$$mu^2 = mc^2\left[1 - \gamma^{-2}\right]. \tag{5.16}$$

$f_j\left(W\right)$, as a function of the excitation pathway j, has the form of

$$f_j(W) = \begin{cases} f_j^0 \sqrt{\alpha_j/\pi} e^{[-\alpha_j (W-w_j)^2]}, & \text{if } j = \widetilde{A}^1 B_1,\ \widetilde{B}^1 A_1 \\ f_j^0 \alpha_j e^x / \left(1+e^x\right)^2, & \text{otherwise} \end{cases} \tag{5.17}$$

where $x = \alpha_j(W - w_j)$ and f_j^0, α_j, w_j are parameters with their values summarized in Table 5.2. Under the assumption that the proton only loses a small portion of its kinetic energy to excite a water molecule, i.e. $\frac{W}{E_k} \ll 1$, Equation (5.15) can be used to calculate the total cross section for excitation channel j as

$$\sigma_j^{exc} = \int_{W_{min}}^{W_{max}} \frac{d\sigma_j^{exc}}{dW} dW. \tag{5.18}$$

In principle, the upper and lower boundaries of the integration can be E_k and 0. However, in practical usage, it is common to set $W_{max} = 50\ eV$ and $W_{min} = 2\ eV$. The reason is that $\frac{d\sigma_j^{exc}}{dW}(W)$ drops to a negligible value when $W \notin [W_{min},\ W_{max}]$ and the boundary cutoffs also assures a positive and convergent integrated total cross section.

Table 5.2. parameters used in Equations (5.17).

j	$\widetilde{A}^1 B_1$	$\widetilde{B}^1 A_1$	plasma mode
f_j^0	0.0187	0.0157	0.7843
α_j	3 (eV^{-2})	1 (eV^{-2})	0.6 (eV^{-1})
w_j	8.4	10.1	21.3

When a proton's energy is smaller than 500 keV, Born approximation is no longer a good approximation [265] and Equation (5.15) may have problem in evaluating the cross sections. We then applied the semi-empirical model [265] to obtain the excitation cross section for a low energy proton as

$$\sigma_j^{exc}(E_k) = \frac{\sigma_0 (Za)^{\Omega} (E_k - E_j)^v}{J^{\Omega+v} + E_k^{\Omega+v}}. \tag{5.19}$$

Here, j denotes the excitation channels $\widetilde{A}^1B_1$, $\widetilde{B}^1A_1$, Ryd A+B, Ryd C+D and diffusion band. The corresponding energy loss E_j of the proton is discrete instead of continuum. Further details of the model can be referred from [265].

With the excitation cross section given in Equation (5.18) and relevant parameters determined, we could integrate it numerically to obtain the excitation cross section table for different sub-shells of a water molecule at proton energies above 500 keV. Meanwhile, we could rely on Equation (5.19) to handle protons with energies below 500 keV. To make the cross section data computed from the two models smoothly connected at the proton energy of 500 keV, we adjusted the obtained cross section data as follows. We applied coefficients of 1.23 and 3.5 to the cross section data for $\widetilde{A}^1B_1$ and $\widetilde{B}^1A_1$ channels obtained from Equation (5.18) to make them smoothly connected to that obtained from Equation (5.19) at 500 keV for these two modes. We then multiplied 0.339 to the plasma mode to make the total cross section also smoothly connected. Similar to the strategy applied to obtain the ionization cross section table, we also only needed to compute the excitation cross section table once and stored it in a data file. Its usage on GPU was also given in subsection 5.2.3.1.

5.2.1.3 Charge effect

When charge particles travel through a water medium, except for ionizing or exciting the water molecule, it could also drag electrons from the medium to move with it, forming a reduced effective charge $Z_{\text{eff}} < Z$. This effect is found reversely proportional to the kinetic energy of the incident particle. In our simulation, we adopted the empirical Booth's model [266] to obtain the effective charge Z_{eff} as:

$$Z_{\text{eff}} = Z\left(1 - \exp\left[-1.316y + 0.112y^2 - 0.065y^3\right]\right), \tag{5.20}$$

where $y = 100Z^{-2/3}\sqrt{1-(1+E_k/(AMc^2))^{-2}}$ and A is the mass number of the particle. The correction is larger than 5% ($Z_{\text{eff}} < 0.95 \bullet Z$) when $y < 2.172$, which gives $E_k \sim 18\ MeV$ per nucleon for Fe ion and $0.22\ MeV$ for proton.

5.2.1.4 Cross section for heavy ions

Within the first-order plane wave Born approximation, we could correlate the ionization and excitation cross section for bare and sufficiently fast heavy ions to that of proton by the scaling law. Specifically, for a heavy ion with velocity u and charge number Z, the doubly differential cross section can be scaled from that of proton with same velocity u by a factor Z^2 [267]

$$\frac{d^2\sigma_{ion}}{dWdQ}(u) = Z^2 \times \frac{d^2\sigma_{proton}}{dWdQ}(u), \tag{5.21}$$

where W and Q refer to the energy transfer and the recoil energy, respectively. After integrating over Q, we could obtain the SDCS as a function of W. Considering that an ion of mass number A and kinetic energy E_k had the same velocity with a proton of kinetic energy $E_{k,p} = E_k\frac{M}{M_{ion}} \approx \frac{E_k}{A}$, we could rewrite the scaling formula as a function of E_k as

$$\frac{d\sigma_{ion}}{dW}(E_k) = Z^2 \times \frac{d\sigma_{proton}}{dW}(E_k/A), \tag{5.22}$$

It holds for ions at both non-relativistic and relativistic formats. The electron attachment effect can be more significant for a heavy ion than for a proton of the same velocity since a heavy ion typically carries more charges than a proton. With the electron attachment effect considered, we replaced Z with Z_{eff} when scaling the

cross section from proton to a heavy ion using equation (5.22), with Z_{eff} calculated from Equation (5.20).

5.2.2 Concurrent transport method

Due to the computational challenge, existing MC tools computed the DNA damage formed by radical attachment typically via two successive steps. First, the radicals were diffused and mutually reacted in the chemical stage without DNA. Second, the coordinates of $OH^{\cdot}$ radicals obtained at the end of the chemical stage were overlapped with DNA geometry such that DNA damages caused by radicals could be computed [52, 259]. We referred this approach as the "overlay method". This approach is effective for simple applications. However, it can be problematic for those scenarios sensitive to radical evolution. In reality, DNA could be present and react with radicals during the radical diffusion. This could affect the radical yields and the damage site distribution on the DNA chain, consequently impacting the final characterization of the DNA strand breaks. To model this effect, in this work, we included the simulation of the reactions between radicals and DNA at the time of transporting the radicals in the chemical stage and referred this approach as the "concurrent transport method".

In our previous development of gMicroMC without considering DNA in the chemical stage, we simulated the diffusion and reactions among radicals in a step-by-step fashion. The relevant parameters are the diffusion coefficient for each radical species and the reaction rates for possible radical-radical reaction types. To include DNA into this transport frame, we need to know the diffusion coefficient of DNA and the reaction rates between radicals and DNA. Considering the relatively large mass of DNA, we assumed that the whole DNA was static during the chemical transport and took its diffusion coefficient as 0 to simplify the simulation. As for the reaction

rates between radicals and DNA, we considered two types of reactions based on the DNA model for a whole lymphocyte cell nucleus [52]. The DNA was described in a voxel-based format with each voxel of side length 55 nm. The voxel is either empty or filled with a DNA chain that connects two faces of the voxel. The DNA chain consists of a group of spheres representing the basic structures of the DNA: the base pair, sugar-phosphate group and histone protein. With it, we considered the first reaction type as the damaging effect of $OH^{\cdot}$ and e_h radicals on the DNA bases and sugar-phosphate groups. The reaction rates were listed in Table 5.3. Here, although there were four types of DNA bases, that is adenine (A), guanine (G), cytosine (C) and thymine (T) bases, associated with four different reaction rates with $OH^{\cdot}$ or e_h radical, we used the average reaction rate in our simulation since our DNA model had no differentiation among the base types. The second type was the scavenging reaction for all radical species by the histone protein. In this reaction, the radical was assumed to be fully absorbed once it was within the histone protein volume.

Table 5.3. Reaction rates ($\times 10^9$ $L \bullet mol^{-1} \bullet s^{-1}$) used in gMicroMC for concurrent DNA transport [271].

Radicals	**A**	**G**	**C**	**T**	**DNA base**	**DNA sugar-phosphate group**
$OH^{\cdot}$	6.1	9.2	6.4	6.1	6.95	1.9
e_h	9	14	18	13	13.5	-1^*

* Negative value means no reaction between the radical and the DNA sub-structure.

After introducing DNA into the chemical stage simulation, two consequences required special attention. First, radicals were not supposed to be produced inside the DNA region, hence at the beginning of the chemical stage, we needed to exclude those radicals produced inside the chromatin zone from the subsequent diffusion [240]

without recording any damages on DNA. Second, as there were a huge number of DNA basic structures in our DNA model, for instance, 6.2×10^9 base pairs, the checking for reactions between radicals and DNA after each diffusion step would generate numerous computations. To circumvent the problem, we defined a time interval t_i to control the frequency to check for reactions between radicals and DNA. During the simulation of the chemical stage, as the time evolution occurred, we only checked for radical-DNA reactions every t_i. In the limit of a small t_i, the frequent inspection for reactions ensures simulation accuracy. In the other extreme of a large t_i, the DNA related reactions will be less frequently checked, which eventually converged to the overlay picture. We studied the impact of t_i in later sections.

5.2.3 GPU implementation

5.2.3.1 Physical transport for protons and heavy ions

Before transporting protons and heavy ions on GPU, we prepared lookup tables on CPU host to store the tabulated cross sections for a proton as stated in sections 5.2.1. The lookup tables were then transferred to GPU texture memory such that we could employ the GPU built-in fast interpolation technique to obtain cross section data for particle transport. We supported two types of source particle generations: reading from a Phase Space File (PSF) or sampling from a given distribution. We sorted the source particles in a descending order based on their charge number Z. If the particles were protons or heavy ions, we transported the sorted particles in groups using the GPU kernel we developed in this work dedicating for proton and heavy ion transport. If they were electrons, we transported them with our previously developed kernel for electron transport [52]. The purpose of particle sorting

and grouping was to minimize the thread divergence on GPU and hence to improve simulation efficiency[53, 54].

For the GPU kernel in charge of the transport of protons and heavy ions, each thread takes care of one primary particle. For a particle with charge number Z, atomic mass number A and incident energy E_k, the thread sampled its free travel distance s in water and its interaction with the water molecules in iteration. Specifically, we first calculated the effective charge number Z_{eff} according to Equation (5.20) and the kinetic energy $E_p = \frac{E_k}{A}$ for proton with the same velocity as that of the primary particle. Based on the logarithmic value of E_p, we interpolated the lookup tables to obtain the cross section $\sigma_i(E_p)$ for proton. Here, i represented all ionization and excitation channels listed in the tables. We then scaled and summed σ_i to obtain the total cross section for the primary particle as $\sigma_t = Z_{\text{eff}}^2 \sum \sigma_i$ based on Equation (5.22). With σ_t, we sampled the free travel distance s in water as $s = -\frac{M_w}{\rho \bullet \sigma_t \bullet N_A} \ln \zeta$, where ρ and M_w are the density and atomic mass of water. N_A is the Avogadro constant and ζ is a random number uniformly distributed between 0 and 1. We forwarded the particle position by s along the momentum direction followed by a sampling of the interaction type based on the relative cross section distribution $\frac{\sigma_i}{\sum \sigma_j}$.

If the sampled interaction i_0 was an ionization event, we then sampled the energy E_e and the emission angle of the ejected secondary electron, along with updating the kinetic energy of the primary particle. Noticing that the partial SDCS in Equation (5.1) had the form of $\frac{d\sigma_i^{ion}}{dw} \propto f(w)\,\phi(w)$, with $f(w) = (F_1(\nu) + wF_2(\nu))/(1+w)^3$ that was relatively easy to integrate and $\phi(w) = 1/(1+\exp[\alpha(w-w_i)/\nu])$, we took $f(w)$ as a sampling function and $\phi(w)$ as the rejection function to effectively sample E_e. Specifically, for a given proton energy E_p, ν can be solely determined based on Equation (5.11) and hence $F_1(\nu)$ and $F_2(\nu)$ are just numbers. We wrote them as

F_1 and F_2 for simplicity in the following equations. Applying the direct inversion method, we could sample w_s from $f(w)$ as

$$w_s = (-F_1 + 2N_c\zeta + \sqrt{F_1^2 + 2F_2N_c\zeta - 2F_1N_c\zeta})/(F_1 + F_2 - 2N_c\zeta). \tag{5.23}$$

Here, $\zeta \in [0,\ 1)$ is a randomly sampled number and N_c has the form of

$$N_c = \int_0^{w_m} f\,(w)\,dw = (w_m\,(F_2w_m + 2F_1 + F_1w_m))/(2\,(1 + w_m)^2). \tag{5.24}$$

We repeatedly sampled w_s with Equation (5.23) and updated $\phi(w_s)$ until we obtained $\phi(w_s) > \zeta'$ with ζ' a random number $\in [0,\ 1/(1 + e^{-\alpha w_i/v})]$. Once reaching this stopping criteria, we accepted w_s and computed E_e as

$$E_e = w_s * B_{i_0}. \tag{5.25}$$

The polar scattering angle θ_e of the electron relative to the moving direction of the primary particle satisfied $\cos\theta_e = \sqrt{\frac{E_e}{4*T}}$ for $E_e > B_{i_0}$ and uniformly distributed between 0 and π otherwise [**cobut1998monte**]. The azimuth scattering angle was uniformly sampled between 0 and 2π. The residual energy of the primary particle after ionization was $E'_k = E_k - E_e - B_{i_0}$ and its polar scattering angle was 0.

If the sampled interaction i_0 belonged to the excitation category, there was no secondary electron emission and we only needed to sample the energy loss W of the primary particle. In this case, the polar scattering angle for the primary particle was 0 as well. When $E_p > 500$ keV, we sampled W based on Equation (5.15). Noticing that $\frac{d\sigma_{i_0}^{exc}}{dW} \propto f_{i_0}\,(W)\,g(W)$, where $g\,(W) = \frac{1}{W}ln(\frac{4T}{W})$, we then used $f_{i_0}(W)$ for the sampling of W and $g(W)$ for rejection. For $\widetilde{A}^1B_1$ and $\widetilde{B}^1A_1$ channels, W_s can be directly sampled as

$$W_s = w_{i_0} + \frac{1}{\sqrt{2\alpha_{i_0}}}\zeta_n, \tag{5.26}$$

where ζ_n is a random number following the standard normal distribution. As for the plasma mode, we applied the direct inversion method to get W_s as

$$W_s = w_{i_0} + \frac{1}{\alpha_{i_0}} \ln\left(\frac{u_1}{1 - \alpha_{i_0} u_1 N_c \zeta} - 1\right). \tag{5.27}$$

Here ζ is a random number $\in [0,\ 1)$ and N_c has the form of

$$N_c = \int_{W_{min}}^{W_{max}} f_{i_0}(W)\, dW = \frac{1}{\alpha_{i_0}} \left(\frac{1}{u_1} - \frac{1}{u_2}\right), \tag{5.28}$$

with $u_1 = 1 + e^{\alpha_{i_0}(W_{min} - w_{i_0})}$ and $u_2 = 1 + e^{\alpha_{i_0}(W_{max} - w_{i_0})}$. We repeated the sampling of W_s and updating $g(W_s)$ until obtaining $g(W_s) > \zeta'$ with ζ' a random number $\in [0, \frac{1}{W_{min}} \ln\left(\frac{4T}{W_{min}}\right)]$. The residual energy of the primary particle after excitation is then $E'_k = E_k - W_s$. When $E_p \leq 500$ keV, the energy loss E_{i_0} was directly obtainable from the discrete energy spectrum[267]. The residual energy of the primary particle was then $E'_k = E_k - E_{i_0}$.

After transporting the primary particle with one step and simulating its interaction with one water molecule, we updated E_k with E'_k and started the next round of transport sampling until the kinetic energy of primary particle reached cutoff energy or ran out of the simulation region. During the process, all secondary electrons were stored in a global stack to be further simulated using our previously developed kernel in charge of electron transport, the physics models in which covered the electron spectrum as low as a few eV [52]. The ionized and excited water molecules were also tagged for further analysis.

5.2.3.2 Concurrent transport

In the concurrent transport picture, we simulated the reactions among radicals and DNA and the diffusion of the radicals in a step-by-step manner. Considering the complex structure of DNA and the possibly different checking frequencies for radical-DNA interactions and radical-radical reactions depending on the value of t_i, we utilized two GPU kernels for the chemical stage transport at the presence of DNA. One GPU kernel is responsible for the interactions between radicals and DNA, and the other kernel is in charge of the radical-radical reactions and the diffusion of the radicals.

For the GPU kernel managing the reactions between radicals and DNA, each GPU thread is responsible for one radical. To obtain the possible reaction and reaction type between the radical and DNA, we needed to search the DNA geometry and compute the distances from the radical to the centers of DNA basic structures (DNA base, sugar-phosphate group and histone protein). The smallest distance d_{min} was then compared to the reaction range of $R + R_c$ with R the radius of that DNA structure. $R_c = k/4\pi N_A D$ for reactions between the radical and DNA base or sugar-phosphate group, where k is the reaction rate, N_A is the Avogadro constant and D is the diffusion rate for the radical. For all considered radical species, R_c was < 1 nm. Due to the lack of experimental data for the reaction between radicals and histone protein, we assumed that the radical was only absorbed when it hit the histone and hence set $R_c = 0$ for this case. If $d_{min} < R + R_c$, a reaction was recorded. Otherwise, the Brownian bridge method [52] was applied to compensate for possible reactions between radical and DNA during the diffusion. As our DNA model was constructed with a huge amount of the basic structures, it would be too time consuming to search the entire space to obtain the smallest distance from radical to DNA. To reduce the

searching burden, we relied on the voxelized geometry of the DNA model and only performed the search at most in two voxels. Specifically, noticing that the outer boundary of the DNA chain was ¿ 2 nm away from all edges of the voxel it occupied [52] and $R_c < 1$ nm for all reactions between radical and DNA, it indicated that a radical was only possible to react with those DNA structures in two special voxels: the current voxel it located and the adjacent voxel having the surface closest to it. The latter voxel was not considered unless the radical was < 2 nm from its closest surface. In this way, we reduced the searching burden significantly. Once a reaction was recorded, the radical was removed from the reactant list. If the reaction was with the DNA base or sugar-phosphate group, the reaction site was stored in a global stack for further analysis.

For the radical-radical reactions and radical diffusion, we continued to employ the GPU kernel developed in our previous work [52]. Each thread is in charge of one radical. To reduce the searching burden for mutual reactions, the entire space was divided into small grids with the grid size twice the largest reaction radius. It ensures that each radical only reacted with other radicals in the same or adjacent grids. The distances from the radical to other radicals were then computed and compared to the reaction radii to obtain whether a reaction would occur. If a reaction happened, the new products were placed and radical-radical reactions were checked again. Otherwise, the radical was diffused by one step followed by the check for radical-radical reactions based on the Brownian bridge method.

At the beginning of the chemical stage, the GPU kernel for the DNA-radical reactions was executed to remove the radicals within the chromatin region from subsequent chemical stage simulation. It was followed by the launch of the GPU kernel in charge of the radical-radical reaction and radical diffusion. After that, we compared t_{elap}, the time elapsed from the last execution of the former GPU kernel, to t_i. If

$t_{\text{elap}} \geq t_i$, the former and latter kernels were called in sequence. Otherwise, only the latter kernel was executed. The process was repeated until reaching the end of the chemical stage.

5.2.4 Simulation setup

5.2.4.1 Simulation setup for transport of protons and heavy ions

We performed a series of simulations to validate the physical stage transport for proton and heavy ions. These include 1) the computations of the cross section, linear energy transfer (LET) and traveling range, 2) the validation of the energy spectrum of secondary electrons, the radial dose distribution and the track structure and 3) the evaluation of the DNA damage spectrum.

We first calculated the total cross section for both ionization and excitation channels according to Equations (5.8) and (5.18), under the relativistic formats. The results were compared to Plante *et. al.*'s [264] and Dingfelder *et. al.*'s [265] works, as shown in Figure 5.1. Based on it, we calculated the track-length-averaged unrestricted LET for different ion species with their energy ranging from $0.1 \sim 10^4$ MeV amu^{-1}. For an ion with energy E_k, we sampled the energy loss of primary particles ε_i and the free-fly distance s_i. We then repeated the simulation for $N = 10^5$ times, computed the length-averaged unrestricted LET as

$$LET = \sum_{i=1}^{N} \frac{\varepsilon_i}{s_i} \bullet \frac{s_i}{\sum_{j=1}^{N} s_j} = \frac{\sum_{i=1}^{N} \varepsilon_i}{\sum_{j=1}^{N} s_j}. \tag{5.29}$$

We compared the LETs to those reported by Plante *et. al.* [264]. After that, we simulated the proton range by tracking its starting and ending positions for proton energy of $0.1 \sim 100$ MeV and compared to NIST data. We showed both results in Figure 5.2.

As for the validation of the energy spectrum of secondary electrons, we simulated the interactions of 5 MeV proton and 4 MeV alpha particles with liquid water target, recorded the energy of the secondary electrons, and compared to those obtained with GEANT4-DNA simulation [234] (GEANT4 version 10.5.1). The result was plotted in Figure 5.3. As for the radial dose distribution, we transported 5 and 10 MeV protons within a water slab of 10 μm thick and infinitely long at the other two dimensions, and analyzed the dose distribution within a thin slice 4 to 6 μm away from the proton starting point along the thickness direction. We accounted the dose distributed in an annular ring with inner and outer radii of r and $r + \Delta r$ as dose at radius r. We set $\Delta r = 1\ nm$, same as that used in Wang *et. al.*'s work [272]. We repeated the simulation for 10^5 times, averaged the obtained radial dose and compared with that reported in Wang *et. al.*'s work [272]. Finally, we showed a representative physical track structure for a 5 MeV proton in Figure 5.5, including the track for both primary proton and secondary electrons.

We used the lymphocyte nucleus model developed in our previous work for this evaluation study [52]. We initiated a proton emission plane of $11 \times 11\ \mu m^2$ and 5.5 μm away from the center of the cell nucleus for two proton energies, 0.5 and 0.9 MeV. For each energy, we randomly sampled the proton position at the emission plane and its momentum towards positive z direction, transported the proton until reaching a cutoff energy of 1 keV and recorded the dose inside the cell nucleus. We repeated the simulation until reaching the accumulated dose of 2 Gy. After that, we simulated the physio-chemical and chemical stage with the chemical stage duration $t_c = 1\ ns$. We then applied the overlay method to obtain the DNA damage sites and grouped them into DNA single strand break (SSB) and double strand break (DSB)[259]. The result was compared to Nikjoo *et. al.*'s work with KURBUC model [273] and shown in Table 5.4.

5.2.4.2 Simulation setup for concurrent transport

We studied the impact of t_i on the radical yields. We simulated the cases with chemical stage duration t_c = 1, 10 ns and 1 μs, and t_i from 1 ps to 1 μs with an increment of 1 at the logarithmic 10 scale. Again, the lymphocyte cell nucleus with radius 5.5 μm was used as the region of interest (ROI). As for the radical yielding, we transported a 4.5 keV electron with its initial position randomly sampled inside the ROI and its direction towards the ROI center. We then took the generated radicals as inputs for the chemical stage simulation. The final G values for e_h, $OH^{\cdot}$, $H^{\cdot}$ and H_2O_2 radicals were recorded. We repeated the simulation for 100 times to reduce statistical uncertainties and reported the averaged G values over all simulations. The results were shown in Figure 5.6.

We also computed the DNA damage as a function of the incident proton energy and the chemical stage duration under the concurrent DNA transport frame. Proton energy E_k of 0.5, 0.6, 0.8, 1.0, 1.5, 2, 5 10, 20 and 50 MeV and chemical stage duration t_c of 1, 2.5 and 10 ns were considered, following the parameters used in Zhu *et. al.*'s work [240]. We initiated the proton on a spherical shell with a radius of 5.5 μm and shot it randomly towards the inner space of the sphere. We repeated the simulation until having the accumulated dose in the sphere of 1 Gy. We then simulated the chemical stage with DNA concurrent transport (t_i = 1 ps) and computed the total DSB yield. For each proton energy, using DSB yield at t_c = 1 ns as a reference, we defined $R(t) = N_{DSB}(t_c = t)/N_{DSB}(t_c = 1\ ns)$ to represent the relative DSB yields at $t_c = t$. For each pair of E_k and t_c, we ran the simulation for 20 times and computed the mean and standard deviation for the relative DSB yield. We then compared the data with t_c = 2.5 ns (R(2.5)) and 10 ns (R(10)) to Zhu *et. al.*'s work [240] and showed the results in Figure 5.7.

5.3 Results

5.3.1 Validation of development for protons and heavy ions

Figure 5.1 presented the total and partial cross sections for ionization and excitation as a function of incident proton energy. From Figure 5.1(a), the total cross section for ionization from our simulation agreed well with that from Plante *et. al.*'s work [264]. From Figure 5.1(b), for proton energy > 500 keV, our simulated total cross section for excitation matched that from Plante *et. al.*'s work [264]. As for the slow proton, it followed that from Dingfelder *et. al.*'s work [**dingfelder2000inelastic**]. The results revealed that the ionization model and the two-stage excitation model was successfully implemented as expected.

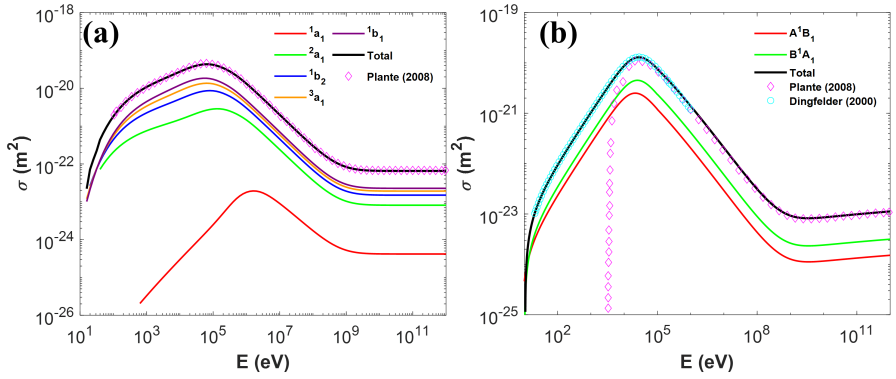

Figure 5.1. Total and partial cross sections of (**a**) ionization and (**b**) excitation channels for protons with different energies..

In Figure 5.1(b), we noticed a dramatic drop-off of the total excitation cross-section at around 10 keV for the Plante model. This is due to that the cross section formula shown in Equation (5.15) depends on the scaled energy $T = \frac{m}{M}E_k$. When E_k drops below 10 keV, T is too small to excite even the lowest excitation channel ($j = \widetilde{A}^1B_1$) . After replacing it with the Dingfelder's model (Equation (5.19)) at the

low energy region, excitation cross section drops much slower. Considering that the low energy proton largely appears after the Bragg peak, a proper excitation model could be important for the distal dose computation in proton therapy.

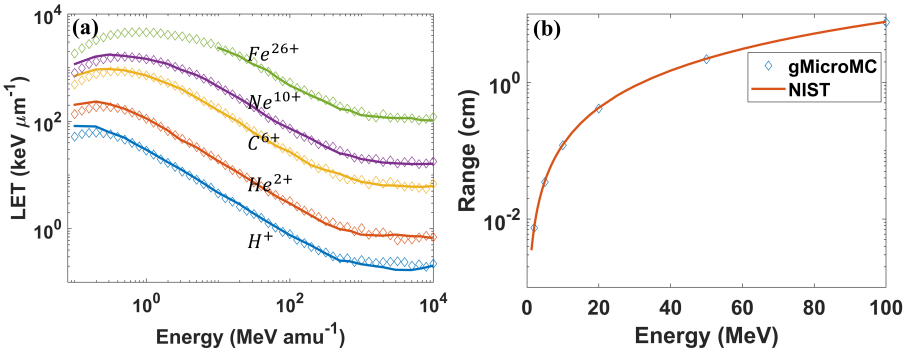

Figure 5.2. (**a**) The unrestricted LET for different ions with different energies. The unit amu^{-1} means per nucleon. Solid lines represent data extracted from Plante *et. al.*'s work while data with diamond symbol are from our simulation with gMicroMC. (**b**) The simulated proton range for different energies..

The calculated unrestricted LET for different ions were plotted in Figure 5.2(a). They agreed well with Plante *et. al.*'s work for ions with energy larger than 0.5 MeV per nucleon. At the low energy range, LETs from our simulation are lower than that from Plante *et. al.*'s work, which can be explained by the different excitation models used in the two simulations. As shown in Figure 5.1(b), the excitation cross section from our work was higher than that from Plante *et. al.*'s work at the low energy range, resulting in a higher sampling rate of excitation interactions in our simulation. Considering that the energy loss from an excitation event was typically smaller than that from an ionization event (Table 5.1), a higher sampling of excitation could result in a lower LET. In Figure 5.2(b), we showed the proton range from our simulation and its comparison with NIST data. As is shown, our simulation result matched well with

NIST PSTAR data (https://physics.nist.gov/PhysRefData/Star/Text/PSTAR.html) with the relative difference smaller than 1%.

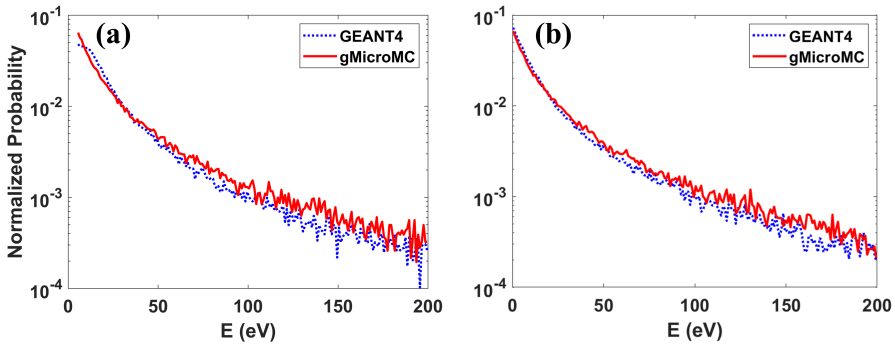

Figure 5.3. Secondary electron spectrum for (**a**) 5 MeV proton (**b**) 4 MeV alpha particle..

Figure 5.3 shows the energy spectrum of secondary electrons generated from 5 MeV proton and 4 MeV alpha particle. From the figure, the yielding rates of secondary electrons drop quickly along with the increase of the electron energy. For the entire plotting, our simulated results agreed well with that from GEANT4-DNA. We didn't compare the spectrum for electron energy larger than 200 eV due to a too low yielding rate and a consequent large uncertainty.

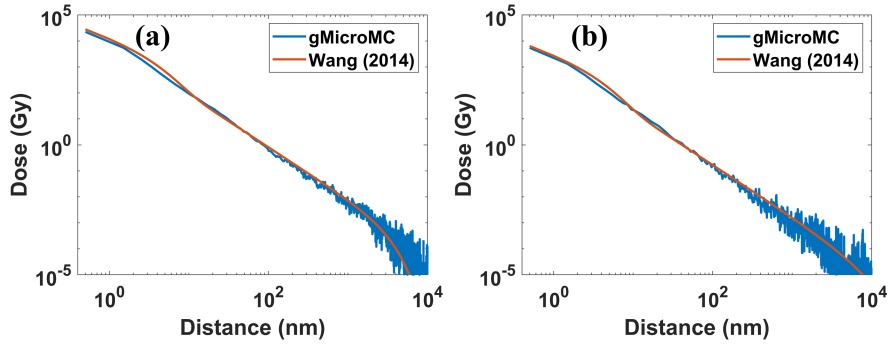

Figure 5.4. Radial dose distributions for (**a**) 10 MeV (**b**) 50 MeV protons..

In Figure 5.4, we see the radial dose distributions for 10 and 50 MeV protons from our and Wang *et. al.*'s work (Equations (1)-(7) in [272]) under a same setup. As is shown, the two curves matched quite well, although the curve from our simulation suffered a relatively large statistical fluctuation for the regions ¿ 1000 nm from the primary track axis. Figures 5.3 and 5.4 together validated the energy spectrum and angular distribution of secondary electrons from our simulation, furthering proving the successful implementation of the transport models for proton and heavy ions.

We then presented a track structure for a 5 MeV primary proton and its produced secondary electrons in liquid water in Figure 5.5. For simplicity, we only presented the entrance (Figure 5.5(a)) and Bragg peak (Figure 5.5(b)) regions. At the entrance region, the secondary electron tracks are quite sparse. In contrast, they are much denser at the Bragg peak region. In addition, the electron track lengths are shorter at the Bragg peak region. This is mainly due to that the kinetic energy of the proton is much higher at the entrance than the Bragg peak region. It leads to smaller total cross section and longer interval between the production of secondary electrons. Plus, high energy electrons (Equation (5.23)) would be favored when the proton energy is high. In general, most of the electrons travel a tiny distance before locally deposited, forming the dense blue area around the central proton line and hence a high radial dose distribution at the regions with small radii (Figure 5.4).

Finally, in Table 5.4 we reported the DNA damages in the form of DSBs induced by 0.5 and 0.9 MeV protons. The results from our simulation were compared with that from Nikjoo *et. al.*'s work with KURBUC model [273]. The difference was found within 10%.

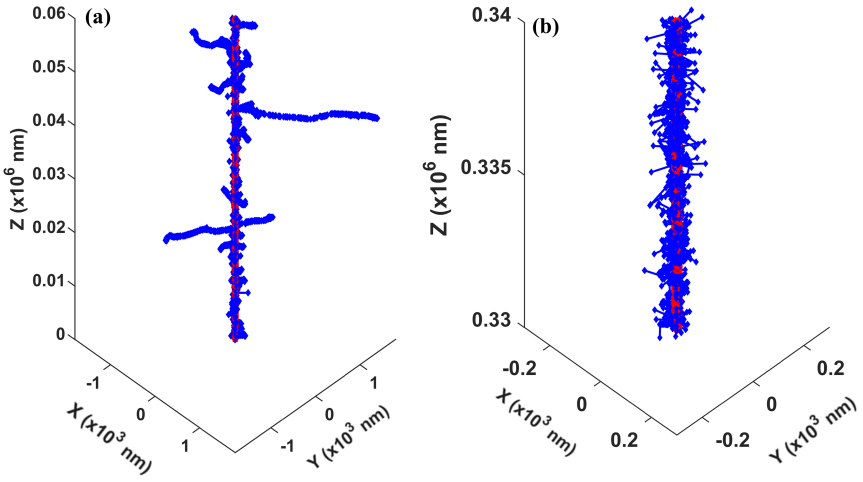

Figure 5.5. A representative track structure for a 5 MeV proton at the entrance part (**a**) and the Bragg peak region (**b**). The proton was emitted along positive Z direction. Red and blue dots represent the energy depositions by the proton and secondary electrons, respectively. Note: in the two subplots, we kept the same aspect ratio between z and x/y axes but plotted with different ranges..

5.3.2 Validation of the concurrent transport

As for the validation of the concurrent DNA transport module, we first studied the influence of different checking time interval t_i and chemical stage duration t_c on the yields of different radicals. As shown in Figure 5.6, at a fixed t_i, the yields of e_h and $OH^{\cdot}$ radicals reduced when t_c increased. This is because longer t_c enabled more reactions among radicals and DNA. For e_h and $OH^{\cdot}$radicals, these reactions

Table 5.4. The DSB yields (number per Gy per Gbp) obtained under the overlay method for two proton energies.

Energy (MeV)	from gMicroMC	from Nikjoo's work
0.9	20.1	18.2
0.5	25.1	23.9

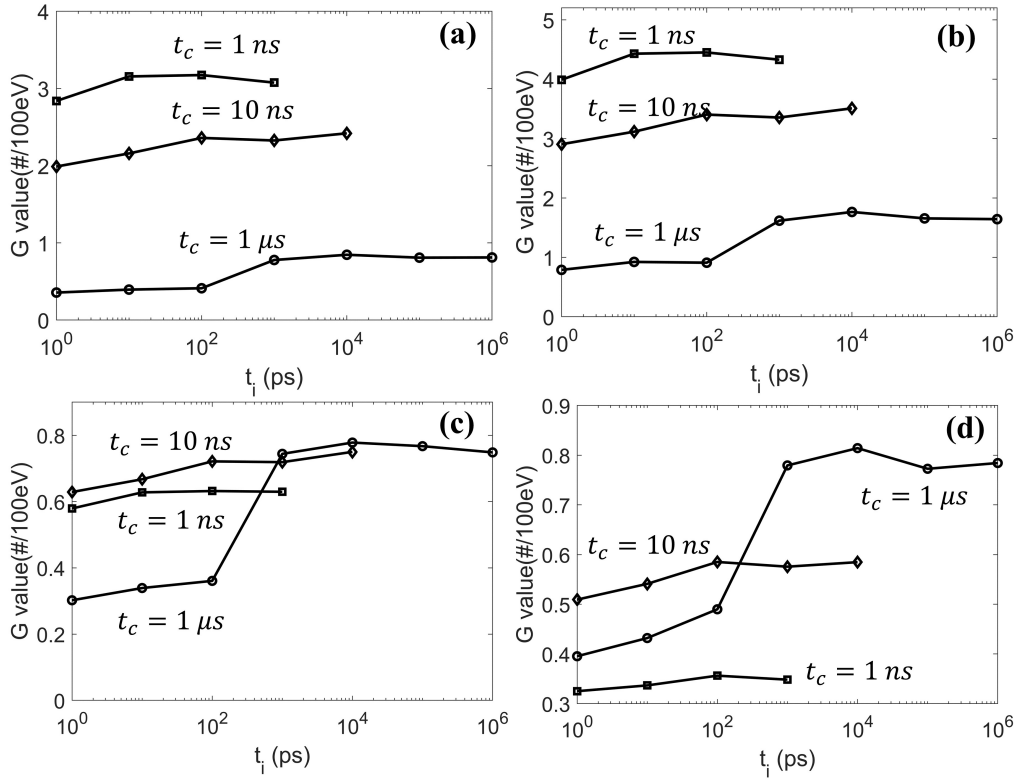

Figure 5.6. The yields of (**a**) e_h (**b**) $OH^{\cdot}$ (**c**) $H^{\cdot}$ and (**d**) H_2O_2 chemical species at different checking time intervals t_i and chemical stage duration t_c..

were mainly consumption channels, resulting in a reduced yielding rate when t_c increased. In contrast, although the presence of DNA also consumed $H^{\cdot}$ and H_2O_2 radicals, reactions among radicals could contribute positively to the yields of these two radicals. Hence, the production of $H^{\cdot}$ and H_2O_2 radicals could be dependent on t_c in a more complex way. In addition, at a fixed t_c, varying t_i from $1ps$ to t_c transforms the simulation from the concurrent method to the overlay method. All lines were connected smoothly and the G value with $t_i = t_c$ matched with that in our previous publication under overlay method, indicating the self-consistence of the concurrent DNA transport in gMicroMC.

After examining the self-consistence of the developed concurrent DNA transport method, we comprehensively studied the DSB yields as a function of proton energies E_k and chemical stage duration t_c. The results were compared to Zhu *et. al.*'s work [240] and shown in Figure 5.7. From the figure, all data points have relative DSB yields ¿1 and R(10) values are larger than R(2.5) for same E_k. This indicates the DSB yields increase when the chemical stage expands from 1 ns to 10 ns under the concurrent transport frame. The reason is that the longer the chemical stage lasted, the more checks between radicals and DNA were performed, and hence the more DSBs could be formed. Along with the increase of the proton energy, the relative DSB yields exhibit maximum in the middle energy range. Compared the data from our simulation to that from Zhu *et. al.*'s work, the trends generally agree, especially for the R(2.5) data. Some larger discrepancies exist for R(10) values, which could be explained partially by the different radical diffusion rates and different DNA geometries applied in the two works. For example, the diffusion rate of $OH^{\cdot}$ radical is larger in our package. It could make the $OH^{\cdot}$ diffuse longer and experience a higher scavenge rate from the histone protein within one diffusion step. In addition, a larger diffusion rate could result in a smaller reaction radius between $OH^{\cdot}$ and DNA sugar phosphate moiety. Both led to a reduced DSB yield. The longer the t_c is, the more reduction effect it could create, such that we would get a smaller relative DSB yield than that from Zhu *et. al.*'s work for the R(10) data than for the R(2.5) data.

5.3.3 Computational efficiency

After evaluating the two newly developed features of gMicroMC by comparing to NIST data or simulation results from other packages, it is important to evaluate the time performance of the new modules for practical applications. In Table 5.5, we showed the simulation time for the physical transport of 1, 10 and 100 protons

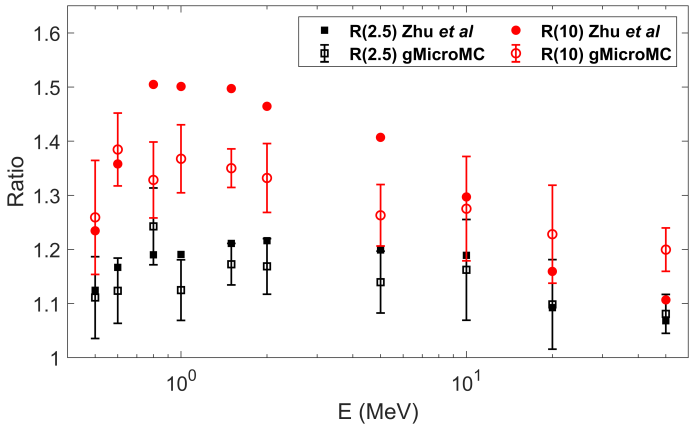

Figure 5.7. The relative DSB yields at different chemical stage durations t_c and different proton energies with $R(t) = \frac{DSB(t_c=t)}{DSB(t_c=1\ ns)}$. The data from gMicroMC simulation were compared to that from Zhu et. al.'s work [240]..

at 1 and 10 MeV with gMicroMC on a single GPU card (Nvidia V100). As can be seen, it only takes 2 and 4 seconds to transport a single proton with initial kinetic energy of 1 and 10 MeV. In contrast, it could take multiple hundreds to thousands of seconds to perform similar simulations with single-CPU based packages, showing the high efficiency of gMicroMC. It is also important to point out that when raising the proton numbers from 1 to 100, the simulation time only increased by ¡ 5 and 10 folds for 1 and 10 MeV proton, respectively. This feature is against the linearly increasing behavior for typically CPU based simulations, making gMicroMC especially suitable for large-scale simulations. Actually, when the proton number is small, the parallel computing capacity of GPU is far from fulfilled when launching the kernel for primary particle transport, such that increasing the proton number, the running time will not significantly increase.

As for the simulation time of the concurrent transport ($t_i = 1\ ps$) in the chemical stage, it could be affected by many parameters, such as the number of radicals, the chemical stage duration and the DNA complexity. Here we reported the simulation

Table 5.5. The simulation time (seconds) of physically transporting 1, 10 and 100 protons for proton energies at 1 and 10 MeV by gMicroMC on a single GPU card.

Energy (MeV)	Number of primary protons		
	1	10	100
1	1.9	3.1	9.3
10	3.9	9.8	40.5

time for a representative case. Considering that the number of radicals produced from one 100 keV electron or 1 MeV proton is roughly 10^5 and the longest chemical stage duration used in the overlay method is $\sim 1\ \mu s$, we set the initial number of radicals $N_i = 10^5$ and chemical stage duration $t_c = 1\ \mu s$ in our simulation. We have also included our DNA model containing $\sim 6.2 \times 10^9$ bps for a human lymphocyte cell nucleus in the simulation, the complexity of which is high. The simulation time was found 470 seconds with gMicroMC on a single GPU. Compared to the simulation time of 31 seconds under the overlay scheme for gMicroMC, the concurrent transport frame is still quite efficient since the simulation becomes much more sophisticated with the presence of DNA. This indicates that gMicroMC can be applied for simulations with realistic settings. In comparison, restrictions on the reaction region and time duration, etc., were typically required in other packages for memory or time saving purpose [205, 207].

5.4 Discussions

This is a continuous development work of gMicroMC. In this work, we successfully implemented the physical transport for proton and heavy ions, and the concurrent transport of radicals and DNA in the chemical stage. For the former implementation, we considered the ionization, excitation and charge effect during the

transport, and performed a series of case studies to validate the development. The obtained results matched well with literature reports. We then computed the DNA DSBs for two proton energies and the results agreed with that computed with the KURBUC model in Nikjoo *et. al.*'s work [273] within 10%. As for the latter, we considered the interaction of radicals with DNA histone protein, base and sugar-phosphate groups during the chemical transport. To validate it, we first performed a self-consistency check for the evolution of chemical radicals and induced DNA DSBs under different checking frequencies for radical-DNA interactions. The result showed high self-consistency of the developed module. We then did a comprehensive study of the DSB yields as a function of the chemical stage duration and incident particle energies under the DNA concurrent transport frame. The results generally followed that from Zhu *et. al.*'s work. The use of GPU made the code of high computational efficiency. Running gMicroMC on a single GPU card, it takes only 41 s to transport 100 protons with a kinetic energy of 10 MeV and around 8 mins to transport 10^5 radical up to 1 μs with the presence of a DNA model containing $\sim 6.2 \times 10^9$ base pairs. The high computational performance of gMicroMC makes it suitable to simulate complex radiation scenarios like proton FLASH radiotherapy, which is our next step work. To benefit the community, we are also working on to release the newly developed features of gMicroMC on GitHub (https://github.com/utaresearch/gMicroMC) .

Despite of the above success, there are also some limitations in our current development. In the physical transport of protons and heavy ions, we ignored the nuclear inelastic interaction, nuclear and electromagnetic elastic scattering. Among them, the nuclear inelastic interaction can fragment the target and/or projectile nuclei, which is a main factor to remove primaries from the projectile beam. However, due to the complexity of the fragmentation process and its products, this process is typically not directly included in any mechanistic MC simulation tools at this mo-

ment [274]. Since this work mainly focuses on novel GPU implementation of existing models, it will be our next step work for a possible inclusion of the nuclear inelastic scattering process. As for the elastic scattering, it could change the direction of the primaries, hence affect the track structure and radical dose distributions. However, elastic scattering mainly dominants interactions between proton and water medium at very low energy range and the scattering angle is typically small [274, 275]. Hence we expect it will not affect much the accuracy of the DNA damage computation. Considering the powerful computational capacity of GPU, it is promising to consider a more complete modeling of the physical interactions between ions and water molecules, making gMicroMC versatile for advanced applications.

It is also worthy to point out that we applied a low-energy five-pathway model and a high-energy three-pathway model to simulate the proton-induced excitation of a water molecule such that both very low energy and relativistic situations could be covered. Yet, this could cause a concern that some excitation pathways could be discontinuous at the model switching point. A previous study showed that the low-energy model could be extended up to 80 MeV with some proper parameter fitting [264]. We hence made it an option in our package to only apply Equation (5.19) to model the excitation process up to 80 MeV. In addition, for the two-model picture, although we currently set the model switching point at 500 keV to distinguish the slow and fast proton behavior following the same logic as stated in [265], it deserves a further study to investigate its impact on the subsequent radical yielding process.

Another important procedure that could affect the computational accuracy of the proton and heavy ion induced DNA damage was the modeling of the secondary electron transport, especially for the low-energy electrons (sub keV range). Previous studies revealed their critical importance in determining the initial distribution of radicals and the consequent DNA damage patterns [50]. However, due to the lack

of sufficient experimental data, uncertainties on the simulation results could be introduced by the inaccurate modeling of this process. For instance, with different models adopted in gMicroMC and Geant4-DNA, the maximal discrepancies of the track length and penetration depth for electrons below 1 keV computed by the two packages were around 10 and 4 nm, respectively [52]. In recent years, there were a lot of efforts contributing to improve the accuracy of describing the low energy electron transport process [247–251, 276]. However, more efforts are required to fully elucidate this problem.

In addition, as discussed in our previous study [259], the cross section used to simulate the ionization and excitation processes from electrons could significantly impact the accuracy of the finally obtained DSB yields. In the case of proton and heavy ions, due to the lack of experimental data, the cross sections and models could also be associated with large uncertainties, causing concerns for the robustness of the simulation results. To reduce these uncertainties, there have been multiple experiments and models [47, 249, 277–283] developed in a more elaborate fashion. Yet, more studies are needed to more thoroughly understand the relevant processes.

In our previous study [259] with the overlay method, the DSB yields reduced when the chemical stage duration enlarged, which was against the trend obtained in this work with the concurrent DNA transport method (Figure 5.7). This is due to that in the overlay method, the radical-DNA interaction was only simulated after the chemical stage simulation. The longer the chemical stage lasts, the more the $OH\cdot$ radicals were consumed during the mutual radical reactions, and the fewer the DSBs could be formed. Nonetheless, the controversial behavior between the concurrent and overlay frames reminds us to watch carefully about the parameters used in our simulation. One such parameter is the scavenging probability from histone proteins to chemical radicals, the value of which was not well regulated by current

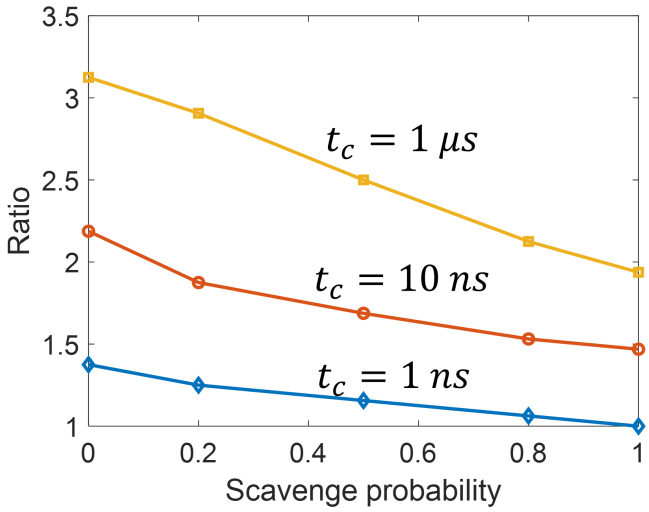

Figure 5.8. Ratio of DSB yields with different scavenge probability..

experiments. We performed a new simulation to study its impact on DSB yield by gradually reducing the scavenging probability P_s from 1 to 0. Here, $P_s = 1$ means total scavenge once radicals hit histone proteins. Taking the DSB yields at $P_s = 1$ and $t_c = 1\ ns$ as reference, we computed the relative DSB yields at other P_s's and t_c's. The results were shown in Figure 5.8. Clearly, DSB yields increased when P_s decreased. However, even under a same P_s, when t_c differs, P_s could have different impacts on the relative DSB yield. For instance, the relative DSB yield was 1.4 for $t_c = 1\ ns$ while it was 3.1 for $t_c = 1\ \mu s$ when $P_s = 0$. It indicated that to make the simulation tool robust for various applications, we need apply a proper cutoff on t_c and a detailed coordination of multiple parameters used in the chemical stage simulation. This should be considered in future studies.

In our development of the concurrent transport module, we used a complete set of cellular DNA at the base-pair resolution to simulate the radical-DNA interactions. Previous studies have incorporated other DNA models, including the simple cylinder DNA [50], other cellular DNAs [181, 233, 240, 284] and DNA model at the

atomic resolution [236, 285]. Due to the different simulation setups and different DNA structures adopted, the absolute DSB yields from different studies were typically non-comparable [286]. However, there were some common trends shared among different studies. For example, the DSB yields were found increasing and then decreasing when the LET increases. The maximal yields of DSB occurred at the LET value around 60 $keV/\mu m$ in [233] and around 27.2 $keV/\mu m$ (LET value for 1 MeV protons [205]) for gMicroMC and TOPAS-nBio, respectively. These consistences motivated further studies with the concurrent simulation scheme while the expense was the lowered simulation efficiency. Our adoption of the GPU-based acceleration could shed light onto this issue upon experiences from previous studies [52, 201, 258, 287].

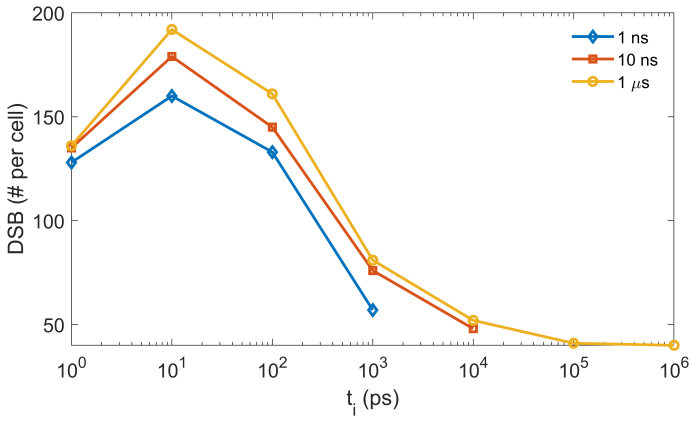

Figure 5.9. The yields of DSB at different t_i and t_c from gMicroMC simulation..

At last, we performed a further study on the effect of t_i, which was introduced to balance the simulation efficiency and accuracy. We have shown the obvious impact of t_i on the radical evolution. It would be interesting to see how it could consequently affect the final DNA damage. As DSB is widely accepted as the most important factor for cell death, it is thus reasonable to use DSB as a metric to evaluate this impact of t_i. We initiated a 4.5 keV electron with its position randomly sampled inside a

sphere of radius 6.1 μm and its direction following isotropic distribution. The sphere was concentric with the cell nucleus of our DNA model. We repeated the simulation until the accumulated dose inside the cell nucleus region reached 1 Gy, equivalent to simulating $\sim$ 2000 electrons. The generated radicals were then transported in the chemical stage with considering the radical-DNA reactions. We calculated the resulted DNA DSBs as a function of t_i and showed it in Figure 5.9. For the three t_c studied, the DSB lines showed similar trend when t_i increased. The maximal DSB was obtained at $t_i = 10\ ps$. The result could be interpreted as follows. At the beginning of the chemical stage, all generated radicals has a relatively dense distribution. When t_i slightly increased, the $OH^{\cdot}$ radical could diffuse a longer distance away from its initial position before it reacted with DNA, while its reaction probability with other radicals was not much affected. Hence, a sparser but equivalent (or slightly reduced) number of DNA damage sites could be formed, which could lead to more generations of simple DSBs (composed of 2 damage sites) rather than DSB+ (composed of multiple damage sites). In this way, the total DSB yields could increase. However, along with the further increase of t_i, the checking frequency for radical-radical reactions would be much higher than that for radical-DNA reactions. This could lead to a higher consumption of $OH^{\cdot}$ radicals through radical-radical reactions than through DNA damaging reactions, which resulted in a reduced DSB yield.

5.5 Conclusions

We have successfully developed and validated two new features in gMicroMC, the transport of proton and heavy ions in the physical stage and the concurrent transport of DNA in the chemical stage. We implemented the two features on the GPU parallel computing platform, resulting in a remarkable time performance. The physical transport of 100 protons with initial kinetic energy of 10 MeV can be finished

in seconds. The chemical simulation with concurrent DNA transport is far more complex, but it still just took a few minutes to run a representative case. The two newly developed features in gMicroMC that is of both high accuracy and efficiency, makes gMicroMC of high promise to solve large-scale problems in active radiation research areas.

CHAPTER 6

APPLICATIONS OF GMICROMC

Starting from this chapter, we will discuss the application of gMicroMC to three scenarios that may be challenging for other MC packages. These studies do not only prove the advantage of computational efficiency of gMicroMC because of utilization of GPU, but also make sense that the improvement of computational efficiency extend our understanding of radio-biology in these scenarios. In this chapter, we discuss the proton damage pattern in a millimeter scale and our attempts to connect the SF with this pattern. We will also discuss the protection effect by hypothermia. This simulation requires a DNA damage simulation up to 40 Gy. In the next chapter (Chapter 7), we will discuss the oxygen effect and oxygen enhancement on DNA damage. This knowledge will then be applied under FLASH condition.

6.1 Pattern analysis of proton damage

6.1.1 Introduction

For many microscopic simulations [50, 205, 207, 240, 288, 289], DNA damage simulation is only done in micrometer scale, i.e. in the cell. The source particles, either electron or proton, merely start from a position inside the cell or near the cell. The energy deposition events inside the cell are used to determined the dose level. Yet, dose is not a good indicator when the volume becomes very small. dose would be divergent if the sampling volume approaches a point from its definition $D = \frac{\Delta E}{\rho \Delta V}$, where ΔE is the energy deposited inside the volume ΔV with density ρ. In other words, while the clinic dose may be smooth in the whole region because it is

measured in a millimeter scale, dose for a small volume suffers from large fluctuation possibly, leading to the mismatch between simulation dose and clinical dose and the invalidity between simulation results and experimental results. The severity of this issue depends on the scale of the volume we are interested and the pattern of energy deposition events. For photon and electron cases, their energy depositions become uniform rapidly even in a scale of cell because their tracks can be bent and it requires a number of tracks to deposit even a few Gy. Yet, since proton and heavy ions basically travel straightly in water medium and secondary electrons from the primary track can only carry energy several μm away, the energy deposition for a proton or heavy ion track is very dense along the track while very sparse just a few μm away from the track. In addition, proton or heavy ions deposit energy very efficiently that the number of primary particles required to deposit same dose for proton or heavy ions is much smaller than that for electron or photon. Hence, only when dose level is large enough could the dose distributions in a scale of micrometer be regarded as uniform. In the following discussion, we then restrict ourselves in proton cases without losing generality to present this issue.

The concentration of energy deposition along the proton track makes us overestimate our simulation doses if we limits ROI to only a cell in the simulation. This overestimation means our results, for example the number of DNA SBs versus simulation dose, need to be shifted to lower doses. Hence, the relationship between derived results, say SF, from DNA damage and simulation dose need to be corrected as well. However, the shift is not the same for different dose levels, which makes the problem complex. Additionally, cells in different positions experience different dose levels because of the inhomogeneity of dose deposition. Hence, any biological endpoints on many cells are an average effect, which makes the comparison between simulation results from one cell further deviated from the experimental truth.

One straightforward way is to capture the fluctuation of energy deposition in analysis by statistical method like what is done in microdosimetry [47]. we could summarize the frequency of deposited energy $f(q)$ and use it to calculate other parameters such as linear energy $\overline{y}_D$ for further analysis [36]. Because the simulation for physics stage is not very time consuming, we could afford ROI being in a scale of millimeter and obtain $f(q)$ with good statistical properties. Yet, there are two disadvantages for adopting this method. First, as we emphasized through this thesis, DNA damage is more directly connected with the cell death and subsequent biological effect. Such analysis via microdosimetry method ignores the DNA structure and cannot capture the biological part of the radiation. For example, the protection effect by folding DNA structure (geometry part) and oxygen enhancement (chemical part). Second, this analysis ignored the spaces among cells, or specifically cell nucleus. The behavior of $f(q)$ applied to the whole sampling region with equal importance. But, the damage should be inside cell nucleus primarily to be effective for cell death.

To solve the above two issues, a full mechanistic microscopic MC simulation should be done in a scale of millimeter and sample cell nucleus accordingly. This goal is hard to achieve because of unaffordable simulation time. We then use gMicroMC to finish this simulation and present the results of DNA damage patterns. Furthermore, we used a network to find the relationship between DNA damage and SF.

6.1.2 Methods

The overall idea is shown in Figure 6.1. We constructed a Biology-guided Cell Survival deep neural network (BgCSDNN). The network structure was designed based on prior information of cell repair pathways [261], where each node represented the function reflected by its name. Each node included a sub fully connected network (not shown), whose connections were assumed to be the interaction of different proteins.

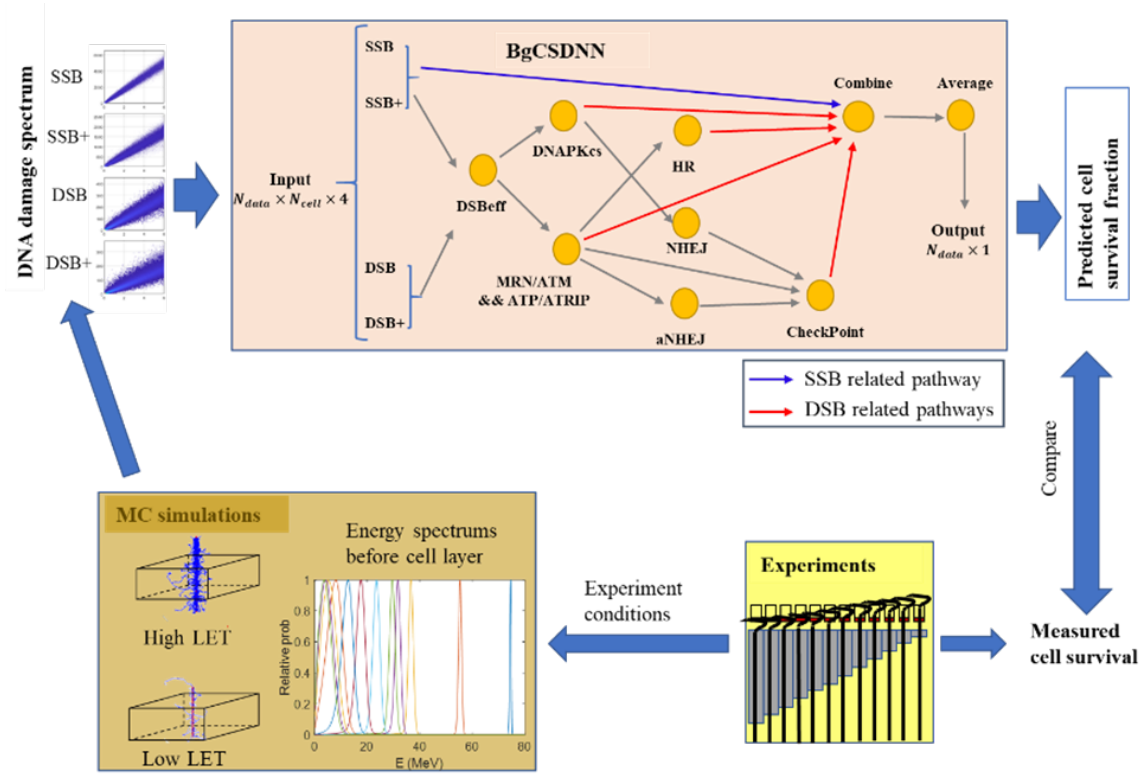

Figure 6.1. Workflow of generating data for the network and prediction of the network.

The input to BgCSDNN is the spectrum of DNA damages of different complexities. We chose this as input for two reasons. First, DNA damages are quantities directly affecting cell survival that can be computed via MC simulations. Using DNA damages as input avoids the task of extracting hidden biologically relevant information. Second, the energy depositions under proton irradiation are concentrated along the proton tracks, and DNA damages vary depending on cell positions relative to the tracks. The spectrum of DNA damages calculated for cells at different positions represent the average survival effect, which was characterized by the SF measured in experiments.

The output of BgCSDNN is a single number representing the SF under the input variables. As discussed on the above, SF is the average effect of cells experiencing

different dose levels. Hence, the "Combine" function node has one more sigmoid layer to output the survival state of each cell based on the DNA damage on it. The survival state can be either alive or dead (1 or 0). Then the "Average" layer averages the number of survived cells to give the final SF (number between 0 and 1). In fact, the "Average" is just a linear layer with same weight on different cells since we have no priority for the cells that we sampled in the MC simulation. It does not participate in the gradient backward process.

The goal of the network was to find the correspondance between DNA damage and SF. Therefore, We trained BgCSDNN by solving an optimization problem

$$\underset{\theta}{\operatorname{argmin}} \sum_{j=1}^{N_{data}} [\ln \sum_{i}^{N_{cell}} \frac{f(x_i^j, \theta)}{N_{cell}} - \ln S_j]^2 \tag{6.1}$$

where j is the index for different target dose, i the index for different cell positions, S_j the corresponding survival ratios measured in experiment. N_{data} and N_{cell} are the number of dose levels and cell positions we sampled. $f(x_i^j, \theta)$ denotes the BgCSDNN function, with θ the parameters in the network, and x_i^j is input DNA damage data.

Data and Model training We considered a previous experiment of high throughput measurement on cell survival fractions under different doses and LETs [290]. We used GEANT4 ([182]) to acquire the kinetic energy spectrum of the protons before they reached the cell layer. gMicroMC was then used to compute physical and chemical stages of water radiolysis to compute positions of energy deposition events and radicals at 1 ns for a pool of proton tracks. Protons' energy was sampled from the energy spectrum described on the above. ROI was 360×360×33 μm^3 while protons started in a 370×370 μm^2 plane on one side of ROI along dimension with 33 μm. For every given dose levels, we randomly chose proton tracks from the pool until the dose inside ROI reached the target dose. We then randomly sampled N_{cell} cells in the middle

11 μm of ROI and obtained the DNA damage based on the track structure inside these sampled cells. To eliminate correlation between diferent runs, cell positions were updated for every new dose values. $N_{data} = 300$ dose values in an interval from 0.02 to 6 Gy and $N_{cell} = 1000$ were used in the MC simulation. In this manner, DNA damages on 0.3 million cells were recorded. The DNA damage was classified into four categories:SSB, SSB+, DSB, DSB+, which could be referenced to previous chapters for definition.

The training was performed with PyTorch Adam optimizer and initial learning rate 0.001. We used data in ten LETs (1.2-17.7 $keV/\mu m$) to train the network, and the remaining two LETs (0.9 and 19.0 $keV/\mu m$) to test the model. The range of testing data is outside LET range of training data to test generalizability of the model. We also did a simulation for x-ray (^{137}Cs) to see if the network could be applied as well.

6.1.3 Results

We first show explicitly that the DNA damages varied in different cells even if the dose inside ROI was of little fluctuations. Figure 6.2 presented the probability histograms of the number of DSB (N_{DSB}) among cells and dose in ROI. Generally, N_{DSB} increases with dose level and LETs. At a given dose level and LET, it was also noted that there is a spread of N_{DSB} among cells, indicating the heterogeneity among cells under a given experimental condition. Numerically, at 6 Gy, when LET increases from 0.9 to 19.0 keV/µm, N_{DSB} increases from 334±26.7 to 574±101.7 (mean ± standard deviation).

The results on training and testing data were shown in Figure 6.3(a-b). The mean relative error on training and testing data were 0.1 and 0.11, respectively. As experiment data has relatively large uncertainty, we did not further reduce the errors to avoid over fitting. It should be emphasized that although dose and LET were

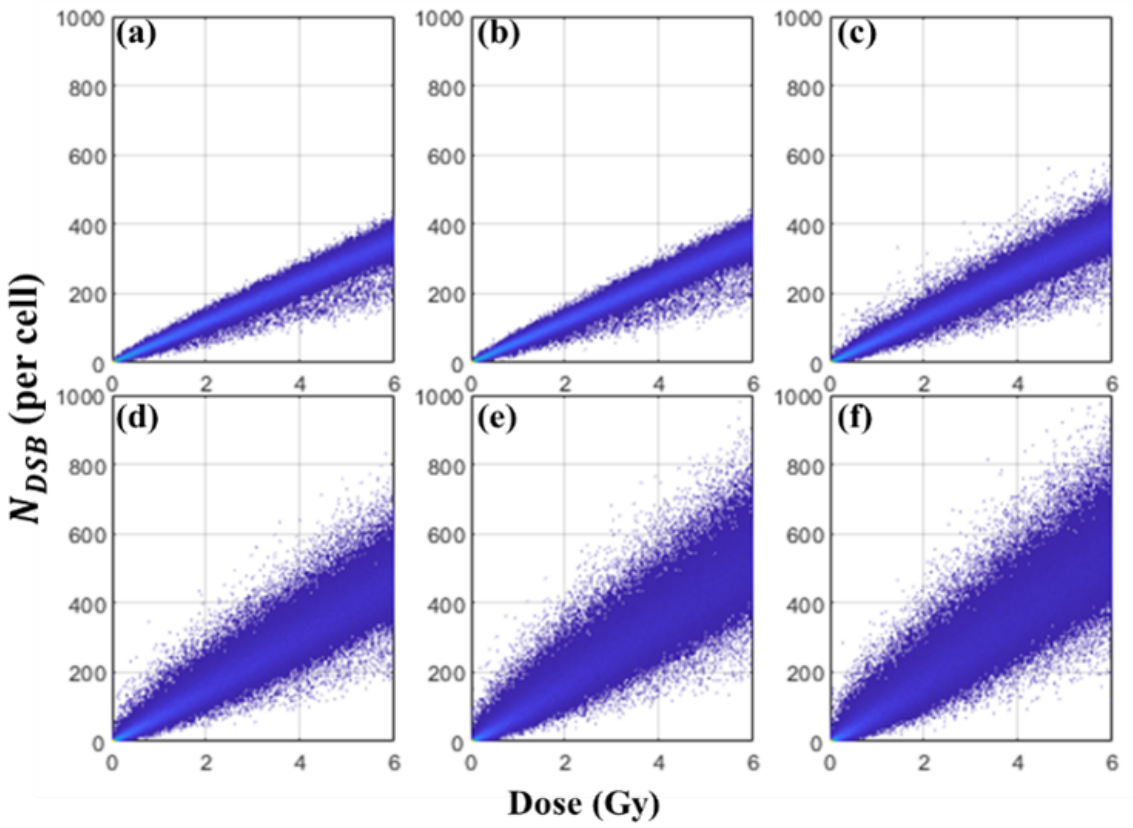

Figure 6.2. Probability histograms of the number of DSB and deposited dose for protons with different LET (a) 1.9 (b) 2.3 (c) 5.1 (d) 10.8 (e) 15.2 (f) 17.7 in units of $keV/\mu m$..

used in the plotting, we did not use such a tag in the model. The agreement on both training data and test data implies a universal model without the involvement of LET, if we chose DNA damages as independent variables.

We show in Figure 6.3(c) the plots of fitting of α and β by polynomials. As can be inferred from the figure, their values agreed quite well with the experimental one, which was determined by fitting experimental SF data with LQ model [4, 21]. Yet, with predicted α and β outside the fitting LET range (0.9 and 19 $keV/\mu m$), it did not do well for those two SF curves. The mean relative error was 0.23. Comparing the maximum difference between (b) and (d), predictions from network based on the DNA

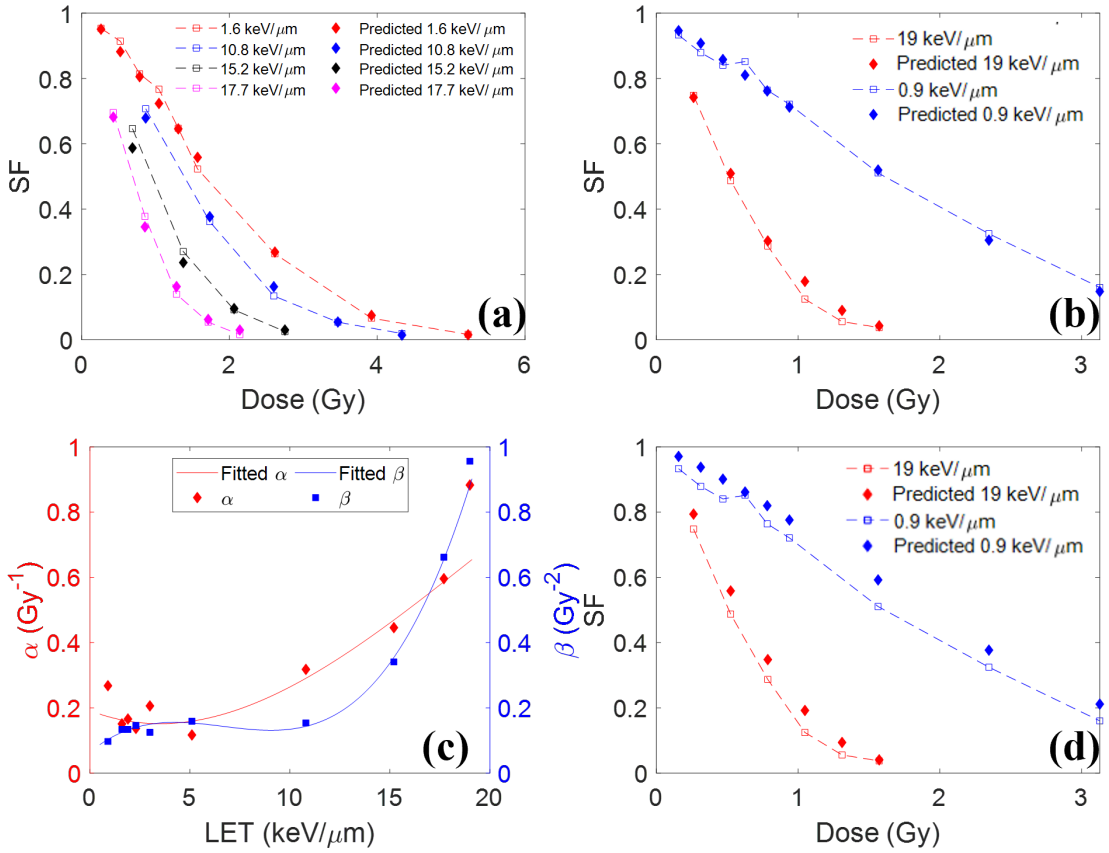

Figure 6.3. Comparison of ground truth and predicted results on (a) training data (b) test data. (c) comparison of ground truth and the predicted results using fitted α and β by polynomials..

damage simulaitons outperform that from fitting LQ parameters. This comparison indicated better generalizability of our model explaining the experimental data.

A motivation of BgCSDNN was to incorporate the biological basis in the network to allow interpretation. After training the network, we examined the weights on SSB related and DSB related pathways represented by blue and red arrows in Figure 6.1. It was found that weights for DSB related pathways ranged from 0.2 to 0.55, substantially larger than weights for single strand break of 0.008, indicating the importance of DSBs in cell kills under proton irradiation. Besides, we included x-ray data into training data and test it on another two LET values. The result was shown

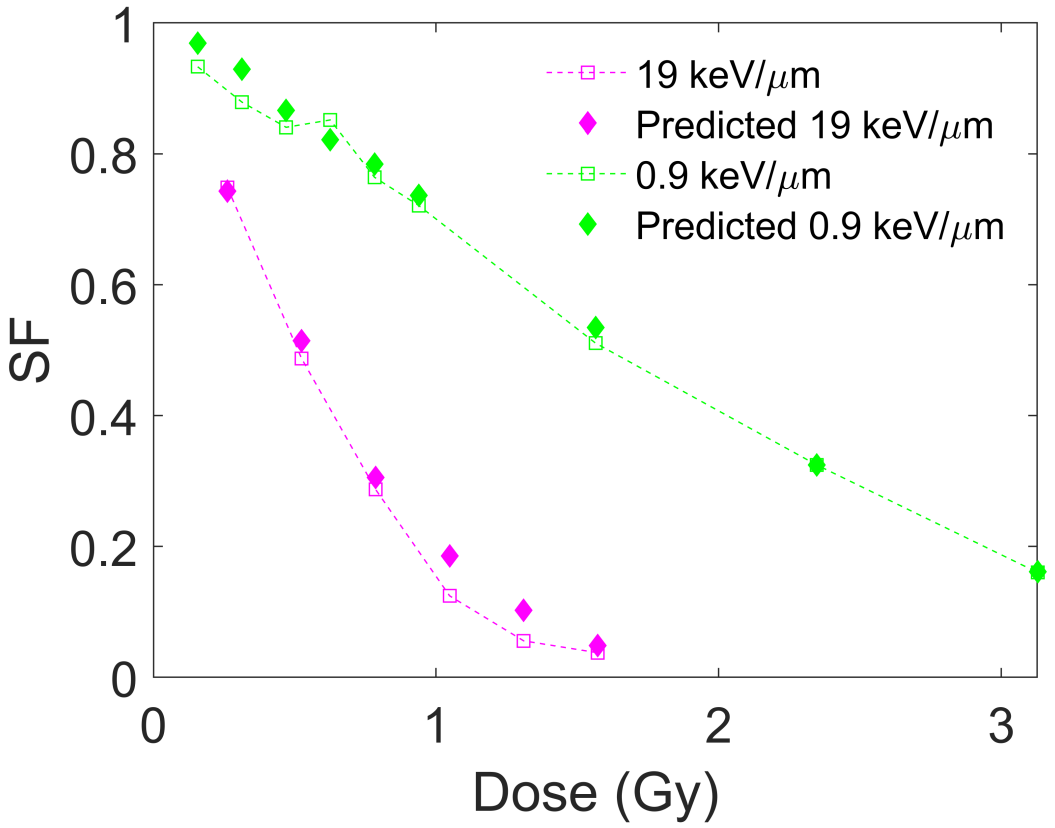

Figure 6.4. Predictions of SF when x-ray data was included.

in Figure 6.4. It could be seen that the inclusion of x-ray data had little effect on the performance of network predictions on test data. The mean error now became 0.14, as compared to previous 0.11. The consistence between this two scenarios means that cells respond similarly for x-ray and proton with LET up to 20 $keV/\mu m$ and function from DNA damage to SF preserves.

6.2 Hypothermia

6.2.1 Introduction

Since radiation do damage to cells regardless of whether they are in tumor or normal tissue, it is always of great importance to restrict the damage. One straightforward way is to improve apply radio-protective effect to normal tissues. Such methods are quite beneficial even for the use of new radiation technology. For example, SBRT. Although it emerged as a cost-effective, convenient radiation therapy method because of technology advances of imaging guidance [18], its escalation of dose per fraction still poses potential harm, which weighed against its benefits.

One well known radio-protective effect is brought by hypothermia through decades of study on the interaction between temperature and ionizing radiation. It was found that hibernating squirrel survived more to radiation when under 5 ^oC than under normal temperature [291]. Later experiments on ilium crypt cells also proved it [292]. Control tests on mice were done and again showed the reduction of tissue toxicity of rectum [293]. There are a lot hypothesis on the mechanism. Dang et al suggested that low temperatures reduce the cellular proliferation rate and micro-nucleus frequency [294]. It was also found out that hypothermia could suppress pro-inflammatory cytokines tumor necrosis factor-α and interleukin-6 [295] and protect cells from stimulated apoptosis through p53-dependent and -independent mechanisms [296]. Baird et al observed that DNA damage repair was postponed under hypothermia and it protected cells from being killed [297]. Lisowska et al proposed that low temperature could reduce the transformation from DNA damage to chromosome aberration [298]. From above memorization, the central idea is about the DNA damages. Considering that normal temperature would be restored after the radiation, we would naturally think of that it is the process during the radiation

affected by low temperature that causes different patterns of DNA damage and later different responses to DNA damages.

The low temperature has two effects on radiation outcomes. Physically, low temperature alters the diffusion rates and chemical reaction rates, which change the yields of radicals and DNA damages. On the other side, biologically, it could also affect the activities of some enzymes, which makes the cell respond differently. In this work, we want to test if the change on physical properties would result in large enough change of DNA damages that could explain the radio-protective effect by hypothermia. We did not choose the biological factor for two reasons. First, low temperature was only applied during radiation for several minutes [294]. The time is so short that we might regard that most DNA damage repair did not even start. Yet, radio-protective effect could still be observed. Second, many biological explanations were based on DNA damages as well, for example adding radical scavenger eliminated the radio-protective effect for reducing DNA damages [299].

Hence, the purpose of this work is two folds. One is to simulate the variation of DNA damages versus temperature based on some assumptions about how those coefficients vary with temperature. Another is to explain the experimental results [293] based on our simulation results.

6.2.2 Methods

6.2.2.1 Diffusion, chemical reaction and temperature

The relationship between chemical reaction rate and temperature could be described by Arrhenius equation [300], that is,

$$k(T) = k_0 e^{-\frac{E_a}{RT}}. \tag{6.2}$$

Here, $k(T)$ means reaction rates at certain absolute temperature T and E_a means the activation energy for a reaction to happen in unit of J/mol. $R = 8.31 J/(mol \bullet K)$ is the gas constant. k_0 is called pre-exponential factor. For our interest, we would only concern two experimental temperatures [293], $T_L = 15\ ^oC$ $(288\ K)$ and $T_H = 37\ ^oC$ $(310\ K)$. Hence, given we know $k(T_H)$, we need to multiply coefficients $c(T_L)$ to $k(T_H)$ to obtain $k(T_L)$. $c(T_L)$ was calculated as

$$c(T_L) = e^{-\frac{E_a}{RT_L}} / e^{-\frac{E_a}{RT_H}} \tag{6.3}$$

All values of E_a were retrieved from reference [301]. Those reactions that cannot be found in this reference, we used averaged value 11 kJ/mol.

As for diffusion, its relationship to temperature should be similar, i.e., following exponential form [302]. Considering in solid case, one atom needs to gain enough energy to leave the original place and hop into nearby places. liquid may not be well ordered like solid crystals, but the diffusion mechanism could be retained [303]. Hence, $D(T) = D_0 e^(- E_a^d/RT)$. As summarized in reference [301], most activation energy E_a^d for diffusion ranges 15 kJ/mol to 19 kJ/mol. In this simulation, we just set $E_a^d = 17.5 kJ/mol$ for all radicals. This gave the reduction coefficient for diffusion constant 0.6, meaning the diffusion constant at T_L was 0.6 times the value at T_H.

6.2.2.2 Simulation setup

After clarifying the values for diffusion and chemical reaction rate at different temperature, we just need to score the number of DNA damage versus the simulated dose in a cell for different temperature. The simulation was decribed in the following steps.

1. We irradiated photons from 225 kVp into a thin water layer with thickness 1 mm to obtain the energy spectrum of secondary electrons.

Table 6.1. Activation energy and reduction coefficients for different reactions in gMicroMC

Index	Reaction channels	E_a (kJ/mol)	$c(T_L)$
1	$e_h + H^{\cdot} \rightarrow OH^- + H_2$	11	0.7217
2	$OH^{\cdot} + H^{\cdot} \rightarrow H_2O$	8	0.7888
3	$H^{\cdot} + H^{\cdot} \rightarrow H_2$	8	0.7888
4	$H_2 + OH^{\cdot} \rightarrow H^{\cdot}$	11	0.7217
5	$e_h + H_2O_2 \rightarrow OH^{\cdot} + OH^-$	15	0.6410
6	$e_h + H^+ \rightarrow H^{\cdot}$	11	0.7217
7	$H^+ + OH^- \rightarrow H_2O$	11	0.7217
8	$e_h + OH^{\cdot} \rightarrow OH^-$	8	0.7888
9	$OH^{\cdot} + OH^{\cdot} \rightarrow H_2O_2$	7.7	0.7959
10	$e_h + e_h \rightarrow 2OH^- + H_2$	23	0.5056
11	$H^{\cdot} + O_2 \rightarrow HO_2^{\cdot}$	10.6	0.7303
12	$e_h + O_2 \rightarrow O_2^{\cdot -}$	11	0.7217
13	$H^{\cdot} + O_2^{\cdot -} \rightarrow HO_2^-$	11	0.7217
14	$OH^{\cdot} + HO_2^{\cdot} \rightarrow O_2$	11	0.7217
15	$OH^{\cdot} + O_2^{\cdot -} \rightarrow O_2 + OH^-$	8	0.7888
16	$OH^{\cdot} + HO_2^- \rightarrow HO_2^{\cdot} + OH^-$	11	0.7217
17	$H^{\cdot} + HO_2^{\cdot} \rightarrow H_2O_2$	11	0.7217
18	$e_h + HO_2^{\cdot} \rightarrow HO_2^-$	11	0.7217
19	$e_h + O_2^{\cdot -} \rightarrow 2OH^- + H_2O_2$	11	0.7217
20	$H^+ + O_2^{\cdot -} \rightarrow HO_2^{\cdot}$	11	0.7217
21	$H^+ + HO_2^- \rightarrow H_2O_2$	11	0.7217

2. We randomly sampled electrons in a sphere with radius 70 μm. Its momentum direction was also sampled randomly. The energy of electrons was sampled from the energy spectrum obtained at step 1.
3. Transport electrons one by one. If there was any water radiolysis events inside the center sphere with 5.5 μm (cell nucleus radius of our DNA model), continue; otherwise, go to step 2.
4. Simulate the subsequent physicochemical and chemical stage and record the damage site by hydroxyl.

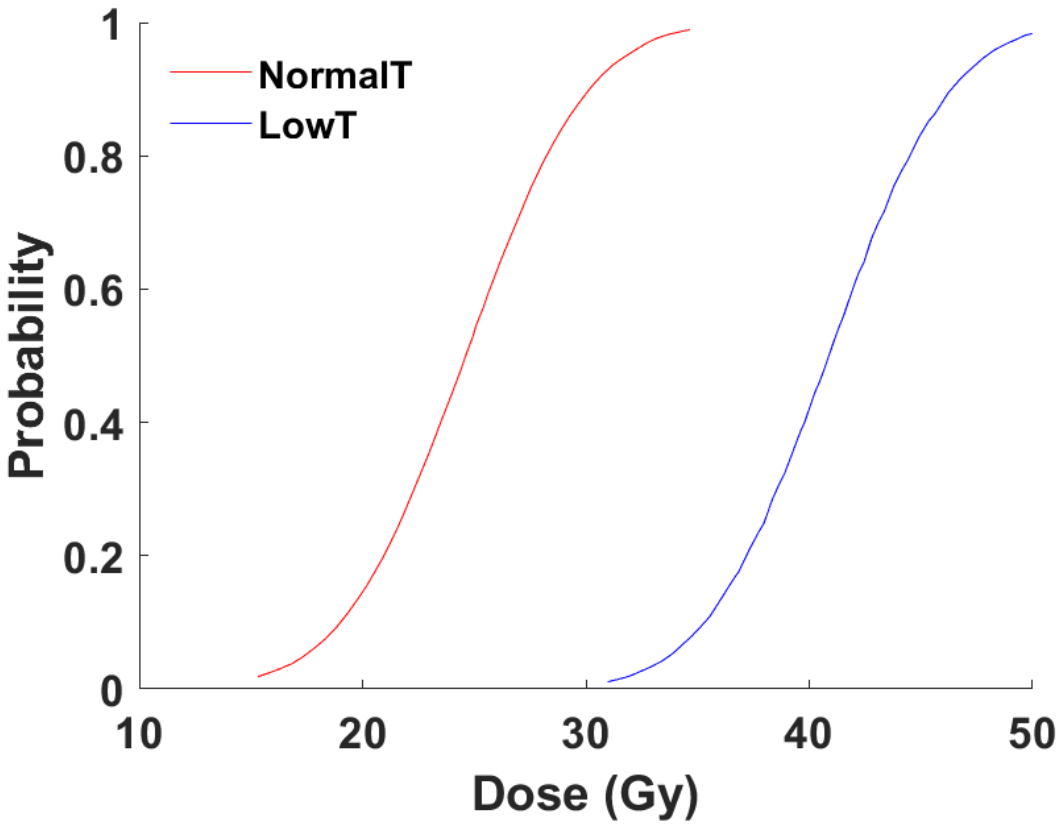

Figure 6.5. Fitted NTCP as a function of dose for different temperatures [293].

5. determine DNA damage with chemical attack in step 4 and direct damage in step 3.
6. Repeat step 2 to 5 until dose inside the cell nucleus reached 40 Gy.
7. Do steps 2 to 6 for a different temperature. The things that have to be altered are the values of diffusion rates and chemical reaction rates.

6.2.2.3 Analysis setup

From the paper [293], we could have normal tissue complexity probability (NTCP) as a function of dose D for different temperature T, denoting as $f_T(D)$. These lines are shown in Figure 6.5. From the simulation, we obtained curves be-

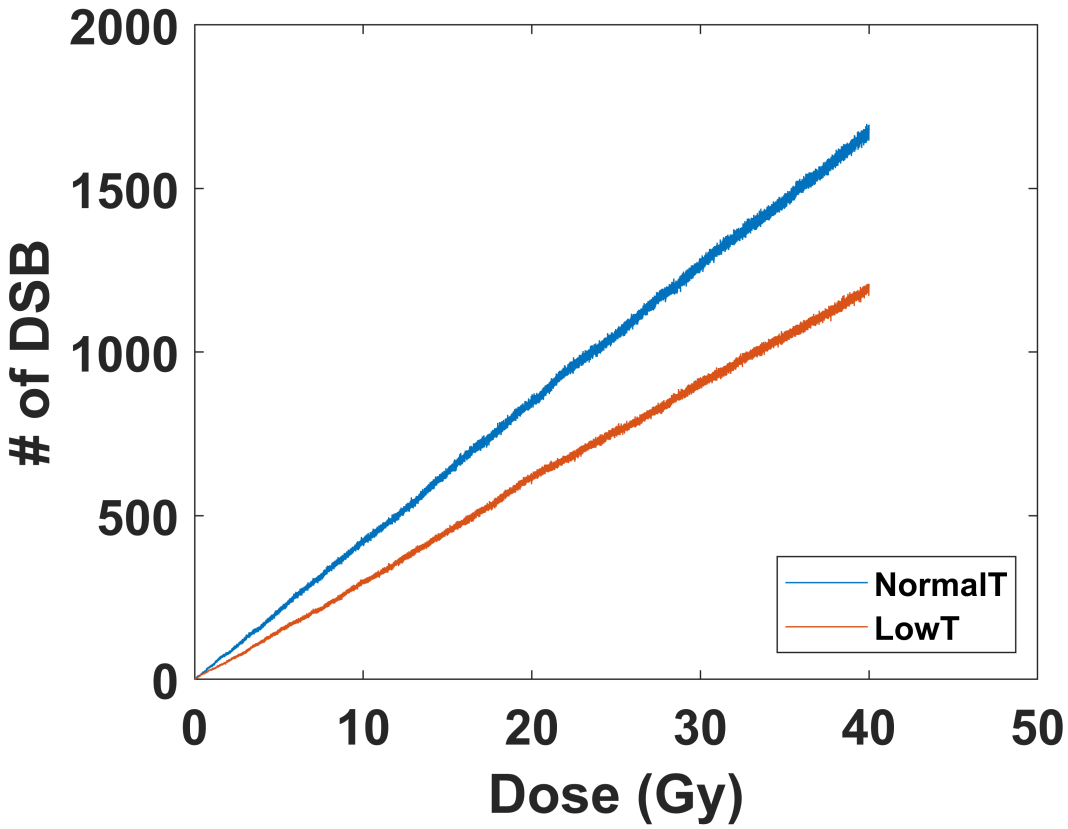

Figure 6.6. Simulated DSB versus dose at different temperature.

tween number of DSB N_{DSB} and dose D at different temperature T, denoting as $N_T(D)$. Then, we could find NTCP as a function of number of DNA damages, using the inverse function of $N_T(D)$ and substituting it into $f_T(D)$.

6.2.3 Results and discussions

Figure 6.6 showed the computed number of DSBs versus dose. We could clearly see that fewer DNA damages were recorded at lower temperature.

Figure 6.7 showed the NTCP as a function of number of DNA damages. By doing the variable transformation, all the experimental points were collapsed together, which might indicate a uniform relationship between NTCP and DNA damage. The

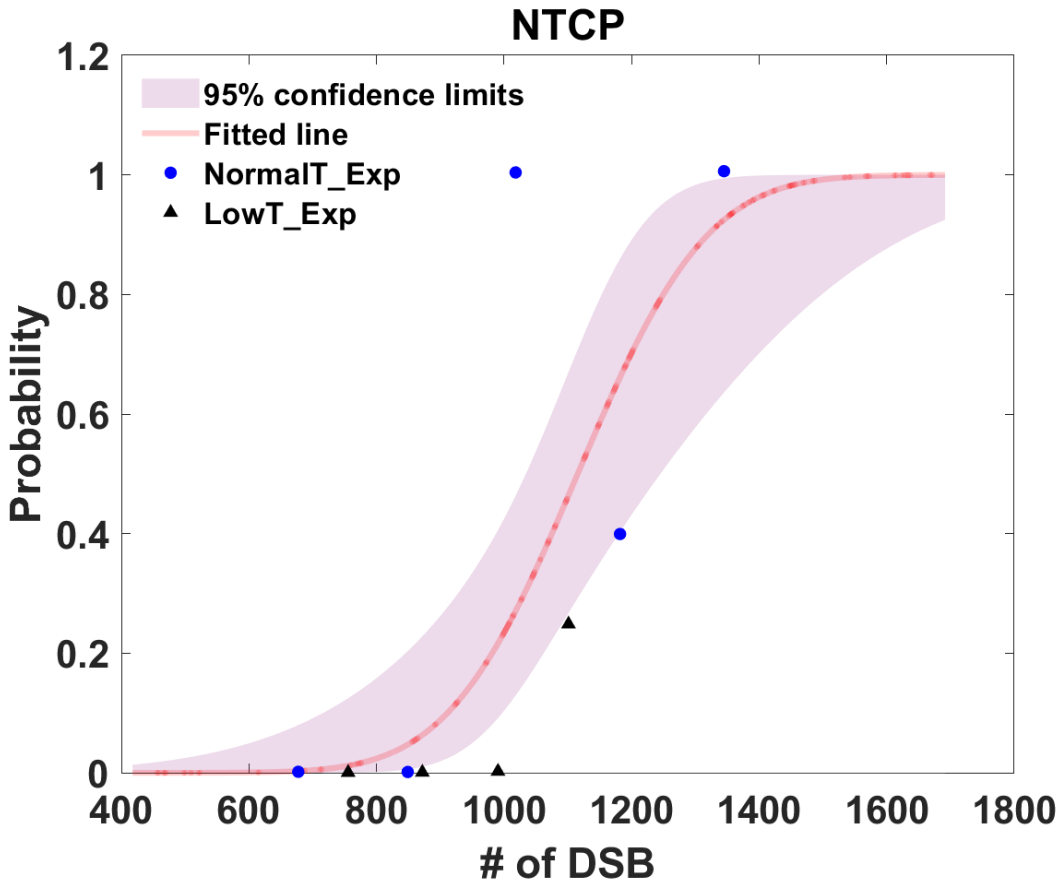

Figure 6.7. Probit analysis using all observations. Shaded area means 95% confidence level.

effect of temperature was automatically considered through the low yield of DNA damage at lower temperature. We further did a probit analysis with number of DSBs as independent variable, the fitted line was shown in Figure 6.7 as well. Shaded area means 95% confidence level. All experimental points were well described by such fitting line. The analysis suggested that the raddioprotective effect by hypothermia was majorly the effect of temperature on radical diffusion and chemical reactions. With smaller diffusion rates, diffusion length of radicals especially hydroxyl became smaller. Yet, their average distance at the beginning of chemical stage was not changed by temperature. They were still dense in the beginning. Hence, the slowed diffusion

gave radicals more time to react locally, resulting in smaller probability to touch DNA components and fewer DNA damages.

6.3 Conclusion

In this chapter, we discussed two problems that need to run tens of thousands of primary particle tracks. Such problems bring about an issue of great computational burden. With improved efficiency in chemical stage and searching DNA damages through the DNA chain, these issues were investigated by gMicroMC.

We pointed out that if the sampled region is not large enough for proton cases, the simulated dose was not consistent with the target one. When cells were irradiated by a beam, cells experienced a large variation of dose and hence the DNA damages. SF, an average parameter to determine how many cells are able to proliferate, must be considered as a function of DNA damages that span a wide range, rather than the single value of experimental dose. We further developed a network to describe this mapping function, which mapped the simulation results to experimental SF values quite well. Under this scheme, the x-ray data could be included into the proton's.

We also studied the radio-protective effect by hypothermia during radiotherapy. Based on the fact that diffusion rates of radicals and reaction rates among radicals are affected by temperature, we simulated the DNA damage with different system temperature. We found out that lower temperature did induced fewer DNA damages. By mapping the data, the probability of complexity can be represented as a single function of DNA damages for both low and high temperature. Our simulation results consistently support the idea that change of DNA damages by different temperature may be the primary reason for radio-protective effect for hypothermia.

CHAPTER 7

OXYGEN EFFECT AND FLASH

7.1 oxygen effect on radical yields

7.1.1 Introduction of oxygen effect

It is well known that oxygen plays a critical role in DNA damages produced by ionizing radiation. First, dissolved oxygen promotes the production of deleterious reactive oxygen species (ROS), such as superoxide and hydroperoxyl radicals, which are very toxic to cells. Second, oxygen can fix the DNA damages rapidly after their occurrence, forming stable organic peroxides and making it difficult to repair them ([304]). It is an important research topic to accurately model the presence of oxygen in the water radiolysis process and the impact on radio-biological endpoints, such as DNA damages.

Monte Carlo (MC) simulation is commonly accepted as one of the most accurate methods to model radiation transport and interactions with matters because of the faithful modeling based on physics principles. Yet, in the context of studying the oxygen effects, simplifications in modeling have to be made in most of the MC packages due to the heavy computational burden, primarily in the modeling of the chemical stage of the water radiolysis process. In fact, MC simulations of the chemical stages is challenging due to the spatial-temporal simulation that spans over multiple order of magnitudes in time and the transport of a large number of radicals, which is an interacting many-body problem caused by the mutual competitive chemical reactions between the radiolytic molecules. Hence, to reduce the computational burden, the oxygen is sometimes ignored [205, 241] or treated as a temporally constant and

spatially uniform background [256, 305] that serves as a scavenger for the radiolytic radicals. The method assuming a constant uniform background ignores the spatial and temporal variations of chemical reactions, an important factor in certain scenarios. For instance, when rapid consumption of oxygen due to reactions with radicals occur, temporal variation of oxygen concentration may not be omitted. Meanwhile, as the oxygen distribution is sparse compared to the very short reaction radii, reactions with oxygen happens non-uniformly, making spatial variation a factor to consider.

Modeling the effect of oxygen is of particular importance in the context of ultra-high dose rate radiotherapy termed as FLASH radiotherapy [306] that has lately attracted a lot of attentions. FLASH radiotherapy holds the potential of better sparing normal tissue, while maintaining the tumor control probability, than radiotherapy delivered at a conventional dose rate, as having been demonstrated using electron [307] , photon [308, 309], and proton beams [310]. However, the mechanism of FLASH radiotherapy remains unclear and oxygen depletion has been pointed out as one of the factors contributing to the advantage of FLASH radiotherapy [311, 312]. In this hypothesis, a hypoxia or anoxic environment created by radiolytic oxygen depletion [313, 314] under the FLASH condition in normal tissue raises its radiation tolerance, hence enlarging the window between normal tissue complication probability and tumor control probability. To understand the effect of oxygen, several studies have been performed [312, 315]. Spitz et al estimated the constant of oxygen consumption rate (OCR) due to different factors. Pratx et al further investigated whether oxygen depletion could occur during the chemistry stage of radiolysis under different dose rates with a constant OCR independent of the initial oxygen concentration. Yet, as oxygen concentration decreases, the probability for oxygen molecules reacting with other molecules is expected to decrease, leading to a gradually reduced OCR. Hence,

it is desired to perform a detailed mechanistic modeling study to investigate the time evolution of chemical yields under the FLASH condition.

The purpose of this work is twofold. First, We will present the implementation in gMicroMC to process the chemical stage with the presence of oxygen. This development is expected to greatly facilitate the research using MC simulations to investigate the impacts of oxygen effects. The second purpose is to use the improved gMicroMC package to study the hypothesis of oxygen depletion in the FLASH condition, which could demonstrate the advantages of gMicroMC in terms of supporting large scale microscopic MC simulations. Specifically, we will apply gMicroMC under the FLASH condition to investigate the OCR under different dose rates and initial oxygen concentrations. To our knowledge, this is the first time that the time evolution of radical yields under the FLASH condition are computed in a step-by-step MC simulation program with oxygen species explicitly included in the modeling.

7.1.2 Materials and methods

7.1.2.1 Implementation of oxygen in gMicroMC

The development of physics and chemical stage have been illustrated in 4 and 5. The advantage of gMicroMC is the high computational efficiency realized via GPU parallelization and GPU-friendly parallel simulation algorithms in all four stages, which substantially improves the efficiency of this computationally challenging problem. The initial development of gMicroMC did not include oxygen in the simulation process. To enable this feature, we considered oxygen-related reactions with parameters listed in previously published studies [186]. Because of the absence of $O^{\cdot -}$, O_3, O_3^-, $O(3P)$ in the physicochemical stage, we only considered three radicals in addition to those already included in the original gMicroMC, namely hydroperoxyl radical

Table 7.1. Radical species and diffusion coefficients D. The root-mean-square distance λ traveled for $t = 1\ \mu s$ was calculated as $\lambda = \sqrt{6Dt}$.

Species	D ($\times 10^9\ nm^2 s^{-1}$)	$\lambda(nm)$	Reference
e_h	4.9	171.5	[180]
$OH^{\cdot}$	2.8	129.6	[180]
$H^{\cdot}$	7.0	204.9	[180]
H^+	9.0	232.4	[180]
H_2	4.8	169.7	[180]
OH^-	5.0	173.2	[180]
H_2O_2	2.3	117.5	[180]
O_2	2.4	120.0	[186]
$HO_2^{\cdot}$	2.3	117.5	[186]
$O_2^{\cdot -}$	1.75	102.5	[186]
HO_2^-	1.4	91.7	[186]

$HO_2^{\cdot}$, superoxide radical $O_2^{\cdot -}$ and hydroperoxide anion HO_2^-. All the chemical species are listed in Table 7.1.

As for the simulation, we first sampled the initial position of oxygen molecules. Let us denote the oxygen concentration in percentage by $P_{o_2}(\%)$, which means the ratio of partial oxygen pressure in water to the atmosphere pressure P_{atm} with $P_{atm} = 760\ mmHg$. Equivalently, P_{O_2} can be expressed in mmHg, i.e. the partial oxygen pressure in water. $P_{O_2}(mmHg) = P_{o_2}(\%) * P_{atm}$. Additionally, we will also use P_{O_2} in $\mu M(P_{O_2}(\mu M))$ to denote the concentration of dissolved oxygen molecules in the unit of μM. $P_{O_2}(\mu M) = P_{O_2}(mmHg) * H_c$ with $H_c = 1.26\ \mu M/mmHg$ being the coefficient of Henry's Law for oxygen dissolving in water [316]. In this section, $P_{O_2}(\%)$ will be always used to specify the oxygen concentration, while $P_{O_2}(\%)(P_{O_2}(mmHg), P_{O_2}(\mu M))$ will be explicitly stated in some places. For a region of interest (ROI) studied, we first extended the volume along both directions of the x, y and z axes by Δr, which is estimated as the root-mean-square diffusion length of the oxygen under a given temporal duration t of the chemical stage. For

example, we took $\Delta r = 120\ nm$ when $t = 1\mu s$ since the diffusion length was about 120 nm (Table 7.1). Once other t values were used, we would change Δr accordingly. The purpose of this extension is to ensure an equilibrium oxygen diffusion background within the ROI during the simulation, especially at the area close to the ROI boundaries. We denoted the volume of the extended region as V. The number of initial oxygen molecules was decided as $N_{O_2} = P_{O_2}(\%) * P_{atm} * H_c * N_A * V$, which were then uniformly sampled inside the region.

The existence of oxygen was assumed to not affect the physical stage and the physicochemical stage. In fact, the concentration of water molecule is $55.6M$ but the concentration of dissolved oxygen is $0.2mM$ for $P_{o_2} = 21\%$. Hence, the probability for the incident initial particles to collide with dissolved oxygen in the physical stage is low and can be safely ignored. However, the dissolved oxygen molecules could play a crucial role in determining the temporal production and spatial distribution of radicals, as the chemical stage can last for microseconds and radicals can spread out through diffusion. The oxygen is then expected to have a high probability to participate in the reactions with radicals. The chemical reactions included in this study are summarized in Table 7.2. During the transport simulation of the chemical stage, we followed the same algorithm as described in our previous publication [201].

7.1.2.2 Studies to validate simulations of the chemical stage with oxygen included

During the development of gMicroMC, we noticed that another MC simulation package TRAX-Chem (Boscolo et al., 2020) had updated its functions to support the oxygen in chemical stage simulation by treating oxygen as a uniform constant background. The results have been compared with other studies for 5 MeV proton

Table 7.2. Chemical reactions and reaction rate constants k_{obs}. H_O molecules were ignored in the chemical equations assuming they were everywhere.

Index	Reaction channels	$k_{obs}(10^{10}\ L \bullet mol^{-1} \bullet s^{-1})$	Reference
1	$e_h + e_h \rightarrow 2OH^- + H_2$	0.5	[180]
2	$e_h + OH^{\cdot} \rightarrow OH^-$	2.95	[180]
3	$e_h + H^{\cdot} \rightarrow OH^- + H_2$	2.65	[180]
4	$e_h + H^+ \rightarrow H^{\cdot}$	2.11	[180]
5	$e_h + H_2O_2 \rightarrow OH^{\cdot} + OH^-$	1.41	[180]
6	$OH^{\cdot} + OH^{\cdot} \rightarrow H_2O_2$	0.44	[180]
7	$OH^{\cdot} + H^{\cdot} \rightarrow H_2O$	1.44	[180]
8	$H^{\cdot} + H^{\cdot} \rightarrow H_2$	1.20	[180]
9	$H^+ + OH^- \rightarrow H_2O$	14.3	[180]
10	$H_2 + OH^{\cdot} \rightarrow H^{\cdot}$	0.00417	[180]
11	$e_h + O_2 \rightarrow O_2^{\cdot -}$	1.74	[186]
12	$e_h + HO_2^{\cdot} \rightarrow HO_2^-$	1.29	[186]
13	$e_h + O_2^{\cdot -} \rightarrow 2OH^- + H_2O_2$	1.29	[186]
14	$OH^{\cdot} + HO_2^{\cdot} \rightarrow O_2$	0.79	[186]
15	$OH^{\cdot} + O_2^{\cdot -} \rightarrow O_2 + OH^-$	1.07	[186]
16	$OH^{\cdot} + HO_2^- \rightarrow HO_2^{\cdot} + OH^-$	0.832	[186]
17	$H^{\cdot} + O_2 \rightarrow HO_2^{\cdot}$	2.1	[186]
18	$H^{\cdot} + HO_2^{\cdot} \rightarrow H_2O_2$	1.0	[186]
19	$H^{\cdot} + O_2^{\cdot -} \rightarrow HO_2^-$	1.0	[186]
20	$H^+ + O_2^{\cdot -} \rightarrow HO_2^{\cdot}$	4.78	[186]
21	$H^+ + HO_2^- \rightarrow H_2O_2$	5.0	[186]

under oxygen partial pressure of $P_{O_2} = 21\%$ (160 $mmHg$, 201.1μM). This study provided a CPU-based simulation code to benchmark our development.

We used GEANT4-DNA [182] to produce secondary electrons generated by an incident 5 MeV bombarding into a 10 μm thick water slab. The reason to choose a thin slab as the simulation volume of interest was to ensure that the proton does not lose energy significantly within the volume of interest, and hence the results were relevant to the proton with 5 MeV energy. As such, we simulated the proton transport using GEANT4-DNA (GEANT4 version 10.5.1) and recorded the initial positions, energy values, and directions of secondary electrons, as well as locations and types of ionized

and excited water molecules caused by the proton inside the water slab. After that, electron transport simulation in the physical stage was performed using gMicroMC, generating ionized and excited water molecules. These water molecules, together with those directly generated from protons, were fed into the physicochemical stage simulation of gMicroMC, generating the initial distribution of chemical radicals. These radicals were subsequently simulated to go through the chemical stage. During the simulation, we recorded the yield, or G value, of different radicals and compared the time evolution of yield of hydrated electron with published data from previous works [256, 305] . The G value calculates the ratio between the number of molecules of the chemical species and the deposited energy to generate such a number of molecules in the unit of number of molecules per 100 eV. In addition, we also performed simulations for 10 MeV proton beams. The simulation setup was the same as we did for the 5 MeV one. Radicals in the first 10 μm water slab were tracked and the yields of e_h, $H^{\cdot}$, $O_2^{\cdot}$ and $HO_2^{\cdot}$ at 1 μs under oxygen concentration levels of $P_{O_2} = 0$, 0.1%, 0.5%, 1%, 3%, 5% and 7% were recorded and compared to the results reported by Boscolo et al. [256].

7.1.2.3 Simulation setup under a conventional dose rate

Conventional dose rate usually refers to an average dose rate less than 0.03 Gy/s (Favaudon et al., 2014; Vozenin et al., 2019b). For a primary electron with a kinetic energy of 4.5 keV and a mass stopping power of $\frac{S}{\rho} = 4.0 \times 10^9\ MeV \bullet \mu m^2/g$, this low dose rate $\dot{D}$ would be equivalent to an electron fluence $\phi = \dot{D}/(\frac{S}{\rho}) \approx 0.05\ electron\ \mu m^{-2} s^{-1}$. Considering a cross section with a radius of 2 μm, approximately twice the lateral spread-out of the primary electron, this fluence corresponds to a time interval $\Delta t = 1.59\ s$ between two adjacent primary electrons. Noticing that the typical consideration of the physical and chemical duration triggered by an

incident particle in the DNA damage computation is 10^{-6} second, it is then unlikely that secondary products from different primary particles would overlap spatially or temporally. Hence, to study the impacts of oxygen on radical yields, it is sufficient to consider the single electron irradiation. We initialized an electron ($E_k = 4.5\ keV$) at the origin of the global coordinate with its momentum direction randomly sampled in the 4π angular range. We then performed the first two stage simulation in gMicroMC and recorded the initial radical distribution. Considering the stochastic nature of MC simulations, we repeated the simulation for N times and determined the ROI as the smallest circle containing all radicals from all runs. Assuming the chemical stage last for 1 μs, we sampled the initial oxygen distribution in an extended region . We then performed the chemical stage simulation for each radical list with the presence of oxygen, in which, the radicals and molecules were tracked until they reacted or the chemical stage ended. Oxygen concentrations of $P_{O_2} = 0$, 3%, 9% and 21% were considered to cover different scenarios of biological interest. $P_{O_2} = 21\%$ (160 $mmHg$, 201.1 μM) corresponds to the normoxia situation under the standard atmosphere. $P_{O_2} = 3\%$ (23 $mmHg$, 28.7 μM) and $P_{O_2} = 9\%$ (69 $mmHg$, 86.1 μM) cover the physoxia condition [317, 318]. We empirically chose N=1000 times for each configuration as a tradeoff between the simulation accuracy and simulation time cost, and reported the average G values of different chemical species as a function of time after irradiation. With 1000 simulations, the maximum uncertainty of G values was reduced to 0.5%, while the total simulation time was tolerable, ranging from less than one hour to a few days.

7.1.2.4 Simulation setup under the FLASH condition

Under FLASH condition, there is a high chance that chemical species from different initial particle tracks can react with each other due to a much shorter time

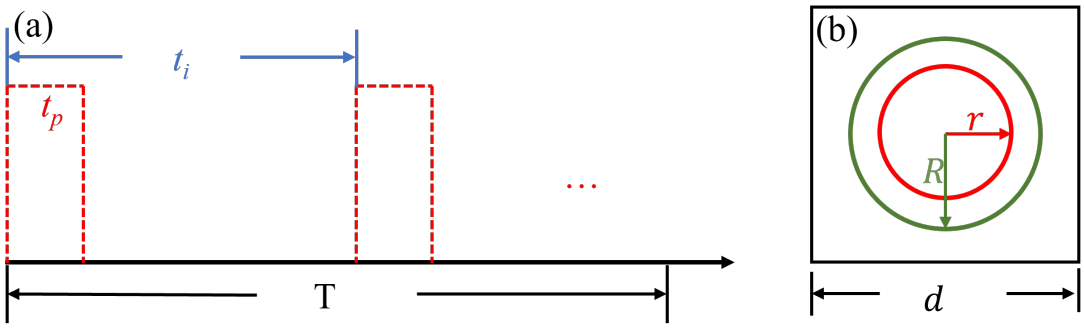

Figure 7.1. (a) Time structure of radiation in FLASH condition. T: total irradiation time. t_i: time interval between the beginning of two successive pulses. t_p: temporal width of a single pulse. (b) Cross section of the simulation geometry. Inner circle with a radius of r is the ROI. The circle with a radius of R is the sampling region for source particles. The square with side d is the sampling region for oxygen molecules..

interval between two adjacent source particles. Still take the 4.5 keV primary electron as an example. An instantaneous dose rate of 10^6 Gy/s will be equivalent to $\Delta t = 5.3$ ns for a cross section with a radius of 2 μm, which is much shorter than the chemical duration of 1 μs. Hence, the beam time structure is one of the most important issues to be considered in the simulation. As shown in Figure 1, there can be multiple temporal-scales to be considered. The total irradiation time is labeled as T, which was used to calculate the nominal average dose rate $\dot{D}_a = D_{total}/T$, whereD_{total} is the total delivered dose. The criteria of 40 Gy/s for $\dot{D}_a$ was reported to define the FLASH condition in early studies [307], which was in contrast with the dose rate for conventional photon beam of only 0.03 Gy/s. The radiation is usually delivered in a pulse mode, for instance, using a medical linear accelerator. Let t_i represent the time interval between two adjacent pulses and t_p the duration of a pulse. The instantaneous dose rate can be computed as $\dot{D}_i = \frac{D_{total}}{T} * \frac{t_i}{t_p}$. For a typical linear accelerator, t_i is of the order of milliseconds with t_p of microseconds, which makes $\dot{D}_i$ about three orders of magnitudes larger than $\dot{D}_a$. Specific values of $\dot{D}_i$ for observing a reproducible FLASH effect ranges from 10^4 Gy/s to 10^9 Gy/s (Bourhis

et al., 2019). In this study, we will focus on $\dot{D}_i$ rather than $\dot{D}_a$ to test the oxygen depletion hypothesis, because $\dot{D}_i$ characterizes the reaction intensity between radicals and oxygen molecules. From the time structure shown above, oxygen regeneration can be ignored within a pulse, because the pulse only lasts for microseconds and one microsecond corresponds a diffusion distance of the oxygen molecule of only 120 nm (Table 7.1), 1 percent of the cell nucleus dimension (11 µm).

In this study, we focused on the simulation of electron particles with kinetic energy E_k=4.5 keV from a pulse width t_p=1 μs. The chemical stage is determined as t_c=1 μs post irradiation, to ensure enough time for radicals produced at the end of the pulse to propagate. The simulation geometry is shown in Figure 1(b). We set the ROI as a sphere with radius $r = 1.5\mu m$. The initial electrons were sampled inside a sphere $V_(e)$ with radius $R = r + l(E_k)$ with $l(E_k)$ being the maximum length that an electron with kinetic energy E_k can travel. Here, $l(E_k)$ is taken as 1 μm. The oxygen molecules were initialized in a cubic volume with each side $d = 2(r + \Delta r)$. Here, $\Delta r = 300nm$, is computed with the method given in Table 7.1, using the reference time duration t=$t_p + t_c$=$2\mu s$. As mentioned in above, the purpose of this extension is to ensure an equilibrium oxygen diffusion background within the ROI during the simulation, especially at the ROI boundaries.

With the beam temporal structure considered, we initialized an electron with its spatial position randomly sampled within $V_(e)$, initial time randomly within $[0, t_p]$, and traveling direction uniformly in the 4π spherical anglar range. We then simulated its physical and physicochemical stages, and recorded all the produced chemical species. We repeated this process until the deposited energy E_d inside the ROI reached the predefined value of $\dot{D}_i * t_p * 4\pi r^3\rho/3$, where $\rho = 1\ g/cm^3$ is the density of the

medium. In this way, we obtained the initial temporal and spatial distributions of all radicals from these primary electrons.

Next, we performed the chemical stage simulation in a step-by-step fashion. Every time when the simulation process was advanced by a time interval, we checked the pre-generated group of radicals, and included those initiated inside the time step into the simulation. This approach allowed us to model the time evolution of the chemical stage with radicals triggered by source electrons gradually included into the simulation. Through the entire simulation, all radicals and molecules were tracked until they reacted or the chemical stage ended.

We considered cases with different dose rates $\dot{D}_i = 10^6$, 10^7, 10^8 Gy/s and oxygen concentrations $P_{O_2} = 0.01\%$, 0.1%, 0.5%, 1%, 3%, 9%, 21%. The dose rates were chosen to be consistent with the one pulse mode implemented in the current FLASH radiotherapy experiments, in which the dose rate started above 10^6 Gy/s. We included 0.01% and 1% in this section to cover the hypoxia condition [317, 318]. For each case, we tracked the G-values evolution for all radical types and calculated the OCR defined as the ratio between the reduction of oxygen concentration and the dose of the pulse for the specific oxygen concentration P_{O_2}, $OCR(P_{O_2}) = \Delta N(O_2)/N_A * \rho/E_d$. Here, $\Delta N(O_2)$ is the difference in the number of oxygen molecules between the beginning of the pulse and 1 μs post irradiation. N_A is the Avogadro constant. The unit for OCR is $\mu M/Gy$. The G-values and OCRS were averaged on 20 times of simulation to account for the uncertainty.

7.1.2.5 Evaluation of oxygen concentration evolution and oxygen enhancement ratio

The OCR computed above depends on the initial oxygen concentration level. Under the irradiation, as the oxygen concentration is continuously consumed, the variation of the oxygen concentration is governed as

$$\frac{dP_{O_2}}{dt} = -OCR(P_{O_2}) * \dot{D}_i. \tag{7.1}$$

To quantitatively describe this process, we first fit the OCR computed above under different oxygen concentrations as a continuous function of oxygen concentration in the hyperbolic form [319, 320]

$$OCR(P_{O_2}) = OCR_{max} * P_{O_2}/(P_{O_2} + \alpha) \tag{7.2}$$

where OCR_{max} and α are fitting parameters.

During an experiment, a number of pulses of radiation are delivered. The oxygen concentrations and cumulative delivered dose between two successive pulses can be expressed as

$$P_{O_2}(j+1) = P_{O_2}(j) - OCR(P_{O_2}(j)) * \dot{D}_i * t_p \tag{7.3}$$

$$D(j+1) = D(j) + \dot{D}_i * t_p, \tag{7.4}$$

where j is the index of pulses. This expression allowed us to iteratively evaluate time evolution of oxygen concentration. Note that this expression only considered oxygen consumption by radiation and ignored oxygen regeneration caused by diffusion. In contrast, if the OCR is assumed to be a constant, OCR_C, the residual oxygen concentration would be $P_{O_2}(0) - OCR_C * D(j)$.

We further estimated changes in biological effects due to changes in oxygen concentration using oxygen enhancement ratio (OER), which is the ratio of radiation

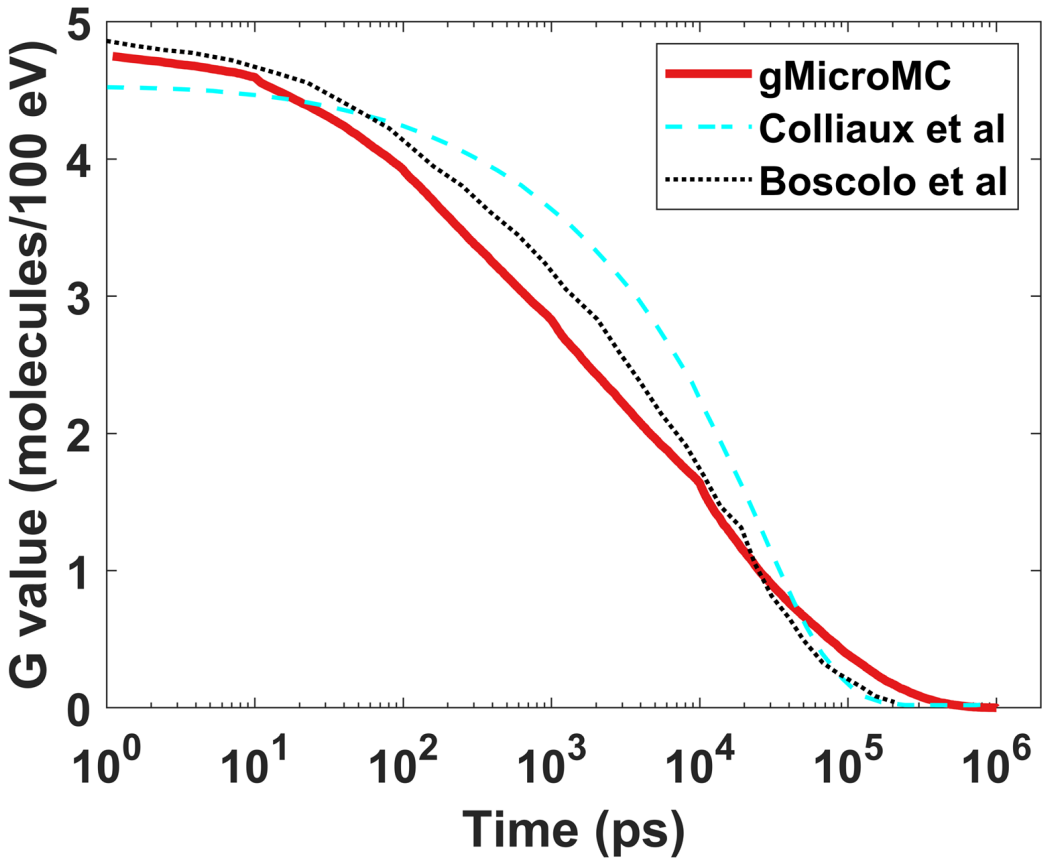

Figure 7.2. Time-dependent yield of e_h radical produced by a 5 MeV proton for $P_{O_2} = 21\%$ (160 $mmHg$, 201.1 μM).

dose without oxygen to that with oxygen to achieve the same biological effect. An empirical formula was used [321],

$$OER(P_{O_2}) = 1 + \Phi_O/\Phi_D * (1 - e^{-\phi P_{O_2}}) \tag{7.5}$$

where $\Phi_O/\Phi_D = 1.63$ and $\phi = 0.26 mmHg^{-1}$.

7.1.3 Results and discussions

7.1.3.1 Validation of simulations of the chemical stage with oxygen included

Figure 7.2 shows the comparison of the calculated chemical yield of hydrated electron e_h for a 5 MeV proton as a function of time after irradiation computed by our

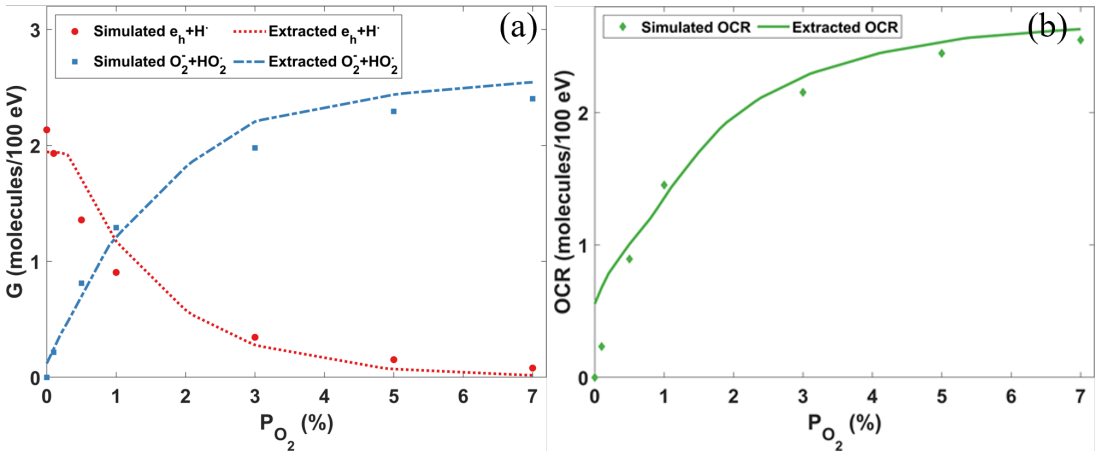

Figure 7.3. (a) Yields of different radicals and (b) oxygen consumption rate (OCR) at 1 μs as a function of oxygen concentration levels for the 10 MeV proton beam. Extracted data were from [256].

study and two other previous studies [256, 305]. The oxygen concentration was 21% (160 $mmHg$, 201.1 μM). $t = 0$ was the moment for the proton entering into the water. The simulation results of gMicroMC generally agreed well with results in the other two works. The differences, mainly the quicker consumption of hydrated electrons by gMicroMC before 10 ns, may be attributed to different values of diffusion rates and reaction rates from different studies and different simulation methods. For example, Brownian bridge method [184] was employed in gMicroMC to take the 'crossing' event into consideration, whereas the other two studies did not considered this effect.

Figure 7.3 showed the comparison of the yields of different radicals and the oxygen consumption rate at 1 μs for a 10 MeV proton beam between our package and the work of [256]. In general, the yields of O_2^- and HO_2, the major product of reactions with oxygen, were consistent between two packages. The oxygen consumption rates matched with each other as well. Yet, there are also some notable differences. For example, as shown in Figure 3 (a), difference exists for the absolute residual amounts of e_h and $H^{\cdot}$, the main radicals reacting with oxygen, and the absolute yields of O_2^-

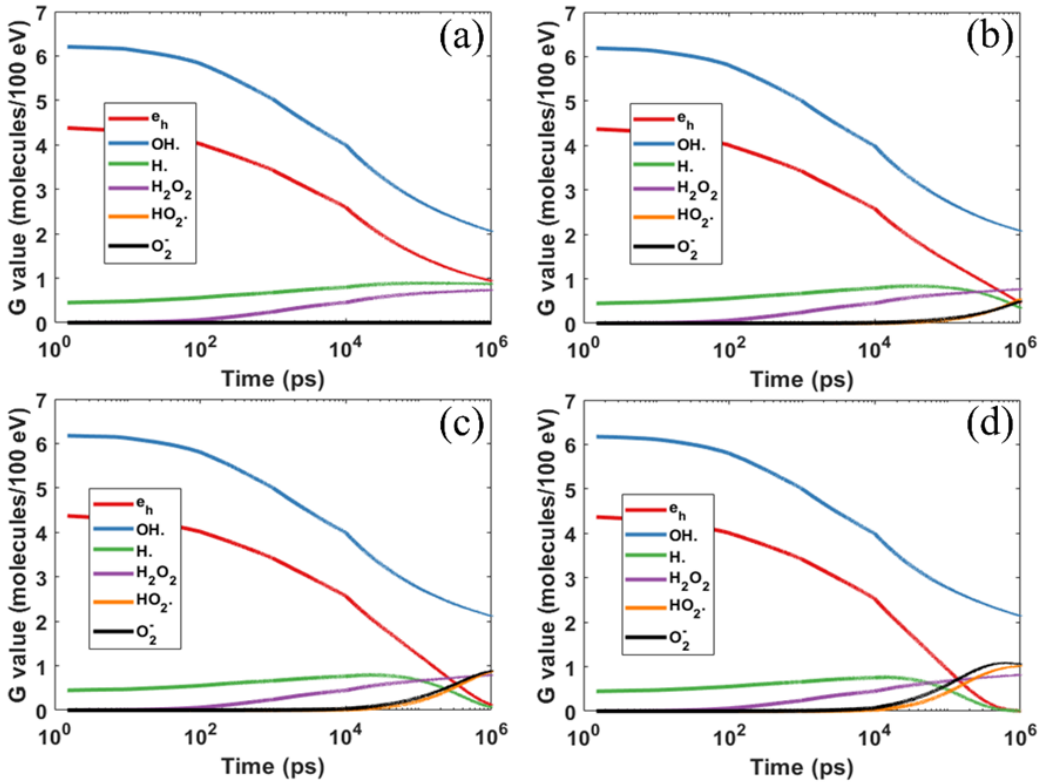

Figure 7.4. Yields of different chemical species as a function of diffusion time under different oxygen concentrations of (a) 0 (b) 3% (c) 9% and (d) 21%..

and HO_2 at different oxygen levels. Since we are using different packages to generate the initial distribution of the radicals from water radiolysis, the observed difference may come from different parameters in different packages. When comparing the OCRs at the low oxygen concentration level from the two simulations, our simulated OCR goes down closer to 0 when the oxygen level drops to 0, which is more consistent with the real situation.

7.1.3.2 Effect of oxygen under a conventional dose rate

Figure 7.4 shows the time evolution of the yields of major chemical species under different oxygen concentrations. There are a few important observations. First,

Table 7.3. G values (molecules/100 eV) of different molecules at 1 μs under different oxygen concentrations

P_{O_2}	e_h	$OH^{\cdot}$	$H^{\cdot}$	$H_2\ O_2$	$HO_2^{\cdot}$	$O_2^{\cdot -}$
0%	0.94	2.02	0.87	0.73	0	0
3%	0.46	2.08	0.34	0.77	0.55	0.50
9%	0.12	2.12	0.07	0.79	0.87	0.89
21%	0.00	2.14	0.00	0.82	1.02	1.06

the impacts of oxygen on various chemical species were found to be different. The reductions of hydrated electron e_h and hydrogen radical $H^{\cdot}$ became more significant with an increasing oxygen concentration level. Yet, yields of hydroxyl $HO^{\cdot}$ and hydroperoxide H_2O_2 only increased slightly. This can be understood as following. As indicated in Table 7.2, oxygen predominantly reacts with e_h and $H^{\cdot}$ (lines 11 and 17), which accounts for the rapid reduction of e_h and $H^{\cdot}$ with the increase of oxygen concentration. Meanwhile, the active reactions of oxygen with e_h and $H^{\cdot}$ radicals in turn reduce the reaction probabilities of $OH^{\cdot}$ with e_h and $H^{\cdot}$ radicals. This leads to a reduced consumption of $OH^{\cdot}$, and hence an increased production of H_2O_2. Numerical results are shown in Table 7.3. The production of $OH^{\cdot}$ and H_2O_2 increased by 6% and 12%, respectively, when P_{O_2} increased from 0 to 21%. Second, massive amounts of $HO_2^{\cdot}$ and $O_2^{\cdot -}$ were produced, but the productions saturated after a certain time, which was found to be dependent on the initial oxygen concentration. The saturation time for P_{O_2}=9% occurred at about 1 μs, while it was around 0.4 μs for P_{O_2}=21%. This trend was also observed by Boscolo et al [256], while a slight difference existed regarding the specific values for the saturation time between the two works.

Third, it required 10 ns to observe a noticeable oxygen effect. From a probabilistic perspective, the species e_h and $H^{\cdot}$ must diffuse a long enough distance to meet oxygen molecules and react with them. Take the case with P_{O_2}=21% (160

$mmHg$,201.1 μM) as an example, where the rise of the yield of O_2^- and HO_2^- can be clearly seen at 10 ns. The average distance d_{O_2} between oxygen molecules can be estimated as $d_{O_2}\ \sqrt[3]{1/(P_{O_2} * N_A)} = 20.2nm$. The time it takes for e_h to meet with an oxygen molecule can be estimated by $\sqrt{6 * (D_(O_2) + D_(e_h)) * \Delta t} = d_{O_2}$, which gave $\Delta t = 9.3\ ns$. This fact also highlighted the need to perform simulations for a relatively long time to investigate effects of oxygen via MC simulations. Previous simulations sometimes stop the chemical stage at 1 ns or 2.5 ns to reduce the computational burden, which is likely not sufficient to fully capture the effect of oxygen.

It can be observed that the time evolution of the yield curves contained some discontinuities, for instance, at 10 ns. This was caused by the change of time step size in gMicroMC. A larger time step size generally leads to a higher reaction probability and hence a steeper change of G value shown in the logarithmic plot. The same reason for the discontinuities in Figure 7.5.

7.1.3.3 Effect of oxygen under the FLASH condition

Figure 7.5 shows the evolution of the chemical yields for different instantaneous dose rates $\dot{D}_i$ under different P_{O_2} with the initial electron energy of E_k=4.5 keV. One notable feature in these curves is the existence of spikes. These spikes were caused by the inclusion of new $OH^{\cdot}$ and e_h radicals generated by new primary electrons at the corresponding moments. Specifically, the large number of additional $OH^{\cdot}$ and e_h radicals increased G values, causing spikes in these two species. In contrast, since the numbers of other radicals were unchanged, and the deposit energy was increased, the G values of radicals other than $OH^{\cdot}$ and e_h were reduced at those moments. Comparing the three columns of Figure 7.5, it was found that the dose rate has impacts on radical yields due to spatial density of radicals. We then summarized the mean G values from the 20 runs for critical radicals in Table 7.4. From both Figure

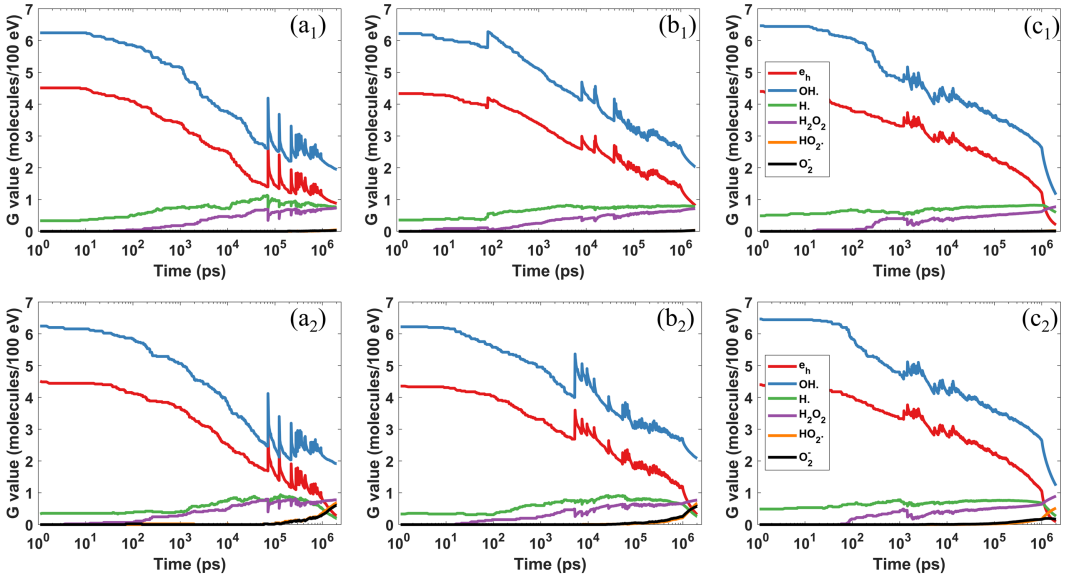

Figure 7.5. Comparison of the chemical yields under different dose rates of FLASH radiation with $\dot{D}_i$i= (a) 10^6 Gy/s (b) 10^7 Gy/s and (c) 10^8 Gy/s. Top and bottom rows represent P_{O_2}=0.1% (hypoxia) and 3% (physoxia). Note, the result was taken from one simulation to show the evolution of radicals specifically and the spikes may be different for different simulation runs..

Table 7.4. G values (molecules/100 eV) of different molecules at 1 μs post irradiation under different oxygen concentrations

Dose rate (Gy/s)	P_{O_2}	e_h	$OH^{\cdot}$	$H^{\cdot}$	H_2O_2	$HO_2^{\cdot}$	$O_2^{\cdot-}$
10^6	0.1%	0.83	1.92	0.79	0.75	0.04	0.03
	3%	0.28	1.94	0.21	0.81	0.70	0.62
	21%	0	2.04	0	0.82	1.05	1.03
10^7	0.1%	0.82	2.03	0.78	0.72	0.03	0.03
	3%	0.32	2.08	0.26	0.77	0.67	0.58
	21%	0	2.13	0.01	0.82	1.11	1.01
10^8	0.1%	0.20	1.16	0.60	0.78	0.02	0.01
	3%	0.09	1.23	0.27	0.90	0.52	0.17
	21%	0	1.31	0.02	1.00	1.24	0.40

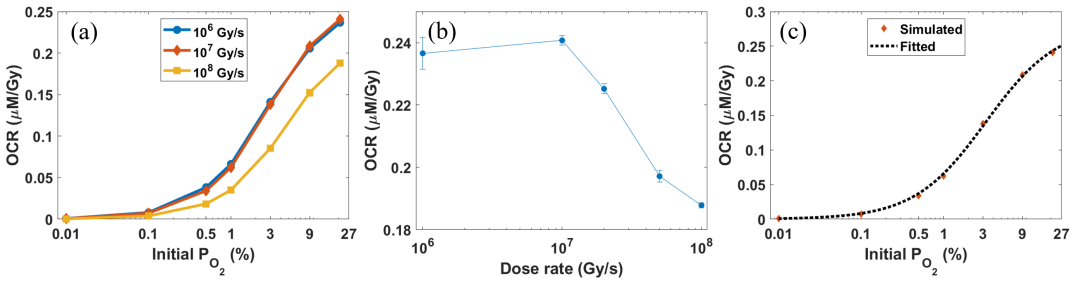

Figure 7.6. (a) Average OCRs for different instantaneous dose rates $\dot{D}_i$i from our simulation study. (b) The average OCRs for different dose rate with P_{O_2}=21%. Error bars represent the standard deviation from 20 simulation runs. (c) The simulated OCRs and the fitted OCR curve under different initial oxygen concentration levels with $\dot{D}_i$i=10^7 Gy/s. .

7.5 and Table 4, the results indicated that the probability of mutual reactions among radicals generated by initial electrons increased along with the increased dose rate, as the spatial density of radicals increased, and hence they were more likely to react. This can be seen from two aspects. First, both yields of e_h and O_2^- decreased for $\dot{D}_i$=10^8 Gy/s compared to that for $\dot{D}_i$=10^7 Gy/s. As O_2^- can only be generated by the reactions between oxygen and e_h, simultaneous reduction of e_h and O_2^- implied that $e_h$was largely consumed even without the participation of oxygen. Second, the yield of $OH^{\cdot}$ reduced for $\dot{D}_i$=10^8 Gy/s, compared to that for $\dot{D}_i$=10^7 Gy/s. But as discussed in above, the inclusion of oxygen dose not lead to the reduction of $OH^{\cdot}$. Hence, the reduction of $OH^{\cdot}$ suggested increased reactions between $OH^{\cdot}$ and other radicals.

The dependence of OCR on initial P_{O_2} levels for different $\dot{D}_i$ are plotted in Figure 7.6(a) with E_k=4.5 keV. The OCR quickly dropped as the initial oxygen concentration decreased because of the reduction in reaction probability between oxygen and radicals. Numerically, for $\dot{D}_i$=10^7 Gy/s, the OCR dropped from 0.23 $\mu M/Gy$ for an oxygen concentration level of 21% to 0.0007 $\mu M/Gy$, when the concentration

was decreased to 0.01%. In terms of the dependence on dose rate, for P_{O_2}=21%, it remained unchanged at 0.22-0.23 $\mu M/Gy$ for $\dot{D}_i$=10^6 10^7 Gy/s. When the dose rate was increased to 10^8 Gy/s, OCR dropped rapidly to 0.19 $\mu M/Gy$. We knew from Figure 5 that radicals must travel a long enough distance to react with oxygen molecules from a probabilistic view. Mutual reactions between radicals may happen before they collide with oxygen molecules, but the overlap between different tracks was very unlikely for small $\dot{D}_i$. Only when $\dot{D}_i$ exceeds a certain threshold, it will show the consequence of reduced OCR. To investigate this threshold, we have performed two new simulations with $\dot{D}_i$=2×10^7 Gy/s and $\dot{D}_i$=5×10^7 Gy/s. We plotted the variation of OCR versus dose rate with P_{O_2}=21% in Figure 7.6(b). We found that for all simulated dose rates larger than 10^7 Gy/s, the OCR drops quickly. We hence estimate that the threshold dose rate is around $\dot{D}_i$=10^7 Gy/s, under the current setting with pulse width of 1 μs.

From Figure 7.6(a), we used Equation (7.2) to fit $OCR(P_{O_2})$. As an illustration, we showed the results for $\dot{D}_i$=10^7 Gy/s in Figure 7.6(c). The fitting parameters OCR_{max} and α were 0.270 $\mu M/Gy$ and 0.030, respectively.

With the fitted OCR curve, we computed the time evolutions of oxygen concentration using Equation (7.3) for the irradiations under a dose rate of $\dot{D}_i$=10^7 Gy/s and an initial oxygen concentration of P_{O_2}=21% and 0.1%, respectively. The results are plotted in Figure 7.7(a). If 0.001% was taken as the criteria of oxygen depletion, it would require 1770 Gy and 500 Gy to reduce oxygen to this level for initial P_{O_2}=21% and 0.1%, respectively. On the other hand, after D_{total}=30 Gy, a typical dose used in FLASH experiments, the residual oxygen concentrations for different initial P_{O_2} were computed and plotted in Figure 7.7(b). Notably, the final oxygen concentration was always above zero. As a comparison, we plotted the residual P_{O_2} under the as-

sumption of a constant OCR_C=0.42 $mmHg/Gy$ (0.53 $\mu M/Gy$) [315]. In this case, the oxygen would be depleted, if the initial P_{O_2} was lower than 1.6%.

In the low dose rate conventional radiotherapy, oxygen regeneration should be considered, and the cells can be viewed as exposing to a constant oxygen concentration surrounding. Consequently, we used the initial P_{O_2} value to compute the OER for conventional radiotherapy. Its behavior with different initial P_{O_2} was plotted in Figure 7.7(c) by the red solid line. As for the FLASH radiation, assuming the oxygen regeneration is ignored, we then computed its OER with the oxygen level at the end of the radiation. Its behavior with different initial P_{O_2} and a total dose of 30 Gy is plotted in Figure 7.7(c) by the dash lines. OER dropped from 1.3 to 1.2 for the initial hypoxia oxygen concentration of P_{O_2}=0.1%, from 2.63 to 2.62 for physoxia condition of P_{O_2}=3%, and stayed almost unchanged for normoxia condition of P_{O_2}=21%. In contrast, with a constant consumption rate of OCR_C=0.42 $mmHg/Gy$ [315], the changes in OER were from 1.3 to 1 for P_{O_2}=0.1%, and from 2.63 to 2.50 for P_{O_2}=3%.

The reduction in OER for FLASH radiotherapy compared to conventional radiotherapy provides the possibility of dose escalation, with potentially improved dose tolerance of normal tissues (Vozenin et al., 2019a). The ratio between OERs of the conventional radiotherapy and that of FLASH radiotherapy is plotted in Figure 7.7(d). With a constant OCR, an OER ratio as large as 2.61 at the initial oxygen level of 1.6% can be obtained, which corresponds to the sharp fall-off of OER for FLAH-RT with constant OCR in Figure 7.7(c). In contrast, the maximum ratio was only about 1.08, once the varied OCR obtained from our simulation was used for the computation of the OER. We comment that the calculation overestimated the oxygen concentration for conventional radiotherapy and hence its OER, because oxygen consumption occurs, as long as there exists radiation radicals. Meanwhile, it underestimated the oxygen concentration for FLASH radiotherapy and its OER,

because we used the minimum value of oxygen concentration after the radiation and ignored oxygen regeneration. Therefore, we overestimated the ratio between OER of conventional radiotherapy and that of FLASH radiotherapy.

7.1.3.4 Computational efficiency

Since one of the motivations of this study was to demonstrate the practical value of gMicroMC to handle computationally challenging MC simulation problems in the presence of oxygen, we report the computational time required to perform the study. Due to the lack of the step-by-step simulation support of oxygen effect in the chemical stage in other CPU-based MC packages, we effectively evaluated the efficiency of our package by comparing to GEANT4-DNA under simulations of approximately the same number of molecules in the region of interest for the chemical stage. Although Geant4-DNA is distinct from gMicroMC that it cannot simulate radical interactions from different tracks simultaneously, this comparison is still valid, because the simulation time is mainly determined by the number of molecules. For the simulation of 103 molecules (P_{O_2}=0%) with the chemical stage ending at 1 μs, the speedup factor was 30 for gMicroMC running on one Nvidia Titan Xp GPU (1.58 GHz) card as compared to GEANT4-DNA running on a single core of Intel i7-6850K CPU (3.6 GHz). When the molecule number increased to 105 (P_{O_2}=3%), the speedup factor increased to 1228 (Table 7.5). We did not perform the simulations for the case of P_{O_2}=21% with Geant4-DNA, because the computation time can be 4 5 orders higher than that for the zero-oxygen case. In contract, gMicroMC can handle the simulation in an affordable time. It took twenty hours to simulate seven million molecules for the FLASH cases with the chemical stage ends at 2 μs. It needs to be pointed out that both techniques can be further accelerated using, e.g. multi GPUs for gMicroMC or a CPU cluster for GEANT4-DNA.

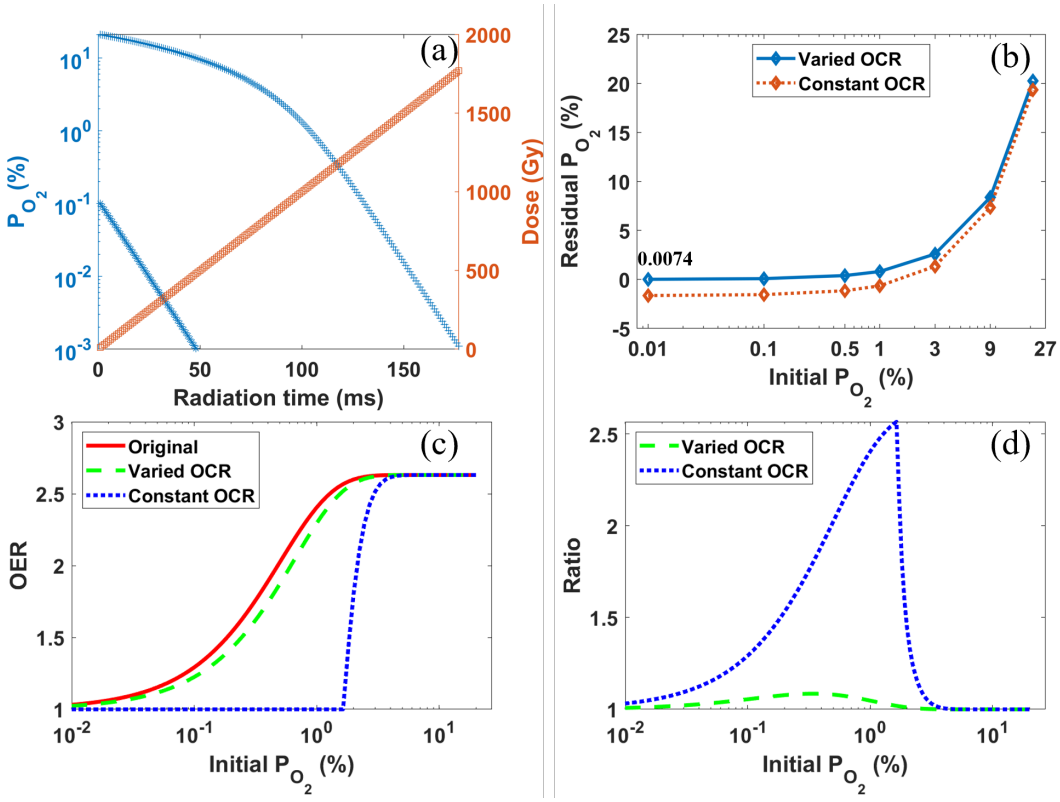

Figure 7.7. (a) The time evolution of oxygen concentration P_{O_2} and total dose for $\dot{D}_i$=10^7 Gy/s with two different initial oxygen levels. (b) The residual oxygen concentration for $\dot{D}_i$=10^7 Gy/s after receiving a dose of 30 Gy. (c) The OERs as a function of the initial oxygen concentration levels under conventional radiotherapy ("Original"), and under FLASH radiotherapy of $\dot{D}_i$=10^7 Gy/s with a constant OCR ("Constant OCR") and from our calculation ("Varied OCR"). (d) The ratio of OER between conventional radiotherapy and FLASH radiotherapy as a function of different initial oxygen levels, with constant and varied OCRs, respectively. .

Table 7.5. Time performance for gMicroMC and GEANT4-DNA running same number of molecules to 1 μs

P_{O_2}	Number of molecules	GEANT4-DNA	gMicroMC
0%	10^3	61 s	2 s
3%	10^5	70000 s	57 s
21%	10^6	$*$	227 s

$*$ simulation not performed due to long computation time.

7.1.4 Discussion

The current study only investigated the impact of oxygen on the chemical yields of radicals. It is probable of more relevance to study the impact on DNA damages. Actually, gMicroMC is able to achieve this goal with its DNA geometry model. However, as the DNA damages are generated only by the hydroxyl radicals in gMicoMC, and the existence of oxygen was not found to significantly change the hydroxyl radical yield (Table 7.3 and Figure 7.5), oxygen in the simulation would then unlikely change the DNA damages. We have performed a simulation to compute DNA damages under the conventional dose rate and compared the results with those at P_{O_2}=0%. The damages were found to be slightly increased by 8% at P_{O_2}=3% and 10% at P_{O_2}=21%. Moreover, the DNA damage calculation in current gMicroMC did not consider other aspects of oxygen, such as the oxygen fixation hypothesis on the DNA repair process triggered by the initial damages. To consider the biological consequence of DNA damages, it would be necessary to include these into the simulation, for instance, by considering the variation of DNA damage probability with regards to oxygen concentration [229].

When we computed the G-values for different chemical species, we considered only those secondary electrons initially produced inside the 10 um water slab. This may cause a concern that the boundary-crossing electrons could alter the computational results. Yet, when we simulated the secondary electron distributions for the first few tens of micrometers along its depth direction with Geant4, we found that the kinetic energies of most secondary electrons were of a few hundred eVs, or equivalently, their travel lengths were of a few hundred nanometers. Hence, only those secondary electrons produced a few hundred nanometers away from the slab boundary could have a non-zero boundary-crossing probability. Additionally, the produced radicals all had diffusion lengths of a few hundred nanometers with a chemical stage

duration of 1 μs (Table 7.1), which further implied that the boundary effect was quite limited. To verify our estimation, we performed a new simulation by considering all secondary electrons in a slab 2 μm thicker than the slab-of-interest and computed the G values for radicals inside the slab-of-interest. Comparing the newly obtained G values to that obtained in section 2.2, the mean absolute and maximum differences between the two simulations were found of 2% and 3.8%, respectively, for all radicals with G value higher than 0.1 per 100 eV, indicating that the boundary-crossing electrons did have limited impact on the simulation results.

Pratx and Kapp [315] analyzed the oxygen depletion at different dose rates. They solved differential equations for the diffusion of dissolved oxygen molecules from a blood microvascular structure to the cells under different dose rates and estimated the OER according to different remaining oxygen concentration after radiation. It was concluded that the oxygen depletion can be achieved at a low oxygen concentration level with a high dose rate. However, under a typical dose level of 30 Gy used in FLASH experiments, we found the oxygen is unlikely to be depleted, although it may occur at a very high dose level, e.g. 1000 Gy. In addition, due to the decreased OCR with reduced oxygen concentration, our simulation results showed a relatively small OER change. The different conclusions between Pratx et al. and ours were caused by the different treatments of OCRs. A constant OCR (the 'L_{ROD}' term in their paper) was assumed, whereas the OCR may not be a constant, as shown in our simulation via mechanistic modeling of the chemical stage, because the probability for radicals to meet and react with oxygen molecules decreases, as the oxygen distribution gradually becomes sparser in the space. On the other hand, Labarbe et al. [322] considered the oxygen effect in FLASH by solving a system of ordinary differential equations (ODEs) representing the biological reactions at more than 1 μs post irradiation with presence of oxygen. They reported that the oxygen reactions were suppressed under

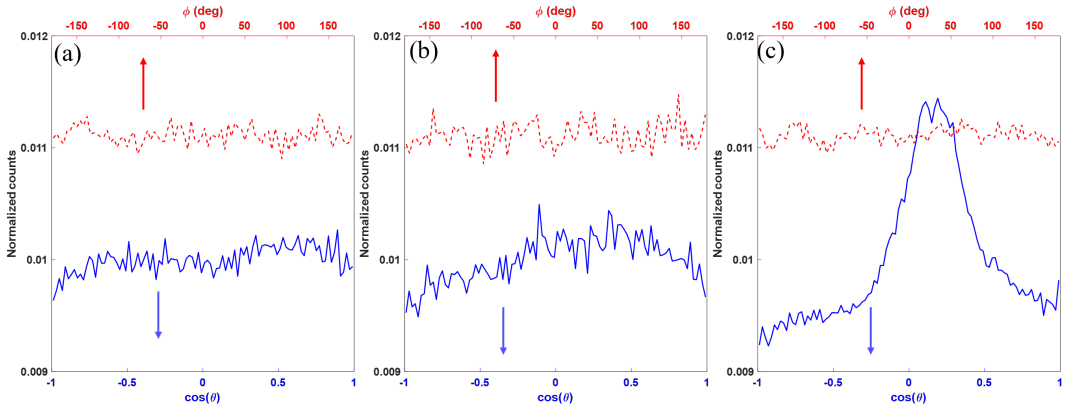

Figure 7.8. Angular distributions of secondary electrons from (a) 1 MeV photon (b) 1 MeV electron and (c) 4.5 MeV proton beams. θ and ϕ are polar and azimuth angles in the spherical coordinate system. The incident beam direction is along z axis..

FLASH dose rates. However, the reason differs. They attribute the decreased oxygen reaction, and hence a reduced production of the radiobiological damaging radicals to an increase of self-recombination of alkyl radical $R^{\cdot}$ after typical chemical stage of 1 μs. In our simulation, the reduced OCR is due to an increased mutual reaction between radicals in chemical stage. It may require more efforts to specify the overall oxygen effects in the FLASH radiotherapy.

The computations were performed using electrons with E_k=4.5 keV. We have also performed the simulation using electrons with E_k=0.3 keV, as the two energies play important roles in water radiolysis, creating spurs, blobs, and short tracks for DNA damages (Ward, 1988). Quantitative results were slightly different. For instance, for E_k=0.3 keV, the calculated OCR were 0.31, 0.32 and 0.23 $\mu M/Gy$ for dose rates of 10^6 , 10^7 and 10^8 Gy/s, respectively, at the oxygen concentration level of 21%. However, the same behavior in terms of OCR reduction with reduced oxygen concentration was observed. The oxygen may not be depleted under FLASH condition and the consequent change of OER due to oxygen consumption was also small.

With a further analysis, the findings from our current simulation studies could be extendable to the preclinical photon or electron FLASH radiotherapy. The reason is of two-fold. First, in our simulation study, we initialized our primary electrons with a uniform spatial distribution and an isotropic momentum direction, which is found consistent with secondary electron distributions from MeV photon or electron beams in a water phantom (Figure 7.8). We obtained Figure 9 via shooting three irradiation beams (1 MeV photon, 1MeV electron and 4.5 MeV proton) along the z axis into a water phantom and recording the secondary electron distributions in the spherical coordinate system. From Figure 7.8, the maximum difference for the polar($\cos(\theta)$) distribution of secondary electrons from the photon and electron beams are 3.1% and 4.5%, and that for the azimuthal (ϕ) distribution are 0.4% and 0.6%, respectively. In contrast, there is a significant forward distribution for the simulation case with a proton beam, which alters the uniform distribution assumption. Second, the electron energies of 4.5 keV and 0.3 keV used in our study are also found representative for the second electron spectrum from the MeV photon and electron beams. Specifically, we found that the portions of secondary electrons with kinetic energies ≤ 4.5 keV are 64.9% and 99.9% for 1 MeV photon and 1 MeV electron beams, respectively. In the former case, if we take those secondary electrons produced from the photon interactions as primary, their further induced secondary electrons have kinetic energies well below 4.5 keV, just as that for the 1 MeV electron case. In the overall water radiolysis process triggered by the 1 MeV photon or electron beams, these low energy secondary electrons (below 4.5 keV) contribute more than 99% of the total radical productions. Combining all these factors, we reasonably referred that the simulated energies of the electrons well represent the situation for x-ray or electron beam FLASH radiotherapy.

As shown in our previous study [259] and other similar studies [207, 240, 279], one important aspect affecting result validity in MC simulations is the uncertainty

introduced by unrefined parameter values. As specific to this study, uncertainties in the diffusion and reaction rates can be of concern. Take reaction 11 in Table 2 as an example, total diffusion rates of 7.3 and 6.6 nm^2/ns, and reaction rates of 1.74×10^10 and 1.9×10^10 $dm^3 mol^{-1} s^{-1}$ were used in gMicroMC and TRAX-CHEM [256], respectively. There was a 10% difference between the two packages, which will lead to about 10% differences of the reaction radii. To study its impact on our simulation results, we reperformed the computations at P_{O_2}=21% for electrons with E_k=4.5 keV and the reaction radii changed by 10%. The yields of different chemical species were found only minimally changed with a maximum of the change being 0.3%. The robustness can be understood as following. Oxygen distribution is very sparse compared to the reaction radii. Mean distance between oxygen molecules is 20 nm for P_{O_2}=21% (160 $mmHg$,201.1 μM) while the radii are usually less than 1 nm. Hence, the uncertainties in the reaction radii caused by different reaction rates and diffusion rates is very small compared to the large distance between reactants. Asides from the uncertainty of parameters, the stochastic nature of MC simulation would cause uncertainty of results as well. Unlike the case for conventional dose rate mode, where 1000 runs were needed to reduce uncertainty to 0.5% level, the simulation results for FLASH mode were relative more robust because there are already many electrons inside one pulse. For all oxygen concentrations, 20 runs per simulation were adequate to reduce the uncertainty to a level of 3% for 10^6 Gy/s and well below 2% for cases with dose rate higher than it.

As discussed in [305], it is expected that the results, e.g. in terms of yields, computed by explicitly treating oxygen as molecules and as a continuum background in MC simulations should be similar. However, this is only valid in certain scenarios. For instance, when the oxygen consumption occurs in a spatially small and temporally large scale, oxygen diffusion can compensate the consumption, making the oxygen

distribution spatially and temporally approximately unchanged. Another scenario is when irradiation tracks are dense enough and most reactions happen among radicals. In this case, the effect of oxygen inhomogeneity may be ignored. However, the FLASH condition does not fall in these categories, which hence likely requires the method explicitly treating oxygen as molecules. Oxygen diffusion length for 2 μs is only 170 nm and it would be difficult for oxygen to diffuse from the outside of the ROI to the middle of the ROI to compensate the oxygen consumption.

7.1.5 Conclusions

In this work, we reported our recent progress on the modeling of the chemical stage of the water radiolysis with an explicit consideration of the oxygen reaction effect, and its implementation in the open-source GPU-based MC simulation tool, gMicroMC. To demonstrate the practical value of gMicroMC in large scale simulation problems, we applied the oxygen-simulation-enabled gMicroMC to compute the yields of chemical radicals under a high instantaneous dose rate $\dot{D}_i$ to study the oxygen depletion hypothesis in FLASH experiments. We computed the time evolution of oxygen concentration under FLASH irradiation setups. At the dose rate level of 10^7 Gy/s and initial oxygen concentrations from 0.01% 21%, the oxygen is unlikely to be fully depleted with an accumulative dose of 30 Gy, which is a typical dose used in most FLASH experiments. gMicroMC is found efficient in simulating the chemical stage with oxygen effect explicitly considered. With an initial oxygen concentration of 3% (105 molecules), a speedup factor of 1228 was achieved for gMicroMC on a single GPU card when comparing with Geant4-DNA on a single CPU. This implementation makes a more elaborate model of oxygen enhancement on DNA damages, which will be presented in the following sections.

CHAPTER 8

OER MODEL AND REINVESTIGATION ON FLASH

8.1 Oxygen enhancement ratio

8.1.1 Introduction of oxygen enhancement on DNA damages

It has long been known that the existence of molecular oxygen can modify radio-sensitivity ([23, 24, 304]). Higher oxygen concentration leads to cells being more vulnerable to ionizing radiation. There are two reasons for this phenomenon. First, molecular oxygen can react with chemical products of water radiolysis process ([323]), altering the yields of different radicals ([258]). For instance, high concentration of oxygen can effectively eliminate hydrated electrons and hydrogen radicals and produce toxic superoxide $O_2^{\cdot-}$ radical and its protonated form $HO_2^{\cdot-}$. Second, molecular oxygen can react with DNA radicals, which are carbon-centered radicals after ionization radiation ([28, 29]). The product of this reaction is easier to cause strand break (SB) than the initial DNA radicals themselves ([29, 324]). To quantify the degree to which the vulnerability of cell has been changed, the concept of oxygen enhancement ratio (OER) is introduced. It is defined as the ratio between doses required to achieve same biological effects without and with oxygen,

$$OER(p_{O_2}) = \frac{D(0)}{D(p_{O_2})}|_{isoeffect} \tag{8.1}$$

where p_{O_2} represents the partial oxygen pressure and $D(p_{O_2})$ the dose for certain biological endpoint with p_{O_2}.

It is important to model OER from both clinical and mechanism aspects. Clinically, an OER model may help design treatment plan for tumor with hypoxia areas, which would be radio-resistant (OER 1). On the other side, an OER model may help

understand clinic phenomenon and testify hypothesis. For example, the role of oxygen in a recent hot topic FLASH radiotherapy ([325, 326]) and relationship between OER and linear energy transfer (LET) ([327]).

Current OER models could be divided into three categories based on the methods used in different models. First category is based on linear quadratic (LQ) model ([4, 21]). For this category, assumptions were made on the dependencies between parameters *alpha* and *beta* of LQ model and p_{O_2} and LET ([328, 329]). Usually, the values of parameters in the assumption were obtained from experimental data. However, this fitting procedure suffered from the dependence between OER and choices of biological endpoints. Second is based on statistical analysis of collisions between oxygen molecules and DNA ([321]). But, this study has limitations in application to high LET cases because of the Poisson distribution, as concluded in the paper. Another one is based on microscopic Monte Carlo (MC) simulations, where track structures ([274]) are involved. For this category, either dose-mean lineal energy y_D ([283]) or DSB damage clusters ([229]) were used to further evaluate OER. However, the absence of DNA structure and oxygen in simulating track structures makes the results defective in principle.

From the above works, we can infer a good OER model should

1. capture the biological features of OER to be more robust in principle.
2. explain the behavior between OER and other experiment conditions such as LET.
3. have fitted model parameters irrelevant to source types or choices of biological endpoints. In other words, these parameters should be intrinsic properties of the biology system.

For the above purposes, OER models based on microscopic MC simulations would be preferable. On one side, MC simulation is faithful to physics principles and gives

details about the interaction events. On the other side, experimental conditions like different source particles can be used as input to match OER variation tendency, leaving model parameters universal. However, Fully mechanistic modelling of water radiolysis via microscopic MC simulation, especially with presences of DNA structure and oxygen molecules, is quite difficult because of computational burdens in both memory and time.

Graphical Processing Unit (GPU)-based parallel computing can be a cost-effective option ([53, 54]) to accelerate the simulation. Our group has done a lot of continuous work to develop the GPU-based programs, gMicroMC. We initially focused on the chemical stage simulation among radicals ([201]) and later a whole package enabling simulation of the physical track for electrons and DNA damages with a DNA model of a lymphocyte cell nucleus at the base-pair resolution ([52]). Recently, we have also tested simulation of oxygen molecules in the chemical stage with a step-by-step manner ([258]) and updated support to transport for protons and heavy ions and simulation with presence of DNA in chemical stage ([72]). With these efforts, we were able to quantitatively study problems that are computationally demanding. For example, the radiolytic depletion of oxygen under ultra-high dose rate radiation (FLASH) ([258]). The first version can be downloaded on GitHub https://github.com/utaresearch/gMicroMC while developing version can be obtained via request. In this work we report our recent work on modelling OER via microscopic MC simulation on DNA damage. The primitive objectives of this work were

1. to provide a model for OER with biological explanations based on mechanistic simulation.
2. to achieve experimentally observed values of OER for different cases.

8.1.2 Methods

8.1.3 Modelling oxygen enhancement on DNA double strand break

8.1.3.1 Brief introduction of gMicroMC

gMicroMC is a GPU-based microscopic MC simulation package that is able to compute DNA damages with the built-in DNA model of lymphocyte cell ([52, 72]). The simulation is divided into four stages–physical stage, physicochemical stage, chemical stage and searching for DNA damage. In the physical stage, it transports primary particles and secondary electrons, producing ionized and excited water molecules. The time for a source particle traversing several micrometers, which is often the scale of region of interest (ROI), is only of magnitude 10^{-18} seconds. The information of every energy deposition events, such as positions and excitation types, is recorded. In the physicochemical stage, the de-excitation process of those recorded molecules is simulated, generating the initial distribution of radicals at a preset time 10^{-12} seconds. These radicals then diffuse in chemical stage in an environment with DNA structures and oxygen molecules. Along with the diffusion, reactions among radicals, between radicals and DNA components and between radicals and oxygen molecules are examined in a step-by-step simulation scheme. Hence, the DNA damage sites attacked by hydroxyl could be recorded. Finally, deposited energy is accumulated to its nearest DNA components and is used to determine a strand break (SB) together with information of DNA damage sites by hydroxyl. To keep this article concise, details about explicit simulation parameters such as searching radius and SB criteria are omitted here. Interested readers could find more explanations in our previous publications ([52, 72, 259]).

8.1.3.2 Oxygen enhancement

We consider the oxygen enhancement on radio-sensitivity only stems from the interplay between oxygen molecules and DNA radicals $R^{\cdot}$. The existence of oxygen not affecting the physical stage and the physicochemical stage is a reasonable assumption because of very short time scale of these two stages and the relative few number of oxygen molecules in aqueous environment. In fact, the concentration of water molecule is $55.6\ M$ but the concentration of dissolved oxygen is $0.2\ mM$ for normoxia. And the root-mean-square diffusion length of oxygen in $1\ ps$ is only $0.12\ nm$, given the diffusion constant of oxygen $D_{O_2} = 2.4\ nm^2/ns$. Hence, either the incident particles or the excited water molecules basically only "see" water molecules around them in a vert short time.

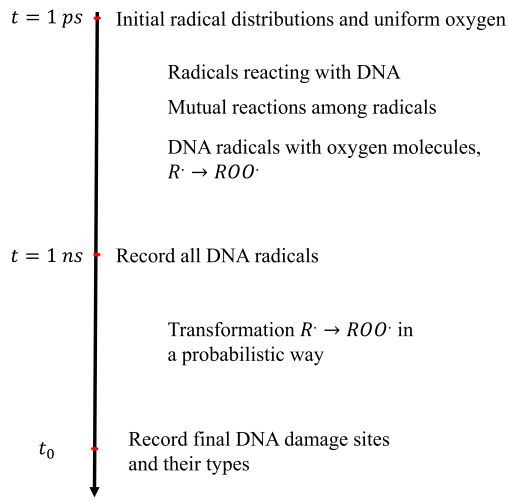

Figure 8.1. Illustration of the simulation scheme.

The essential idea of our model is the usage of two kinds of DNA radicals, $R^{\cdot}$ and $ROO^{\cdot}$, where $ROO^{\cdot}$ is the product of chemical reaction

$$R^{\cdot} + O_2 \rightarrow ROO^{\cdot} \tag{8.2}$$

As shown in Fig. 8.1, the production of $ROO^{\cdot}$ comes from two aspects. In the beginning of chemical stage, the reactions among radicals are quite intense and hydroxyl radicals could continuously attack DNA if they are not consumed. Hence, we adopted step-by-step (SBS) manner to simulate this process. To include DNA radicals into the simulation scheme, $R^{\cdot}$ or $ROO^{\cdot}$ is considered as a point with same position as that of hydroxyl, which could react with DNA sugar-phosphate moiety. Reaction (8.2) is thus considered as fully diffusion-controlled with reaction rate $k_0 = 5 \times 10^7\ (mol/L)^{-1}s^{-1}$ ([330]). Under this scheme, the influence of the presence of DNA structure and oxygen molecules on radical yield and distribution of DNA radicals is considered naturally. We chose the first 1 ns to conduct such SBS simulation because it is considered to be the lifetime of hydroxyl in cell environment.

Then we introduced the first parameter t_0 into our model. It represents the time interval, within which oxygen molecules must be present near $R^{\cdot}$ to make reaction (8.2) happen. This is related to a fact that no increase in OER occurs if oxygen is added too late post irradiation ([331]). The threshold is considered to be several milliseconds, which would be the magnitude of parameter t_0. From termination of hydroxyl radicals till t_0, we considered every remaining $R^{\cdot}$ was bathed in a background of oxygen and its probability to transform into a $ROO^{\cdot}$ could be expressed ([186]).

$$P(R^{\cdot} \rightarrow ROO^{\cdot}) = e^{-k_0 * t_0 * p_{O_2}} \tag{8.3}$$

Here, p_{O_2} should be expressed in unit of mol/L, consistent with the unit of k_0. The unit transformation (percentage, mol/L and $mmHg$) of p_{O_2} has been illustrated in our previous work ([258]) with the help of Henre's law

$$p_{O_2}(\mu mol/L) = 1.26 * p_{O_2}(mmHg) = 957.6 * p_{O_2}(\%). \tag{8.4}$$

For the following text, we will treat the three units equally and use them without further explanation.

So far, we recorded the positions and types of two kinds of DNA radicals. We made another assumption that they had different potential to cause SBs. We assigned two probabilities p_0 and p_1 for $R^{\cdot}$ and $ROO^{\cdot}$, respectively. To determine whether a SB should be recorded, we could sample random numbers ξ between 0 and 1 for each DNA radicals and compare it with the probability associated to this location. If $\xi < p_0$ or $\xi < p_1$, depending on the type of DNA radicals, a SB was formed and could be used later for grouping into double strand breaks (DSBs).

8.1.4 Computation of OER

Conventionally OER is defined with biologically measurable endpoint, such as cell survival fraction (SF). Although are many studies ([48, 332, 333] that aim to related microscopic simulation results with SF, we argued that it may not be a good option to do so for two reasons. First, these models relied on obtaining the relationship between parameters of LQ model and simulation results like linear energy $\overline{y}$. Their accuracy would be affected by the deviation of LQ model from experimental results ([21]) and the model parameter fitting process for benchmark. The uncertainty of predicting SF would make calculation of OER suffering from larger uncertainty and thus nor reliable. Second, most of these models were case dependent, for instance, more applicable to high LET case ([48]), losing generality. Hence, in this work, we

directly used the number of DSB as the endpoint to measure biological effect. This was because DSB was considered as the lethal factor to cell death after ionization radiation. Similar idea was used in ([229, 334]). The difference was that we only assumed one-to-one function between the number of DSB and SF but we did not know the exact form. It implied that same number of DSB was related to same SF, i.e. same biological endpoint. Thus, from equation (8.1) OER could be expressed as

$$OER(p_{O_2}) = \frac{D(0)}{D(p_{O_2})}|_{N_{DSB}}. \tag{8.5}$$

8.1.5 Evaluation

For the purposes described in Section 8.1.1, we first conducted simulations of photon cases (X-ray 280 kvp) as described in ([24]) and used it to benchmark the three parameters t_0, p_0, p_1 for our model. The simulation is divided into two steps ([208]). We first obtained the electron energy spectrum from the photon source and then sample electron from the spectrum but uniformly distributed in space ([258]) one by one until the dose inside the cell nucleus reached target dose. Number of oxygen is calculated as $N_{O_2} = P_{O_2}(\mu mol/L) \times V_{cell} \times N_A$, where V_{cell} is the volume of cell nucleus and N_A Avogadro constant. Oxygen molecules were also uniformly distributed in the space at the beginning of chemical stage. After we obtained the relationship between N_{DSB} and dose D, we could find the fitting slope m by applying $N_{DSB} = m \times D$. Because typically OER for x-ray scenarios does not depend on the selection of biological endpoints, equation (8.5) is equal to

$$OER(p_{O_2}) = \frac{m(p_{O_2})}{m(0)}. \tag{8.6}$$

The adjustment was performed as following. First, we set $p_{O_2} = 0$. Then, t_0 and p_1 is of no use and we could adjust p_0 to match the absolute DSB yield per Gy per Gbp, whose value was 8 ([208]) in our simulation. Next, we set $p_{O_2} = 21\%$.

Under this case, we could assume all $R^{\cdot}$ has been transformed into $ROO^{\cdot}$ because of the saturation behavior of OER at large oxygen concentration. we could adjust p_1 so that the maximum of OER matched experiment results, which was 3 in our simulation. Finally, We simulated cases with $P_{O_2} = 0.1\%, 0.5\% and 1\%$. We adjusted t_0 to match the trend between OER and p_{O_2} in the range $0 - 2\%$.

To further validate this model, we applied it directly to the proton cases. The proton source is a beam with energy $79.7MeV$. Cells were put at different depth along the beam to undergo proton radiation of different LET. We chose the same depth point as in reference ([290]). We examined the obtained OER for protons with LET 1.8 $keV/\mu m$. Then we calculated maximum OER versus LET and the maximum of OER versus dose for LET 15.2 $kev/\mu m$ and compared them to reported results in other literature.

8.1.6 Comparison with other works

After the process described in section 8.1.5, the parameter values were $t_0 = 3.8\ ms$, $p_0 = 0.08$ and $p_1 = 0.28$. The obtained OER results were shown in Fig. 8.2. As can be seen from the figure, the simulated OER generally matched the experimental one, especially for the region with low oxygen concentration. The mean relative error is 3.18%. The fitted line from mechanically statistical analysis was within error bar of the simulated results as well. But they deviated from experimental results when oxygen partial pressure larger than 20 mmHg, while our simulation results captured the trend within uncertainties.

With the implemented model, we further analyzed the OER of protons with LET=1.8 $keV/\mu m$. It is known that proton has lower OER than photon beams. From our calculation, the OER for proton was 2.93 at oxygen partial pressure 15.2 mmHg, slightly smaller than that of photon beams (OER = 3.04). We then show the

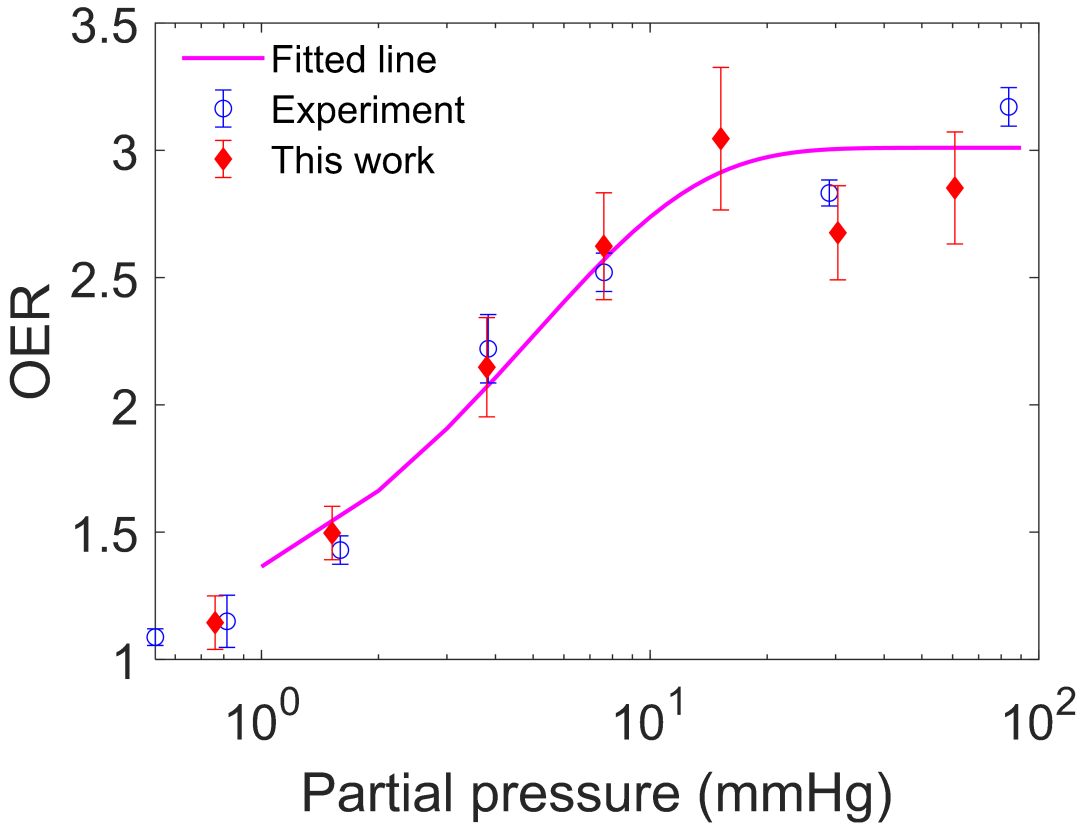

Figure 8.2. OER versus P_{O_2} for x-ray case. Fitted line was from reference ([321]). Experiment results were extracted from reference ([24]). Error bar shows the standard deviation..

OER versus LET in Fig. 8.3. our results well showed the decreasing trend between OER and LET.

We then picked a case with LET 15.2 $keV/\mu m$ to illustrate the effect of selecting different biological endpoints. From the SF versus dose curve shown in [290], we could know that dose of 1, 2, 3 Gy is equal to SF of 0.62, 0.15, 0.01 while SF under 4 Gy radiation is unknown experimentally for H460 cells. Our simulation suggested around 10% increase of OER when SF changed two magnitudes. This trend is very close on the results on V79 cell while different for those on T1 cell ([336]).

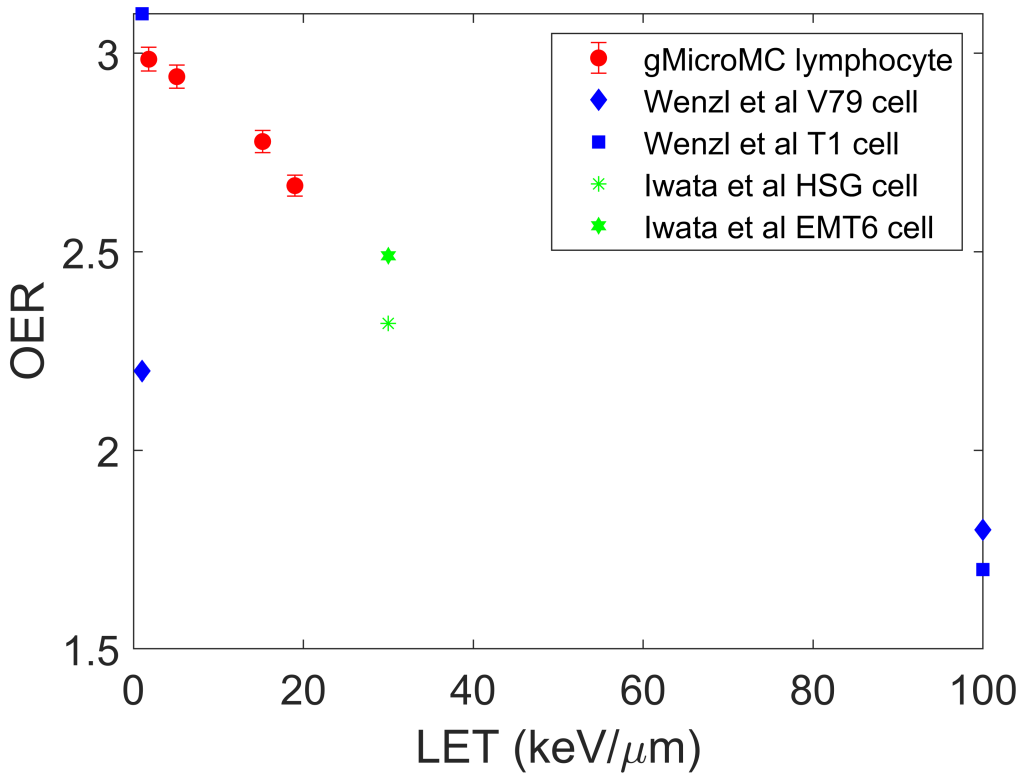

Figure 8.3. OER versus LET for proton cases. Experiemtnal results were from references ([329, 335]).

8.1.7 Discussions

First, we want to comment on the values we got from the benchmark of this model to experimental results for x-ray case. $t_0 = 3.8\ ms$ is of same magnitude suggested by other papers ([315, 331]). It is a very long time period, compared to lifetime of most radicals, which are just several microseconds or even less ([271, 337]). This is why we can view oxygen as a background after for the period from 1 μs to t_0 and use probabilistic method to find the transformation probability of $R^{\cdot}$. $p_0 = 0.08$ and $p_1 = 0.28$ means $ROO^{\cdot}$ is easier to cause SB than $R^{\cdot}$ since $p_1 > p_0$, which is the basis of OER. Yet, one thing worthy being noted is that the resolution of our DNA model is base pairs and it cannot distinguish different carbon atoms in the sugar-

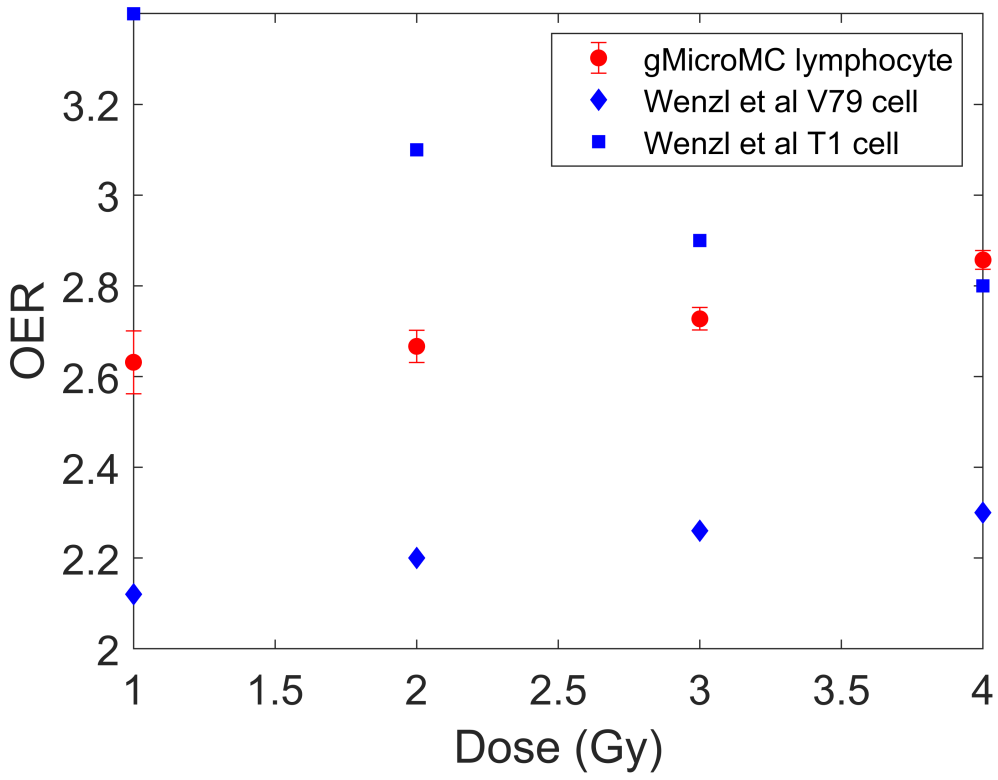

Figure 8.4. OER versus dose endpoints for proton case with LET 15.2 $kev/\mu m$. Data was extracted from Figure 2 of [336]..

phosphate moiety or in the base. Thus, $R^{\cdot}$ or $ROO^{\cdot}$ is a so crude description that it ignores the different properties of DNA radicals centered at different carbon atoms. For example, $C2'$ radical is easier to combine with oxygen and cause strand breaks almost for certain ([29]). Therefore, p_0 and p_1 are just an average effect of causing strand break for all kinds of DNA radicals. That is why their calues are smaller than expected, for instance, $p_1 = 1$.

Second, our model considered the enhancement of DNA radicals only by indirect effect, i.e. attack by hydroxyl. This is actually limited by our model of determining direct damage. Although we know biologically there exists DNA radicals from direct effect either through ionization or electron transfer from hydration shell ([28, 29]),

only accumulated energy on one sugar-phosphate group was used as criteria, which is widely accepted for simulation of DNA damage for various simulation ([51, 207, 273]). Without modification to the model, no DNA radical is recorded along with energy deposition process. However, such modification further requires more elaborate description of DNA structure and physics models for site-specific interactions, which is beyond the scope of this paper. In addition, typically, indirect effect causes more than half to 70% of total SBs ([205, 207, 240]). The OER model based on DNA radicals by indirect effect would be enough to capture the main behavior.

Following this, we can discuss about the decreasing of OER with increasing LET. From our simulation, there are two reason for this. One is that SBs from direct effect becomes more important for higher LET, which shows no OER from the above discussion. Another is shorter average distance between damage sites along with higher LET because of larger cross sections ([72]) and shorter mean free length. Hence, it is easier to cause DSB if we have more damage sites locally.

Finally, we want to point out a future direction for this model. one hidden logic for sampling track one by one and safely using probabilistic method for transformation of DNA radicals after termination of hydroxyl is that no inter-track effect ([181]) is considered nor oxygen concentration should undergoes large variation. Otherwise, we cannot guarantee uniform background of oxygen for every DNA radicals. There are scenarios where dose rate is so high that chemical stages of different tracks could have overlap and local oxygen regeneration is prominent, for example FLASH radiotherapy ([307, 309]). For these cases, oxygen diffusion and probabilistic method should be consider in a very careful way. However, due to the simplicity and integration with step-by-step method, our model could be easily extended with oxygen regeneration via diffusion ([315]) to consider pulse radiation in FLASH radiotherapy. We will present this issue in a future paper.

8.2 FLASH

The effects on radical yield by FLASH was studied on Section 7.1. However, there were two defects for that work. One is that the change of radical yield cannot fully represent the oxygen effect in terms of biological effect. Second, pulse number and width were not considered which ignores the oxygen regeneration. To include all these two factors, we have to consider DNA structure during chemical stage and oxygen diffusion between pulses.

8.2.1 Oxygen diffusion

The oxygen diffusion could be described by the partial equation [315]

$$\frac{\partial P_{O_2}}{\partial t} = D_{O_2}\nabla^2 P_{O_2} - \lambda \tag{8.7}$$

P_{O_2} is the oxygen concentration in unit of μM and λ means the metabolism consumption rate in unit of $\mu M/s$. Different research reported or used different values for λ. For example, 4.1 $\mu M/s$ in [315], 2.6 $\mu M/s$ in [338] and 2.7 $\mu M/s$ for whole body[339]. In this work, we used a value of 3 $\mu M/s$.

As the detailed vascular map in μm scale is not known to us, we just simulated a free space with a center straight artery for illustration of oER under FLASH and effect of number of pulses in FLASH. We set $P_0 = 60$ μM to account for typical value at the end of micro-vascular artery [317]. Under such cylindrical symmetry, the steady state could be easily solve along radial direction

$$D_{O_2}\frac{d^2}{dr^2}P_{O_2} - \lambda = 0 \tag{8.8}$$

The numerical solution by finite element method (FEM) is shown in Figure 8.5. The penetration depth is around 100 μm, which is similar to what has been done in [315]. We labeled the steady distribution as $P^S_{O_2}$.

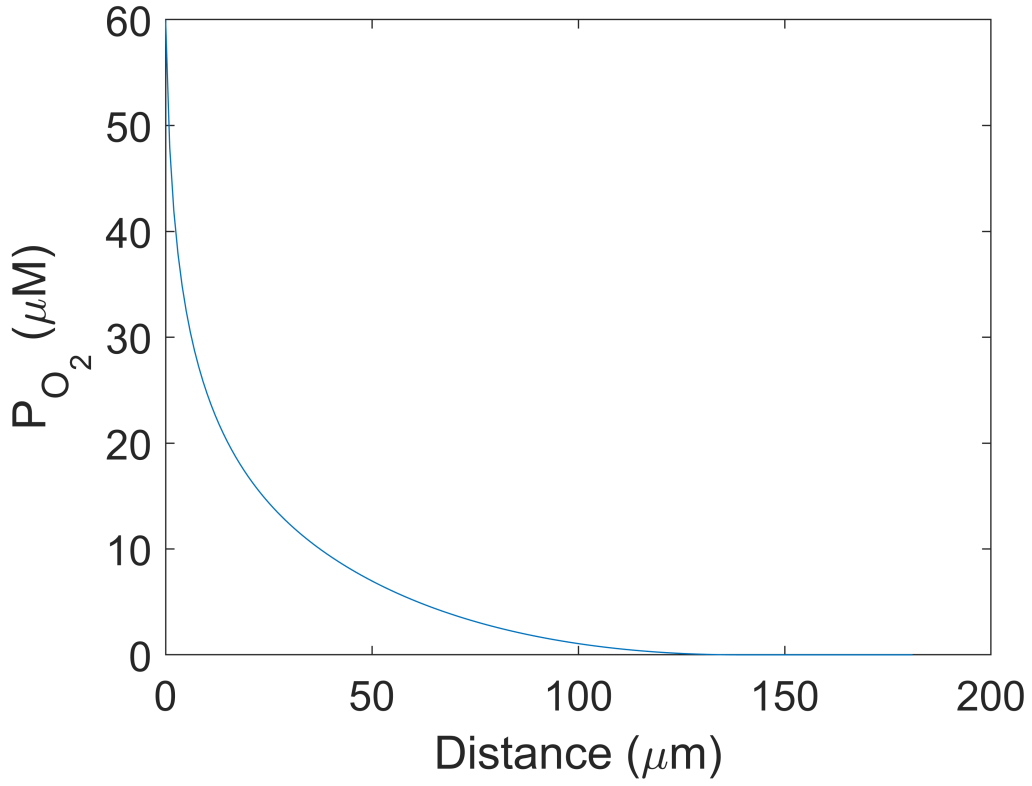

Figure 8.5. Radial oxygen concentration for steady state.

According to results in section 7.1, the OCR only depends on the initial oxygen concentration under FLASH (Equation (7.2) and Figure 7.6). We presume that this relationship holds for all FLASH conditions. Hence, if the FLASH beam shoot along the cylinder axis and covers at least 200×200 μm^2 field, the oxygen drop would preserve the cylindrical symmetry and so would oxygen regeneration. We still only need to consider radial part by equation

$$\frac{\partial P_{O_2}}{\partial t} = D_{O_2} \frac{\partial^2}{\partial r^2} P_{O_2} - \lambda \tag{8.9}$$

with reduced oxygen distribution $P_{O_2}^R$ as the initial state. The recovering time from $P_{O_2}^R$ to $P_{O_2}^S$ is usually of ms scale, which is just the scale of OER taking effect shown in section 8.1. An illustration of recovering time has been shown in Figure 8.6. Typically,

it would require 3, 10 and 30 ms if the oxygen concentration drops by 20, 50 and 80 percent, respectively.

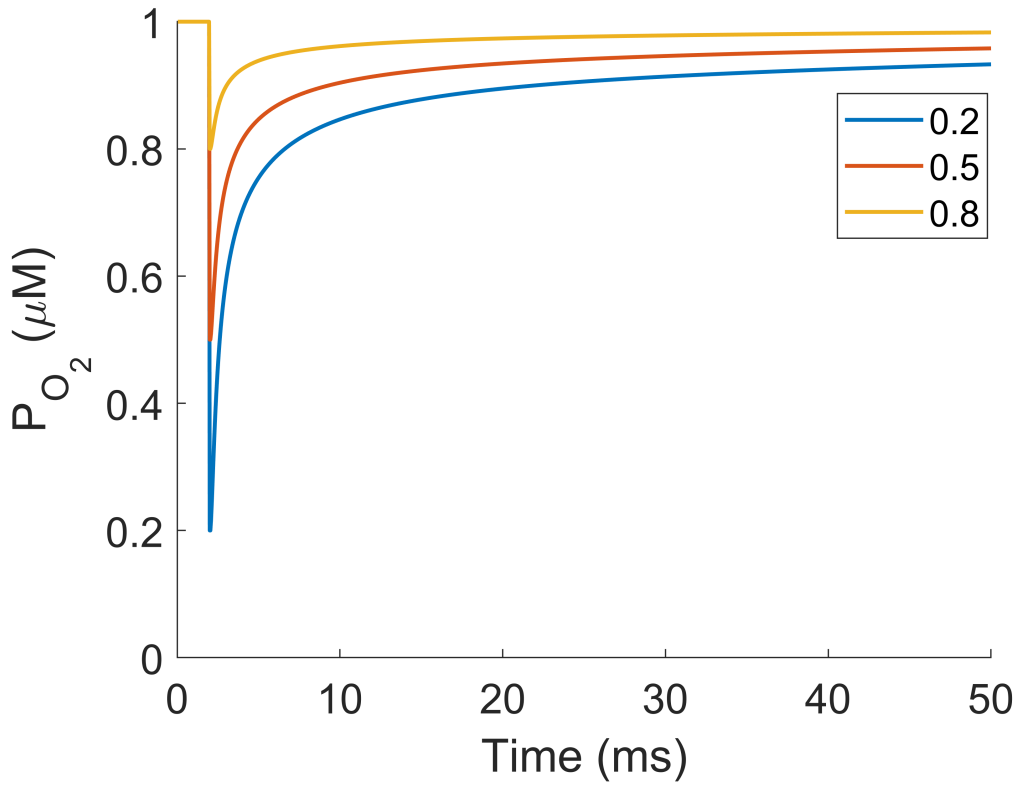

Figure 8.6. Oxygen recovering at 20 μm away from the artery for sudden drop of oxygen with different ratios.

8.2.2 Simulation of OER on DNA damage for proton FLASH

Like what we did in section 8.1, we applied the OER model to find OER on DNA damages. The difference now is we have to consider oxygen diffusion since the time interval between two particles may be shorter than t_0 and the recovering time may approximate t_0 as well depending on the drop of oxygen concentration during

the pulse. To integrate the OER model, we adopted the following steps for FLASH conditions.

1. Defining oxygen concentration array P_{O_2} and solve the steady state $P_{O_2}^S$ for given P_0 and λ by Equation (8.8).
2. For given target dose D_t, simulated all the physics tracks that could deposit enough energy $D_t * V_{ROI}$ and prepare the initial radicals for all tracks. We denoted all energy deposition events that belongs to particle i as Y_i^{phys} and corresponding radicals as Y_i^{chem}.
3. Based on a given time structure, we sampled the time point when particles entered the ROI. We did a time structure for synchrocyclotron, namely pulse width t_p of μs and pulse interval Δt of ms [340, 341]. We then sorted the time in ascending order denoted as T and assign them to the particle tracks we just simulated. All Y_i^{phys} and Y_i^{chem} have same T_i.
4. At the beginning of jth pulse, uniformly sampling $N_{O_2} = P_{O_2}^j \times V_{ROI}$ inside ROI. Here, temporary initial oxygen concentration $P_{O_2}^j$ is equal to $P_{O_2}(r_0)$ where r_0 is the center of ROI.
5. For T_i that was in jth pulse, read Y_i^{chem} into chemical stage one by one and simulate chemical stage by concurrent transport method. Record all $R^{\cdot}$ and $ROO^{\cdot}$.
6. For the interval between jth and $j+1$th pulses, we update the whole P_{O_2} array by Equation (7.2) at the beginning of the interval. This served as the initial condition for Equation (8.9). In this manner, we obtained P_{O_2} array for $j+1$th pulse.

7. The transformation probability from $R^{\cdot}$ to $ROO^{\cdot}$ (Equation (8.3)) should then be revised because of the oxygen variation during the pulse interval. The updated version was

$$P(R^{\cdot} \rightarrow ROO^{\cdot}) = e^{-k_0 * \int_0^{\Delta t} p_{O_2}(r_0) dt}. \tag{8.10}$$

   where Δt is the time interval between jth and $j+1$th pulses. As an approximation, $\int_0^{\Delta t} p_{O_2}(r_0)dt$ could be replaced by $(p_{O_2}(r_0, t_j + t_p) + p_{O_2}(r_0, t_{j+1}))/2$. Here, t_j and t_{j+1} represented the beginning time of jth and $j+1$th pulses.
8. Repeat steps 4-7 for all pulses.

8.2.3 Results and discussion

We presented the summarized results in Table 8.1 for a total dose of 10 Gy. The proton source is what used for section 6.1 with LET=19.2 $keV/\mu m$. DNA damage under conventional dose rate was obtained by simulating track one by one without any consideration of oxygen diffusion and recovering. It is always under oxygen concentration P_0. OER model was applied for both conventional and FLASH conditions, though.

As described in the section 8.2.2, the different initial oxygen concentration was achieved by put cell at different distance r_0 from the region with constant oxygen concentration $P_0 = 60\ \mu M$. Our simulation suggested no difference of DNA damage reduction with initial oxygen concentration ranging from 4.8 to 19.2 μM, which are typical values for tissue oxygen level. For the characters of proton beam, number of pulses, pulse width and pulse interval all had great impact on the yielded DNA damage. The larger their values were, the less prominent the radio-protective effect by FLASH. This is because the lifetime of radicals are limited and the proton track must be close enough in both temporal and spatial dimensions so that radicals may

Table 8.1. DNA damage for FLASH with different parameters

Number of pulse	t_p (μs)	Δt (ms)	Initial oxygen concentration (μM)	Reduced ratio (%)
1	1	100	4.8	10
3	1	100	4.8	8
5	1	100	4.8	7
10	1	100	4.8	3
1	0.001	100	4.8	43
1	0.01	100	4.8	30
1	0.1	100	4.8	10
3	1	10	4.8	13
3	1	50	4.8	11
3	1	500	4.8	5
3	1	1000	4.8	3
3	1	100	19.2	8
5	1	100	19.2	7

Reduced ratio was compared to corresponding number of DNA DSBs with conventional dose rate and same iniital oxygen concentration

interact with each other between tracks. Yet, the number of proton track required to obtain same target dose is much less than electron cases, increasing the difficulty of two tracks meeting spatially and temporally. Hence, those values must be small enough to enlarge the radio-protective effect. The maximum reduction of number of DNA DSBs from our results was with 1 pulse, 1 ns pulse width and 100 ms pulse interval.

8.3 Conclusion

We developed an OER model and applied it to FLASH condition. OER model was based on mechanistic modelling of DNA damage via GPU-based MC simulation package, gMicroMC. Only three parameters were included in our model. Yet it was

effective to match with experimental results for photon cases. The model was also applicable to proton cases, replicating the tendency between oER and LET and different biological endpoints. The simple yet effective model did not ruin the computational efficiency and was applied to FLASH condition with consideration of oxygen diffusion. We found that number of pulses, pulse width and pulse interval all had great impact on the yielded DNA damage. If their combined effect was to enlarge the oxygen drop and enhance the inter-track radical reactions, then the protective effect by FLASH could be maximized. For proton cases, the pulse width should be as short as of ns scale because the number of proton track required to obtain same target dose is much less than electron cases, increasing the difficulty of two tracks meeting spatially and temporally.

CHAPTER 9

CONCLUSIONS AND FUTURE DIRECTIONS

To summarize, this thesis presented several GPU MC applications for radiotherapy:

1. We implemented the crystal detector part for PET simulation. We applied it to systematically study the performance of PET detector versus several key factors such as coincidence time window and DOI.
2. We implemented electron transport in a magnetic field in gDPM. Source models for MeV beams were built to do the dose calculation. It achieved good agreement with current TPS while pushing the simulation time to less than one minutes, making it possible for onsite dose calculation.
3. We developed a microscopic simulation package gMicroMC. It now supports the transport of electrons and protons. Heavier ions could also be considered is scale of z_{eff}^2 was applied to obtain cross section. We included DNA structure, oxygen molecules into chemical stage.

All of them are either open-source or obtained upon request. With the involvement of GPU, the computational performances have been greatly improved, which targets one of the biggest barrier of applying MC in radiotherapy. The improvement of computational performance is not just an application of a new technology, but also makes it possible for increasing the problem scale, studying the mechanisms in a fundamental way. For this point of view, we particularly pointed out what we obtained with gMicroMC when we shifted our focus from dose to DNA damage.

1. We analyzed the DNA damage pattern by proton beams in ROI with dimensions of mm scale. Large variation ($\pm 20\%$) of DNA damage induced inside cells was obtained even when dose variation is only of 0.1% for ROI. We thus used the DNA damage pattern as input to a network and tried to find connections between DNA damage and cell SF. A network was trained, which work for x-ray cases and proton cases ranging from $\sim 1keV/\mu m$ to $\sim 20keV/\mu m$.
2. We analyzed DNA damage yield with hypothermia. We found the radioprotective effect could be explained by the reduced DNA DSBs under low temperature, which is because of more chemical reactions locally.
3. we studied radical yield change and oxygen consumption during FLASH condition. We suggested that oxygen depletion was not achievable only from radiolytic oxygen depletion.
4. We built an OER model, which applied well to both x-ray cases and proton cases. We then considered FLASH again based this OER model with oxygen diffusion and recovering effect included. We found that the inter-track radical reactions, together with the lower level of oxygen concentration during the pulse interval, could reduce the number of DNA DSBs. Hence, we suggest reducing the number of pulses, pulse width and also pulse interval to enhance the FLASH effect of sparing normal tissue. We did not study why FLASH would remain effective to tumors.

Based on what we have now, we could picture a variety of future directions.

1. Auto-commissioning method by [342] could be integrated with the suoce model to have better adjustment of parameters.
2. Tumor growth models were proposed by several groups as summarized in [343]. We could integrate DNA damage simulation with tumor growth model to better

describe the radiation effect on tumor. This method could be even combined with deep learning to optimize best treatment plan [344].

3. We could study more complex cases with nano-particles, for instance nonuniform distribution in the cell to specifically evaluate the performance of nano-particles in terms of DNA damage.
4. We could apply the same method in Section 8.2 to electron and photon cases to test if our explanation to the simulation results preserve.

APPENDIX A

LIST OF ABBREVIATIONS AND SYMBOLS

This table lists the abbreviations used in this thesis for readers' reference.

Table A.1. Summary of common abbreviations used in this thesis

Abbreviations	Explanations
AAPM	American Association of Physicists in Medicine
BgCSDNN	Biology-guided Cell Survival deep neural network
CSDA	continuous slowing down approximation
CT	computerized tomography
DNA	deoxyribonucleic acid
DSB	double strand break
GPU	graphical processing unit
LET	linear energy transfer
LINAC	linear accelerator
MC	Monte Carlo
MLC	multi leaf collimator
MRI	magnetic resonance imaging
MU	monitor unit
OCR	oxygen consumption rate
OER	oxygen enhancement ratio
PET	positron emission tomography
RBE	relative bioilogical effect
ROI	region of interest
ROS	reactive oxygen species
RRS	Radiation Research Society
SB	strand break
SSB	single strand break
SSD	source surface distance
SF	survival fraction
SRS	Stereotactic radiosurgery
SBRT	Stereotactic Body Radiation Therapy
TPS	treatment planning system

This table lists the symbols used in this thesis for readers' reference.

Table A.2. Summary of symbols used in this thesis

Symbols	Explanations
M (as a unit)	mol/L
$\overline{y}_D$	linear energy
D_{O_2}	diffusion constants of oxygen
$U(a,b)$	uniform distribution in $[a,b]$
$N(\mu,\sigma)$	Gaussian distribution with mean value μ and standard deviation σ.
z_{eff}	effective atomic number
e_h, e^-_{aq}	hydrated electrons

APPENDIX B

RESEARCH ACCOMPLISHMENT

AWARDS

- Truman D. Black Endowed Scholarship in Physics, 2021.
- Dr. John L. Fry Endowment for the Department of Physics, 2020.
- IEEE Trainee Grant for NSS/MIC conference, 2020.
- Student Travel Award, RRS 2019 annual meeting, Radiation Research Society 2019.
- Michael and Wanda Ray Fellowship, 2019.

PUBLICATIONS

- Huang Y, Hu X, Zhong Y, Lai Y, Shen C and Jia X. Improving dose calculation accuracy in preclinical radiation experiments using multi-energy element resolved cone beam CT. Physics in Medicine and Biology. 2021, Accepted.
- Lai Y, Wang Q, Zhou S, Xie Z, Qi J, Cherry SR, Jin M, Chi Y, Du J. H2RSPET: a 0.5 mm resolution high-sensitivity small-animal PET scanner, a simulation study. Physics in Medicine and Biology. 2021 Mar 8;66(6):065016.
- Huang Y, Yang K, Lai Y, Liu H, Shen C, Zhong Y, Shao Y, Li X, Liu B, Jia X. Experimental and numerical studies on kV scattered x-ray imaging for real-time image guidance in radiation therapy. Physics in Medicine and Biology. 2021 Feb 10;66(4):045022.
- Lai Y, Jia X, Chi Y. Modeling the effect of oxygen on the chemical stage of water radiolysis using GPU-based microscopic Monte Carlo simulations, with an application in FLASH radiotherapy. Physics in Medicine and Biology. 2021 Jan 22;66(2):025004.
- Lai Y, Jia X, Chi Y. Recent Developments on gMicroMC: Transport Simulations of Proton and Heavy Ions and Concurrent Transport of Radicals and DNA. International journal of molecular sciences. 2021 Jan;22(12):6615.

- Chalise AR, Chi Y, Lai Y, Shao Y, Jin M. Carbon-11 and Carbon-12 beam range verifications through prompt gamma and annihilation gamma measurements: Monte Carlo simulations. Biomedical physics and engineering express. 2020 Sep 29;6(6):065013.
- Zhong Y, Lai Y, Saha D, Story MD, Jia X, Stojadinovic S. Dose rate determination for preclinical total body irradiation. Physics in Medicine and Biology. 2020 Sep 4;65(17):175018.
- Lai Y, Tsai MY, Tian Z, Qin N, Yan C, Hung SH, Chi Y, Jia X. A new open-source GPU-based microscopic Monte Carlo simulation tool for the calculations of DNA damages caused by ionizing radiation—Part II: sensitivity and uncertainty analysis. Medical physics. 2020 Apr;47(4):1971-82.
- Tsai MY, Tian Z, Qin N, Yan C, Lai Y, Hung SH, Chi Y, Jia X. A new open-source GPU-based microscopic Monte Carlo simulation tool for the calculations of DNA damages caused by ionizing radiation—Part I: Core algorithm and validation. Medical physics. 2020 Apr;47(4):1958-70.
- Lai Y, Zhong Y, Chalise A, Shao Y, Jin M, Jia X, Chi Y. gPET: a GPU-based, accurate and efficient Monte Carlo simulation tool for PET. Physics in Medicine and Biology. 2019 Dec 13;64(24):245002.

CONFERENCE PRESENTATIONS

- Oral presentation in *2021 Virtual AAPM annual meeting*
- Poster presentation in *2021 Flash Radiotherapy and Particle Therapy*
- Poster with recorded video presentation in *2021 Virtual IEEE Nuclear Science Symposium and Medical Imaging Conference*
- Oral presentation in *2020 Virtual AAPM annual meeting*

- Oral presentation in *2020 Virtual IEEE Nuclear Science Symposium and Medical Imaging Conference*
- Poster presentation in *2020 Virtual RRS annual meeting*
- Oral presentation in *2019 The International Conference on the Use of Computers in Radiation Therapy and the International Conference on Monte Carlo Techniques for Medical Applications at Montreal*
- Oral presentation in *2019 AAPM annual meeting at San Antonio*
- Poster presentation in *2019 RRS annual meeting at San Diego*
- Poster presentation in *2019 IEEE Nuclear Science Symposium and Medical Imaging Conference*

APPENDIX C

REPRODUCTION STATEMENT

REFERENCES

[1] J Ferlay et al. *Global cancer observatory: cancer today. Lyon: International Agency for Research on Cancer; 2018*. 2020. URL: `https://gco.iarc.fr/today` (visited on 10/06/2021).

[2] World Cancer Research Fund/American Institute for Cancer Research. "Diet, nutrition, physical activity and cancer: a global perspective". In: *Continuous Upyear Project Expert Report* (2018).

[3] Catherine de Martel et al. "Global burden of cancer attributable to infections in 2018: a worldwide incidence analysis". In: *The Lancet Global Health* 8.2 (2020), e180–e190.

[4] Michael C Joiner and Albert J van der Kogel. *Basic clinical radiobiology*. CRC press, 2018.

[5] Edward Chu and AC Sartorelli. "Cancer chemotherapy". In: *Basic & clinical pharmacology* 9 (2004), pp. 898–930.

[6] Roland T Skeel and Samir N Khleif. *Handbook of cancer chemotherapy*. Lippincott Williams & Wilkins, 2011.

[7] Sofia Farkona, Eleftherios P Diamandis, and Ivan M Blasutig. "Cancer immunotherapy: the beginning of the end of cancer?" In: *BMC medicine* 14.1 (2016), pp. 1–18.

[8] Geoff Delaney et al. "The role of radiotherapy in cancer treatment: estimating optimal utilization from a review of evidence-based clinical guidelines". In: *Cancer: Interdisciplinary International Journal of the American Cancer Society* 104.6 (2005), pp. 1129–1137.

[9] Gillian C Barnett et al. "Normal tissue reactions to radiotherapy: towards tailoring treatment dose by genotype". In: *Nature Reviews Cancer* 9.2 (2009), pp. 134–142.

[10] Rajamanickam Baskar et al. “Cancer and radiation therapy: current advances and future directions”. In: *International journal of medical sciences* 9.3 (2012), p. 193.

[11] Serena Gianfaldoni et al. “An overview on radiotherapy: from its history to its current applications in dermatology”. In: *Open access Macedonian journal of medical sciences* 5.4 (2017), p. 521.

[12] Philip P Connell and Samuel Hellman. “Advances in radiotherapy and implications for the next century: a historical perspective”. In: *Cancer research* 69.2 (2009), pp. 383–392.

[13] Jacques Bernier, Eric J Hall, and Amato Giaccia. “Radiation oncology: a century of achievements”. In: *Nature Reviews Cancer* 4.9 (2004), pp. 737–747.

[14] Emil H Grubbé. “Priority in the therapeutic use of X-rays”. In: *Radiology* 21.2 (1933), pp. 156–162.

[15] ED Courant. “Early milestones in the evolution of accelerators”. In: *Reviews Of Accelerator Science And Technology: Volume 1*. World Scientific, 2008, pp. 1–5.

[16] MN Martins and TF Silva. “Electron accelerators: History, applications, and perspectives”. In: *Radiation Physics and Chemistry* 95 (2014), pp. 78–85.

[17] Dieter Schardt, Thilo Elsässer, and Daniela Schulz-Ertner. “Heavy-ion tumor therapy: Physical and radiobiological benefits”. In: *Reviews of modern physics* 82.1 (2010), p. 383.

[18] J Martin Brown, David J Carlson, and David J Brenner. “The tumor radiobiology of SRS and SBRT: are more than the 5 Rs involved?” In: *International Journal of Radiation Oncology* Biology* Physics* 88.2 (2014), pp. 254–262.

[19] K Noda et al. “Recent progress and future plans of heavy-ion cancer radiotherapy with HIMAC”. In: *Nuclear Instruments and Methods in Physics Research*

Section B: Beam Interactions with Materials and Atoms 406 (2017), pp. 374–378.

[20] S Lovell. *An introduction to radiation dosimetry*. 4. CUP Archive, 1979.

[21] Stephen Joseph McMahon. "The linear quadratic model: usage, interpretation and challenges". In: *Physics in Medicine & Biology* 64.1 (2018), 01TR01.

[22] Stephen J Mcmahon et al. "Biological consequences of nanoscale energy deposition near irradiated heavy atom nanoparticles". In: *Scientific Reports* 1 (2011), p. 18.

[23] C. Clifton Ling et al. "Oxygen Diffusion into Mammalian Cells Following Ultrahigh Dose Rate Irradiation and Lifetime Estimates of Oxygen-Sensitive Species". In: *Radiation Research* 76.3 (1978), pp. 522–532.

[24] C Clifton Ling et al. "Oxygen sensitization of mammalian cells under different irradiation conditions". In: *Radiation research* 86.2 (1981), pp. 325–340.

[25] Elizabeth Cohen–Jonathan, Eric J. Bernhard, and W. Gillies McKenna. "How does radiation kill cells?" In: *Current Opinion in Chemical Biology* 3.1 (1999-02-01), pp. 77–83.

[26] IR Radford et al. "Radiation response of mouse lymphoid and myeloid cell lines. Part II. Apoptotic death is shown by all lines examined". In: *International journal of radiation biology* 65.2 (1994), pp. 217–227.

[27] Raymond L Warters. "Radiation-induced apoptosis in a murine T-cell hybridoma". In: *Cancer research* 52.4 (1992), pp. 883–890.

[28] Clemens von Sonntag. *Free-Radical-Induced DNA Damage and Its Repair*. Springer, 2006.

[29] Miral Dizdaroglu and Pawel Jaruga. "Mechanisms of free radical-induced damage to DNA". In: *Free Radical Research* 46 (2012), pp. 382–419.

[30] Ian R Radford. "The level of induced DNA double-strand breakage correlates with cell killing after X-irradiation". In: *International Journal of Radiation Biology and Related Studies in Physics, Chemistry and Medicine* 48.1 (1985), pp. 45–54.

[31] C Clifton Ling, Ellen Yorke, and Zvi Fuks. "From IMRT to IGRT: frontierland or neverland?" In: *Radiotherapy and oncology* 78.2 (2006), pp. 119–122.

[32] Paul Suetens. *Fundamentals of medical imaging*. Cambridge university press, 2017.

[33] Hany Kasban, MAM El-Bendary, and DH Salama. "A comparative study of medical imaging techniques". In: *International Journal of Information Science and Intelligent System* 4.2 (2015), pp. 37–58.

[34] Simon R Cherry, James A Sorenson, and Michael E Phelps. *Physics in nuclear medicine e-Book*. Elsevier Health Sciences, 2012.

[35] Nicholas Metropolis and Stanislaw Ulam. "The monte carlo method". In: *Journal of the American statistical association* 44.247 (1949), pp. 335–341.

[36] Oleg N Vassiliev. "Monte Carlo methods for radiation transport". In: *Fundamentals and Advanced Topics* (2017).

[37] David John Cameron Mackay. "Introduction to monte carlo methods". In: *Learning in graphical models*. Springer, 1998, pp. 175–204.

[38] DWO Rogers. "Fifty years of Monte Carlo simulations for medical physics". In: *Physics in Medicine & Biology* 51.13 (2006), R287.

[39] Pedro Andreo. "Monte Carlo techniques in medical radiation physics". In: *Physics in Medicine & Biology* 36.7 (1991), p. 861.

[40] Joao Seco and Frank Verhaegen. *Monte Carlo techniques in radiation therapy*. CRC press, 2013.

[41] J. Sempau, S. J. Wilderman, and A. F. Bielajew. "DPM, a fast, accurate Monte Carlo code optimized for photon and electron radiotherapy treatment planning dose calculations". In: *Phys Med Biol* 45.8 (Aug. 2000), pp. 2263–91.

[42] Xun Jia et al. "Development of a GPU-based Monte Carlo dose calculation code for coupled electron – photon transport". In: *Physics in Medicine and Biology* 55 (2010), pp. 3077–3086.

[43] N. Qin et al. "Full Monte Carlo-Based Biologic Treatment Plan Optimization System for Intensity Modulated Carbon Ion Therapy on Graphics Processing Unit". In: *Int J Radiat Oncol Biol Phys* 100.1 (2018-01-01). Edition: 2017/10/29, pp. 235–243.

[44] Sami Hissoiny et al. "GPUMCD: a new GPU-oriented Monte Carlo dose calculation platform". In: *Medical physics* 38.2 (2011), pp. 754–764.

[45] Harald Paganetti et al. "Clinical implementation of full Monte Carlo dose calculation in proton beam therapy". In: *Physics in Medicine & Biology* 53.17 (2008), p. 4825.

[46] H Nikjoo et al. "Track-structure codes in radiation research". In: *Radiation Measurements* 41.9 (2006), pp. 1052–1074.

[47] T. Liamsuwan et al. "Microdosimetry of low-energy electrons". In: *Int J Radiat Biol* 88.12 (2012-12). Edition: 2012/06/07, pp. 899–907.

[48] Yuki Kase et al. "Microdosimetric measurements and estimation of human cell survival for heavy-ion beams". In: *Radiation research* 166.4 (2006), pp. 629–638.

[49] Stefanos Margis et al. "Microdosimetric calculations of the direct DNA damage induced by low energy electrons using the Geant4-DNA Monte Carlo code". In: *Physics in Medicine & Biology* 65.4 (2020-02-12), p. 045007.

[50] H Nikjoo et al. “Computational modelling of low-energy electron- induced DNA damage by early physical and chemical events”. In: *International Journal of Radiation Biology* 71 (1997), pp. 467–483.

[51] Werner Friedland et al. “First steps towards systems radiation biology studies concerned with DNA and chromosome structure within living cells”. In: *Radiation and Environmental Biophysics* 47 (2008), pp. 49–61.

[52] MinYu Tsai et al. “A new open-source GPU-based microscopic Monte Carlo simulation tool for the calculations of DNA damages caused by ionizing radiation — Part I: Core algorithm and validation”. In: *Medical Physics* 47.4 (2020), pp. 1958–1970.

[53] Philippe Després and Xun Jia. “A review of GPU-based medical image reconstruction”. In: *Physica Medica* 42 (2017), pp. 76–92.

[54] Xun Jia, Peter Ziegenhein, and Steve B Jiang. “GPU-based high-performance computing for radiation therapy”. In: *Physics in Medicine & Biology* 59.4 (2014), R151.

[55] Tolga Soyata. *GPU parallel program development using CUDA*. CRC Press, 2018.

[56] E Alerstam, T Svensson, and S Andersson-Engels. “CUDAMCML-User manual and implementation notes”. In: *Lund University, Lund* (2009).

[57] Erik Alerstam et al. “Next-generation acceleration and code optimization for light transport in turbid media using GPUs”. In: *Biomedical optics express* 1.2 (2010), pp. 658–675.

[58] N. A. Carbone, D. I. Iriarte, and J. A. Pomarico. “GPU accelerated Monte Carlo simulation of light propagation in inhomogeneous fluorescent turbid media: application to whole field CW imaging”. In: *Biomedical Physics & Engineering Express* 3.4 (2017-07-06), p. 045012.

[59] Andreu Badal and Aldo Badano. "Accelerating Monte Carlo simulations of photon transport in a voxelized geometry using a massively parallel graphics processing unit". In: *Medical physics* 36.11 (2009), pp. 4878–4880.

[60] Xun Jia et al. "Fast Monte Carlo simulation for patient-specific CT/CBCT imaging dose calculation". In: *Physics in Medicine and Biology* 57.3 (2012-01-06), pp. 577–590.

[61] Xun Jia et al. "A GPU tool for efficient, accurate, and realistic simulation of cone beam CT projections". In: *Medical physics* 39.12 (2012), pp. 7368–7378.

[62] Y. Xu et al. "Metropolis Monte Carlo simulation scheme for fast scattered X-ray photon calculation in CT". In: *Opt Express* 27.2 (2019-01-21). Edition: 2019/01/31, pp. 1262–1275.

[63] Sami Hissoiny et al. "Validation of GPUMCD for low-energy brachytherapy seed dosimetry". In: *Medical physics* 38.7 (2011), pp. 4101–4107.

[64] Z. Tian et al. "Monte Carlo dose calculations for high-dose–rate brachytherapy using GPU-accelerated processing". In: *Brachytherapy* 15.3 (2016-05-01), pp. 387–398.

[65] Andrea Frezza et al. "Validation of irtGPUMCD, a GPU-based Monte Carlo internal dosimetry framework for radionuclide therapy". In: *Physica Medica* 73 (2020), pp. 95–104.

[66] X Jia et al. "GPU-based fast Monte Carlo simulation for radiotherapy dose calculation". In: *Physics in Medicine and Biology* 56 (2011), pp. 7017–7031.

[67] Lennart Jahnke et al. "GMC: a GPU implementation of a Monte Carlo dose calculation based on Geant4". In: *Physics in Medicine & Biology* 57.5 (2012), p. 1217.

[68] Nan Qin et al. “Recent developments and comprehensive evaluations of a GPU-based Monte Carlo package for proton therapy”. In: *Physics in Medicine and Biology* 61 (2016), pp. 7347–7362.

[69] Xun Jia et al. “GPU-based fast Monte Carlo dose calculation for proton therapy”. In: *Physics in Medicine and Biology* 57.23 (2012-11-06), pp. 7783–7797.

[70] Nan Qin et al. “Initial development of goCMC: a GPU-oriented fast cross-platform Monte Carlo engine for carbon ion therapy”. In: *Physics in Medicine and Biology* 62.9 (2017-04-05), pp. 3682–3699.

[71] Shogo Okada et al. “MPEXS-DNA , a new GPU-based Monte Carlo simulator for track structures and radiation chemistry at subcellular scale”. In: *Medical Physics* 46 (2019), pp. 1483–1500.

[72] Youfang Lai, Xun Jia, and Yujie Chi. “Recent Developments on gMicroMC: Transport Simulations of Proton and Heavy Ions and Concurrent Transport of Radicals and DNA”. In: *International Journal of Molecular Sciences* 22.12 (2021), p. 6615.

[73] I. Buvat and D. Lazaro. “Monte Carlo simulations in emission tomography and GATE: An overview”. English. In: *Nuclear Instruments & Methods in Physics Research Section a-Accelerators Spectrometers Detectors and Associated Equipment* 569.2 (Dec. 2006), pp. 323–329.

[74] P. J. Slomka et al. “Advances in SPECT and PET Hardware”. In: *Prog Cardiovasc Dis* 57.6 (May 2015). Edition: 2015/02/28, pp. 566–78.

[75] A. Mehranian et al. “PET image reconstruction using multi-parametric anato-functional priors”. English. In: *Physics in Medicine and Biology* 62.15 (Aug. 2017), pp. 5975–6007.

[76] W. Tao et al. “Simulation study of a high-performance brain PET system with dodecahedral geometry”. In: *Med Phys* 45.7 (July 2018). Edition: 2018/05/26, pp. 3297–3304.

[77] Y. C. Zhong et al. “Quantitative 4D-PET Reconstruction for Small Animal Using SMEIR-Reconstructed 4D-CBCT”. English. In: *Ieee Transactions on Radiation and Plasma Medical Sciences* 2.4 (July 2018), pp. 300–306.

[78] D. Sarrut et al. “A review of the use and potential of the GATE Monte Carlo simulation code for radiation therapy and dosimetry applications”. English. In: *Medical Physics* 41.6 (June 2014).

[79] H. Paganetti. “Range uncertainties in proton therapy and the role of Monte Carlo simulations”. In: *Phys Med Biol* 57.11 (June 2012). Edition: 2012/05/11, R99–117.

[80] X. Zhu and G. El Fakhri. “Proton therapy verification with PET imaging”. In: *Theranostics* 3.10 (Sept. 2013). Edition: 2013/12/07, pp. 731–40.

[81] A. C. Knopf and A. Lomax. “In vivo proton range verification: a review”. In: *Phys Med Biol* 58.15 (Aug. 2013). Edition: 2013/07/19, R131–60.

[82] J. Bauer et al. “Implementation and initial clinical experience of offline PET/CT based verification of scanned carbon ion treatment”. In: *Radiother Oncol* 107.2 (May 2013). Edition: 2013/05/08, pp. 218–26.

[83] A. C. Kraan. “Range Verification Methods in Particle Therapy: Underlying Physics and Monte Carlo Modeling”. In: *Front Oncol* 5 (2015). Edition: 2015/07, p. 150.

[84] C. Gianoli et al. “First clinical investigation of a 4D maximum likelihood reconstruction for 4D PET-based treatment verification in ion beam therapy”. In: *Radiother Oncol* 123.3 (June 2017). Edition: 2017/05/10, pp. 339–345.

[85] M. L. Chen et al. “Mid-range probing-towards range-guided particle therapy”. English. In: *Physics in Medicine and Biology* 63.13 (July 2018).

[86] S. Agostinelli et al. “GEANT4 - A simulation toolkit”. In: *Nuclear Instruments and Methods in Physics Research, Section A: Accelerators, Spectrometers, Detectors and Associated Equipment* 506 (2003), pp. 250–303.

[87] Walter R Nelson, Hideo Hirayama, and David WO Rogers. *EGS4 code system*. Tech. rep. Stanford Linear Accelerator Center, Menlo Park, CA (USA), 1985.

[88] Judith F Briesmeister. *MCNP–A general Monte Carlo code for neutron and photon transport*. Los Alamos National Laboratory, 1986.

[89] S. Jan et al. “GATE: a simulation toolkit for PET and SPECT”. In: *Physics in Medicine and Biology* 49.19 (2004-09-10), pp. 4543–4561.

[90] CJ Thompson, J Moreno-Cantu, and Y Picard. “PETSIM: Monte Carlo simulation of all sensitivity and resolution parameters of cylindrical positron imaging systems”. In: *Physics in medicine and biology* 37.3 (1992), p. 731.

[91] TK Lewellen, RL Harrison, and S Vannoy. “The simset program”. In: *Monte Carlo Calculations in Nuclear Medicine* (1998), pp. 77–92.

[92] S. Espana et al. “PeneloPET, a Monte Carlo PET simulation tool based on PENELOPE: features and validation”. In: *Phys Med Biol* 54.6 (Mar. 2009), pp. 1723–42.

[93] G. Pratx and L. Xing. “GPU computing in medical physics: a review”. In: *Med Phys* 38.5 (May 2011), pp. 2685–97.

[94] Julien Bert et al. “Geant4-based Monte Carlo simulations on GPU for medical applications”. In: *Physics in Medicine and Biology* 58 (2013), pp. 5593–5611.

[95] Yujie Chi, Zhen Tian, and Xun Jia. “Modeling parameterized geometry in GPU-based Monte Carlo particle transport simulation for radiotherapy”. In: *Physics in Medicine and Biology* 61.15 (2016-07-18), pp. 5851–5867.

[96] A. F. Shields et al. “Imaging proliferation in vivo with [F-18]FLT and positron emission tomography”. In: *Nat Med* 4.11 (Nov. 1998), pp. 1334–6.

[97] W. Enghardt et al. “Dose quantification from in-beam positron emission tomography”. In: *Radiother Oncol* 73 Suppl 2 (Dec. 2004), S96–8.

[98] W. B. Ewbank. “Evaluated Nuclear-Structure Data File (Ensdf) for Basic and Applied-Research”. English. In: *Transactions of the American Nuclear Society* 26 (1977), pp. 566–567.

[99] L. Jodal, C. Le Loirec, and C. Champion. “Positron range in PET imaging: non-conventional isotopes”. In: *Phys Med Biol* 59.23 (Dec. 2014), pp. 7419–34.

[100] A. Rahmim, J. Qi, and V. Sossi. “Resolution modeling in PET imaging: theory, practice, benefits, and pitfalls”. In: *Med Phys* 40.6 (June 2013), p. 064301.

[101] R. L. Harrison et al. “Positron range and coincidence non-collinearity in SimSET”. English. In: *1999 Ieee Nuclear Science Symposium - Conference Record, Vols 1-3* (1999), pp. 1265–1268.

[102] J. Cal-Gonzalez et al. “Positron range estimations with PeneloPET”. In: *Phys Med Biol* 58.15 (Aug. 2013), pp. 5127–52.

[103] M. R. Palmer and G. L. Brownell. “Annihilation density distribution calculations for medically important positron emitters”. In: *IEEE Trans Med Imaging* 11.3 (1992), pp. 373–8.

[104] R Ribberfors and K-F Berggren. “Incoherent x ray scattering functions and cross sections $(\frac{d\sigma}{d\Omega'})_{incoh}$ by means of a pocket calculator”. In: *Physical Review A* 26.6 (1982), p. 3325.

[105] CL Melcher and JS Schweitzer. “Cerium-doped lutetium oxyorthosilicate: a fast, efficient new scintillator”. In: *IEEE Transactions on Nuclear Science* 39.4 (1992), pp. 502–505.

[106] S. Tang et al. “Annihilation gamma-ray spectra from positron-molecule interactions”. In: *Phys Rev Lett* 68.25 (June 1992), pp. 3793–3796.

[107] E. Roncali, M. A. Mosleh-Shirazi, and A. Badano. “Modelling the transport of optical photons in scintillation detectors for diagnostic and radiotherapy imaging”. In: *Phys Med Biol* 62.20 (Oct. 2017). Edition: 2017/10/05, R207–R235.

[108] G. F. Knoll, T. F. Knoll, and T. M. Henderson. “Light Collection in Scintillation Detector Composites for Neutron Detection”. English. In: *Ieee Transactions on Nuclear Science* 35.1 (Feb. 1988), pp. 872–875.

[109] C Simon. “Opticks: GPU Optical Photon Simulation for Particle Physics using NVIDIA® OptiX™”. In: vol. 898. 2017, p. 042001.

[110] Gary D. Hutchins et al. “Small Animal PET Imaging”. In: *ILAR Journal* 49.1 (2008), pp. 54–65.

[111] Terry Jones and David W Townsend. “History and future technical innovation in positron emission tomography”. In: *Journal of Medical Imaging* 4.1 (2017), p. 011013.

[112] David Masopust, Christine P Sivula, and Stephen C Jameson. “Of mice, dirty mice, and men: using mice to understand human immunology”. In: *The Journal of Immunology* 199.2 (2017), pp. 383–388.

[113] Simon R Cherry. “The 2006 Henry N. Wagner Lecture: of mice and men (and positrons)—advances in PET imaging technology”. In: *Journal of Nuclear Medicine* 47.11 (2006), pp. 1735–1745.

[114] Terry Jones. “Total body PET imaging from mice to humans”. In: *Frontiers in Physics* 8 (2020), p. 77.

[115] Ralph Myers. “The biological application of small animal PET imaging”. In: *Nuclear medicine and biology* 28.5 (2001), pp. 585–593.

[116] Robert S Miyaoka and Adrienne L Lehnert. "Small animal PET: a review of what we have done and where we are going". In: *Physics in Medicine & Biology* 65.24 (2020), 24TR04.

[117] Bernard Lanz, Carole Poitry-Yamate, and Rolf Gruetter. "Image-derived input function from the vena cava for 18F-FDG PET studies in rats and mice". In: *Journal of Nuclear Medicine* 55.8 (2014), pp. 1380–1388.

[118] Qiao Huang et al. "Non-invasive determination of blood input function to compute rate of myocardial glucose uptake from dynamic FDG PET images of rat heart in vivo: comparative study between the inferior vena cava and the left ventricular blood pool with spill over and partial volume corrections". In: *Physics in Medicine & Biology* 64.16 (2019), p. 165010.

[119] Simon R. Cherry et al. "MicroPET: a high resolution PET scanner for imaging small animals". In: *IEEE Transactions on Nuclear Science* 44.3 (1997), pp. 1161–1166.

[120] Klaus P Schäfers et al. "Performance evaluation of the 32-module quadHIDAC small-animal PET scanner". In: *Journal of Nuclear Medicine* 46.6 (2005), pp. 996–1004.

[121] Qinan Bao et al. "Performance evaluation of the inveon dedicated PET preclinical tomograph based on the NEMA NU-4 standards". In: *Journal of Nuclear Medicine* 50.3 (2009), pp. 401–408.

[122] Yongfeng Yang et al. "A prototype high-resolution small-animal PET scanner dedicated to mouse brain imaging". In: *Journal of Nuclear Medicine* 57.7 (2016), pp. 1130–1135.

[123] Seiichi Yamamoto et al. "Development of ultrahigh resolution Si-PM-based PET system using 0.32 mm pixel scintillators". In: *Nuclear Instruments and*

Methods in Physics Research Section A: Accelerators, Spectrometers, Detectors and Associated Equipment 836 (2016), pp. 7–12.

[124] Zheng Gu et al. "Performance evaluation of HiPET, a high sensitivity and high resolution preclinical PET tomograph". In: *Physics in Medicine & Biology* 65.4 (2020-02-12), p. 045009.

[125] Arion F Chatziioannou et al. "Performance evaluation of microPET: a high-resolution lutetium oxyorthosilicate PET scanner for animal imaging". In: *Journal of Nuclear Medicine* 40.7 (1999), p. 1164.

[126] Yongfeng Yang et al. "Optimization and performance evaluation of the microPET II scanner for in vivo small-animal imaging". In: *Physics in medicine & biology* 49.12 (2004), p. 2527.

[127] Suleman Surti et al. "Imaging performance of A-PET: a small animal PET camera". In: *IEEE transactions on medical imaging* 24.7 (2005), pp. 844–852.

[128] Yuchuan Wang et al. "Performance evaluation of the GE healthcare eXplore VISTA dual-ring small-animal PET scanner". In: *Journal of Nuclear Medicine* 47.11 (2006), pp. 1891–1900.

[129] K Ishii et al. "First achievement of less than 1 mm FWHM resolution in practical semiconductor animal PET scanner". In: *Nuclear Instruments and Methods in Physics Research Section A: Accelerators, Spectrometers, Detectors and Associated Equipment* 576.2-3 (2007), pp. 435–440.

[130] Richard Laforest et al. "Performance evaluation of the microPET®—FOCUS-F120". In: *IEEE Transactions on Nuclear Science* 54.1 (2007), pp. 42–49.

[131] Brad J Kemp et al. "NEMA NU 2-2007 performance measurements of the Siemens Inveon™ preclinical small animal PET system". In: *Physics in Medicine & Biology* 54.8 (2009), p. 2359.

[132] Istvan Szanda et al. “National Electrical Manufacturers Association NU-4 performance evaluation of the PET component of the NanoPET/CT preclinical PET/CT scanner”. In: *Journal of nuclear medicine* 52.11 (2011), pp. 1741–1747.

[133] Mario Cañadas et al. “NEMA NU 4-2008 performance measurements of two commercial small-animal PET scanners: ClearPET and rPET-1”. In: *IEEE Transactions on Nuclear Science* 58.1 (2010), pp. 58–65.

[134] Z. Gu et al. “NEMA NU-4 performance evaluation of PETbox4, a high sensitivity dedicated PET preclinical tomograph”. In: *Physics in Medicine and Biology* 58.11 (2013-05-10), pp. 3791–3814.

[135] Kálmán Nagy et al. “Performance evaluation of the small-animal nanoScan PET/MRI system”. In: *Journal of Nuclear Medicine* 54.10 (2013), pp. 1825–1832.

[136] Mélanie Bergeron et al. “Imaging performance of LabPET APD-based digital PET scanners for pre-clinical research”. In: *Physics in Medicine & Biology* 59.3 (2014), p. 661.

[137] Samuel España et al. “DigiPET: sub-millimeter spatial resolution small-animal PET imaging using thin monolithic scintillators”. In: *Physics in Medicine & Biology* 59.13 (2014), p. 3405.

[138] Kazuhiro Sato et al. “Performance evaluation of the small-animal PET scanner ClairvivoPET using NEMA NU 4-2008 standards”. In: *Physics in Medicine & Biology* 61.2 (2015), p. 696.

[139] Kenta Miwa et al. “Performance characteristics of a novel clustered multi-pinhole technology for simultaneous high-resolution SPECT/PET”. In: *Annals of nuclear medicine* 29.5 (2015), pp. 460–466.

[140] JM Vrigneaud et al. “Initial performance evaluation of a preclinical PET scanner available as a clip-on assembly in a sequential PET/MRI system”. In: *Physics in Medicine & Biology* 63.12 (2018), p. 125007.

[141] Srilalan Krishnamoorthy et al. “Performance evaluation of the MOLECUBES β-CUBE—a high spatial resolution and high sensitivity small animal PET scanner utilizing monolithic LYSO scintillation detectors”. In: *Physics in Medicine & Biology* 63.15 (2018), p. 155013.

[142] Willy Gsell et al. “Characterization of a preclinical PET insert in a 7 tesla MRI scanner: beyond NEMA testing”. In: *Physics in Medicine & Biology* 65.24 (2020-12-10), p. 245016.

[143] Zhonghua Kuang et al. “Design and performance of SIAT aPET: a uniform high-resolution small animal PET scanner using dual-ended readout detectors”. In: *Physics in Medicine & Biology* 65.23 (2020-11-27), p. 235013.

[144] Tom K Lewellen. “Recent developments in PET detector technology”. In: *Physics in Medicine & Biology* 53.17 (2008), R287.

[145] Junwei Du et al. “Physical properties of LYSO scintillator for NN-PET detectors”. In: *2009 2nd International Conference on Biomedical Engineering and Informatics*. IEEE. 2009, pp. 1–5.

[146] Jinhun Joung, Robert S. Miyaoka, and Thomas K. Lewellen. “cMiCE: a high resolution animal PET using continuous LSO with a statistics based positioning scheme”. In: *Nuclear Instruments and Methods in Physics Research Section A: Accelerators, Spectrometers, Detectors and Associated Equipment* 489.1 (2002-08-21), pp. 584–598.

[147] A Kolb et al. “Development of a novel depth of interaction PET detector using highly multiplexed G-APD cross-strip encoding”. In: *Medical physics* 41.8Part1 (2014), p. 081916.

[148] Min Sun Lee and Jae Sung Lee. "Depth-of-interaction measurement in a single-layer crystal array with a single-ended readout using digital silicon photomultiplier". In: *Physics in Medicine & Biology* 60.16 (2015), p. 6495.

[149] I Mohammadi et al. "Minimization of parallax error in positron emission tomography using depth of interaction capable detectors: methods and apparatus". In: *Biomedical Physics & Engineering Express* 5.6 (2019), p. 062001.

[150] Jeffrey P Schmall et al. "Comparison of large-area position-sensitive solid-state photomultipliers for small animal PET". In: *Physics in Medicine & Biology* 57.24 (2012), p. 8119.

[151] Junwei Du et al. "Performance of a high-resolution depth-encoding PET detector module using linearly-graded SiPM arrays". In: *Physics in Medicine & Biology* 63.3 (2018), p. 035035.

[152] Shyr-Yeu Lin et al. "Female infertility and disrupted angiogenesis are actions of specific follistatin isoforms". In: *Molecular Endocrinology* 22.2 (2008), pp. 415–429.

[153] Karen Schellong et al. "Increase of long-term 'diabesity'risk, hyperphagia, and altered hypothalamic neuropeptide expression in neonatally overnourished 'small-for-gestational-age'(SGA) rats". In: *PLoS One* 8.11 (2013), e78799.

[154] William W Moses. "Fundamental limits of spatial resolution in PET". In: *Nuclear Instruments and Methods in Physics Research Section A: Accelerators, Spectrometers, Detectors and Associated Equipment* 648 (2011), S236–S240.

[155] Craig S Levin and Edward J Hoffman. "Calculation of positron range and its effect on the fundamental limit of positron emission tomography system spatial resolution". In: *Physics in Medicine & Biology* 781 (1999).

[156] Jennifer R Stickel and Simon R Cherry. "High-resolution PET detector design: modelling components of intrinsic spatial resolution". In: *Physics in Medicine & Biology* 50.2 (2004), p. 179.

[157] Silin Ren, Yongfeng Yang, and Simon R Cherry. "Effects of reflector and crystal surface on the performance of a depth-encoding PET detector with dual-ended readout". In: *Medical physics* 41.7 (2014), p. 072503.

[158] Youfang Lai et al. "gPET: a GPU-based, accurate and efficient Monte Carlo simulation tool for PET". In: *Physics in Medicine & Biology* 64.24 (2019-12-13), p. 245002.

[159] Qian Yang et al. "Performance comparison of two signal multiplexing readouts for SiPM-based pet detector". In: *Physics in Medicine & Biology* 64.23 (2019), 23NT02.

[160] Sara St James et al. "Simulation study of spatial resolution and sensitivity for the tapered depth of interaction PET detectors for small animal imaging". In: *Physics in Medicine & Biology* 55.2 (2009), N63.

[161] Kuang Gong, Simon R Cherry, and Jinyi Qi. "On the assessment of spatial resolution of PET systems with iterative image reconstruction". In: *Physics in Medicine & Biology* 61.5 (2016), N193.

[162] Andre Z Kyme et al. "Open-field mouse brain PET: design optimisation and detector characterisation". In: *Physics in Medicine & Biology* 62.15 (2017), p. 6207.

[163] Eiji Yoshida et al. "Spatial resolution limits for the isotropic-3D PET detector Xtal cube". In: *Nuclear Instruments and Methods in Physics Research Section A: Accelerators, Spectrometers, Detectors and Associated Equipment* 728 (2013), pp. 107–111.

[164] Artem Zatcepin et al. “Improving depth-of-interaction resolution in pixellated PET detectors using neural networks”. In: *Physics in Medicine & Biology* 65.17 (2020), p. 175017.

[165] Seungeun Lee et al. “Recovery of inter-detector and inter-crystal scattering in brain PET based on LSO and GAGG crystals”. In: *Physics in Medicine & Biology* 65.19 (2020), p. 195005.

[166] Zhonghua Kuang et al. “Dual-ended readout small animal PET detector by using 0.5 mm pixelated LYSO crystal arrays and SiPMs”. In: *Nuclear Instruments and Methods in Physics Research Section A: Accelerators, Spectrometers, Detectors and Associated Equipment* 917 (2019), pp. 1–8.

[167] Junwei Du, Xiaowei Bai, and Simon R Cherry. “A depth-encoding PET detector for high resolution PET using 1 mm SiPMs”. In: *Physics in Medicine & Biology* 65.16 (2020), p. 165011.

[168] Yang Lv et al. “Mini EXPLORER II: a prototype high-sensitivity PET/CT scanner for companion animal whole body and human brain scanning”. In: *Physics in Medicine & Biology* 64.7 (2019), p. 075004.

[169] Simon R Cherry et al. “Total-body PET: maximizing sensitivity to create new opportunities for clinical research and patient care”. In: *Journal of Nuclear Medicine* 59.1 (2018), pp. 3–12.

[170] Zhen Tian et al. “An analytic linear accelerator source model for GPU-based Monte Carlo dose calculations”. In: *Physics in Medicine & Biology* 60.20 (2015), p. 7941.

[171] Reid Townson, Hilary Egglestone, and Sergei Zavgorodni. “A fast jaw-tracking model for VMAT and IMRT Monte Carlo simulations”. In: *Journal of applied clinical medical physics* 19.4 (2018), pp. 26–34.

[172] Zakaria Aboulbanine and Naima El Khayati. "Validation of a virtual source model of medical linac for Monte Carlo dose calculation using multi-threaded Geant4". In: *Physics in Medicine & Biology* 63.8 (2018), p. 085008.

[173] Stephen A Graves et al. "Commissioning and performance evaluation of RadCalc for the Elekta unity MRI-linac". In: *Journal of applied clinical medical physics* 20.12 (2019), pp. 54–62.

[174] Oskar Klein and Yoshio Nishina. "The scattering of light by free electrons according to Dirac's new relativistic dynamics". In: *Nature* 122.3072 (1928), pp. 398–399.

[175] Marc Desrosiers et al. "The importance of dosimetry standardization in radiobiology". In: *Journal of research of the National Institute of Standards and Technology* 118 (2013), p. 403.

[176] G. Poludniowski et al. "SpekCalc: a program to calculate photon spectra from tungsten anode x-ray tubes". In: *Physics in Medicine and Biology* 54.19 (2009-09-01), N433–N438.

[177] Yuncheng Zhong et al. "Dose rate determination for preclinical total body irradiation". In: *Physics in Medicine & Biology* 65.17 (2020), p. 175018.

[178] EJ Hall and AJ Giaccia. "Radiobiology for the Radiologist, Wolters Kluwer". In: (2012). Publisher: Lippincott Williams & Wilkins. Philadelphia, USA.

[179] D. Boscolo et al. "TRAX-CHEM: A pre-chemical and chemical stage extension of the particle track structure code TRAX in water targets". In: *Chemical Physics Letters* 698 (2018). Section: 11, pp. 11–18.

[180] Maximilian S Kreipl, Werner Friedland, and Herwig G Paretzke. "Time- and space-resolved Monte Carlo study of water radiolysis for photon, electron and ion irradiation". In: *Radiation and Environmental Biophysics* 48 (2008), p. 11.

[181] Werner Friedland et al. “Track structures , DNA targets and radiation effects in the biophysical Monte Carlo simulation code PARTRAC”. In: *Mutation Research - Fundamental and Molecular Mechanisms of Mutagenesis* 711 (2011), pp. 28–40.

[182] S Incerti et al. “Comparison of GEANT4 very low energy cross section models with experimental data in water”. In: *Medical Physics* 37 (2010), pp. 4692–4708.

[183] Mathieu Karamitros et al. “Modeling radiation chemistry in the Geant4 toolkit”. In: *Progress in nuclear science and technology* 2.0 (2011), pp. 503–508.

[184] M. Karamitros et al. “Diffusion-controlled reactions modeling in Geant4-DNA”. In: *Journal of Computational Physics* 274 (2014), pp. 841–882.

[185] M. A. Bernal et al. “Track structure modeling in liquid water: A review of the Geant4-DNA very low energy extension of the Geant4 Monte Carlo simulation toolkit”. In: *Physica Medica* 31 (2015), pp. 861–874.

[186] Ianik Plante. “A Monte–Carlo step-by-step simulation code of the non-homogeneous chemistry of the radiolysis of water and aqueous solutions. Part I: theoretical framework and implementation”. In: *Radiation and Environmental Biophysics* 50 (2011), pp. 389–403.

[187] Ianik Plante. “A Monte-Carlo step-by-step simulation code of the non-homogeneous chemistry of the radiolysis of water and aqueous solutions—Part II: calculation of radiolytic yields under different conditions of LET, pH, and temperature”. In: *Radiation and Environmental Biophysics* 50 (2011), pp. 405–415.

[188] Francesca Ballarini. “From DNA Radiation Damage to Cell Death: Theoretical Approaches”. In: *Journal of Nucleic Acids* 2010 (2010-10-05), p. 350608.

[189] M Dingfelder. “Track structure: time evolution from physics to chemistry”. In: *Radiation protection dosimetry* 122.1-4 (2006), pp. 16–21.

[190] Liming Zhang and Zhenyu Tan. "A new calculation on spectrum of direct DNA damage induced by low-energy electrons". In: *Radiation and environmental biophysics* 49.1 (2010), pp. 15–26.

[191] H Nikjoo et al. "Track-structure codes in radiation research". In: *Radiation Measurement* 41 (2006), pp. 1052–1074.

[192] J P Santos, F Parente, and Y-K Kim. "Cross sections for K-shell ionization of atoms by electron impact". In: *Journal of Physics B: Atomic, Molecular and Optical Physics* 36 (2003), pp. 4211–4224.

[193] Yong-Ki Kim, José Paulo Santos, and Fernando Parente. "Extension of the binary-encounter-dipole model to relativistic incident electrons". In: *Physical Review A* 62 (2000), p. 52710.

[194] Michael Dingfelder et al. "Electron inelastic-scattering cross sections in liquid water". In: *Radiation Physics and Chemistry* 53 (1998), pp. 1–18.

[195] JJ Olivero, RW Stagat, and AES Green. "Electron deposition in water vapor, with atmospheric applications". In: *Journal of Geophysical Research* 77.25 (1972), pp. 4797–4811.

[196] DJ Brenner and M Zaider. "A computationally convenient parameterisation of experimental angular distributions of low energy electrons elastically scattered off water vapour". In: *Physics in Medicine & Biology* 29.4 (1984), p. 443.

[197] Gert Moliere. "Theorie der streuung schneller geladener teilchen ii mehrfach- und vielfachstreuung". In: *Zeitschrift für Naturforschung A* 3.2 (1948), pp. 78–97.

[198] Charles E Melton et al. "Principles of mass spectrometry and negative ions". In: (1970).

[199] M. C. Bordage et al. “Implementation of new physics models for low energy electrons in liquid water in Geant4-DNA”. In: *Phys Med* 32.12 (2016-12). Edition: 2016/10/25, pp. 1833–1840.

[200] Sandrine Edel. “Modélisation du transport des photons et des électrons dans l’ADN plasmide”. PhD thesis. Thèse de Doctorat, Université Paul Sabatier, Toulouse, France, 2006.

[201] Zhen Tian, Steve B Jiang, and Xun Jia. “Accelerated Monte Carlo simulation on the chemical stage in water radiolysis using GPU”. In: *Physics in Medicine and Biology* 62 (2017), pp. 3081–3096.

[202] M A Bernal et al. “The invariance of the total direct DNA strand break yield”. In: *Medical Physics* 38 (2011), p. 4147.

[203] G. Kreth et al. “Radial Arrangement of Chromosome Territories in Human Cell Nuclei: A Computer Model Approach Based on Gene Density Indicates a Probabilistic Global Positioning Code”. In: *Biophysical Journal* 86.5 (2004-05-01), pp. 2803–2812.

[204] G Kreth, P Edelmann, and C Cremer. “Towards a dynamical approach for the simulation of large scale, cancer correlated chromatin structures”. In: *Ital. J. Anat. Embryol* 106 (2001), pp. 21–30.

[205] Sylvain Meylan et al. “Simulation of early DNA damage after the irradiation of a fibroblast cell nucleus using Geant4-DNA”. In: *Scientific Reports* 7 (2017), p. 11923.

[206] M Von Smoluchowski. “Three discourses on diffusion, brownian movements, and the coagulation of colloid particles”. In: *Phys. Z. Sowjet.* 17 (1916), pp. 557–571.

[207] Nathanael Lampe et al. “Mechanistic DNA damage simulations in Geant4-DNA Part 2: Electron and proton damage in a bacterial cell”. In: *Physica Medica* 48 (2018), pp. 146–155.

[208] Y. Hsiao and R. D. Stewart. “Monte Carlo simulation of DNA damage induction by x-rays and selected radioisotopes”. In: *Phys Med Biol* 53.1 (2008-01-07). Edition: 2008/01/10, pp. 233–44.

[209] Ph Bernhardt et al. “Modeling of ultrasoft X-ray induced DNA damage using structured higher order DNA targets”. In: *International Journal of Mass Spectrometry* 223 (2003), pp. 579–597.

[210] Yong-Ki Kim and M Eugene Rudd. “Binary-encounter-dipole model for electron-impact ionization”. In: *Physical Review A* 50.5 (1994), p. 3954.

[211] M Terrissol and A Beaudre. “Simulation of space and time evolution of radiolytic species induced by electrons in water”. In: *Radiation Protection Dosimetry* 31.1-4 (1990), pp. 175–177.

[212] D Emfietzoglou. “Inelastic cross-sections for electron transport in liquid water: a comparison of dielectric models”. In: *Radiation Physics and Chemistry* 66.6 (2003), pp. 373–385.

[213] E Huttel et al. “Screening corrections to the Rutherford cross section”. In: *Nuclear Instruments and Methods in Physics Research Section B: Beam Interactions with Materials and Atoms* 12.2 (1985), pp. 193–199.

[214] Nevill Francis Mott and Harrie Stewart Wilson Massey. “The theory of atomic collisions”. In: (1965).

[215] M Michaud, A Wen, and L Sanche. “Cross sections for low-energy (1–100 eV) electron elastic and inelastic scattering in amorphous ice”. In: *Radiation research* 159.1 (2003), pp. 3–22.

[216] Steven G Swarts et al. “Mechanisms of Direct Radiation Damage in DNA, Based on a Study of the Yields of Base Damage, Deoxyribose Damage, and Trapped Radicals in d(GCACGCGTGC)2”. In: *Radiation Research* 168 (2007), pp. 367–381.

[217] Pablo de Vera et al. “Simulation of the ion-induced shock waves effects on the transport of chemically reactive species in ion tracks”. In: *The European Physical Journal D* 72.9 (2018).

[218] Maximilian Stephan Kreipl, Werner Friedland, and Herwig G Paretzke. “Interaction of ion tracks in spatial and temporal proximity”. In: *Radiation and Environmental Biophysics* 48 (2009), p. 349.

[219] D Emfietzoglou and H Nikjoo. “Accurate Electron Inelastic Cross Sections and Stopping Powers for Liquid Water over the 0.1–10 keV Range Based on an Improved Dielectric Description of the Bethe Surface”. In: *Radiation Research* 120 (2007), pp. 110–120.

[220] A Munoz et al. “Single electron tracks in water vapour for energies below 100 eV”. In: *International Journal of Mass Spectrometry* 277 (2008), pp. 175–179.

[221] R Bruinsma et al. “Fluctuation-Facilitated Charge Migration along DNA”. In: *Physical Review Letters* 85 (2000), pp. 4393–4396.

[222] LA Morgan. “Electron impact excitation of water”. In: *Journal of Physics B: Atomic, Molecular and Optical Physics* 31.22 (1998), p. 5003.

[223] Hiroto Tachikawa, Akihiro Yabushita, and Masahiro Kawasaki. “Ab initio theoretical calculations of the electronic excitation energies of small water clusters”. In: *Physical Chemistry Chemical Physics* 13 (2011), pp. 20745–20749.

[224] Frédéric Martin et al. “DNA Strand Breaks Induced by 0–4 eV Electrons: The Role of Shape Resonances”. In: *Physical Review Letters* 93 (2004), p. 68101.

[225] F Ballarini et al. “Stochastic aspects and uncertainties in the prechemical and chemical stages of electron tracks in liquid water: a quantitative analysis based on Monte Carlo simulations”. In: *Radiation and Environmental Biophysics* 39 (2000), pp. 179–188.

[226] Qingqing Guo et al. “How far can hydroxyl radicals travel? An electrochemical study based on a DNA mediated electron transfer process”. In: *Chemical Communications* 47 (2011), pp. 11906–11908.

[227] Liset de la Fuente Rosales et al. “Accounting for radiation-induced indirect damage on DNA with the Geant 4-DNA code”. In: *Physica Medica* 51 (2018), pp. 108–116.

[228] Nathanael Lampe et al. “Mechanistic DNA damage simulations in Geant4-DNA part 1: A parameter study in a simplified geometry”. In: *Physica Medica* 48 (2018), pp. 135–145.

[229] Jake C. Forster et al. “Monte Carlo Simulation of the Oxygen Effect in DNA Damage Induction by Ionizing Radiation”. In: *Radiation Research* 190 (2018), pp. 248–261.

[230] D. E. Charlton and J. L. Humm. “A Method of Calculating Initial DNA Strand Breakage Following the Decay of Incorporated 125I”. In: *International Journal of Radiation Biology* 53.3 (1988-01-01), pp. 353–365.

[231] Hooshang Nikjoo and Peter Girard. “A model of the cell nucleus for DNA damage calculations”. In: *International Journal of Radiation Biology* 88 (2012), pp. 87–97.

[232] H Nikjoo et al. “Track structure in radiation biology: theory and applications”. In: *International Journal of Radiation Biology* 73 (1998), pp. 355–364.

[233] W. Friedland et al. “Comprehensive track-structure based evaluation of DNA damage by light ions from radiotherapy-relevant energies down to stopping”. In: *Scientific Reports* 7 (2017), pp. 1–15.

[234] S. Incerti et al. “THE GEANT4-DNA PROJECT”. In: *International Journal of Modeling, Simulation, and Scientific Computing* 01.2 (2010), pp. 157–178.

[235] Shubhadeep Purkayastha, Jamie R Milligan, and William A Bernhard. “On the chemical yield of base lesions, strand breaks, and clustered damage generated in plasmid DNA by the direct effect of X rays”. In: *Radiation research* 168 (2007), pp. 357–366.

[236] Bulent Aydogan et al. “Monte Carlo Simulations of Site-Specific Radical Attack to DNA Bases”. In: *Radiation Research* 169 (2008), pp. 223–231.

[237] Peggy L Olive, Danuta Wlodek, and Judit P Banath. “DNA double-strand breaks measured in individual cells subjected to gel electrophoresis”. In: *Cancer research* 51.17 (1991), pp. 4671–4676.

[238] M. Belli et al. “DNA DSB induction and rejoining in V79 cells irradiated with light ions: a constant field gel electrophoresis study”. In: *Int J Radiat Biol* 76.8 (2000-08). Edition: 2000/08/18, pp. 1095–104.

[239] Preety M. Sharma et al. “High Throughput Measurement of γH2AX DSB Repair Kinetics in a Healthy Human Population”. In: *PLOS ONE* 10.3 (2015), e0121083.

[240] Hongyu Zhu et al. “A parameter sensitivity study for simulating DNA damage after proton irradiation using TOPAS-nBio”. In: *Physics in Medicine & Biology* 65.8 (2020), p. 085015.

[241] J. Ramos-Mendez et al. “Monte Carlo simulation of chemistry following radiolysis with TOPAS-nBio”. In: *Physics in Medicine & Biology* 63.10 (2018-05-17), p. 105014.

[242] K. P. Chatzipapas et al. “Ionizing Radiation and Complex DNA Damage: Quantifying the Radiobiological Damage Using Monte Carlo Simulations”. In: *Cancers (Basel)* 12.4 (2020-03-26). Edition: 2020/04/01.

[243] Herwig G Paretzke. “Radiation track structure theory”. In: *J Kinetics of Non-Homogeneous Processes* (1987).

[244] F. A. Cucinotta et al. “Track structure model for damage to mammalian cell cultures during solar proton events”. In: *Int J Rad Appl Instrum D* 20.1 (1992-01). Edition: 1992/01/01, pp. 177–84.

[245] V. Michalik and M. Begusova. “Target model of nucleosome particle for track structure calculations and DNA damage modelling”. In: *Int J Radiat Biol* 66.3 (1994-09). Edition: 1994/09/01, pp. 267–77.

[246] H Nikjoo et al. “Track-structure codes in radiation research”. In: *Radiation Measurements* 41.9-10 (2006), pp. 1052–1074.

[247] Dimitris Emfietzoglou et al. “Inelastic cross sections for low-energy electrons in liquid water: exchange and correlation effects”. In: *Radiation research* 180.5 (2013), pp. 499–513.

[248] I Kyriakou, S Incerti, and Z Francis. “Improvements in geant4 energy-loss model and the effect on low-energy electron transport in liquid water”. In: *Medical physics* 42.7 (2015), pp. 3870–3876.

[249] M. Dingfelder. “Upyeard model for dielectric response function of liquid water”. In: *Appl Radiat Isot* 83 Pt B (2014-01). Edition: 2013/02/19, pp. 142–7.

[250] Takeshi Kai et al. “Cross sections, stopping powers, and energy loss rates for rotational and phonon excitation processes in liquid water by electron impact”. In: *Radiation Physics and Chemistry* 108 (2015), pp. 13–17.

[251] W-G Shin et al. “Development of a new Geant4-DNA electron elastic scattering model for liquid-phase water using the ELSEPA code”. In: *Journal of Applied Physics* 124.22 (2018), p. 224901.

[252] E Pomplun. “A new DNA target model for track structure calculations and its first application to I-125 Auger electrons”. In: *International journal of radiation biology* 59.3 (1991), pp. 625–642.

[253] J Schuemann et al. “TOPAS-nBio : An Extension to the TOPAS Simulation Toolkit for Cellular and Sub-cellular Radiobiology”. In: *Radiation Research* 191 (2019), pp. 125–138.

[254] Louis Harold Gray et al. “The concentration of oxygen dissolved in tissues at the time of irradiation as a factor in radiotherapy”. In: *The British journal of radiology* 26.312 (1953), pp. 638–648.

[255] Cherupally KK Nair, Dillip K Parida, and Taisei Nomura. “Radioprotectors in radiotherapy”. In: *Journal of radiation research* 42.1 (2001), pp. 21–37.

[256] D. Boscolo et al. “Impact of Target Oxygenation on the Chemical Track Evolution of Ion and Electron Radiation”. In: *Int J Mol Sci* 21.2 (2020-01-09). Edition: 2020/01/16.

[257] D Sakata et al. “An implementation of discrete electron transport models for gold in the Geant4 simulation toolkit”. In: *Journal of Applied Physics* 120.24 (2016), p. 244901.

[258] Youfang Lai, Xun Jia, and Yujie Chi. “Modeling the effect of oxygen on the chemical stage of water radiolysis using GPU-based microscopic Monte Carlo simulations, with an application in FLASH radiotherapy”. In: *Physics in Medicine & Biology* 66.2 (2021), p. 025004.

[259] Youfang Lai et al. “A new open-source GPU-based microscopic Monte Carlo simulation tool for the calculations of DNA damages caused by ionizing radia-

tion — Part II: sensitivity and uncertainty analysis". In: *Medical Physics* 47.4 (2020), pp. 1971–1982.

[260] Harald Paganetti et al. "Relative biological effectiveness (RBE) values for proton beam therapy". In: *International Journal of Radiation Oncology* Biology* Physics* 53.2 (2002), pp. 407–421.

[261] E. T. Vitti and J. L. Parsons. "The Radiobiological Effects of Proton Beam Therapy: Impact on DNA Damage and Repair". In: *Cancers* 11.7 (2019-07-05). Edition: 2019/07/10.

[262] Kyle G. Reeves and Yosuke Kanai. "Electronic Excitation Dynamics in Liquid Water under Proton Irradiation". In: *Scientific reports* 7 (2017), pp. 40379–40379.

[263] M. E. Rudd et al. "Electron production in proton collisions with atoms and molecules: energy distributions". In: *Reviews of Modern Physics* 64.2 (1992), pp. 441–490.

[264] Ianik Plante and Francis A. Cucinotta. "Ionization and excitation cross sections for the interaction of HZE particles in liquid water and application to Monte Carlo simulation of radiation tracks". In: *New Journal of Physics* 10.12 (2008-12-04), p. 125020.

[265] Michael Dingfelder, Mitio Inokuti, and Herwig G Paretzke. "Inelastic-collision cross sections of liquid water for interactions of energetic protons". In: *Radiation physics and chemistry* 59.3 (2000), pp. 255–275.

[266] W. Booth and I. S. Grant. "The energy loss of oxygen and chlorine ions in solids". In: *Nuclear Physics* 63.3 (1965-03-01), pp. 481–495.

[267] M. Dingfelder et al. "Heavy ion track structure simulations in liquid water at relativistic energies". In: *Radiation Protection Dosimetry* 122.1 (2006), pp. 26–27.

[268] M.E. Rudd. “Cross Sections for Production of Secondary Electrons by Charged Particles”. In: *Radiation Protection Dosimetry* 31.1 (1990), pp. 17–22.

[269] G. J. Kutcher and A. E. S. Green. “A Model for Energy Deposition in Liquid Water”. In: *Radiation Research* 67.3 (1976), pp. 408–425.

[270] V Cobut et al. “Monte Carlo simulation of fast electron and proton tracks in liquid water-I. Physical and physicochemical aspects”. In: *Radiation Physics and Chemistry* 51.3 (1998-03-01), pp. 229–243.

[271] George V. Buxton et al. “Critical Review of rate constants for reactions of hydrated electrons, hydrogen atoms and hydroxyl radicals in Aqueous Solution”. In: *Journal of Physical and Chemical Reference Data* 17.2 (1988-04-01), pp. 513–886.

[272] He Wang and Oleg N Vassiliev. “Radial dose distributions from protons of therapeutic energies calculated with Geant4-DNA”. In: *Physics in Medicine and Biology* 59.14 (2014-06-13), pp. 3657–3668.

[273] H Nikjoo et al. “Computational Approach for Determining the Spectrum of DNA Damage Induced by Ionizing Radiation”. In: 583 (2001), pp. 577–583.

[274] H Nikjoo et al. “Radiation track , DNA damage and response — a review”. In: *Reports on Progress in Physics* 79 (2016), p. 116601.

[275] Hooshang Nikjoo et al. “Can Monte Carlo track structure codes reveal reaction mechanism in DNA damage and improve radiation therapy ?” In: *Radiation Physics and Chemistry* 77 (2008), pp. 1270–1279.

[276] V. Lemelin et al. “Low energy (1-19 eV) electron scattering from condensed thymidine (dT) I: absolute vibrational excitation cross sections”. In: *Phys Chem Chem Phys* 21.43 (2019-11-07). Edition: 2019/09/11, pp. 23808–23817.

[277] Dimitris Emfietzoglou, George Papamichael, and Hooshang Nikjoo. "Monte Carlo electron track structure calculations in liquid water using a new model dielectric response function". In: *Radiation research* 188.3 (2017), pp. 355–368.

[278] José Ramos-Méndez et al. "Independent reaction times method in Geant4-DNA: Implementation and performance". In: *Medical Physics* 47.11 (2020), pp. 5919–5930.

[279] W-G Shin et al. "Evaluation of the influence of physical and chemical parameters on water radiolysis simulations under MeV electron irradiation using Geant4-DNA". In: *Journal of Applied Physics* 126.11 (2019), p. 114301.

[280] Hooshang Nikjoo et al. "Heavy charged particles in radiation biology and biophysics". In: *New journal of physics* 10.7 (2008), p. 075006.

[281] I Kyriakou et al. "The impact of new Geant4-DNA cross section models on electron track structure simulations in liquid water". In: *Journal of Applied Physics* 119.19 (2016), p. 194902.

[282] Sebastien Incerti et al. "Geant4-DNA example applications for track structure simulations in liquid water: A report from the Geant4-DNA Project". In: *Medical physics* 45.8 (2018), e722–e739.

[283] Yusuke Matsuya et al. "Modeling of yield estimation for DNA strand breaks based on Monte Carlo simulations of electron track structure in liquid water". In: *Journal of Applied Physics* 126.12 (2019), p. 124701.

[284] S. Meylan et al. "Geant4-DNA simulations using complex DNA geometries generated by the DnaFabric tool". In: *Computer Physics Communications* 204 (2016), pp. 159–169.

[285] CCW Verlackt et al. "Atomic-scale insight into the interactions between hydroxyl radicals and DNA in solution using the ReaxFF reactive force field". In: *New Journal of Physics* 17.10 (2015), p. 103005.

[286] Jan Schuemann et al. “A new standard DNA damage (SDD) data format”. In: *Radiation research* 191.1 (2018), pp. 76–92.

[287] Georgios Kalantzis, Dimitrios Emfietzoglou, and Panagiotis Hadjidoukas. “A unified spatio-temporal parallelization framework for accelerated Monte Carlo radiobiological modeling of electron tracks and subsequent radiation chemistry”. In: *Computer Physics Communications* 183.8 (2012), pp. 1683–1695.

[288] Werner Friedland et al. “Simulation of DNA Damage after Proton Irradiation”. In: *Radiation Research* 159.3 (2003), pp. 401–410.

[289] W. Z. Xie et al. “Simulation on the molecular radiosensitization effect of gold nanoparticles in cells irradiated by x-rays”. In: *Physics in Medicine and Biology* 60.16 (2015-07-30), pp. 6195–6212.

[290] Fada Guan et al. “Spatial mapping of the biologic effectiveness of scanned particle beams: towards biologically optimized particle therapy”. In: *Scientific reports* 5.1 (2015), pp. 1–10.

[291] X. J. Musacchia and R. E. Barr. “Survival of Whole-Body-Irradiated Hibernating and Active Ground Squirrels; Citellus tridecemlineatus”. In: *Radiation Research* 33.2 (1968), pp. 348–356.

[292] Bernard N Jaroslow et al. “Radiosensitivity of ileum crypt cells in hibernating, arousing, and awake ground squirrels (Citellus tridecemlineatus)”. In: *Radiation research* 66.3 (1976), pp. 566–575.

[293] Brian A. Hrycushko et al. “Local Hypothermia as a Radioprotector of the Rectal Wall During Prostate Stereotactic Body Radiation Therapy”. In: *International Journal of Radiation Oncology*Biology*Physics* 98.1 (2017-05-01), pp. 75–82.

[294] Li Dang et al. “Radioprotective effect of hypothermia on cells–a multiparametric approach to delineate the mechanisms”. In: *International journal of radiation biology* 88.7 (2012), pp. 507–514.

[295] Nobutoshi Kawamura et al. “Multiple effects of hypothermia on inflammatory response following ischemia–reperfusion injury in experimental ischemic neuropathy”. In: *Experimental neurology* 202.2 (2006), pp. 487–496.

[296] Toshiharu Sakurai et al. “Low temperature protects mammalian cells from apoptosis initiated by various stimuli in vitro”. In: *Experimental cell research* 309.2 (2005), pp. 264–272.

[297] Brandon J Baird et al. “Hypothermia postpones DNA damage repair in irradiated cells and protects against cell killing”. In: *Mutation Research/Fundamental and Molecular Mechanisms of Mutagenesis* 711.1 (2011), pp. 142–149.

[298] Halina Lisowska et al. “Hypothermia modulates the DNA damage response to ionizing radiation in human peripheral blood lymphocytes”. In: *International Journal of Radiation Biology* 94 (2018), pp. 551–557.

[299] Kinga Brzozowska et al. “Effect of temperature during irradiation on the level of micronuclei in human peripheral blood lymphocytes exposed to X-rays and neutrons”. In: *International journal of radiation biology* 85.10 (2009), pp. 891–899.

[300] Keith J Laidler. *Chemical Kinetics*. Pearson Education Inc. and Dorling Kindersley Publishing Inc., 1987.

[301] Allen John Elliot. “A pulse radiolysis study of the temperature dependence of reactions involving H, OH and e-aq in aqueous solutions”. In: *International Journal of Radiation Applications and Instrumentation. Part C. Radiation Physics and Chemistry* 34.5 (1989), pp. 753–758.

[302] Tibor Erdey-Grúz and Tibor Erdey-Grúz. *Transport phenomena in aqueous solutions*. John Wiley & Sons, 1974.

[303] J Daniel Gezelter, Eran Rabani, and BJ Berne. "Calculating the hopping rate for diffusion in molecular liquids: CS 2". In: *The Journal of chemical physics* 110.7 (1999), pp. 3444–3452.

[304] Tikvah Alper and P Howard-Flanders. "Role of oxygen in modifying the radiosensitivity of E. coli B". In: *Nature* 178.4540 (1956), pp. 978–979.

[305] Anthony Colliaux et al. "Simulation of ion-induced water radiolysis in different conditions of oxygenation". In: *Nuclear Instruments and Methods in Physics Research Section B: Beam Interactions with Materials and Atoms* 365 (2015). Section: 596, pp. 596–605.

[306] J. Bourhis et al. "Clinical translation of FLASH radiotherapy: Why and how?" In: *Radiother Oncol* 139 (2019-10). Edition: 2019/06/30, pp. 11–17.

[307] Vincent Favaudon et al. "Ultrahigh dose-rate FLASH irradiation increases the differential response between normal and tumor tissue in mice". In: *Science Translational Medicine* 6 (2014), 245ra93 LP –245ra93.

[308] Pierre Montay-gruel et al. "X-rays can trigger the FLASH effect : Ultra-high dose-rate synchrotron light source prevents normal brain injury after whole brain irradiation in mice". In: *Radiotherapy and Oncology* 129 (2018), pp. 582–588.

[309] Pierre Montay-gruel et al. "Irradiation in a flash : Unique sparing of memory in mice after whole brain irradiation with dose rates above 100 Gy / s". In: *Radiotherapy and Oncology* 124 (2017), pp. 365–369.

[310] Manuela Buonanno, Veljko Grilj, and David J Brenner. "Biological effects in normal cells exposed to FLASH dose rate protons". In: *Radiotherapy and Oncology* 139 (2019), pp. 51–55.

[311] Marie-Catherine Vozenin et al. “The Advantage of FLASH Radiotherapy Confirmed in Mini-pig and Cat-cancer Patients”. In: *Clinical Cancer Research* 25.1 (2019). Section: 35, pp. 35–42.

[312] Douglas R. Spitz et al. “An integrated physico-chemical approach for explaining the differential impact of FLASH versus conventional dose rate irradiation on cancer and normal tissue responses”. In: *Radiotherapy and Oncology* 139 (2019), pp. 23–27.

[313] P. Wilson et al. “Revisiting the ultra-high dose rate effect: implications for charged particle radiotherapy using protons and light ions”. In: *Br J Radiol* 85.1018 (2012-10). Edition: 2012/04/13, e933–9.

[314] H. Weiss et al. “Oxygen Depletion in Cells Irradiated at Ultra-high Dose-rates and at Conventional Dose-rates”. In: *International Journal of Radiation Biology and Related Studies in Physics, Chemistry and Medicine* 26.1 (1974-01-01), pp. 17–29.

[315] Guillem Pratx and Daniel S. Kapp. “A computational model of radiolytic oxygen depletion during FLASH irradiation and its effect on the oxygen enhancement ratio”. In: *Physics in Medicine & Biology* 64.18 (2019-09-11), p. 185005.

[316] R. H. Wenger et al. “Frequently asked questions in hypoxia research”. In: *Hypoxia (Auckl)* 3 (2015). Edition: 2016/10/25, pp. 35–43.

[317] S. R. McKeown. “Defining normoxia, physoxia and hypoxia in tumours-implications for treatment response”. In: *The British journal of radiology* 87.1035 (2014), pp. 20130676–20130676.

[318] K. Zhang et al. “Dissolved oxygen concentration in the medium during cell culture: Defects and improvements”. In: *Cell Biol Int* 40.3 (2016-03). Edition: 2015/12/10, pp. 354–60.

[319] David Robert Grimes et al. “A method for estimating the oxygen consumption rate in multicellular tumour spheroids”. In: *Journal of The Royal Society Interface* 11.92 (2014-03-06), p. 20131124.

[320] I. S. Longmuir et al. “Nonclassical respiratory activity of tissue slices”. In: *Microvascular Research* 3.2 (1971-04-01), pp. 125–141.

[321] David Robert Grimes and Mike Partridge. “A mechanistic investigation of the oxygen fixation hypothesis and oxygen enhancement ratio”. In: *Biomedical physics & engineering express* 1.4 (2015), p. 045209.

[322] Rudi Labarbe et al. “A physicochemical model of reaction kinetics supports peroxyl radical recombination as the main determinant of the FLASH effect”. In: *Radiotherapy and Oncology* (2020).

[323] Sophie Le Caër. “Water Radiolysis: Influence of Oxide Surfaces on H2 Production under Ionizing Radiation”. In: *Water* 3.1 (2011), pp. 235–253.

[324] J. A. Imlay and S. Linn. “DNA damage and oxygen radical toxicity”. In: *Science* 240.4857 (1988), p. 1302.

[325] Gabriel Adrian et al. “The FLASH effect depends on oxygen concentration”. In: *The British Journal of Radiology* 93.1106 (2020), p. 20190702.

[326] Jeannette Jansen et al. “Does FLASH deplete Oxygen? Experimental Evaluation for Photons, Protons and Carbon Ions”. In: *arXiv preprint arXiv:2102.12762* (2021).

[327] BD Michael. “A multiple-radical model for radiation action on DNA and the dependence of OER on LET”. In: *International journal of radiation biology* 69.3 (1996), pp. 351–358.

[328] David J Carlson, Robert D Stewart, and Vladimir A Semenenko. “Effects of oxygen on intrinsic radiation sensitivity: A test of the relationship between

aerobic and hypoxic linear-quadratic (LQ) model parameters a". In: *Medical physics* 33.9 (2006), pp. 3105–3115.

[329] T. Wenzl and J. J. Wilkens. "Modelling of the oxygen enhancement ratio for ion beam radiation therapy". In: *Phys Med Biol* 56.11 (2011-06-07). Edition: 2011/05/05, pp. 3251–68.

[330] A. Ayala, M. F. Munoz, and S. Arguelles. "Lipid peroxidation: production, metabolism, and signaling mechanisms of malondialdehyde and 4-hydroxy-2-nonenal". In: *Oxid Med Cell Longev* 2014 (2014). Edition: 2014/07/08, p. 360438.

[331] P Howard-Flanders and D Moore. "The time interval after pulsed irradiation within which injury to bacteria can be modified by dissolved oxygen: I. A search for an effect of oxygen 0.02 second after pulsed irradiation". In: *Radiation Research* 9.4 (1958), pp. 422–437.

[332] DE Charlton and R Sephton. "A relationship between microdosimetric spectra and cell survival for high-LET irradiation". In: *International journal of radiation biology* 59.2 (1991), pp. 447–457.

[333] W. Wang et al. "Modelling of Cellular Survival Following Radiation-Induced DNA Double-Strand Breaks". In: *Sci Rep* 8.1 (2018-11-01). Edition: 2018/11/06, p. 16202.

[334] Y. Matsuya et al. "A theoretical cell-killing model to evaluate oxygen enhancement ratios at DNA damage and cell survival endpoints in radiation therapy". In: *Phys Med Biol* 65.9 (2020-04-28). Edition: 2020/03/07, p. 095006.

[335] H Iwata et al. "Oxygen Enhancement Ratio of Proton Beams: The Precise Report of the Same Institution's Experiments Using the Clinical Equipments". In: *International Journal of Radiation Oncology• Biology• Physics* 90.1 (2014), S779.

[336] Tatiana Wenzl and Jan J Wilkens. "Theoretical analysis of the dose dependence of the oxygen enhancement ratio and its relevance for clinical applications". In: *Radiation oncology* 6.1 (2011), pp. 1–9.

[337] EDWIN J Hart and Michael Anbar. "The hydrated electron". In: *Survey of Progress in Chemistry*. Vol. 5. Academic Press London, 1969, pp. 129–182.

[338] M Kwan, J Woo, and T Kwok. "The standard oxygen consumption value equivalent to one metabolic equivalent (3.5 ml/min/kg) is not appropriate for elderly people". In: *International journal of food sciences and nutrition* 55.3 (2004), pp. 179–182.

[339] Scott Brady. *Basic neurochemistry: molecular, cellular and medical aspects*. Elsevier, 2005.

[340] Konrad P. Nesteruk and Serena Psoroulas. "FLASH Irradiation with Proton Beams: Beam Characteristics and Their Implications for Beam Diagnostics". In: *Applied Sciences* 11.5 (2021). Section: 2170.

[341] A. Darafsheh et al. "Feasibility of proton FLASH irradiation using a synchrocyclotron for preclinical studies". In: *Med Phys* 47.9 (2020-09). Edition: 2020/05/27, pp. 4348–4355.

[342] Zhen Tian et al. "Moving GPU-Open CL-based Monte Carlo dose calculation toward clinical use: Automatic beam commissioning and source sampling for treatment plan dose calculation". In: *Journal of applied clinical medical physics* 18.2 (2017), pp. 69–84.

[343] Tiina Roose, S Jonathan Chapman, and Philip K Maini. "Mathematical models of avascular tumor growth". In: *SIAM review* 49.2 (2007), pp. 179–208.

[344] Parisa Yazdjerdi et al. "Reinforcement learning-based control of tumor growth under anti-angiogenic therapy". In: *Computer methods and programs in biomedicine* 173 (2019), pp. 15–26.

BIOGRAPHICAL STATEMENT

Youfang Lai was born in Yichun, China, in 1994. He received both B.S. degree in Physics and M.S. degree in Condensed Matter Physics from Peking University, China, in 2015 and 2018, respectively. From 2018 to 2021, he was with the Department of Physics in The University of Texas at Arlington as a graduate student and took medical physics courses in University of Texas Southwestern Medical Center in the same time. His research was also affiliated with innovative Technology Of Radiotherapy Computation and Hardware (iTORCH) laboratory in University of Texas Southwestern Medical Center. The research was mainly about GPU-based Monte Carlo applications in radiotherapy and radio-imaging under supervision of Dr. Chi and Dr. Jia.